Stand-Alone Submission to the Decadal Survey

Previously Overlooked/Ignored Electronic Charge Carriers in Rocks

Friedemann Freund

NASA Ames Research Center

Department of Physics
San Jose State University
San Jose, CA 95192-0106

Earth Science Division, 242-4
Moffett Field, CA 94035-1000
friedemann.t.freund@nasa.gov

Principal Investigator
Carl Sagan Center, SETI Institute
Mountain View, CA 94043

I would like to draw the attention of members of the Decadal Survey Committee to a rather fundamental discovery, which (I believe) will have a major impact on the Earth and Planetary Sciences in the coming years.

We have been able to establish that all igneous and high-grade metamorphic rocks, e.g. essentially the majority of the rocks in Earth's crust, presumably also on Mars, Venus and Moon, contain electronic charge carriers that have been overlooked/ignored. These charge carriers pre-exist in the constituent minerals, albeit in an electrically inactive, dormant form. The charge carriers are activated by (i) heat, (ii) stress and probably (iii) UV. They have the unusual capability to flow out of the heated/stressed volume and to spread into the surrounding colder/unstressed rocks. The charge carriers travel fast and far. Their phase velocity is of the order of 200 m/sec. They can propagate over meters in laboratory experiments, presumably kilometers to tens of kilometers in the field. They traverse solid rocks, sedimentary rocks, sand and soil. They set up electrical potentials. They flow into water, oxidizing water to hydrogen peroxide. When they arrive at the Earth's surface, they cause a plethora of interesting effects, both physical and chemical.

The discovery of these electronic charge carriers has been long in coming. The earliest observations date back to the 1970's and 1980's, when they were first characterized in single crystal oxides and silicates. For several years we covered the solid state physics aspects, deploying a wide variety of techniques. Unfortunately, though the distinctly interdisciplinary importance of these charge carriers soon became obvious, the Earth and Planetary Science communities at large did not take notice.

Lately the widespread presence of these charge carriers has attracted some attention. Understanding what they are and how they behave in the Earth's crust when rocks are subjected to increasing levels of tectonic stress provides an opportunity to decipher a wide range of signals, which the Earth reportedly sends out before major earthquakes.

I apologize for not having prepared a full report for consideration by the Decadal Survey Committee members. Instead I append a collection of recent papers to the topic of these electronic charge carriers in rocks that have just been published or will come out soon in EPSL, J Atmosph. Solar-Terrestr. Phys., Acta Geophys. and J. Asian Earth Sci. as well as in Contemporary Physics. I also add an Abstract of a presentation to be given at the AGU Fall 2009 meeting on a topic related to Venus.

Friedemann Freund Sept. 15, 2009

Pre-Earthquake Signals

Introduction to Basic Solid State Processes

Friedemann Freund

NASA Ames Research Center, MS 242-4
Moffett Field, CA 94035-1000
e-mail friedemann.t.freund@nasa.gov
++++++++++++++++++++++++++++++
Department of Physics
San Jose State University
++++++++++++++++++++++++++++++
Principal Investigator
Carl Sagan Center (CSC), SETI Institute
++++++++++++++++++++++++++++++

Abstract

Prior to large earthquakes the Earth reportedly sends out transient signals, often subtle and fleeting, sometimes strong. They consist of local magnetic field variations, electromagnetic (EM) emissions over a wide range of frequencies, atmospheric and ionospheric phenomena. Since the processes deep in the Earth's crust and at the Earth surface capable of producing such a wide range of phenomena are basically not understood, the field of pre-earthquake science is in disarray. Studies of O^{2-}/O^{-} valence fluctuations in the oxygen anion sublattice in MgO single crystals has led to the discovery of positive holes charge carriers $h^{\bullet}$, They also exist in rocks. Normally the $h^{\bullet}$ charge carriers lie dormant in the matrix of rock-forming minerals in the form of self-trapped positive hole pairs, equivalent to peroxy bonds, $O_3Si/^{OO}\backslash SiO_3$. When stresses are applied, the peroxy bonds break, releasing $h^{\bullet}$ charge carriers and causing the stressed rock volume to turn into a battery from where electric currents can flow out. The current outflow will generate local magnetic field variations and EM emissions. When the $h^{\bullet}$ charge carriers arrive at the Earth's surface, they lead to a range of effects including massive ionization of air at the ground-air interface, upward expansion of the volume of ionized air, which in turn leads to perturbations in the ionosphere. Recombination of $h^{\bullet}$ charge carriers at the surface leads to a spectroscopically distinct, non-thermal IR emission and possibly to the emission of electronically excited O atoms, which luminesce at 630 nm. Understanding the underlying solid state processes opens a window of opportunity to study the wide range of non-seismic pre-earthquake signals from a unifying solid state physics perspective.

Keywords: Earthquake; pre-earthquake signals; valence fluctuations; peroxy; positive holes.

1 Introduction

1.1 Scale of Earthquakes

Earthquakes range from nearly imperceptible seismic noise that registers on the Richter scale around or below magnitude (M) 1 to large catastrophic events. Among the most powerful events in recent history are the M=9.3 Chilean earthquake of 1961 [1], the M=9 Alaskan "Good Friday" earthquake of 1964 [2], and the Dec. 26, 2004 M=9.3 earthquake off the coast of Sumatra, which created a tsunami across the Indian Ocean with disastrous consequences [3]. The Richter scale is logarithmic with energy increasing by a factor of 30 per magnitude increment. Between an M=1 event and an M=9 event the total seismic energy released increases by a factor of $\sim 10^{12}$, from about 10^8 to 10^{20} Joule, the equivalent of an explosion of 3 kilogram TNT (tri-nitro-toluene) versus an explosion of nearly 3 gigatons.

Given the enormous power unleashed by large earthquakes one would think that it should be possible to detect early signs during the build-up of tectonic stresses. The stakes are high, given the extensive damage that large earthquakes can cause and the great potential for loss of life. Uyeda et al. [4] have recently given a status report on the entanglement between earthquake science and politics, which – for decades – has effectively prevented any concerted effort to study pre-earthquake (pre-EQ) signals. Prominent seismologists have declared categorically: "Earthquakes cannot be predicted" [5]. To understand such a statement, it behooves us to look at the tools of seismology.

1.2 Tools of Seismology

Earthquakes can be viewed as flashlights, which illuminate the interior of the Earth. The tools of seismology are designed to analyze the reflected and refracted P and S waves, compressional and traverse respectively, which travel at different velocities. Such studies provide unique information about the Earth's layered structure from the crust through the mantle to the core as well as finer details within the Earth's crust such as the faults, along which earthquakes often take place.

The seismology approach to "predicting" earthquakes consists of estimating the probability of future seismic events by collecting as many data as possible from past earthquakes and combining them with geodesic data on how fast tectonic plates, or sections of plates, move relative to each other along given faults. The seismological approach is thus inherently retrospective, leading to wide uncertainty windows, typically on the order of years, often 30 years and more [6-8]. Occasionally small to medium-sized "foreshocks" precede large events [9]. Unfortunately, no earthquake can ever be called a "foreshock" until the main shock has occurred. There are also cases where large earthquakes strike along faults, which have not ruptured in historical times. In the absence of a prior seismic record seismology lacks the tools to provide even an estimate of a future event. For instance, the M=7.9 Wenchuan earthquake of May 12, 2008 in China's Sichuan Province occurred along a fault that seems not have failed in historical time. Hence, seismologists in charge of providing seismic hazard assessments for this region had to admit that this earthquake took them by surprise [10].

At the same time the literature is replete with reports about non-seismic pre-EQ signals that have been observed in all seismically active regions of the world. As Tributsch [11] describes in his classical book "When the Snakes Awake", some these reports, notably those on animal behavior, have come down to us from 2500 years ago. Others are part of the oral history of peoples living

under the constant threat of destructive earthquakes. Others yet have been added on the basis of modern ground-based and air-borne or satellite-borne instrumentation [12, 13].

Reported non-seismic pre-EQ phenomena include fog, haze, clouds and other atmospheric effects, low to ultralow-frequency electromagnetic emissions from within the Earth, increased noise in the radiofrequency range, anomalous infrared emission from areas around future epicenters as seen in night-time infrared satellite images, and ionospheric perturbations.

Indeed, from a physics perspective, the notion is hard to accept that huge stresses accumulating in the Earth's crust, capable of releasing seismic energy equivalent to megatons TNT, even gigatons explosions should not lead to some form of precursory signals.

In this report evidence will be presented that many, if not all of the reported pre-EQ signals can be traced to a single solid state process taking place in rocks when they are subjected to deviatoric stresses. It involves the activation of dormant electronic charge carriers in the rocks. In the past the very presence of these electronic charge carriers had been overlooked or ignored.

1.3 Controversy Surrounding Pre-Earthquake Signals

What had not been available until now was a deeper understanding of the physical cause, or causes, of the wide range of reported pre-EQ phenomena. Researchers from different disciplines proposed different explanations, mostly specific to their respective fields of expertise, which were often rejected by others. The controversy was fueled by disappointments in the seismology community after the widespread optimism in the 1970s and 1980s that effective earthquake early warning could be achieved within a matter of a few years [14-16]. When this optimism soured, an attitude hostile to any studies of pre-EQ signals took root. The discovery of changes in the valence state of oxygen anions in common rock-forming minerals and of the stress-activation of mobile electronic charge carriers is now leading to a re-evaluation of pre-EQ signals.

In Section 2 will lay the foundation by focusing on the temperature-activated valence changes in the oxygen anion sublattice of MgO single crystals and on the appearance of electronic charge carriers in such an otherwise highly insulating oxide material.

In Section 3 the focus shifts to polycrystalline materials such as rocks, to the stress-activation of the same type of electronic charge carriers flowing through the bulk of large chunks of rocks and to their surfaces at the scale of laboratory experiments.

Section 4 correlates laboratory observations with pre-EQ signals reported from the field identifying processes at the Earth's surface-to-air interface, in the atmosphere and the ionosphere.

Section 5 discusses some of the conclusions that are likely to emerge from this work.

2 Valence Changes on the Oxygen Anion Sublattice of Oxide Materials

The valence of oxygen anions in oxide materials is generally assumed to be 2–. Even in the copper oxide-based high T_c superconducting materials the emphasis is placed more on copper changing its valence from Cu^{2+} to Cu^{+} than on oxygen anions in the Cu–O planes fluctuating between the valence states 2– and 1–. For non-transition metal oxides such as MgO, Al_2O_3, SiO_2, and for all naturally occurring silicates the oxygen anions are tacitly assumed to be locked in the 2– state.

It is seldom appreciated that O^{2-} is energetically unstable. The first electron affinity of O is positive but to add a second electron to O^{-} to make O^{2-} costs a considerable amount of energy:

$$O + e^- \Leftrightarrow O^- + 142 \text{ kJ/mol}$$
$$\underline{O^- + e^- \Leftrightarrow O^{2-} - 844 \text{ kJ/mol}}$$
$$O + 2e^- \Leftrightarrow O^{2-} -702 \text{ kJ/mol}$$

For a solid oxide with O^{2-} to be stable this negative electron affinity has to be balanced by energy gains from other sources. In predominantly ionic oxides, most of the energy gain comes from the Coulomb interaction between cations and anions. The Coulomb interaction is proportional to q^2/r^2 where q is the ionic charge and r the interatomic distance. This relationship is borne out in the lattice energies of the isostructural, face-centered cubic alkaline earth oxides [17, 18]. Their lattice energies decrease with increasing cation-anion distances from MgO through BaO. In the binary systems Mg–O, Ca–O and Sr–O the peroxides become progressively more likely to form. In the Ba–O system the peroxide, BaO_2, is thermodynamically more stable than BaO at high pO_2.

2.1 Conversion of Hydroxyl Pairs in MgO to Peroxy plus Hydrogen

However there is a different pathway to introduce oxygen of valence 1– into the matrix of MgO, independent of the oxygen partial pressure and even under highly reducing conditions [19]. This pathway involves hydroxyl anions, OH^-, incorporated into the MgO matrix during crystallization or recrystallization in the presence of H_2O [20]. Writing the incorporation of H_2O as a solid solution formation with $\partial \ll 1$ we have:

$$MgO + \partial\, H_2O \Leftrightarrow Mg_{1-\partial}(OH)_{2\partial}O_{2-2\partial} + \partial\, MgO \qquad (1)$$

For local charge compensation the OH^- will be preferentially associated with Mg^{2+} vacancies. Given the simple fcc[1] structure of MgO, there should be only three types of defects associated with these impurity OH^-: (i) Mg^{2+} vacancies fully compensated by two OH^- on next-nearest neighbor O^{2-} sites, (ii) Mg^{2+} vacancies half compensated by one OH^- on a next-nearest neighbor O^{2-} site, and (iii) OH^- not associated with an Mg^{2+} vacancy. **Figure 1** shows these defects in the MgO (110) plane.

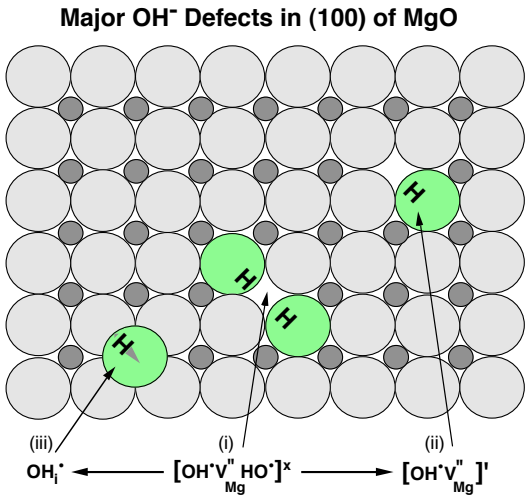

***Figure 1**: Three major OH^- impurity defects resulting from the dissolution of H_2O in MgO*

[1] Face-centered cubic.

Using the Kröger [21] designation for point defects[2] the three defects will be in equilibrium:

$$[OH^{\bullet}V''_{Mg}HO^{\bullet}]^{x} \Leftrightarrow [OH^{\bullet}V''_{Mg}]' + OH^{\bullet}_{i} \qquad (2)$$

$$\text{(i)} \quad \Leftrightarrow \quad \text{(ii)} \quad + \quad \text{(iii)}$$

The fully OH^--compensated, neutral Mg^{2+} vacancy defect (i) on the left will be energetically favored over the half OH^--compensated, singly charged Mg^{2+} vacancy defect (ii) and the interstitial proton defect (iii) on the right. Hence, the equilibrium of eq. (2) should lie on the left.

Each of the OH^--bearing defects has a characteristic infrared (IR) absorption band in the $\nu_{O\text{-}H}$ stretching region between 3300–3700 cm^{-1}. Due to the repulsion between the two H^+ facing each other across the Mg^{2+} vacancy site, the $\nu_{O\text{-}H}$ frequency for the fully OH^--compensated Mg^{2+} vacancy defect (i) will be higher than that for the half OH^--compensated Mg^{2+} vacancy defect (ii). In the case of the interstitial proton defect (iii), will be broadened due to H-bonding with a concomitant increase in the absorption cross section.

Figure 2 shows **(a)** the expected and **(b)** the observed IR absorption spectra of OH^- in the MgO matrix in the $\nu_{O\text{-}H}$ region. The "expected" spectrum in **(a)** depicts the $\nu_{O\text{-}H}$ band of defect (i) with the highest intensity on the high frequency side and that of defect (ii) with low intensity band on the low frequency side. The $\nu_{O\text{-}H}$ band of defect (iii) is drawn as a broad feature spanning the full range of O-H stretching frequencies. The "observed" spectrum in **(b)** was obtained with an MgO single crystal of nominally high purity, 99.99% relative to its cation impurity content, grown from the melt [22]. The spectrum indicates that the intensities of the $\nu_{O\text{-}H}$ bands assigned to defect (i) at 3560 cm^{-1} and defect (ii) at 3300 cm^{-1} are reversed relative to **(a)**. The band at 3560 cm^{-1} due to defect (i) is weak. The band at 3300 cm^{-1} due to defect (ii) is the strong. The broad band spanning the $\nu_{O\text{-}H}$ stretching region between 3300–3700 cm^{-1}, is believed to be due to defect (iii).

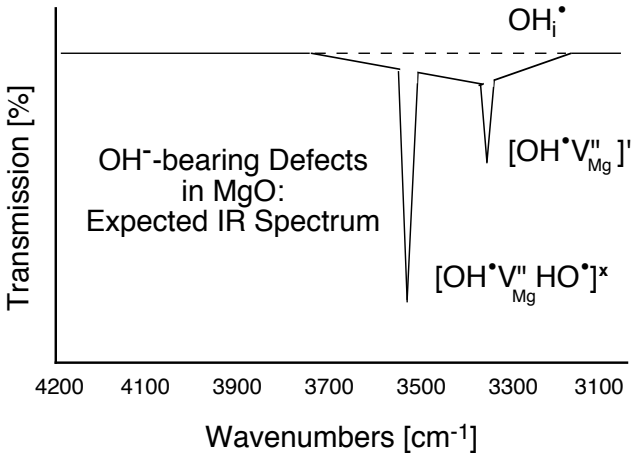

***Figure 2a**: Relative positions and relative intensities expected for OH^- "impurity" defects in MgO.*

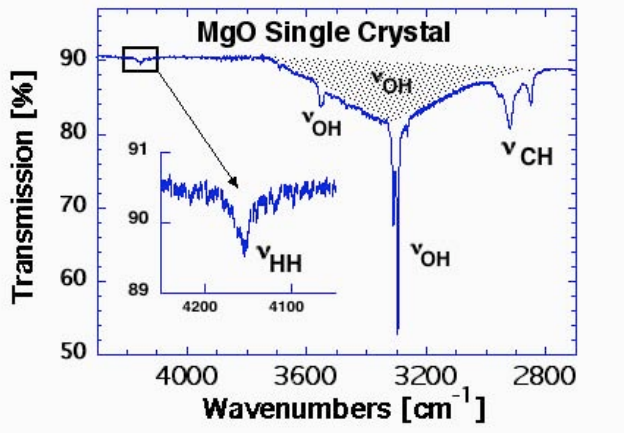

***Figure 2b**: Infrared spectrum of a high purity MgO crystal with "impurity" OH^- with the assignment of O-H and H-H stretching bands, which differ from the "expected" IR spectrum.*

[2] V stands for vacancy. Superscript •, ••, ', ", and ^{x} designate single positive, double positive, single negative, double negative, and neutral charges respectively, relative to the ideal structure. Subscripts indicate the lattice site (omitted in the case of O^{2-} sites) with i standing for interstitial. Square brackets indicate the essential defects.

In addition to the three basic $\nu_{O\text{-}H}$ bands a weak band appears at 4150 cm^{-1}, which is diagnostically distinct. It is due to a phonon combination with the H-H stretching mode, $\nu_{H\text{-}H}$, of molecular H_2 [23]. By subjecting the MgO crystal to stepwise heating and cooling, interrupted by quenching to 77 K for recording the IR spectra, it can be shown that, when the 4150 cm^{-1} band decreases in intensity, the 3560 cm^{-1} increases and vice versa [20]. This suggests that the OH^- pair defects (i) split off H_2 reversibly as part of an electronic rearrangement of the type of a redox reaction:

$$[OH^{\bullet}V''_{Mg}HO^{\bullet}]^{\times} \Leftrightarrow [\begin{matrix} O^{\bullet} \\ O^{\bullet} \end{matrix} (H_2)''_{Mg}]^{\times} \qquad (3a)$$

Given enough time the H_2 can leave the Mg^{2+} vacancy sites to become interstitial $(H_2)_i$.

Eq. (3a) is a redox reaction, driven by the presence of the Mg^{2+} vacancy, which decreases the Coulomb interaction across the Mg^{2+} vacancy site. Each oxygen of the OH^- pair donates an electron to its respective proton, H^+. The two protons reduce to H forming H_2, while two O^{2-} oxidize to O^-. They undergo self-trapping as an O^- pair, forming a peroxy anion, O_2^{2-} :

$$OH^- + OH^- = O_2^{2-} + H_2 \Uparrow \qquad (3b)$$

Loss of H_2 from MgO was observed during a mass-spectroscopic study of ultrahigh purity $Mg(OH)_2$ decomposing to nano-sized MgO [24]. The MgO nanocrystals are initially rich in "impurity" OH^- as shown on the left side of eq. (4), where $\partial \ll 1$. Assuming that all OH^- participate in the redox reaction of eq. [3b/c] and that the H_2 molecules escape, eq. (1) continues:

$$Mg_{1-\partial}(OH)_{2\partial}O_{2-2\partial} \Leftrightarrow Mg_{1-\partial}O^{\bullet}_{2\partial}O_{2-2\partial} + \partial\, H_2 \Uparrow \qquad (4)$$

where the superscript • is used to designate oxygen in the valence 1-. The product on the right side is cation-deficient MgO, $Mg_{1-\partial}O$. with $\partial \gg 1$, this becomes $MgO_{1+\partial}$, e.g. MgO with ∂ excess oxygen.

Figure 3 shows how H_2 evolves as a function of temperature following the decomposition of $Mg(OH)_2$ and formation of OH^--rich nano-sized MgO [24]. The amount of H_2 released between 300-800°C is equivalent to $\partial \approx 0.01$, meaning that ≈2% of all OH^- in the $Mg(OH)_2$ converted to O_2^{2-} plus H_2 molecules[3]. The magnesium oxide thus obtained is $Mg_{0.99}O \approx MgO_{1.01}$.

[3] Above 800°C H_2 starts to be released from the walls of the heated fused silica sample tube.

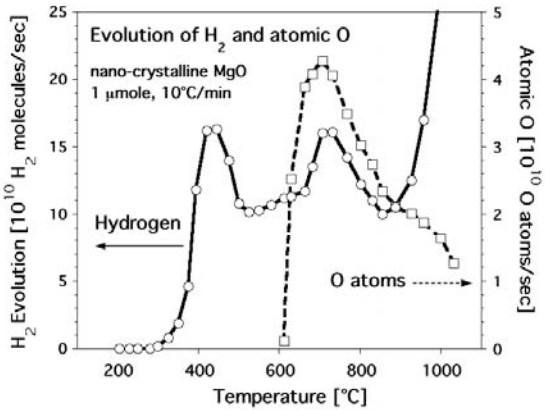

***Figure 3**: Evolution of molecular H_2 and atomic O from extremely high-purity, nano-sized MgO obtained through the thermal decomposition of $Mg(OH)_2$ at a constant heating rate of 20°C min^{-1} measured in a dynamically pumped ultrahigh vacuum system (after Martens et al. 1976).*

MgO with excess oxygen is thermodynamically metastable [25]. **Figure 3** shows that the $MgO_{1+\partial}$ begins to release O atoms at 600°C. This is a disproportionation reaction, whereby the two O^- of the peroxy anion rearrange electronically so as to produce an O^{2-} plus an O atom:

$$O_2^{2-} \Rightarrow O^{2-} + O \Uparrow \qquad (5)$$

The O emission can only take place at the surface. To sustain it, Mg^{2+} vacancies have to diffuse to the surface and anneal out. If the crystallites are nano-sized as in the case presented here, the annealing can go to completion within relatively short time at temperatures above 600-700°C. This marks the return of $MgO_{1.01}$ to stoichiometric $MgO_{1.00}$. If the crystals containing peroxy defects are large, the emission of atomic O from the surface can only be of minor importance. Instead, other processes will prevail.

2.2 Effect of Oxygen Valence Fluctuations on the Physical Properties of MgO

The presence of peroxy anions compensated by excess metal cation vacancies has a disproportionately large effect on essentially all fundamental physical properties of the MgO crystals. Though this observation may appear to be of interest only to the specialist, the same principle applies to minerals, when they contain small and seemingly negligible concentrations of peroxy. In those cases, as will be shown further below, a wide range of fundamental properties of minerals and rocks are noticeably affected. Understanding the role of peroxy in minerals and rocks, hence the role of valence fluctuation on the oxygen anion sublattice, is a prerequisite to understanding processes that are intimately linked to situations developing the Earth's crust prior to earthquakes.

A peroxy defect next to an Mg^{2+} vacancy as depicted on the left of **Figure 4** represent a localized point defect. Such point defects are expected to have little effect. However, upon heating, the peroxy defects break apart in two distinct steps as depicted in **Figure 4**.

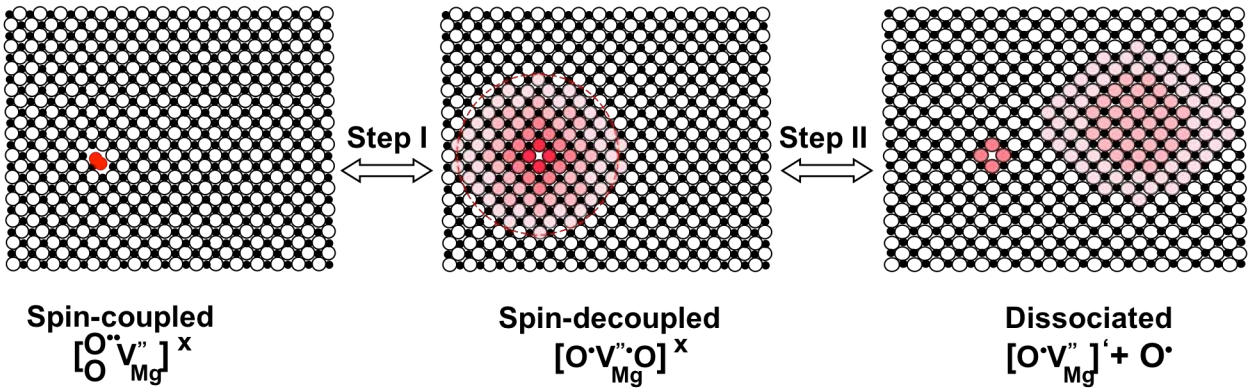

***Figure 4**: 2-stage break-up of the peroxy defect in MgO introduced by the redox conversion of Mg^{2+} vacancy-associated OH^- pairs into H_2 plus peroxy anions, O_2^{2-}.*

At Step I, between 200–300°C, the spins of the two O^- decouple as shown in the center part of eq. (3), leading (i) to a paramagnetic signal, (ii) to distinct changes in the thermal expansion, (iii) to a stepwise increase in the dielectric polarization at the limit of 0 Hertz, and (v) to an increase in the refractive index [26-28]. At Step II, above 430-450°C, the O^- pair defect dissociates. As one O^- state moves away as a mobile positive hole charge carriers, the Mg^{2+} vacancy stays behind with one O^-, forming what is known as V^- center [29].

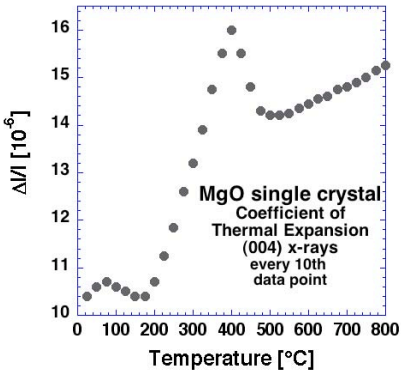

***Figure 5a**: Anomaly in the thermal expansion coefficient of a high purity MgO single crystal measured by x-ray diffraction of the (004) line at a constant heating rate of 2°C min^{-1}.*

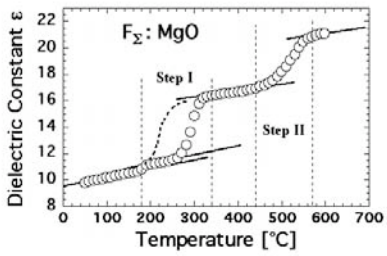

***Figure 5b**: 2-step anomaly in the effective dielectric constant of high purity MgO single crystal measured at the limit of 0 Hz during stepwise heating with 2 min hold time at every temperature point indicated (after Freund et al. 1993).*

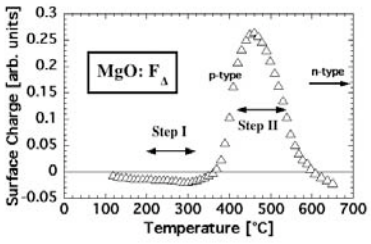

***Figure 5c**: Appearance of positive surface charge on MgO indicative of p-type response changing to n-type around 600°C during stepwise heating (after Freund et al. 1993).*

Figure 5 shows the changes in the thermal expansion, the effective dielectric constant measured at the limit of 0 Hz, and the appearance of a surface charge which signals p-type conductivity transitioning to n-type behavior. Given the low concentration of peroxy defects, equivalent to an O^-/O^{2-} ratio of <1:1000 in melt-grown MgO crystals [28], the magnitude of the observed changes suggests that, during Step I, the wavefunction associated with the O^- state delocalizes over a large number of oxygen positions as depicted in **Figure 4**. The delocalization is consistent with changes observed in the thermal expansion coefficient and in the refractive index n [30].

Eq. (6a/b) summarize the 2-step thermal break-up of peroxy defects in MgO:

Step I: $$\left[\begin{matrix} {}^{\uparrow\downarrow}O^{\bullet} \\ O^{\bullet} \end{matrix} V''_{Mg} \right]^{x} \Leftrightarrow \left[{}^{\uparrow}O^{\bullet} \; V''_{Mg} \; O^{\bullet\downarrow} \right]^{x} \quad (6a)$$

Step II: $$\left[{}^{\uparrow}O^{\bullet} \; V''_{Mg} \; {}^{\bullet}O^{\downarrow} \right]^{x} \Leftrightarrow \left[{}^{\downarrow}O^{\bullet} \; V''_{Mg} \right]^{'} + {}^{\downarrow}O^{\bullet} \quad (6b)$$

At Step II, around 430-550°C, the peroxy dissociates. Detached from the Mg^{2+} vacancy the O^{-} becomes a defect electron or hole $h^{\bullet}$ in the O^{2-} sublattice, also known as positive hole [31] or "phole" for short. The electron, which has jumped into the broken peroxy bond, becomes trapped at this site as a loosely bound electron, e'.

In essence Step II describes the formation of an electron-hole pair, e'–$h^{\bullet}$. In eq. (6b) the $h^{\bullet}$ is given as $O^{\bullet}$. The $h^{\bullet}$ are mobile charge carriers. Their effect on the electrical conductivity of the MgO is pronounced. Since MgO is a good insulator with a conductivity at room temperature well below 10^{-16} Ω^{-1} cm^{-1}, the appearance of the $h^{\bullet}$ charge carriers causes the conductivity to increase by orders of magnitude [32]. The mobile $h^{\bullet}$ turn the MgO first into a p-type semiconductor [27]. Then, above 500°C the e' become thermally activated as well, changing the p-type MgO into n-type MgO at about 600°C [33].

Figure 6 shows the dc conductivity of an MgO single crystal, nominal purity grade 4N = 99.99%, recorded with guard electrodes in high purity argon [32]. The 10°C/min heating–cooling program was designed to display the activation of the $h^{\bullet}$ charge carriers during Step II, e.g. the progressive dissociation of the peroxy bond and activation of mobile $h^{\bullet}$ charge carriers. During the Step II interval the heating of the MgO crystal was reversed four times, followed by reheating, producing the characteristic log σ versus 1/T pattern of **Figure 6**. The conductivity is marked by a steep rise with an apparent activation energy of 3.4 eV, while the three parallel branches obtained during intermediate cooling have the same 1.0 eV activation energy.

In addition there is a shallower branch at the high temperature end of the Step II range. Its activation energy varied from sample to sample and from run to run with values between nil and about 0.3 eV [32]. This high temperature interval marks the transition of the MgO from p-type to n-type, indicating that electrons become thermally activated and begin to dominate the conductivity behavior.

With the on-set of cation diffusion around 700°C [34], the excess Mg^{2+} vacancies begin to anneal out. This marks the return of the MgO to thermal equilibrium in the same way as the emission of O atoms from the surface of nanosized MgO powder shown in **Figure 3** marks the return to stoichiometry.

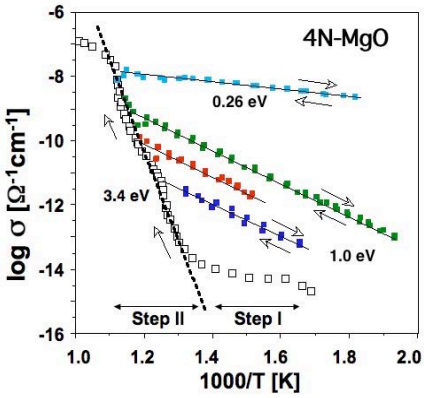

***Figure 6**: Orders of magnitude increase in the d.c. electrical conductivity of high purity MgO during heating in high purity Ar coinciding with Step II of the break-up of the peroxy defects and the generation of mobile positive hole charge carriers. A special heating-cooling protocol was used to bring out the unusual features of the 1 eV activation energy branches obtained during intermittent cooling.*

The log σ versus 1/T plot of **Figure 6** suggests that the steep increase in the conductivity in the Step II range is due to the progressive activation of charge carriers in the MgO with an activation energy of 1.0 eV. The 3.4 eV slope of the steep rise, approximated by the dotted line, is given by the sum of the activation energy needed to generate the charge carriers E_1 through the dissociation of the peroxy defects and the characteristic 1.0 eV activation energy E_2 for the $h^{\bullet}$ conduction. The conductivity σ of the MgO can be given as $\sigma = \sigma_0 \exp[(E_1+E_2)/kT]$, where σ_0 is the frequency factor. If E_2 = 1.0 eV, E_1 = 2.4 eV.

Figure 6 further shows that, at the upper end of the temperature range, the conductivity changes again. There are two possible causes. (i) With increasing thermal activation the $h^{\bullet}$ concentrations may become so high that the delocalized wavefunctions of the $h^{\bullet}$ charge carriers begin to overlap, presumably in the surface/subsurface layer, that the conductivity response becomes quasi-metallic. (ii) With increasing temperature the electrons e', trapped at broken peroxy sites, become activated, causing a change from p-type to n-type behavior. Because the e' charge carriers are expected to be more mobile than the $h^{\bullet}$, the conductivity will increase.

It is also instructive to look at the peroxy anion in MgO from the perspective of molecular orbital theory [35]. The left side of **Figure 7** shows the atomic orbitals (AO) of two O^-, which combine to form the molecular orbitals (MO) of the peroxy anion, O_2^{2-}. The highest energy level is the $3\sigma_u^*$ orbital. Its main contribution comes from the O $2p_z$ AO's where z marks the O^-–O^- bond direction. It is antibonding to the lowest most stable bonding $2\sigma_g^b$ orbital, which concentrates most of the O $2p_z$ density between the two O^- along the z direction[4]. By contrast, the wavefunction of the antibonding $3\sigma_u^*$ orbital points away from the O^-–O^- bond towards the region occupied by neighboring O^{2-}. Importantly, in the case of the peroxy, this orbital is unoccupied.

[4] The double degenerate, non-bonding π-type $1\pi_g^{nb}$ orbital, which derives mainly from the O $2p_{x,y}$ atomic orbitals, is the highest occupied molecular orbital. It forms a torus around the O^-–O^- bond direction but contributes little to the peroxy bond.

The temperature-induced break-up of the peroxy anion can be understood by assuming that, with increasing amplitudes of thermal vibrations, the energy of the unoccupied $3\sigma_u^*$ orbital is lowered, while the energy of one of the non-bonding $1\pi_g^{nb}$ orbitals is raised. At some temperature a cross-over point will be reached, where one of the neighboring O^{2-} transfers an electron into the empty antibonding $3\sigma_u^*$ orbital. The donor O^{2-} thereby turns into an O^-, e.g. a defect electron or positive hole. The broken peroxy bond, which has taken up an extra electron, is thought to rearrange in such a way as to stabilize the new configuration as depicted on the right side of **Figure 7**. In other words, the broken peroxy bond traps the electron and makes the return to the initial state energetically less favorable. The outcome is a long-lived electron-hole pair.

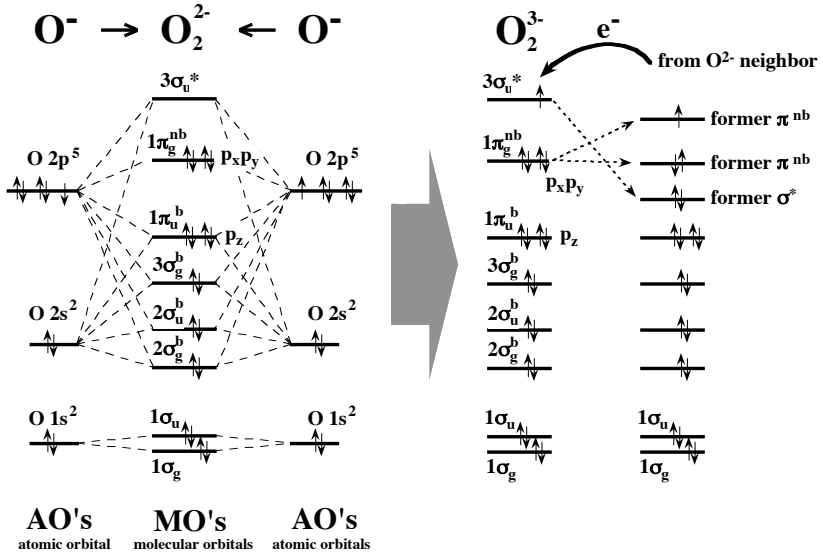

***Figure 7**: Schematic molecular orbital diagram for a peroxy anion, O_2^{2-}, in the MgO structure. Changes in the electronic structure when the double degeneracy of the occupied non-bonding π_g^{nb} is lifted and one of the π_g^{nb} levels is pushed higher in energy than the unoccupied antibonding σ^*, causing (i) a transfer of an electron from an outside O^{2-} into the empty lobe of the σ^* orbital, which extends away from the O–O bond, and (ii) an internal electronic rearrangement, which stabilizes the broken bond configuration.*

This leads to the very important conclusion that, contrary to electron-hole pairs in silicon and other semiconductor materials, e'–$h^\bullet$ pairs in MgO do not recombine fast. Experimental evidence suggests that, once activated, the $h^\bullet$ charge carriers remain active for long time, on the order of 12 hrs or more. This was first noted during electrical conductivity studies and is the reason why we were able to design temperature-time profile that led to the data depicted **in Figure 6** [32].

Residing in the oxygen anion sublattice, the $h^\bullet$ are associated with O 2sp-symmetry energy states at the upper edge of the valence band. They are mobile charge carriers that can propagate along the valence band, probably by way of a phonon-assisted electron hopping mechanism [36]. With the phonon frequency on the order of 10^{12} s^{-1} and 0.3 nm as the distance between O^{2-} sites, their phase velocity can be estimated to be on the order of 300 m/s.

Since all $h^\bullet$ carry the same positive charge, they repel each other electrostatically and are expected to diffuse to the crystal surface. There they set up a thin subsurface charge layer with a positive surface potential and an associated electric field as shown in **Figure 8a/b** respectively.

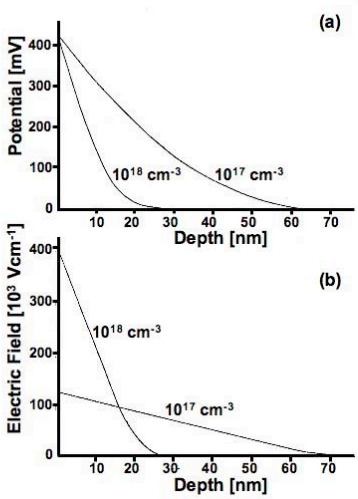

***Figure 8a**: Surface/subsurface potential and **(b)** electric field generated by positive hole charge carriers assumed to be present at concentration levels of 10^{17} and 10^{18} cm^{-3}, corresponding to 10 and 100 ppm respectively, in a dielectric medium with ε = 10 (after [37]).*

For a dielectric constant of 10, close to the value of 9.6 for MgO, the flat surface potential is predicted to be about +400 mV, while the associated electric field increases rapidly from 1.2 x 10^5 V/cm at a charge carrier density of 10^{17} cm^{-3}, equivalent to 10 ppm, to 0.4 x 10^6 V/cm at a charge carrier density of 10^{18} cm^{-3}, equivalent to 100 ppm [37]. At higher charge carrier concentrations or at edges and corners, where the radius of curvature is small, the electric field at the surface will increase significantly. Further below this will become important during the discussion of the field-ionization of air molecules at the rock surface.

2.3 Conclusions from MgO

Being the simplest oxide [38] MgO is thought to be stoichiometric with all oxygen anions fixed in their usual 2- valence state, subject to thermodynamic equilibrium conditions [25]. However, hydroxyl "impurities", introduced into the MgO matrix through dissolution of traces of H_2O, can lead to valence changes on the O^{2-} sublattice. Of prime interest are peroxy defects associated with Mg^{2+} vacancies. When they break apart electron-hole pairs are generated, e'–$h^{\bullet}$, which are long-lived. The activation energy needed to thermally break the O^{-}–O^{-} bond in MgO is 2.4 eV. The activation energy characterizing the $h^{\bullet}$ conductivity is 1.0 eV. In the temperature range where $h^{\bullet}$ charge carriers dominate, MgO is a pure p-type semiconductor. At higher temperatures the p-type conductivity changes to n-type due to the activation of e' charge carriers.

In Section 3 the focus shifts to silicates and to the question how the presence of peroxy defects in silicate minerals and their break-up may affect the properties of common crustal rocks.

3 Valence Changes on the Oxygen Anion Sublattice of Silicate Minerals

Peroxy defects exist in silica, prominently in fused silica glass, O_3Si-OO-SiO_3 [39]. Their presence affects the optical transmission of fused silica fibers due to the radiolysis of the peroxy bond and formation of peroxy radicals, O_3Si-OO•. Peroxy defects also exist in silicates, in particular in naturally occurring silicate minerals where paramagnetic centers can be produced by

low temperature x-ray or gamma irradiation [40]. However, the presence of oxygen in the valence state 1– in minerals, presumably also through dissolution of small amounts of H_2O during crystallization and redox conversion of O_3Si-OH pairs, is much more ubiquitous than commonly believed.

3.1 Stress Activation of Positive Hole Charge Carriers in Rocks

It had long been suspected that the basic reaction in MgO, which converts OH^- pairs into H_2 plus peroxy anions, O_2^{2-}, also takes place in silicate minerals, which invariably dissolve traces of H_2O in the form of O_3Si-OH when crystallizing from H_2O–laden magmas or recrystallizing in high-temperature H_2O–laden environments [41]. Writing the sequence of steps for SiO_2 we have:

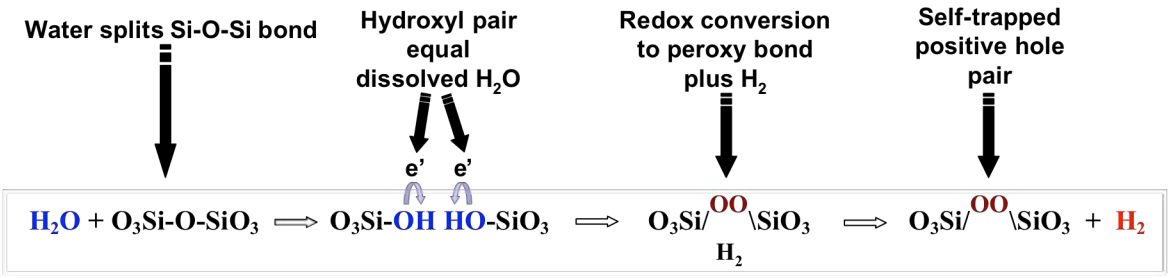

(7)

Eq. (7) describes an internal electronic rearrangement, which chemists commonly call a redox reaction. It is unusual only in the sense that, in the case presented here, a hydroxyl pair (equivalent to a dissolved H_2O molecule) is split into a peroxy link (equivalent to an interstitial O atom) plus an H_2 molecule[5].

From a semiconductor perspective a peroxy bond that links two [SiO_4] units, $O_3Si/^{OO}\backslash SiO_3$, can be viewed as a self-trapped positive hole pair, PHP. It is electrically inactive. The same holds true for the more general description valid for complex silicate minerals, $O_3X/^{OO}\backslash YO_3$, where (X,Y) = Si^{4+}, Al^{3+} etc. PHPs are essentially undetectable as long as they are unperturbed.

When the $O_3Si/^{OO}\backslash SiO_3$ bond breaks, a neighboring O^{2-} sends in an electron in much the same was as discussed above for peroxy in MgO, creating an electron-hole pair. The electron transfer from the outside is depicted in eq. (8).

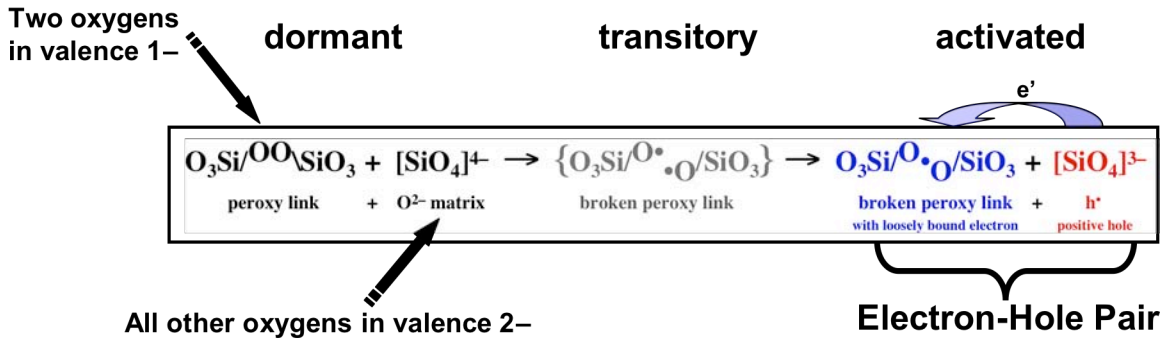

(8)

[5] This is, in essence, a "water splitting reaction", similar what plants can do as part of their oxygenic photosynthesis cycle.

If an increase in amplitudes of the thermal vibrations suffices to break the peroxy bond in MgO above 400-450°C as argued in the preceding section, any process that "wiggles" the $O_3Si/^{OO}\backslash SiO_3$ entity would achieve the same goal. Such a "wiggling" happens whenever a dislocation passes through the peroxy bond. Existing dislocations are mobilized and new dislocations are generated in large numbers whenever mechanical stresses are applied beyond the elastic range.

Eq. (8) describes the basic process that turns a mineral, which can be a near-perfect insulator, into a pure p-type semiconductor. It describes the process that creates long-lived electron hole pairs in minerals and rocks, which affect the electrical properties of the rocks in the Earth's crust, when tectonic stresses are applied.

Figure 9 retraces what happens when a dislocation cuts through the $O_3Si/^{OO}\backslash SiO_3$ entity, straining the $Si/^{OO}\backslash Si$ bond. As depicted on the left side, the unoccupied antibonding $3\sigma_u^*$ orbital will stabilize by shifting downward, while the occupied non-bonding $1\pi_{xy}^{nb}$ orbitals loose their degeneracy. One, lying in the plane of the bending motion, will strongly destabilize, while the other one, lying orthogonal to the plane of bending, will remain nearly unaffected. Similar to the analogous case of MgO, an electron from an outside O^{2-} is then transferred into the strained $O_3Si/^{OO}\backslash SiO_3$ bond, presumably into the antibonding $3\sigma_u$* level as depicted on the left side of **Figure 9.** The $3\sigma_u$* level reaches into the region occupied by neighboring oxygens and should facilitate the electron transfer. This is expected to be followed by an internal electronic rearrangement as depicted on the right side, which stabilizes the new configuration through lattice relaxation around the broken bond defect. This sequence of steps seems to be responsible for creating a long-lived electron-hole pair. The extended lifetime allows the hole state to spread from the site where it was "born".

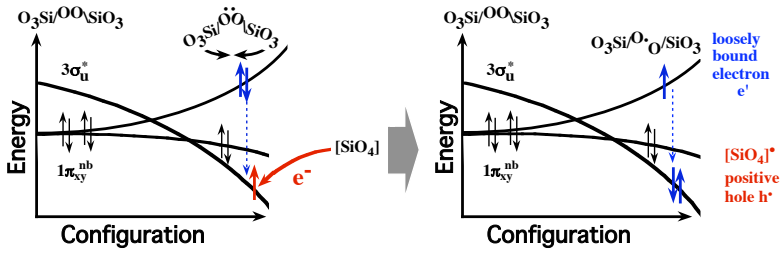

***Figure 9**: Expected changes in the relative positions of the highest occupied non-bonding π^{nb}–type and the unoccupied antibonding σ* orbitals when a dislocation passes through the $O_3Si/^{OO}\backslash SiO_3$ bond and an electron is transferred from the outside into the broken peroxy bond. This creates, through an internal electronic rearrangement, a long-lived electron-hole pair.*

3.2 Positive Hole Charge Carriers Flowing through Rocks

Applying the idea of dislocations mobilized by stress to the activation of mobile positive hole charge carriers in rocks allows us to design a series of basically very simple experiments where we stress one end of a rock activating the positive hole charge carriers $h^\bullet$. This creates a situation where the $h^\bullet$ will spread into the unstressed end. Since the electrons e' cannot follow suit, they remain in the stressed subvolume [42, 43].

Figures 10a-d illustrate the simplicity of these experiments. **Figure 10a** shows the basic set up with a pair of steel pistons stressing one end of a rock. Within the stressed subvolume the concentration of e'–$h^{\bullet}$ increases as shown schematically at the bottom. Following the concentration gradient the $h^{\bullet}$ flow into the unstressed rock volume. The $h^{\bullet}$ outflow sets up a potential difference V_0, which will eventually stop the $h^{\bullet}$ outflow. In addition, because the $h^{\bullet}$ inside the unstressed rock volume repel each other electrostatically, they diffuse to the surface producing an electric field and a surface potential $V_{surface}$ that can be measured with a capacitive sensor as indicated in **Figure 10b**.

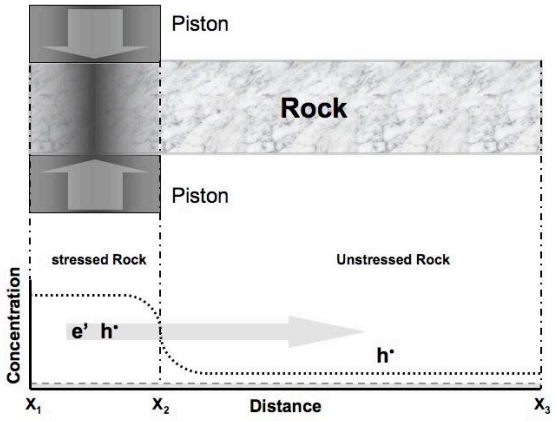

***Figure 10a**: Set-up to demonstrate positive holes flowing out of a stressed rock volume. Bottom: Concentration profile of $h^{\bullet}$ and e' before (dashed) and after (dotted) stress application.*

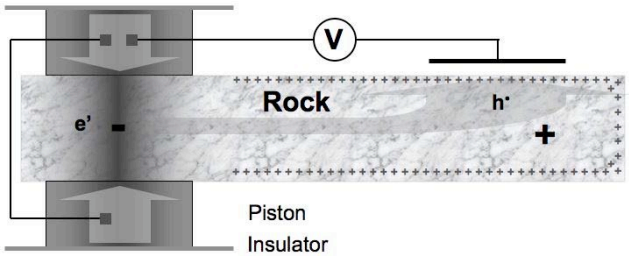

***Figure 10b**: Set-up to measure surface potential with a capacitive sensor.*

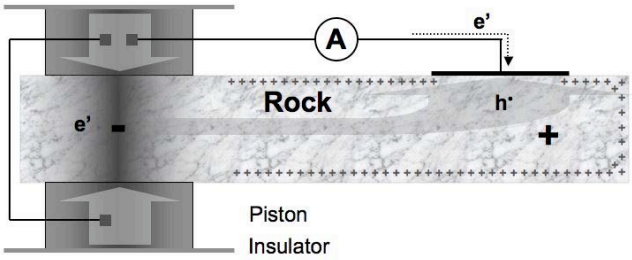

***Figure 10c**: Set-up to measure battery current with a Cu contact directly on the rock.*

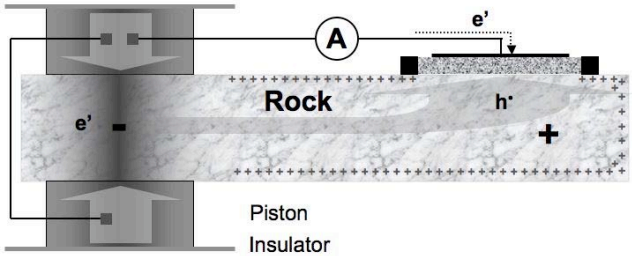

***Figure 10d**: Set-up to measure battery current flowing through sand and/or soil.*

The circuit can be closed by attaching a Cu contact to the rock surface as depicted in **Figure 10c**. The electrons pass from the stressed rock into the metal pistons. They then flow to the Cu contact and recombine with $h^{\bullet}$ across the Cu-rock interface.

This circuit describes, in essence, a semiconductor battery that is analogous to an electrochemical battery. The unstressed rock takes the role of the electrolyte. The $h^{\bullet}$ take on the role of the cations carrying positive charges through the rock. The electrons flow through the external circuit.

The maximum current that can flow will be controlled by the "battery potential" V_0 and the internal resistance R_{int}. While there is certainly some extra resistance across the rock-piston contacts and across the rock-Cu contact, the main controlling factor for the "battery current" will be R_{int} of the unstressed rock.

As stated above, the $h^{\bullet}$ charge carriers propagate along the upper edge of the valence band using energy levels of primarily O 2sp symmetry. However, in order for $h^{\bullet}$ to propagate, the medium through which they flow must have a pre-existing non-zero p-type conductivity. In other words, the minerals in the rocks must contain – already in the unstressed state – a finite concentration of defect electron sites in their oxygen sublattice, e.g. a finite concentration of $h^{\bullet}$ as indicated by the dashed line at the bottom of **Figure 10a**. Rocks or any other materials, which do not contain at least some p-type conductivity, will not be able to conduct $h^{\bullet}$.

Figure 11 presents a selection of log s versus 1/T [K] plots of basic and ultrabasic igneous rocks, basalt/diabase and peridotite respectively, from the large database assembled by Parkhomenko and Bondarenko [44]. This graph draws attention to the fact that, within the temperature range that is typical of the Earth continental crust down to 30-35 km, the electrical conductivity of essentially all rocks, specifically igneous rocks, is p-type, dominated by the same activation energy of ~1 eV as in high purity MgO single crystals (see **Figure 6**). This p-type conductivity of the rocks is important to understand how electric currents can flow in the Earth's crust below the water table and the possible presence of intergranular water films but above the depth range where the temperatures of the rocks reach the on-set of ionic conductivity, around 600°C, characterized by a higher activation energy.

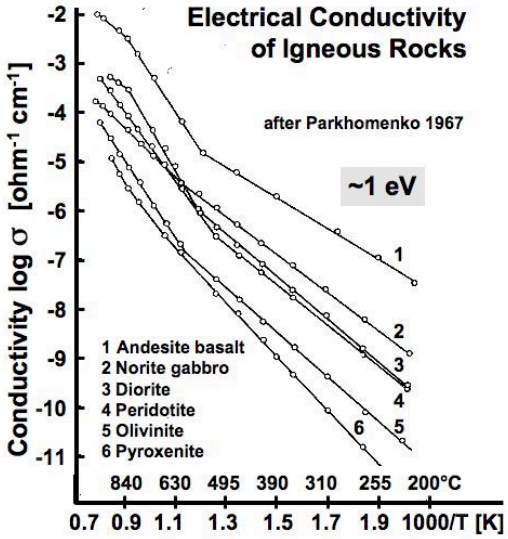

***Figure 11**: Selection of log σ versus 1/T [K] plots to illustrate the near-universal 1 eV activation energy for the electrical conductivity of rocks (after [44]).*

At the same time, the existence of a finite p-type conductivity is a prerequisite for $h^{\bullet}$ to propagate along any concentration gradient from stressed to unstressed rock volumes as depicted in **Figure**

10a. The $h^{\bullet}$ propagate by way of electrons passing in the opposite direction, hopping from O^{2-} to O^{-}. Because the upper edges of the valence bands of different minerals will lie at different energies, energy barriers exist across grain-grain contacts, even in compact rocks. However, with the valence bands forming an energetic continuum, such energy barriers will not prevent the propagation of the $h^{\bullet}$ charge carriers but only add to the resistance R_{int} of the system.

Likewise $h^{\bullet}$ can cross grain-grain contacts in loosely consolidated granular materials, rock dust, sand and soil as depicted in **Figure 10d**. This is crucial for understanding the propagation of $h^{\bullet}$ not only through solid rocks deep in the Earth's crust but also through overlying sediments and even through the top layers of sand and soil.

3.3 Laboratory Implementation of Positive Hole Currents

An experimental set-up with a 4 m long slab of common red granite, using essentially the same circuit at depicted in **Figure 10c** [42], is shown in **Figure 12a**. A wire connects the pistons in the back to the Cu contact at the front passing through a picoammeter. The Cu contact is glued onto the rock surface with a graphite-loaded conductive adhesive. **Figure 12b** plots the load versus time and the current versus time curves.

***Figure 12a**: Laboratory demonstration that a stress-activated electric current can flow through a 4 m long piece of granite.*

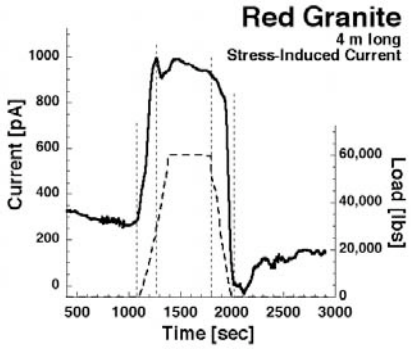

***Figure 12b**: Current versus time upon loading/unloading granite.*

The maximum load of 60,000 lbs (about 30 tons) corresponds to less than 30 MPa, about 1/6th the compressive strength of this rock. The current through the rock begins to flow immediately upon loading. The current saturates about halfway through the loading cycle. It passes through a maximum and then stabilizes, decaying slowly at constant load. During unloading, the current begins to drop rapidly at about ½ the maximum load, passes through a minimum and returns to the background level.

The current at low load indicates that enough dislocations are mobilized at low stress levels to activate a relatively large number of $h^{\bullet}$ charge carriers. Since the rock is a polycrystalline material, there will always be contact points between mineral grains that act as stress concentrators. They cause deformation and, hence, generate or mobilize dislocations in small subvolumes. The modest maximum current of barely 1 nA flowing out a stressed rock of more than 6000 cm^3 is limited by the internal resistance R_{int} of this long piece of rock.

With different geometries and different rocks the stress-activated currents vary widely. For instance, in the case of gabbro, a quartz-free rock similar in mineral composition to basalt and diabase that crystallized deep in the Earth's crust, R_{int} is significantly lower than in the case of granite, which typically consists of nearly one third quartz. Using square gabbro tiles, 30 x 30 x 0.9 cm^3 with a Cu contact along all sides, and loading the center within 5 s to 48 MPa, a 10 cm^3 subvolume can produce currents as large as 20 nA as shown in **Figure 13a**. The current I flows radially out from the stressed rock volume. Keeping the load constant at 48 MPa causes the current to decay rapidly at first and then slowly to about 5 nA within 3 hrs. Plotting the same data as log I versus time reveals at least three sections with different slopes, suggesting different types of $h^{\bullet}$ charge carriers with different lifetimes. The slowest take about 2 ½ months under constant load to decay by 50%.

If we linearly extrapolate to larger volume such a km^3, the currents that could flow out become quite large. **Figure 13b** shows the outflow currents measured from a centrally loaded gabbro tile during loading at different constant rates varying by 5 orders of magnitude. The currents are given in A km^{-3} and the time is plotted on a logarithmic scale. Regardless of the speed with which the rock is stressed, there is always an initial peak, which decreases in intensity with decreasing rate of loading. This consistent pattern seems to confirm that several populations of $h^{\bullet}$ charge carriers are activated during the loading process, each with different lifetimes.

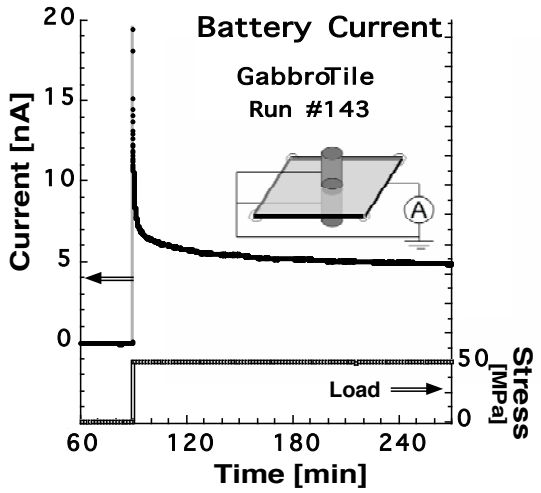

***Figure 13a**: Outflow current from ~10 cm^3 of a stressed gabbro tile measured over 3 hrs at constant load (48 MPa)*

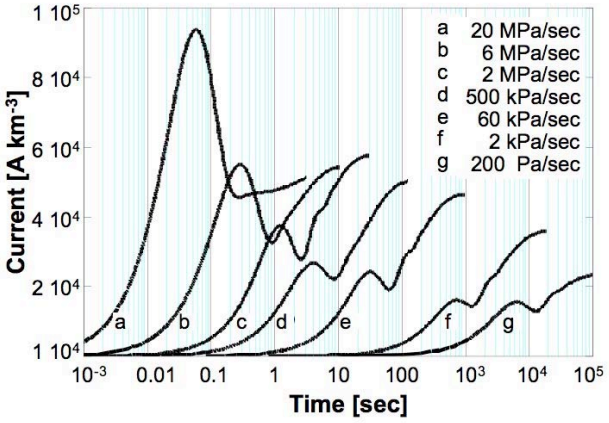

***Figure 13b**: Outflow current from ~10 cm^3 of a stressed gabbro tile measured at different rates of loading. Current given in A/km^3.*

3.4 Conditions for Large Stress-Activated Currents to Flow prior to Earthquakes

Sections 3.2 and 3.3 deal with electric currents, which can be generated in rocks subjected to uniaxial stress under laboratory conditions. These currents are remarkable in as much as the stress-activated positive hole charge carriers $h^{\bullet}$ can travel macroscopic distances through unstressed rocks, even through sand and soil. If the $h^{\bullet}$ can do it under laboratory conditions, there no *a priori* reason to believe that they not be able to conduct currents over large distances in the Earth's crust. Thus, when large rock volumes are subjected to tectonic stresses deep in the Earth's crust prior to earthquakes, the possibility might exist that powerful currents will flow down the stress gradients forming as a result of tectonic forces.

However, sustained currents as demonstrated under laboratory conditions can only flow if the battery circuit is closed. A prerequisite is that the stress-activated electrons e' can also flow out of the stressed rock volume and recombine with the $h^{\bullet}$ charge carriers somewhere down the stress gradient. In the laboratory this condition is readily met by connecting the stressed rock subvolume to the unstressed rock through a wire as depicted in **Figures 10c/d**. In nature, under realistic field conditions, closure of the circuit in the Earth's crust is likely to be achievable only under a set of rather restrictive conditions.

Figure 14 shows a highly schematic, simplified cross section through the continental crust to a depth of about 50 km [12, 13]. The feature of note is the white dashed-dotted line, which marks the depth at which we expect rocks to transition from p-type to n-type behavior. We place this transition at a depth equivalent to a temperature around 550°C, assuming that the laboratory data obtained at 1 bar for the p-n transition are representative for the high pressures deep in the crust. In stable continental shields temperatures around 550°C are believed to be reached at a depth of about 25-35 km. The depth range of 20-30 km coincides with a zone, where the electrical conductivity of the *in situ* rocks is anomalously high [33]. This "High Conductivity Zone" is consistent with the concept presented here that the thermal activation of positive hole charge carriers makes an important, possibly the most important contribution to the electrical conductivity profile through the crust.

Tectonic forces, when acting on sections of the Earth's crust prior to earthquakes, push rocks against each other at a more or less constant speed. If two brittle materials, confined by a large overload, are pushed against each other at constant speed, the stresses increase nonlinearly with time. If the tectonic stress vector is horizontal, the isobars describing surfaces of constant stress expand horizontally as well as upward and downward.

Figure 14a sketches an early situation where stresses begin to build up. The source S represents the rock volume from where $h^{\bullet}$ charge carriers flow out. They spread laterally and upward, setting up a surface charge layer. Rocks close to the surface, within the top 3-5 km, are relatively weak, primarily due to the presence of open, connected, water-filled pores. As a result, these rocks cannot support high stress levels. Further down the pores close and the strength of the rocks increases while they still remain essentially brittle. Still further down, the rocks become ductile due to the increasing temperature along the geotherm. The ductile rocks deform but the dislocations anneal out as fast as they are generated [45]. Therefore the source volume S does not reach down to the p-n transition and the electrons e', co-activated with the $h^{\bullet}$ charge carriers, cannot yet flow out. This situation is equivalent to an open battery circuit as indicated by the inset.

Figure 14b sketches a later stage, closer to an earthquake, when the rate, at which the stresses build up, overrides the annealing of the dislocations. At this stage the source volume has reached across the p-n transition into the portion of the lower crust where the rocks become n-type. The battery circuit closes and electrons e' can flow out of the source volume S to meet the $h^{\bullet}$ which have spread laterally along the stress gradient in the p-type conductive upper crust.

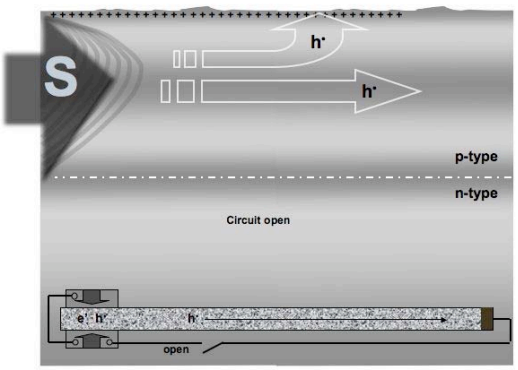

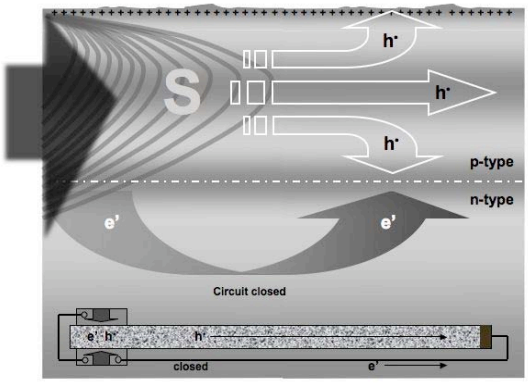

***Figure 14a**: Simplified cross section through the Earth's crust with an assumed p-n transition at a depth of ~25 km. Stress applied laterally initially causes only an outflow of $h^{\bullet}$ from the source volume S. Inset: Open circuit for the battery current.*

***Figure 14b**: Simplified cross section through the Earth's crust with an assumed p-n transition at a depth of ~25 km. Stress applied laterally later causes only an outflow of both $h^{\bullet}$ and e' from the source volume S. Inset: Closed circuit for the battery current.*

If the source volume S comprises hundreds, maybe thousands of km^3 of rocks at high stress levels, the $h^{\bullet}$ currents, which might flow out upon circuit closure deep in the crust, could be millions of amperes strong [12, 13]. If they fluctuate, they would emit low to ultralow frequency (ULF) and extremely low frequency (ELF) electromagnetic radiation, which is only weakly attenuated in the crust.

There are reports of strong ULF and ELF signals recorded prior to large earthquakes, often shortly before the events. A long train of increased ULF emission was observed prior to the M=7.1 Loma Prieta earthquake in California on Oct. 17, 1989 [46, 47]. An attempt was made to account for this EM emission on the basis of streaming potentials that can lead to electrolytical currents when brines move through a porous medium such as the water-saturated gouge along a fault plane [48]. However, streaming potentials can hardly produce sufficiently strong electric currents to account for the intensity of the ULF emissions [49]. Pre-earthquake EM emissions have been generally called into question [50-52]. Specifically, in the case of the ULF signals reported in conjunction with the Loma Prieta earthquake, accusations of data manipulation have been raised without proof [53, 54].

The discovery of positive hole charge carriers in stressed rocks and their outflow into unstressed rocks may help alleviate the division within the scientific community regarding the mechanisms, by which transient electric currents, even powerful electric currents, may flow in the Earth's crust.

3.5 Reactions at the Rock-Water Interface Involving Positive Hole Charge Carriers

Circuit closure as described in Section 3.4, by allowing the "source volume" to discharge through the n-type conductive lower crust, is not the only way how stress-activated $h^{\bullet}$ charge carriers in pre-EQ situations might be able to generate sustained electric currents. There are at least two other mechanisms to consider.

Being defect electrons in the oxygen anion sublattice positive hole charge carriers are chemically equivalent to O^{-} in a matrix of O^{2-}. An O^{-} is an extremely oxidizing radical state. Therefore, when $h^{\bullet}$ charge carriers flowing through rocks and/or soil arrive at a water interface, chemical reactions with H_2O have to be considered [55]. One such reaction that is likely to occur involves O^{-} subtracting H from the H_2O and forming •OH radicals:

$$O^{-}_{surface} + H_2O \Longrightarrow OH^{-}_{surface} + \bullet OH \qquad (9)$$

Two •OH radicals are expected to combine to give a hydrogen peroxide molecule:

$$\bullet OH + \bullet OH \Longrightarrow H_2O_2 \qquad (10)$$

Eqs. (9) and (10) predict that one H_2O_2 molecule will be generated for every two $h^{\bullet}$ charge carriers arriving at the rock–water interface. The OH^{-} formed as part of the reaction remain in the solid interface, leaving excess H_3O^{+} in the water. These H_3O^{+} and other ions in the aqueous phase would continue to carry the current and close the circuit.

$$H_3O^{+} + e^{-} \Longrightarrow H_2O + \tfrac{1}{2} H_2 \qquad (11)$$

We can therefore modify the laboratory experiment depicted in **Figure 10c/d** by inserting a layer of H_2O into the circuit and allowing the stress-activated $h^{\bullet}$ current to flow from the stressed rock through the unstressed rock and into the water to reach the Cu electrode as shown in **Figure 15a**.

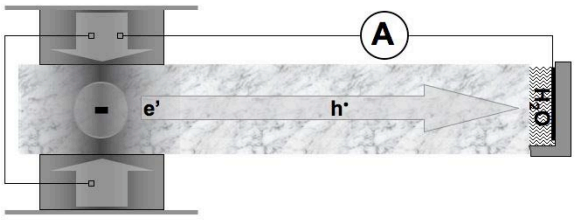

***Figure 15a**: Set-up to demonstrate that the current carried by h• through the rock can close the battery circuit through water.*

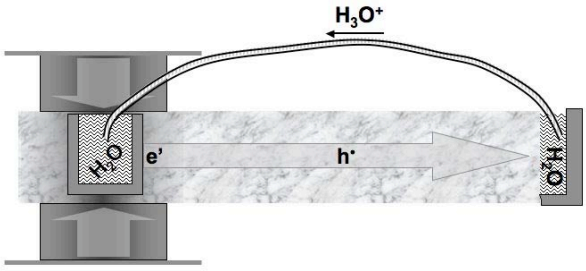

***Figure 15b**: Set-up to demonstrate that the battery circuit can be closed through the electrolytic conductivity of water.*

Indeed, experimentally, a 6 mm thick layer of distilled water does not introduce any noticeable resistance when compared to a Cu contact of the same area placed directly on the rock surface [55]. By measuring the amount of H_2O_2 formed in the water one can show that the stoichiometric reaction holds whereby two $h^\bullet$ generate one H_2O_2 molecule according to eqs. (9) and (10). In other words the $h^\bullet$ charge carriers are quantitatively consumed through the oxidation of H_2O to H_2O_2 at the rock-H_2O interface. The current continues to flow through the water to the Cu contact by way of the electrolytical conductivity of water as indicated by eq. (11). If so, H_2 molecules will be at generated the H_2O-Cu interface equal in number to the H_2O_2 generated at the rock-H_2O interface.

Of course, a circuit like the one depicted in **Figure 15a** does not describe any realistic situation that can be found in nature: there are no metal wires available to close the battery circuit. However, we can close the circuit with a water–filled or brine–filled capillary as depicted in **Figure 15b**. Instead of measuring the electric current with an ammeter we can use the generation of H_2O_2 in the water bath on the right as a proof that a battery current is flowing [55].

This laboratory demonstration of circuit closure through the electrolytical conductivity of water [55] opens the possibilities to understand processes that have most likely taken place throughout Earth's history ever since tectonic forces shaped the continents and built mountain belts. Stress gradients that must have developed between mountain-building regions and bodies of water, including the ocean. The $h^\bullet$ currents flowing along the stress gradient must have led to the oxidation of large quantities of H_2O to H_2O_2 and thereby injected oxygen into Earth's surface environment and hydrosphere. Understanding these processes may help solve the long-standing enigma how the early Earth evolved slowly, but inextricably – over the course of the first 2 billion years – from a pervasively reduced state toward an ever more oxidized state. Large and persistent $h^\bullet$ currents flowing along stress gradients might have contributed significantly to the global oxidation of the early Earth.

With respect to pre-EQ EM signals, the electrolytical conductivity of water or brines can provide a return path for the $h^\bullet$ currents flowing down stress gradients and intersecting faults that are saturated with water or brines. The situation sketched in **Figure 16** represents a case where a fault plane exists that turns subparallel to the surface at relatively shallow depth. Assuming that the

gouge along this fault plane is water– or brine-saturated, it can accept the $h^{\bullet}$ charge carriers flowing ahead of the stress pulse arriving from the left, thus closing the circuit as indicated by the inset.

Such a case might have existed prior to the Sept. 21, 1999 M=7.4 Chi-Chi earthquake in Taiwan, where a fault ruptured over a length of about 120 km with a maximum vertical surface displacement of nearly 10 m. The fault that ruptured at a depth of 16 km was dipping downward at a steep angle at the Earth surface, but turned subparallel at a depth of about 20 km [56]. Two stations of the island-wide magnetometer network located close to the fault recorded at least 7 weeks of intense pre-EQ fluctuations of the local magnetic field with amplitudes up to 250 nT, each lasting several hours. The fluctuations continued for about 6 weeks during the aftershock period and then died down. If the currents, which caused the magnetic field fluctuations recorded at the surface, were flowing at a depth of 10 km during this series of strong magnetic field pulses, they must have been at least 10^6 amp strong [57].

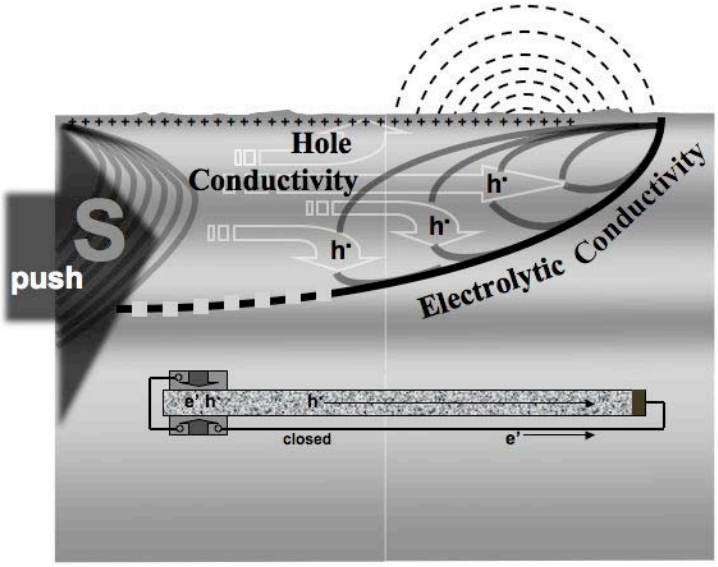

***Figure 16**: Schematic representation of large-scale circuit closure of stress-activated electric currents in the crust through the electrolytic conductivity of water/brines along fault planes.*

There are yet other ways to close the circuit composed of stress-activated $h^{\bullet}$ currents in the Earth's crust. The underlying mechanisms will be described in the next Section.

3.6 Surface Phenomena Caused by Stress-Activated Positive Hole Charge Carriers

Many phenomena suspected to be *bona fide* pre-EQ indicators point to processes at the surface of the Earth. The reported phenomena include

(i) Changes in the atmosphere to a height of 1-10 km,
(ii) Perturbations in the ionosphere above 100 km,
(iii) Luminous phenomena, often called earthquake lights,
(iv) Unusual animal behavior,
(v) Enhanced infrared emission from around the epicentral region seen in satellite images.

The stress-activated positive hole charge carriers have a strong tendency to form surface charge layers. These positive surface charges generate steep electric fields, which are expected to reach or exceed the dielectric breakdown of air even at moderately high charge carrier concentrations as indicated by **Figure 8a/b**. Since positive holes are capable of diffusing not only through compact rocks but also through sand and soil, $h^{\bullet}$ charge carriers that are stress-activated at depth will be able to diffuse to the Earth surface and produce similarly steep electric fields at the ground-to-air interface. The question is whether these surface fields lead to follow-on processes, which help understand the multitude of reported pre-EQ signals.

The surface potential can be measured with a capacitive sensor as sketched in **Figure 10b** [58]. **Figure 16** shows how the surface potential of a block of quartz-free gabbro evolves during loading a rock up to failure. The measurement was conducted inside a Faraday cage on a 30 x 15 x 10 cm^3 piece of gabbro loaded at one end using steel pistons with hardened "teeth", acting as stress concentrators to be able to stress the rock to the breaking point with relatively modest loads on the order of 45,000 lbs, about 20 tons [59].

The surface potential is extremely sensitive to very slight mechanical stresses acting on the rock by, for instance, the platen of the hydraulic press moving upward at the beginning of the experiment (dashed section of the curve). Immediately as the load is applied, the surface potential increases rapidly to about +3 V (significantly higher than the 0.4 V shown in **Figure 8a/b)**. While the load increases further, the surface potential fluctuates. The smooth loading curve is interrupted by periods where the "teeth" sink into the rock. Close ½ to the fracture load, the positive surface potential suddenly collapses and turns negative, while continuing to fluctuate until the rock failed.

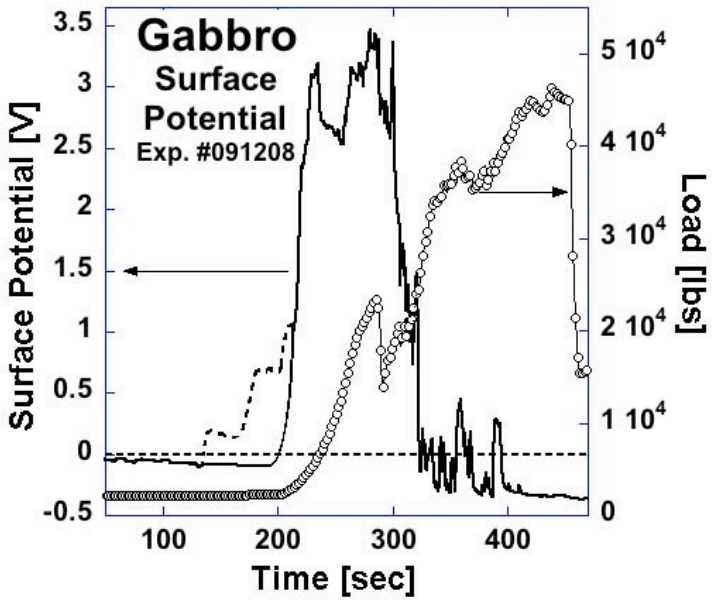

***Figure 17**: Evolution of the surface potential of a gabbro loaded at one end at a constant rate in a hydraulic press using pistons "with teeth" causing massive deformation on a local scale and eventual failure of the rock. Because of the use of pistons with stress concentrators the applied load is given, not the stress in MPa. Immediately upon loading the surface potential becomes*

distinctly positive, then fluctuates and collapses to reverse to weakly negative, still with continuing fluctuations. (Dotted line: unstable initial surface charges caused by slight stresses acting on the rock.)

The initial increase of the surface potential to around +3 V can be readily understood by assuming that $h^{\bullet}$ charge carriers flow out of the stressed rock into the unstressed rock, generating a positive surface/subsurface charge layer as discussed in Section 2.2. Obviously other processes come into play that cause the positive surface potential to fluctuate, then collapse and turn negative.

Using the same basic set-up – a Faraday cage and pistons "with teeth" to load 30 x 15 x 10 cm^3 blocks of gabbro – a negative or positive bias applied to the capacitive sensor turns it into an ion collector for airborne positive and negative ions, respectively. **Figure 18a/b** shows typical results.

Under negative bias, in **Figure 18a**, there is at first no ion current between the rock surface and the ion collector plate. When the load reaches a level where the surface potential has already increased to values around +3 V and begins to fluctuate, an ion current starts to flow. The ion current comes in pulses, which are often correlated with moments when the "teeth" sink into the rock causing massive local deformation. At other times, while the load increases smoothly, pulses of positive ions flow between the rock surface and the ion collector plate. Typically, above the approximate ½ mark to fracture, the positive ion current rises continuously overlain by pulses.

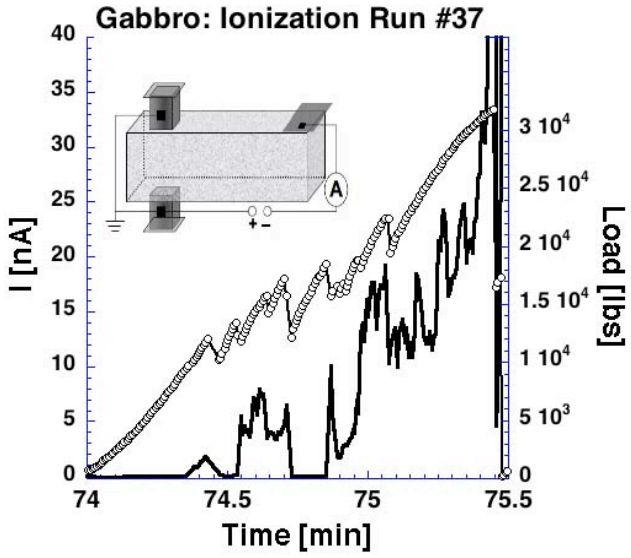

***Figure 18a**: Generation of positive airborne ions upon loading a gabbro at the far end. Inset: Set-up for measuring ± ions.*

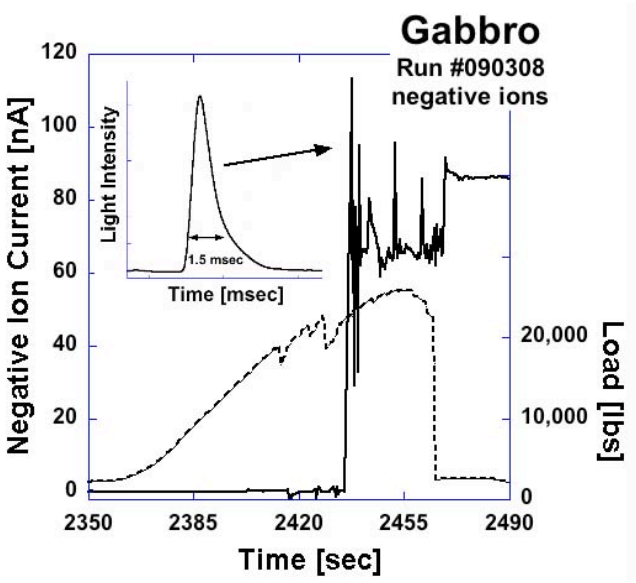

***Figure 18b**: Generation of negative airborne ions and electrons upon loading a gabbro at the far end. Inset: Photodiode signal of light flash.*

Under positive bias, in **Figure 18b**, no current flows until close to or beyond the ½ mark to fracture. The onset usually comes in a sudden burst, accompanied by flashes of light, each lasting for 1-2 ms, followed by a continuous, elevated current with superimposed pulses.

Obviously, during loading, ionization processes take place at the rock surface. They do not start at the beginning of loading but at load levels where, according to the surface potential measurements

such as depicted in **Figure 17**, a relatively strong positive surface/subsurface charge has already built up, around +3 V with the set-up used in these experiments. At first all airborne ions are positive, indicating that air molecules become field-ionized loosing an electron to the rock surface. The rate of formation of positive airborne ions is on the order of 10^9 cm^{-2} s^{-1}.

At higher loads, typically beyond the ½ mark to fracture, corona discharges set in, mostly from corners and edges [43]. They produce free electrons and negative plus positive air ions at rates, which sometimes exceed 10^{10} cm^{-2} s^{-1} [59]. The electrons rain down onto the rock surface, causing the collapse of the positive surface potential as depicted in **Figure 17** and a transition to a weakly negative surface potential.

4 Correlation of Ground-to-Air Processes with Reported Pre-Earthquake Phenomena

If there is a pre-EQ situation, positive hole charge carriers that are stress-activated at depth will flow to the Earth surface. They will set up positive surface potentials, surface/subsurface electric fields, and changes in the electrical conductivity of the top soil. If the electric fields at the ground-to-air interface are as steep as those produced during the laboratory experiments, similar processes are expected to occur as described in the preceding Section 3.6.

4.1 Geo-electric Anomalies

The electrical resistance of the ground has been monitored for many years, in particular in China, using ground electrode arrays derived from the Schlumberger geoelectric sounding techniques [60]. Distinct changes in the resistivity of the have been noted, apparently linked to impending earthquake activity. **Figure 19a** shows the principle of the measurement where the distance AB is typically 1 km and the distance MN on the order of 200 m [61, 62]. The changes in resistivity are usually explained as the result of the build-up of regional or local stresses in the underlying rocks though no detailed understanding seems to be available. Often a tidal component can be seen in the data, indicating that stresses exerted by the tides have the capability to also affect the electrical conductivity of the top soil.

As striking example of the observed ground resistivity changes in the week before the M=7.9 Wenchuan earthquake of May 12, 2008 in Sichuan Province, China, is depicted in **Figure 19b** [63]. Multiple small magnitude changes occurred on an almost daily basis, followed by a large drop in the ground resistivity a few hours before the earthquake.

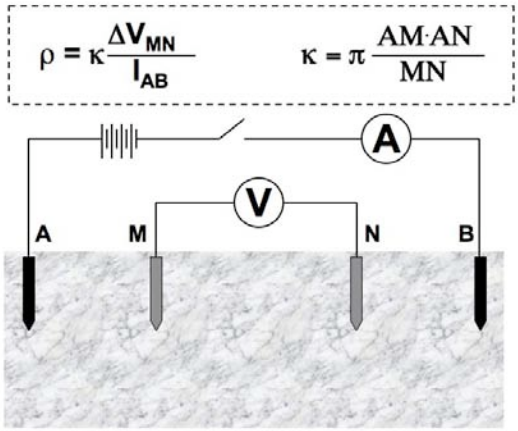

***Figure 19a**: Schematic of geoelectric sounding by means of a Schlumberger array.*

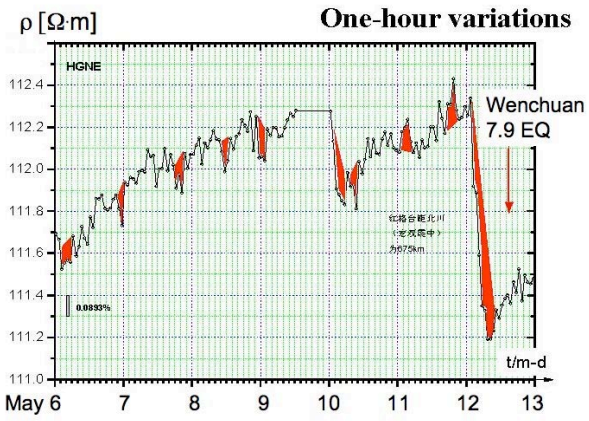

***Figure 19b**: Changes in the electric resistivity of the soil prior to the M=7.9 Wenchuan earthquake (after [63]).*

In view of the stress activation of positive hole charge carriers at depth and their capability to spread to the Earth surface, the recorded changes in the soil resistivity are more likely due to waves of $h^{\bullet}$ charge carriers coming from below rather than to the widely presumed changes in porosity of rocks due to mechanical stresses acting over large distances [61, 62].

4.2 Atmospheric Effects

Massive regional air ionization pulses reaching up to 100,000 ions cm^{-3} and lasting up to 48 hrs have been recorded in Japan by the PISCO network [64, 65]. The ions released into the air were positive, sometimes positive and negative. Starting about 20 hrs before the M=5.4 Alum Rock earthquake of Oct. 30, 2007 in Northern California, a 13 hrs long pulse of massive air ionization was recorded by a CalMagNet station only 2 km from the epicenter [66]. A second station about 35 km away also recorded elevated airborne ion concentrations.

In addition the Alum Rock CalMagNet station recorded a 50 min long train of intense ULF emission. Occurring at the midpoint of the 13 hrs long episode of massive air ionization, the ULF emission suggests a strong current in the ground. The schematic in **Figure 20a** is a proposed variant of the experimental set-up of **Figure 10b** but with the ion collector plate removed. Circuit closure would be provided by airborne ions assumed to be O_2 molecules, which lose an electron to the rock surface and turn into O_2^+. Drifting from the positively charged unstressed end of the rock to the stressed rock volume, which is negatively charged, the airborne ions carry a current and thereby close the battery circuit.

Likewise, in the case of the ULF emission during intense air ionization prior to the Alum Rock earthquake, circuit closure might have been provided through the air. A plausible scenario is depicted in **Figure 20b** assuming an outflow of $h^{\bullet}$ charge carriers from the hypocenter deep below to the Earth surface. At the surface positive airborne ions are generated through field ionization of air molecules. **Figure 20b** further stipulates that the surface/subsurface electric fields become so steep above the volume of maximum stress, e.g. near the epicenter, that corona discharges occur. They are indicated by small "flames". These corona discharges reverse the surface potential from positive to negative, setting up a lateral electric field along which an airborne ion current can flow.

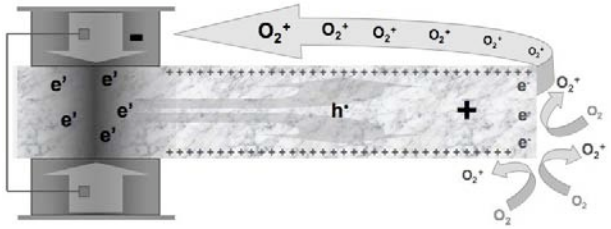

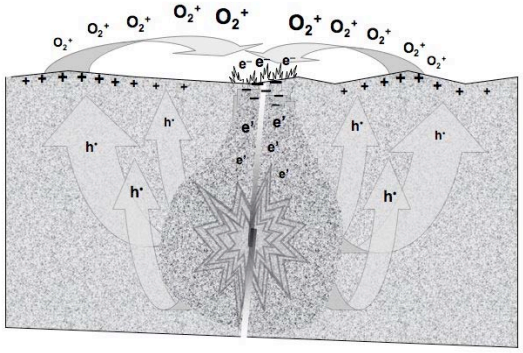

***Figure 20a**: Air ionization at the rock surface and closure of the battery circuit due to the enhanced air conductivity.*

***Figure 20b**: Concept drawing of closure of the battery circuit in the field due to enhanced air conductivity. "Flames": corona discharges.*

Even in the absence of closure of the battery currents inside the Earth, air ionization could have thus provided the return current and thereby allow ground currents to flow. Depending in the magnitude and extent of air ionization and lateral electric fields as sketched in **Figure 20b**, the ground currents might be strong enough to cause measurable ULF signals such observed prior to the M=5.4 Alum Rock earthquake [66].

Injection of ions into the air at ground level will have yet other predictable consequences. The airborne ions can act as condensation nuclei for water droplets, leading to fog and haze. The latent heat released during condensation will warm the air and cause it to rise [67]. Under the right relative humidity conditions clouds can form.

Cloud formation as potential indicator of impending seismic activity has been mentioned repeatedly in the literature [68-70]. A few days before M=6.7 Bam earthquake of Dec. 26, 2003 in Iran a distinct cloud rose above the future epicenter, as documented in **Figure 21** through a sequence of daytime and nighttime MeteoSat images [71]. The cloud started to form on Dec. 20, 2003 and persisted for about 48 hrs. During this time it rose and fanned out, drifting east-south-east for over 2000 km beyond Pakistan to Gujurat, northwest India. No independent confirmation for increased air ionization in the area of Bam around this time is available due to a lack of ground stations.

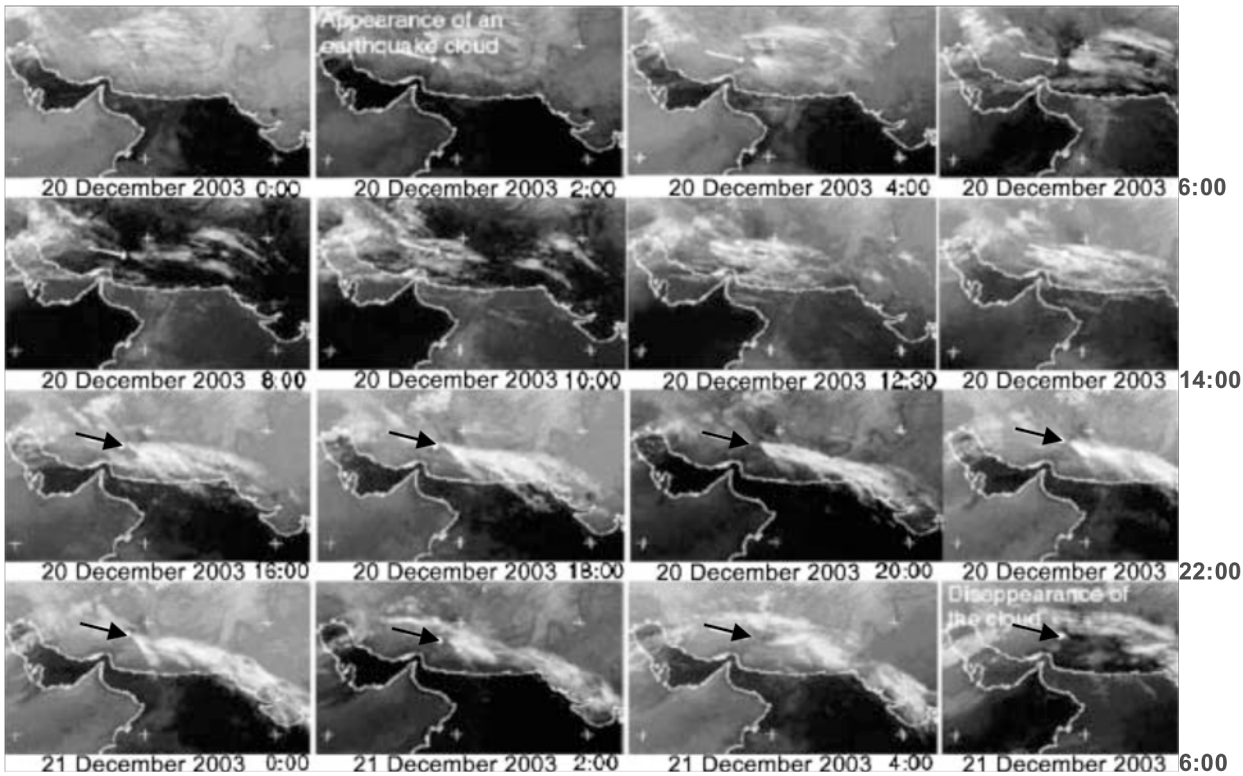

***Figure 21**: Sequence of MeteoSat images prior to the Dec. 26, 2003 Bam earthquake in Iran showing a cloud that originated from a relatively small area near the city of Bam, Iran (arrows), apparently rose to considerable height within a few hours and was then carried by ESE winds over a distance of more than 2000 km to Gujurat, India. [71]. The coastlines of the Persian Gulf, Oman, Pakistan and NW India are emphasized in white. The reversal of contrast between land and water is caused by differences in daytime and night-time lighting.*

4.3 Ionospheric Effects

If airborne ions are injected at the ground level at rates of 10^9–10^{10} cm^{-2} s^{-1} and rise through the atmosphere, they form a vertical current on the order of 10–100 A km^{-2}. Such currents, even if they occur only episodically, may play an important role as part of the global electric circuit [72].

The injection of ions at the ground-to-air interface and upward expansion of clouds of ionized air will modify the vertical electric field between the ground and ionosphere. The effect should be particularly pronounced, if the airborne ions are all or predominantly positive. Such events are expected to lead to perturbations in the uppermost atmosphere and lower ionosphere [73, 74]. Sky radiation measurements have indicated anomalous values several days before a strong earthquake, both in the red and the green parts of the spectrum. Before and after the M=7.4 Petatlán, Mexico earthquake of March 14, 1979, for instance, large fluctuations in sky luminosity were recorded, at times exceeding the standard value for a transparent atmosphere [75]. A possible explanation is that massive injection of positive ions at the ground level and their upward expansion caused electrons at the lower edge of the ionosphere to be pulled down and to interact with the uppermost atmosphere, leading to the excitation of the 630 nm and 557 nm emission lines of atomic O.

Numerous examples of ionospheric perturbations have been reported [76-86]. The perturbations occur in the form of specific changes in the F-region, at altitudes greater than 160 km, and are

typically reported as increases in the Total Electron Content (TEC). The changes in the ionosphere also lead to changes in the subionospheric VLF/LF wave propagation and to shifts of the terminator times [87]. Though these effects are statistically well supported [85] and distinct from the predictions of the International Reference Ionosphere [88], why the ionosphere can be affected in this way seems not to be understood as of yet. The often quoted increase in radon release from the ground, alleged to be due to microfracturing of rocks due to the build-up of regional stress, has been called into question [89, 90]. Highly ionized air injected at ground level over large areas around the future epicenter, its upward expansion and the change in the vertical electric field between the ground and this lower edge of the ionosphere may provide a better physical basis to account for these pre-EQ ionospheric perturbations.

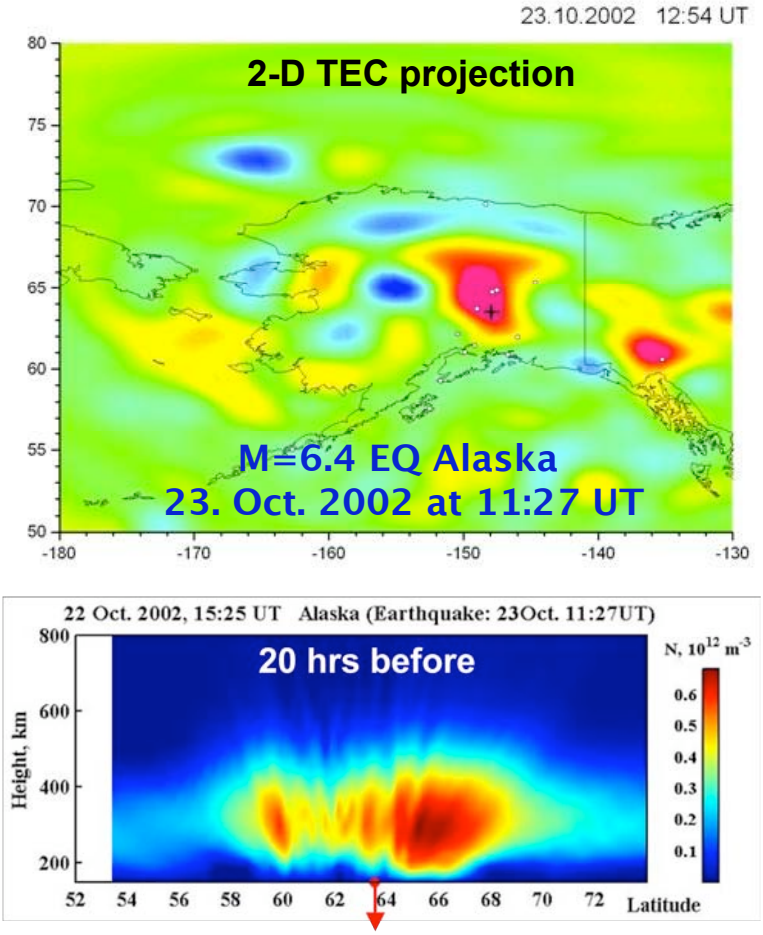

***Figure 22**: Example of a 2-D projection of the Total Electron Concentration (TEC) anomaly prior to a M=6.4 earthquake in Alaska and two S-N cross sections of the TEC anomaly 20 hrs before and 2½ hrs after the event. In the upper left the + sign marks the epicenter. Green colors represent average TEC values, blue represents deficit and yellow/red excess TEC values. In the two panels below the red arrows point to the epicenter. The TEC color code refers to excess TEC values over a presumed unperturbed state.*

Tomographic images of the perturbed ionosphere over regions of impending seismic activity can be obtained using GPS ground station arrays and GPS satellites in geostationary orbits. An example for an M=6.4 earthquake in Alaska is shown in **Figure 22**. **Figure 22** upper left gives the projection of TEC onto the surface of the Earth. **Figures 22** lower left and right show vertical South-North profiles of the anomalous electron density relative to an unperturbed state shortly before and shortly after the event [91]. Observations like these seem to confirm that electrons in the ionospheric plasma are pulled down in response to a positive charge layer moving up through the atmosphere.

4.4 Light Emission and RF Noise

If the surface/subsurface electric fields due to an influx of stress-activated positive hole charge carriers become so steep as to trigger corona discharges, visible light will be emitted. Another, still largely speculative possibility is that, at high concentrations, the delocalized wavefunctions of the positive hole charge carriers should begin to overlap, causing a state which we may describe as solid state plasma. Subvolumes of rocks deep below might enter such a plasma state at high rates of stress increase. If the solid plasma state becomes unstable and expands, it could lead to sudden outbursts of light at the Earth's surface due to volume ionization of the air [92]. Together with corona discharges this and predictable light emission processes falls into the broader group of luminous effects linked to pre-seismic and seismic activity, often referred to as earthquake lights, EQL.

EQLs have been reported since ancient times [93]. They have been witnessed at numerous occasions [94-99], even photographed [100]. Many different explanations have been given [101-103], often considering piezoelectricity as the physical cause [104] or effects of fluids [105, 106]. How positive hole charge carriers and the delocalization of their associated wavefunctions may cause outbursts of light has been discussed with reference to the M=5.9 Saguenay of Nov. 25, 1988 [107], which was remarkable for its 29 km deep hypocenter and large number of EQL reports [98].

EM emissions also occur in other frequency ranges [108-111]. A case where a spread of radiofrequency (RF) emissions might have played a role has been reported from India: the telemetry of a network of seismometer stations covering an area of 10,000 km^2 to monitor a hydropower dam broke down a few days before the on-set of an earthquake swarm about 150 km to the north. The break-down progressed from north to south over the course of several days, suggesting that the telemetry network was overwhelmed by RF noise linked to the impending earthquake swarm. Without operator interference the transmitters operated again normally after the seismic activity to the north had run its course, [112].

4.5 Infrared Emission from around Epicentral Areas

Non-stationary, transient areas of enhanced IR emission have been recognized since the late 1980s and early 1990s in night-time satellite images and linked to impending earthquake activity [113-116]. The reported increase in surface temperatures reach 2-4°C, occasionally higher. This phenomenon has been referred to as "thermal infrared" (TIR) anomalies.

The cause for the TIR anomalies has remained enigmatic [114, 117-120]. In many cases the reported increase in temperature poorly correlates with meteorological ground data. The rapidity with which the effect appears and disappears rules out that it is due to Joule heat from a deep source flowing to the Earth surface. Other processes that have been invoked include: (i) rising fluids which would lead to warm gases from the ground [Gorny et al., 1998]; (ii) rising groundwater levels and changing soil moisture contents [121]; (iii) diffuse CO_2 emanation, causing a "local greenhouse" effect [118, 122, 123]; (iv) Near-ground air ionization due to enhanced radon emission leading to the condensation of water vapor from the atmosphere and, hence, to the release of latent heat [82]. At closer inspection, none of these explanations seems to adequately account for the characteristic features of the reported "thermal anomalies".

A very different approach is based on positive hole charge carriers coming to the surface and forming a surface/subsurface charge layer. Those $h^{\bullet}$ will have a finite probability to recombine

and return to the self-trapped positive hole pair state, which is equivalent to a peroxy link as discussed in Sections 2.2 and 3.1.

We know that it costs energy to break the peroxy bond. In the case of MgO the energy was 2.4 eV. Since the O^-–O^- bond distances are always close to 1.5 Å, even in silica and silicates, irrespective of the chemical surrounding, the energetics will be similar. Hence, whenever two $h^\bullet$ recombine at a surface, they can be expected to regain up to 2.4 eV. This energy will be deposited into the O^-–O^- bond, causing it to be "born" in a vibrationally highly excited state, equivalent to a temperature on the order of 25,000-30,000 K.

There are several channels to shed this excess energy and thermalize. One possibility for the excited O^-–O^- bond to deactivate is to cascade down the vibrational manifold, emitting IR photons corresponding to the downward transitions in the O^-–O^- stretching mode. The transition from the 1st excited state to the ground state, 1 => 0, lies at 10.7 μm or 930 cm^{-1} [124]. Transitions between the higher vibrationally excited states will have energies at longer wavelengths, e.g. lower wavenumbers.

An experiment was set up as shown schematically in the upper right of **Figure 23** [125]. It used a 60 x 30 x 10 cm^3 slab of anorthosite, a monomineralic feldspar rock, stressed at one end. The IR emission spectrum was recorded off the flat rock surface about 50 cm from the stressed volume, using a Bomen MB-100 FT-IR spectroradiometer with a radiometric noise of <10 mK. The IR flux emitted from the rock surface was calculated in brightness temperature T_B, where the intensity at frequency ν is defined as $I_\nu = B_\nu(T_B)$ with B_ν in units of [joule s^{-1} m^{-1} $ster^{-1}$ Hz^{-1}] given as $B_\nu \approx 2\nu^2 kT_B/c^2$, with k the Boltzmann constant, T_B the absolute temperature, and c the speed of light. Expressing T_B in terms of wavelength λ, we obtain $T_B \approx [\lambda^4/2kc] I_\lambda$.

The upper left of **Figure 23** gives the 294K emission spectrum for the 8-12.5 μm window as a function of time. The no-load spectrum was recorded during the first 6 min 40 s. Then the load was applied, increasing at a constant rate until failure of the rock after 30 min. The lower right of **Figure 23** gives the difference spectra obtained by subtracting the average of the no-load spectrum from each of the subsequent scans.

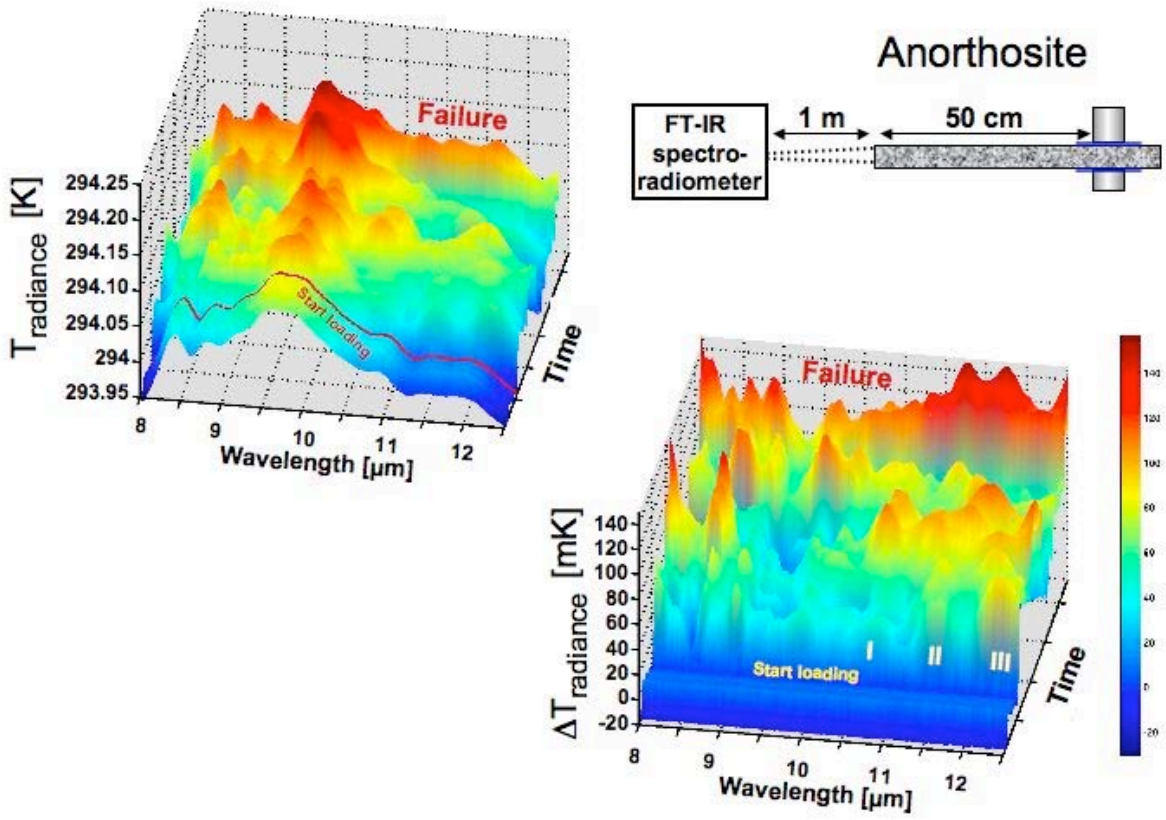

***Figure 23**: Upper right: Experimental set-up to measure the IR emission from the surface of a rock stressed at the far end. Upper left: IR emission in the 8-12.5 µm range before and during loading up to failure. Lower right: Difference spectra showing a series of narrow emission bands.*

Most striking are the immediate and spectroscopically distinct changes in the IR radiation emitted off the rock surface about 50 cm from where the stress was applied. The new IR emission is different with respect to both, intensity and spectral composition. The appearance of narrow bands overlying the broad 294K thermal emission spectrum clearly indicate that these changes are not due to an increase in the rock surface temperature.

Of particular interest are three bands labeled I, II and III in **Figure 23**. They are most clearly defined at the beginning of loading. Band I lies at 10.7 µm (930 cm^{-1}), the energy calculated for the 1 => 0 transition of the O^{-}–O^{-} stretching mode of the O_3Si-OO-SiO_3 link [124] and for O_3Al-OO-SiO_3 in the feldspar structure [Gianfranco Pacchioni, personal communication 2005]. Bands II and III lie at slightly longer wavelengths (smaller wavenumbers), 11.5 µm (870 cm^{-1}) and 12.35 µm (810 cm^{-1}) respectively. They are consistent with transitions beween the 2 =>1 and 3=>2 vibrational states. Other narrow bands in the 8.0–9.0 µm window are indicative of localized Si–O and Al–O stretching modes excited by energy transfer from the O–O vibrations.

The IR intensity around 9.7 µm (1030 cm^{-1}), the maximum of the 294K thermal emission, increased only modestly. This confirms that the temperature of the rock surface barely increased.

Though not simultaneously measured, a positive surface potential certainly appeared during stressing of the rock due to the influx of $h^{\bullet}$ to the surface. A surface potential around 1 V requires a charge carrier density on the order of 10^{-5} Coulomb m^{-2}, equivalent to $\approx 10^{9}$ charges cm^{-2} [42, 43, 58, 126]. To estimate the number of $h^{\bullet}$ pair recombinations necessary to increase $T_{radiance}$ by 150 mK, we may assume that each recombination event regains 2.4 eV. If so, the energy radiated off the rock surface is equivalent to $\sim 10^{4}$ events, indicating that out of all $h^{\bullet}$ arriving at the surface only 10^{-5} need to participate at any time in pairwise recombination events. The pronounced intensity fluctuations of the IR emission suggest that the $h^{\bullet}$ charge carriers arrive in waves at the rock surface, consistent with the fluctuations seen in the surface potential and air ionization at the rock surface as shown in **Figures 17** and **18a/b**.

Figure 24 shows a false color image of the "thermal anomaly" that preceded the M=6.4 Zarand earthquake of Feb. 22, 2005 in Iran as recorded by the NOAA/AVHRR satellite [127]. The anomaly shown in the square box began six days before the event and became quite prominent during the last three days. As indicated by the red color the estimated radiance temperature increase reached almost 10K. On the day of the earthquake the scene was cloudy. The epicenter location listed is marked by the red star. One day after the event the anomaly had disappeared. The lower right of **Figure 24** shows an enlarged view of the boxed area overlain by InSAR data, which translate vertical ground displacements associated with this earthquake into color with red indicating uplift up to 25 cm and blue subsidence up to 17 cm. The area of maximum surface deformation coincides with the area of highest IR emission prior to the earthquake.

No satellite IR imager that is currently in service can provide the spectral resolution necessary to differentiate between the broad thermal IR band and the narrow band emission features expected for stress-activated positive hole luminescence as depicted in the laboratory spectra of **Figure 23**.

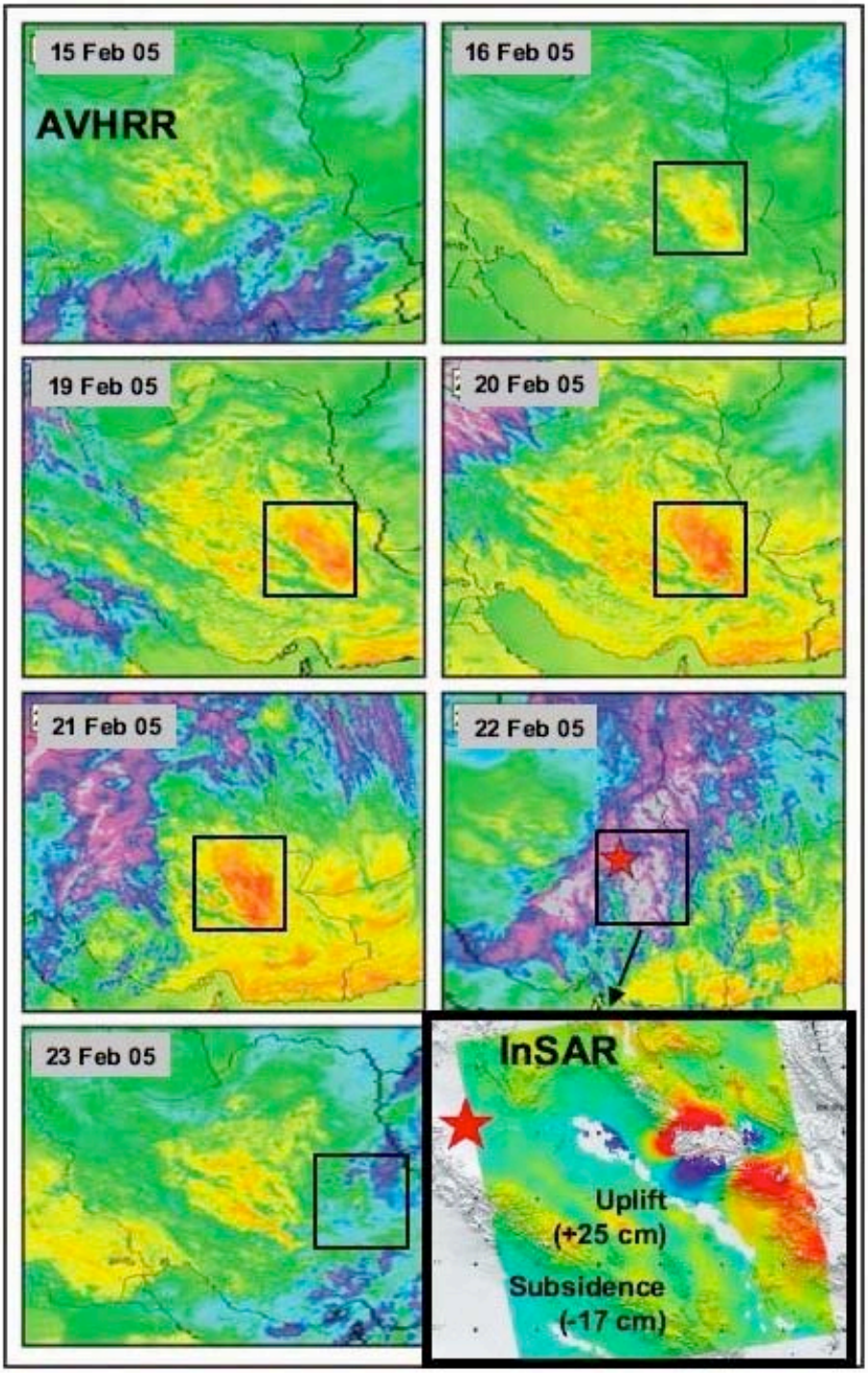

***Figure 24**: Well-developed "TIR anomaly" prior to the M=6.4 Zarand earthquake of Feb. 22, 2005 in Iran as recorded by AVHRR night-time infrared images [127]. The square box marks the area of the anomaly, which reached the equivalent of a 10°C increase in IR radiance. The box is enlarged in the lower right, which shows by means of InSAR data that the region with maximum IR emission cam from the region of maximum vertical coseismic displacement, up to 25 cm uplift (red) and up to 17 cm subsidence (blue) [after Parsons, Oxford U].*

4.6 Emission of Electronically Excited Oxygen Atoms

The radiative decay might not be the only pathway by which vibrationally excited peroxy bonds can get rid of their excess energy. Alternatively, the two O^- can be expected to redistribute their electrons in a way similar to the thermal disproportionation of the peroxy anion in MgO above 600°C as described by eq. (5) and to simultaneously eject an O atom:

$$O_3Si/^{\{OO\}^*}\backslash SiO_3 \Rightarrow O_3Si\text{-}O\text{-}SiO_3 + O^* \qquad [12]$$

where {OO}* indicates the vibrationally excited state of the newly formed peroxy bond.

Evidence for this alternative decay process was accidentally obtained when the light emission was recorded during the failure of rock cylinders using a low-light video camera [128]. **Figure 25a/b** shows a 5 cm diameter granite cylinder in a hydraulic press and a waft of red-glowing air coming off shortly before failure. Though no spectroscopic analysis was presented, the red color is most likely due to the 630 nm emission line arising from the $^1D_2 \leftarrow {}^3P_2$ transition of atomic O. If so, this red glow suggests that O atoms are ejected from the rock surface in an electronically excited state. The excitation energy must be high enough, at least 1.97 eV, to reach the $^3P_2$ level, from where the O atoms can decay to the $^1D_2$ level emitting 630 nm photons. To reflect this as yet tentative explanation a superscript star * is added to the atomic O on the right side of eq. (12). However, the excitation energy is obviously not high enough to excite the green oxygen line at 557 nm, equivalent to 2.22 eV, corresponding to a $^1D_2 \leftarrow {}^1S$ transition.

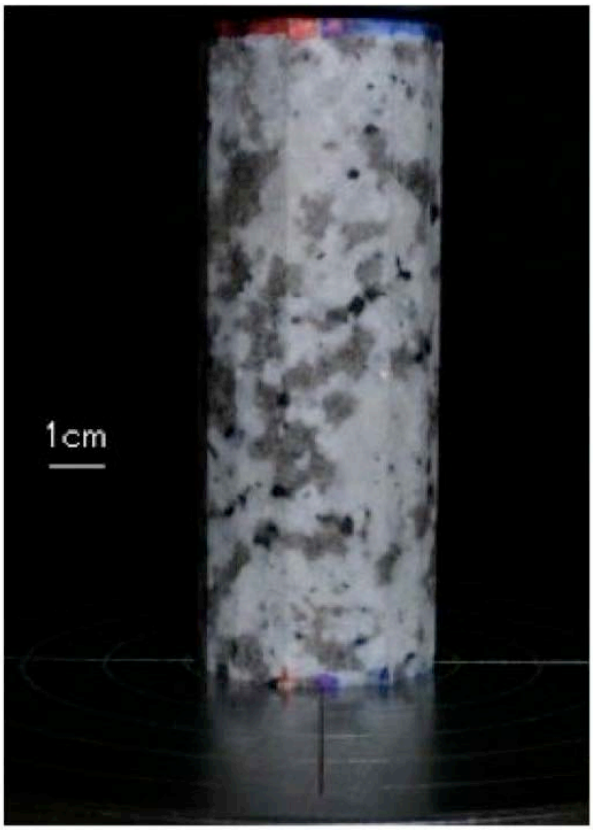

***Figure 25a**: Coarse-grained granite cylinder in a hydraulic press (after [128]).*

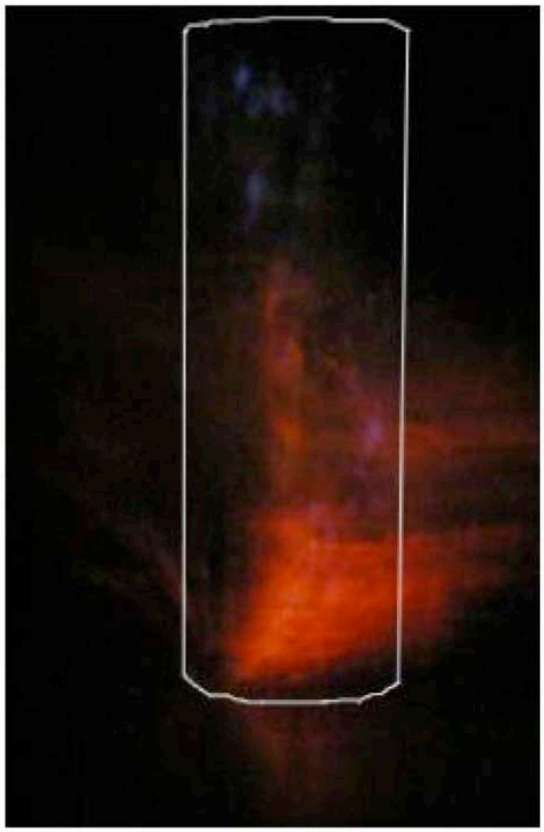

***Figure 25b**: Low-intensity red glow of air streaming off the rock surface before failure.*

If this interpretation is correct, the ejection of O atoms, electronically excited to a level close to 2.0 eV but less than 2.2 eV, would cool the vibrationally excited peroxy links. This mechanism is likely to compete with the de-excitation of the O^-–O^- bond through mid-IR photon emission. It might therefore be possible, under favorable darkness conditions, to detect a weak 630 nm glow close to the ground in satellite images of night-time pre-EQ scenes such as represented in **Figure 23**. This monochromatic red glow would be distinct from the broader spectral range of visible light emissions expected when corona discharges occur over a wide area of the ground as considered in Section 4.2.

4.7 Animal Behavior

Tributsch [129] suggested that the widely reported changes in animal behavior before earthquakes may be caused by charged aerosol particles. Hoenig [130] reported that electrons and positive ions with current levels up to 10^{-11}A are produced as rocks approach failure under laboratory settings. In both cases the production of ions is attributed to piezoelectric effects. In addition to electric currents, other causes for affecting animal behavior before earthquakes have been quoted including very low frequency vibrations, ground tilting, humidity changes, and magnetic field variations [131, 132]. Laboratory observations before the M=7.2 Great Hanshin or Kobe earthquake of Jan. 17, 1995 suggest changes in mouse circadian rhythms [133].

The influence of positive and negative airborne ions on humans and animals has been studied since the 1960's. Though the results were not always unequivocal [134], most studies found that high levels of positive ions, ranging from $2x10^3$ to $1x10^6$ ions/cm^3, have distinct physiological and behavioral effects, possibly related to swelling of the trachea and to increased levels of serotonin (5-hydroxytryptamine, 5-HT) levels in the blood [135]. Serotonin is a neurotransmitter that influences sleep and memory [136, 137]. High levels can result in the "serotonin irritation syndrome" [138] causing headaches, nervousness, and increased sensitivity to pain. Episodes of extreme headaches are consistent with reports on humans said to be sensitive to earthquakes [139].

It is interesting to note that, in many studies, positive airborne ions are considered the most potent agent in soliciting a physiological response both in animals and humans. Piezoelectricity has long been considered to be the only process available in nature through which, by stressing quartz crystals, sufficiently high electric fields can be produced to ionize the air. The discovery of massive air ionization as described in Section 3.6, specifically the selective formation of positive airborne ions, provides an alternative mechanism. It can link the range of atmospheric and ionospheric pre-EQ phenomena to the physiological observations described in this section.

5 Conclusions

Reports from essentially all seismically active regions of the world tell of pre-EQ signals, which the Earth sends out before major seismic events. Some signals appear to be generated deep within the Earth's crust. Others arise at the ground-to-air interface. Others yet point to the ionosphere. The reported pre-EQ signals are diverse, most often subtle and fleeting, only sometimes strong and persistent. Despite many salient observations the prevailing view in the seismology community is that earthquakes strike without prior warning. Some seismologists go so far as to state categorically that "earthquakes cannot be predicted" [5]. Others maintain that pre-EQ signals, including some which have been well documented [46], were probably misinterpreted [50] or may even involve intentional manipulation of data [53, 54].

In a recent report on the status of earthquake-related research Uyeda et al. [4] pointed to the entanglement between seismology-dominated earthquake science and politics, which, for decades, has prevented coordinated efforts to study non-seismic pre-EQ signals.

There are some good reasons why many geophysicists concerned with earthquakes have arrived at a pessimistic outlook about pre-EQ signals. As indicated in Section 1.2 the seismological approach to earthquake prediction is to use information from past earthquakes to estimate the probability of future events. However, most reported pre-EQ signals are non-seismic. The processes, which lead to these signals, obviously take place before the rocks in the Earth's crust reach the point of sudden failure, thereby generating P and S waves, which the seismologists can detect. To study the pre-EQ processes effectively requires a different set of tools than those, which are commonly used in seismology. For this reason seismologists should stand back and let members from other disciplines try to tackle the mystery of pre-EQ signals.

The discovery of O^{2-}/O^{-} valence fluctuations as described in this report provides a way to look at the multitude of reported pre-EQ signals from a very different perspective. They were first noted in MgO single crystals and later found to be ubiquitous in minerals in igneous and high-grade metamorphic rocks. Normally the O^{-} states exist as self-trapped, localized positive hole pairs, which are electrically inactive. Chemically equivalent to peroxy bonds, these positive hole pairs are essentially undetectable. However they become activated (i) when the temperature increases beyond a certain threshold or (ii) when stresses are applied and dislocations move. They then release positive hole charge carriers $h^{\bullet}$ by way of an electron transfer from a neighboring O^{2-}. The $h^{\bullet}$ are associated with energy states at the upper edge of the valence band. The $h^{\bullet}$ flow out of the stressed rock volume, down stress gradients. Their phase velocity is consistent with the postulated phonon-assisted electron hopping. They spread over macroscopic distances, meters in laboratory experiments, most likely kilometers to tens of kilometers in the field. The electrons stay behind.

The outflow of positive holes from the stressed rock volume generates a potential not unlike the outflow of cations from the anode in an electrochemical battery. The potential sets up an electric field that stops the positive hole outflow, until a pathway becomes available for the electrons in the stressed rock volume to also flow out or for other processes to intervene, which can close the battery circuit.

New insight is gained into the generation of pre-EQ signals by studying – in the laboratory – the outflow of positive holes from stressed subvolumes of rocks and the processes at the rock-to-air interface. The work presented here provides some new understanding as to why pre-EQ signals are so diverse, why they are mostly subtle and fleeting, but sometimes strong. Even though these signals are so diverse, they seem to be traceable to one underlying physical process: the stress-activation of positive hole charge carriers from peroxy defects that pre-exist in many rock-forming minerals. This allows us to look at pre-EQ signals not in isolation but as a family of signals, which express themselves during the build-up of tectonic stress in different ways, over different time windows, and at different intensity levels.

Acknowledgments

This paper reviews work that spans several decades. During the past few years the work was carried out in collaboration with Akihiro Takeuchi (supported by a grant from JSPS, Japan Society for the Promotion of Science), Bobby W.S. Lau (supported by a grant from NIMA/NGA, National Imaging and Mapping Agency/National Geospatial Agency), Melike Balk (supported by a travel grant from NOW, Netherlands Organization for Scientific Research), Ipek Kulahci (supported by a grant from NASA Exobiology), Gary Cyr (supported by a grant from NASA's Earth Surface and Interior Program), Milton Bose (supported by a grant from NSF-REU Research Experience for Undergraduates to San Jose State University Physics Department). The work also received partial funding from the NASA Ames Director's Discretionary Fund and the NASA Astrobiology Institute (NAI) Cooperative Agreement NNA04CC05A to the SETI Institute. FF acknowledges the receipt of a Fellowship from the NASA Goddard Earth Science and Technology (GEST) program during part of the time and valuable contributions from Patrick Taylor, Dimitar Ouzounov and Hollis H. Jones (NASA Goddard Space Flight Center). The work benefited from discussions with Vern Vanderbilt and Minoru Freund (NASA Ames Research Center), Max Lazarus (University of Lancaster, UK), Robert Dahlgren (San Jose State University), and from contributions by many students including James King and Jeremy Tregloan-Reed (University of Lancaster, UK), Julia Ling (Princeton University), Matthew Winnick (Vassar College). Access to equipment used in this study was provided by Akthem Al-Manaseer, Department of Civil Engineering, San Jose State University, San Jose, CA, by Charles Schwartz, Department of Civil Engineering, University of Maryland, College Park, MD, and by Jerry Wang, Lynn Hofland, and Frank Pichay, Engineering Evaluation Laboratory at the NASA Ames Research Center.

References

[1] H. Kanamori, *The energy release in great earthquakes*, *1977*, *J. Geophys. Res.* 82, 2981-2987.

[2] Committee on the Alaska Earthquake, *The Great Alaska Earthquake of 1964*, Vol. 1-8, National Academy of Sciences, Washington, DC, 1973.

[3] T. Lay, et al., *The Great Sumatra-Andaman Earthquake of December 26, 2004*, *Science*, 2005, pp. 1127-1133.

[4] S. Uyeda, et al., *Short-term earthquake prediction: Current status of seismo-electromagnetics Tectonophys.*, 2009, pp. 205-213.

[5] R.J. Geller, et al., *Earthquakes cannot be predicted*, *Science*, 1997, pp. 1616-1617.

[6] E.D. Grunewald, and R.S. Stein, *A new 1649-1884 catalog of destructive earthquakes near Tokyo and implications for the long-term seismic process*, *J. Geophys. Res.*, 2006, pp. B12306.

[7] R. Console, et al., *Probabilistic approach to earthquake prediction*, *Ann. Geophys.*, 2002, pp. 723-731.

[8] T.R. Stewart, *Uncertainty, judgment, and error in prediction*, in *Prediction: Science, Decision Making, and the Future of Nature* D. Sarewitz, R. A. Pielke and R. Byerly eds., Island Press, Washington, DC, 2000, pp. 41-57.

[9] D.C. Agnew, and L.N. Jones, *Prediction probabilities from foreshocks*, *J. Geophys. Res.*, 1991, pp. 11,959-11,971.

[10] A. Witze, *The Sleeping Dragon*, *Nature*, 2009, pp. 153-157.

[11] H. Tributsch, *When the Snakes Awake*, The MIT Press, Cambridge, 1982.

[12] F.T. Freund, *Pre-earthquake signals – Part II: Flow of battery currents in the crust*, *Nat. Hazards Earth Syst. Sci.*, 2007, pp. 1-6.

[13] ---, *Pre-earthquake signals – Part I: Deviatoric stresses turn rocks into a source of electric currents*, *Nat. Hazards Earth Syst. Sci.*, 2007, pp. 1-7.

[14] T. Rikitake, *Earthquake Prediction*, Elsevier Sci. Publ. Co., Amsterdam, 1976.

[15] M. McNutt, and T.H. Heaton, *An evaluation of the seismic-window theory for earthquake prediction*, *California Geology*, 1981, pp. 12-16.

[16] Z. Ma, et al., *Earthquake Prediction: Nine major earthquakes in china (1966-1976)*, Springer, Berlin, 1990.

[17] M.F.C. Ladd, and W.H. Lee, *Lattice energies and related topics: Part I*, *Progr. Solid State Chem.*, 1963, pp. 37-82.

[18] ---, *Lattice energies and related topics: Part II*, *Progr. Solid State Chem.*, 1965, pp. 378-413.

[19] H. Kathrein, et al., *O^-- ions and their relation to traces of H_2O and CO_2 magnesium oxide: an EPR study.*, *J. Phys. Chem. Solids*, 1984, pp. 1155-1163.

[20] F. Freund, and H. Wengeler, *The infrared spectrum of OH^--compensated defect sites in C-doped MgO and CaO single crystals*, *J. Phys. Chem. Solids*, 1982, pp. 129-145.

[21] F.A. Kröger, *The Chemistry of Imperfect Crystals*, North-Holland, Amsterdam, 1964.

[22] M.M. Abraham, et al., *Growth of high-purity and doped alkaline earth oxides; Part I: Magnesium oxide and calcium oxide.*, *J. Chem. Phys.*, 1971, pp. 3752-3756.

[23] A.R.W. McKellar, and H.L. Welch, *Anisotropic intermolecular force effects in spectra of molecular hydrogen- and molecular deuterium-rare-gas complexes*, *J. Chem. Phys.*, 1971, pp. 595-609.

[24] R. Martens, et al., *Hydrogen release during the thermal decomposition of magnesium hydroxide to magensium oxide*, *J. Catalysis*, 1976, pp. 366-372.

[25] H.A. Wriedt, *The magnesium-oxygen system*, *Bull. Alloy Phase Diagrams*, 1987, pp. 227-233.

[26] F. Freund, et al., *Highly mobile hole charge carriers in minerals: Key to the enigmatic electrical earthquake phenomena?*, in *Electromagnetic Phenomena Related to Earthquake Prediction*, F. Fujimori and M. Hayakawa eds., Terra Sci. Publ. Co., Tokyo, 1994, pp. 271-292.

[27] ---, *Critical review of electrical conductivity measurements and charge distribution analysis of magnesium oxide*, *J. Geophys. Res.*, 1993, pp. 22209-22229.

[28] F. Batllo, et al., *Positive hole centers in magnesium oxide — correlation between magnetic susceptibility, dielectric anomalies and electric conductivity.*, *J. Appl. Phys.*, 1991, pp. 6031-6033.

[29] B. Henderson, and J.E. Wertz, *Defects in the Alkaline Earth Oxides*, Taylor & Francis, London, 1977.

[30] F. Freund, et al., *Positive hole–type charge carriers in oxide materials*, in *Grain Boundaries and Interfacial Phenomena in Electronic Ceramics*, L. M. Levinson ed., Amer. Ceram. Soc., Cincinnati, OH, 1994, pp. 263-278.

[31] D.L. Griscom, *Electron spin resonance*, *Glass Sci. Technol.*, 1990, pp. 151-251.

[32] H. Kathrein, and F. Freund, *Electrical conductivity of magnesium oxide single crystals below 1200 K.*, *J. Phys. Chem. Solids*, 1983, pp. 177-186.

[33] F.T. Freund, *On the electrical conductivity structure of the stable continental crust*, *J. Geodynam.*, 2003, pp. 353-388.

[34] B.J. Wuensch, et al., *Cation self-diffusion in single crystal MgO.*, *J. Chem. Phys.*, 1973, pp. 5258-5266.

[35] E.-H. Chen, and T.-C. Chang, *Walsh diagram and the linear combination of bond orbital method*, *J. Molec. Struct. Theochem.*, 1998, pp. 127-136.

[36] A.L. Shluger, et al., *Theoretical simulation of localized holes in MgO*, *J. Phys.: Condens. Matter*, 1992, pp. 5711-5722.

[37] B.V. King, and F. Freund, *Surface charges and subsurface space charge distribution in magnesium oxide containing dissolved traces of water.*, *Phys. Rev.*, 1984, pp. 5814-5824.

[38] R.E. Cohen, *MgO - the simplest oxide*, in *Physics Meets Mineralogy*, H. Aoki, Y. Syono and R. J. Hemley eds., Cambridge Univ. Press, 2000, pp. 95-123.

[39] D. Ricci, et al., *Modeling disorder in amorphous silica with embedded clusters: the peroxy bridge defect center*, *Phys. Rev. B*, 2001, pp. 224104 1-8.

[40] A.S. Marfunin, *Spectroscopy, Luminescence and Radiation Centers in Minerals*, Springer Verlag, New York, 1979.

[41] F. Freund, *Conversion of dissolved "water" into molecular hydrogen and peroxy linkages*, *J. Non-Cryst. Solids*, 1985, pp. 195-202.

[42] F.T. Freund, et al., *Electric currents streaming out of stressed igneous rocks - A step towards understanding pre-earthquake low frequency EM emissions*, *Physics and Chemistry of the Earth*, 2006, pp. 389-396.

[43] F. Freund, *Charge generation and propagation in rocks*, *J. Geodynamics*, 2002, pp. 545-572.

[44] E.I. Parkhomenko, and A.T. Bondarenko, *Electrical conductivity of rocks at high pressures and temperatures*, NASA, 1986.

[45] F.T. Freund, and D. Sornette, *Electromagnetic earthquake bursts and critical rupture of peroxy bond networks in rocks*, *Tectonophys.*, 2007, pp. 33-47.

[46] A.C. Fraser-Smith, et al., *Low-frequency magnetic field measurements near the epicenter of the Ms 7.1 Loma Prieta earthquake*, *Geophys. Res. Lett.*, 1990, pp. 1465-1468.

[47] A. Bernardi, et al., *ULF magnetic field measurements near the epicenter of the Ms 7.1 Loma Prieta earthquake*, *Phys. Earth Planet, Inter.*, 1991, pp. 45-63.

[48] M.S. Fenoglio, et al., *Magnetic and electric fields associated with charges in high pore pressure fluids in fault-zone application to the Loma-Prieta ULF emissions*, *J. Geophys. Res. (Solid Earth)*, 1995, pp. 12951-12968.

[49] A. Tzanis, and F. Vallianatos, *A critical review of Electric Earthquake Precursors*, *Ann. Geophysics*, 2001, pp. 429-460.

[50] S.K. Park, et al., *The 2004 Parkfield earthquake: Test of the electromagnetic precursor hypothesis*, *J. Geophys, Res.*, 2007, pp. 10.1029/2005JB004196.

[51] S.K. Park, *Electromagnetic precursors to earthquakes: a search for predictors*, *Science Progress*, 1997, pp. 65-82.

[52] S.K. Park, et al., *Electromagnetic precursors to earthquakes in the ULF band: a review of observations and mechanisms*, *Reviews Geophys.*, 1993, pp. 117-132.

[53] J.N. Thomas, et al., *On the reported magnetic precursor of the 1989 Loma Prieta earthquake*, *Phys. Earth Planet, Inter.*, 2009, pp. 207-215.

[54] W.H. Campbell, *Natural magnetic disturbance fields, not precursors, preceding the Loma Prieta earthquake*, *J. Geophys. Res.*, 2009, pp. A05307.

[55] M. Balk, et al., *Oxidation of water to hydrogen peroxide at the rock–water interface due to stress-activated electric currents in rocks, Earth Planet. Sci. Lett.*, 2009, pp. 87-92.

[56] K.-F. Ma, et al., *Spatial slip distribution of the September 20, 1999, Chi-Chi, Taiwan, earthquake (M_W7.6)-Inverted from teleseismic data*, *Geophys. Res. Lett.*, 2000, pp. 3417-3420.

[57] H.-Y. Yen, et al., *Geomagnetic fluctuations during the 1999 Chi-Chi earthquake in Taiwan*, *Earth Planets Space*, 2004, pp. 39-45.

[58] A. Takeuchi, et al., *Current and surface potential induced by stress-activated positive holes in igneous rocks*, *Physics and Chemistry of the Earth*, 2006, pp. 240-247.

[59] F.T. Freund, et al., *Air ionization at rock surface and pre-earthquake signals*, *J. Atmos. Sol. Terr. Phys.*, 2009.

[60] H.P. Patra, *Schlumberger Geoelectric Sounding Ground Water*, A.A. Balkema, Rotterdam, NL, 1999.

[61] Y.L. Zhao, and F.Y. Qian, *Geoelectric precursors to strong earthquakes in China*, *Tectonophys.*, 1994, pp. 99-113.

[62] F. Qian, et al., *Geoelectric resistivity anomalies before earthquakes*, *Scientia Sinica B*, 1983, pp. 326-336.

[63] Y. Zhao, and F. Qian, *Impending HRT Wave Precursors to the Wenchuan Ms 8.0 Earthquake and Methods of Earthquake Impending Prediction by Using HRT Wave*, *Science in China, Series D: Earth Sciences*, 2009, pp. 11-23.

[64] Y. Wasa, and K. Wadatsumi, *Functional strengthening and employment of Macroscopic Anomaly System by e-PISCO ASP*, *J. Japan Soc. Information and Knowledge*, 2003, pp. 41-47.

[65] K. Hattori, et al., *Variation of Radioactive Atmospheric Ion Concentration Associated With Large Earthquakes*, *AGU Fall Meeting*, San Francisco, CA, 2008, pp. Abstract S52A-03.

[66] T. Bleier, et al., *Investigation of ULF magnetic pulsations, air conductivity changes, and infra red signatures associated with the 30 October Alum Rock M5.4 earthquake*, *Nat. Hazards Earth Syst. Sci.*, 2009, pp. 585-603.

[67] M.A. Dunajecka, and S.A. Pulinets, *Atmospheric and thermal anomalies observed around the time of strong earthquakes in México*, *Atmósfera*, 2005, pp. 236-247.

[68] T. Ondoh, *Anomalous sporadic-E layers observed before M 7.2 Hyogo-ken Nanbu earthquake; Terrestrial gas emanation model*, *Adv. Polar Upper Atmos. Res.*, 2003, pp. 96-108.

[69] V. Tramutoli, *Robust AVHRR Techniques (RAT) for Environmental Monitoring: theory and applications*, in *EUROPTO Conference on Remote Sensing for Geology, Land Management, and Cultural Heritage Ill*, SPIE, Barcelona, Spain, 1998.

[70] D. Lu, *Impending Earthquake Prediction*, Jinangsu Science and Publishing House, Nanjing, China, 1988.

[71] G. Guo, and B. Wang, *Cloud anomaly before Iran earthquake*, *Int. J. Remote Sensing*, 2008, pp. 1921-1928.

[72] M.J. Rycroft, et al., *An Overview of Earth's Global Electric Circuit and Atmospheric Conductivity*, *Space Science Rev.*, 2008, pp. 83-105.

[73] V.M. Sorokin, et al., *Possible DC electric field in the ionosphere related to seismicity*, *Adv. Space Res.*, 2005, pp. 666-670.

[74] H. Rishbeth, *Formation mechanism of the lower-ionospheric disturbances by the atmosphere electric current over a seismic region J. Atmos. Sol. Terr. Phys.*, 2006, pp. 1260-1268.

[75] M.R. Araiza-Quijano, and G. Hernández-del-Valle, *Some observations of atmospheric luminosity as a possible earthquake precursor*, *Geofisica Internacional*, 1996, pp. 403-408.

[76] B. Singh, *Electromagnetic Phenomenon related to Earthquakes and Volcanoes*, Narosa Publ. House, New Delhi, 2008.

[77] K.I. Oyama, et al., *Reduction of electron temperature in low-latitude ionosphere at 600 km before and after large earthquakes*, *J. Geophys. Res.*, 2008, 113, A11317.

[78] I.E. Zakharenkova, et al., *Features of the ionosphere behavior before the Kythira 2006 earthquake Acta Geophysica*, 2007, pp. 524-534.

[79] M. Hayakawa, et al., *Recent progress in seismo electromagnetics and related phenomena*, *Physics and Chemistry of the Earth*, 2006, pp. 129-131.

[80] S. Maekawa, et al., *A statistical study on the effect of earthquakes on the ionosphere, based ont he subionospheric LF propagation data in Japan*, *Ann. Geophys.*, 2006, pp. 2219-2225.

[81] J.Y. Liu, et al., *A statistical investigation of preearthquake ionospheric anomaly,*, *J. Geophys. Res.*, 2006, pp. A05304, doi:10.1029/2005JA011333.

[82] S.A. Pulinets, et al., *Total electron content variations in the ionosphere before the Colima, Mexico, earthquake of 21 January 2003*, *Geofisica Internacional*, 2005, pp. 369-377.

[83] A. Trigunait, et al., *Variations of the ionospheric electron density during the Bhuj seismic event*, *Annales Geophysicae*, 2004, pp. 4123-4131.

[84] J.Y. Liu, et al., *Pre-earthquake ionospheric anomalies registered by continuous GPS TEC measurements, Annales Geophysicae*, 2004, pp. 1585-1593.

[85] Y.I. Chen, et al., *Statistical test for pre-earthquake ionospheric anomaly*, *Terr. Atmo. Ocean. Sci.*, 2004, pp. 385-396.

[86] V. Depuev, and T. Zelenova, *Electron density profile changes in a pre-earthquake period Adv. Space Res.*, 1996, pp. 115-118.

[87] M. Hayakawa, *VLF/LF Radio Sounding of Ionospheric Perturbations Associated with Earthquakes*, *Sensors*, 2007, pp. 1141-1158.

[88] D. Bilitza, *International Reference Ionosphere 2000*, *Radio Sci.*, 2001, pp. 261-275.

[89] H. Rishbeth, *Do Earthquake Precursors Really Exist?*, *EOS*, 2007, pp. doi:10.1029/2007EO290008.

[90] H. Rishbeth, *F-region links with the lower atmosphere?*, *J. Atmos. Sol. Terr. Phys.*, 2006, pp. 469-478.

[91] V.E. Kunitsyn, et al., *Prediction system and method,* US. Patent 7277797, USA, 2007.

[92] F. St-Laurent, *Corona effect and electro-atmospheric discharges: Possible luminous effect following earthquakes?*, *J. Meteorology (UK)*, 1991, pp. 238-241.

[93] J.S. Derr, *Earthquake lights: a review of observations and present theories*, *Bull. Seismol. Soc. Amer.*, 1973, pp. 2177-21287.

[94] I. Galli, *Raccolta e classifzione di fenomeni luminosi osservati nei terremoti*, *Bolletino della Societa Sismological Italiana*, 1910, pp. 221-448.

[95] K. Mack, *Das süddeutsche Erdbeben vom 16. November 1911, Abschnitt VII: Lichterscheinungen*, *Würtembergische Jahrbücher für Statistik and Landeskunde*, Stuttgart, 1912, pp. 131.

[96] T. Terada, *On luminous phenomena accompanying earthquakes*, *Bull. Earthquake Res. Inst. Tokyo Univ.*, 1931, pp. 225-255.

[97] T. Tsukuda, *Sizes and some features of luminous sources associated with the 1995 Hyogo-ken Nanbu earthquake*, *J. Phys. Earth*, 1997, pp. 73-82.

[98] F. St-Laurent, *The Saguenay, Québec, earthquake lights of November 1988-January 1989*, *Seismolog. Res. Lett.*, 2000, pp. 160-174.

[99] T.V. Losseva, and I.V. Nemchinov, *Earthquake lights and rupture processes*, *Natural Hazards and Earth System Sciences*, 2005, pp. 649-656.

[100] J.S. Derr, *Luminous phenomena and their relationship to rock fracture*, *Nature*, 1986, pp. 470-471.

[101] C.-Y. King, *Electromagnetic emission before earthquakes*, *Nature*, 1983, pp. 377.

[102] P. Hedervari, and Z. Noszticzius, *Recent results concerning earthquake lights*, *Annales Geophysicae*, 1985, pp. 705-708.

[103] M. Ouellet, *Earthquake light and seismicity*, *Nature*, 1990, pp. 492.

[104] D. Finkelstein, et al., *The piezoelectric theory of earthquake lightning*, *J. Geophys. Res.*, 1973, pp. 992-993.

[105] A. Nur, *Matsushiro, Japan, earthquake swarm: Confirmation of the dilatancy-fluid diffusion model*, *Geology*, 1974, pp. 217-221.

[106] D.A. Lockner, et al., *A mechanism for the generation of earthquake lights*, *Nature*, 1983, pp. 28-33.

[107] F. St-Laurent, et al., *Earthquake lights and the stress-activation of positive hole charge carriers in rocks*, *Phys. Chem. Earth*, 2006, pp. 305-312.

[108] H. Mitzutani, and T. Ishido, *A new interpretation of magnetic field variation associated with the Matsushiro earthquakes*, *J. Geomagn. Geoelectr.*, 1976, pp. 179 - 188.

[109] P.F. Biagi, et al., *Possible earthquake precursors revealed by LF radio signals*, *Natural Hazards and Earth System Sciences*, 2001, pp. 99 - 104.

[110] K. Ohta, et al., *ULF/ELF emissions observed in Japan, possibly associated with the Chi-Chi earthquake in Taiwan*, *Natural Hazards and Earth System Sciences*, 2001, pp. 37 - 42.

[111] J.Y. Dea, et al., *Sensing of seismo-electromagnetic earthquake precursor radiation signatures along Southern California fault zones: Evidence of long distance precursor ULF signals observed before a moderate Southern California earthquake episode*, in *AGARD, Remote Sensing of the Propagation Environment*, 1992, pp. 13-46.

[112] V.G. Kolvankar, *Report BARC-2001/E/006: Earthquake sequence of 1991 from Valsad region, Guajrat*, Bhabha Atomic Research Centre, Mumbai, India, BARC-2001/E/006, 2001, pp. p. 68.

[113] V.I. Gornyi, et al., *The Earth's outgoing IR radiation as an indicator of seismic activity*, *Proc. Acad. Sci. USSR*, 1988, pp. 67-69.

[114] S.K. Srivastav, et al., *Satellite data reveals pre-earthquake thermal anomalies in Killari area, Maharashtra*, *Current Science*, 1997, pp. 880-884.

[115] Z.J. Qiang, et al., *Abnormal infrared thermal of satellite-forewarning of earthquakes*, *Chinese Sci. Bull.*, 1990, pp. 1324-1327.

[116] Z.-J. Qiang, et al., *Thermal infrared anomaly - precursor of impending earthquakes*, *Chinese Sci. Bull.*, 1991, pp. 319-323.

[117] A.A. Tronin, et al., *Thermal anomalies and well observations in Kamchatka*, *International Journal of Remote Sensing*, 2004, pp. 2649-2655.

[118] A.A. Tronin, *Atmosphere-lithosphere coupling: Thermal anomalies on the Earth surface in seismic process*, in *Seismo-Electromagnetics: Lithosphere-Atmosphere-Ionosphere Coupling*, M. Hayakawa and O. A. Molchanov eds., Terra Scientific Publ., Tokyo, 2002, pp. 173-176.

[119] ---, *Thermal satellite data for earthquake research*, in *IGARSS 2000; IEEE 2000 international geoscience and remote sensing symposium. Taking the pulse of the planet: the role of remote sensing in managing the environment*, IEEE, Honolulu, HI, 2000, pp. 2703-2705.

[120] C. Cui, et al., *Monitoring the thermal IR anomaly of Zhangbei earthquake precursor by satellite Remote sensing technique*, *ACRS*, 1999.

[121] R.K. Chadha, et al., *Search for earthquake precursors in well water levels in a localized seismically active area of Reservoir Triggered Earthquakes in India*, *Geophy. Res. Lett.*, 2003, pp. 69-71.

[122] Z. Quing, et al., *Thermal infrared anomaly- precursor of impending earthquakes*, *Chinese Science Bulletin*, 1991, pp. 319-323.

[123] A.A. Tronin (ed.) *Satellite thermal survey application for earthquake prediction*, in *Atmospheric and Ionospheric Electromagnetic Phenomena Associated with Earthquakes*, Terra Sci. Publ., Tokyo, Japan, 1999.

[124] D. Ricci, et al., *Modeling disorder in amorphous silica with embedded clusters: The peroxy bridge defect center*, *Physical Review B*, 2001, pp. 224104-1 to 224104-8.

[125] F.T. Freund, et al., *Stimulated thermal IR emission from rocks: Assessing a stress indicator*, *eEarth*, 2007, pp. 1-10.

[126] A. Takeuchi, and H. Nagahama, *Interpretation of charging on fracture or frictional slip surface of rocks*, *Phys. Earth Planet. Inter.*, 2002, pp. 285-291.

[127] A.K. Saraf, et al., *Satellite detection of earthquake thermal infrared precursors in Iran*, *Nat. Hazards*, 2008, pp. 119-135.

[128] M. Kato, et al., *Experimental studies on luminescence of visible lights associated with rock fracture*, *IUGG 2007*, Perugia, Italy, 2007, pp. #7501.

[129] H. Tributsch, *When the Snakes Awake: Animals and Earthquake Prediction*, MIT Press, Cambridge, Mass., 1984.

[130] S.A. Hoenig, *Aerosol anomalies preceding earthquakes*, *Nature*, 1979, pp. 169.

[131] J.L. Kirschvink, *Earthquake Prediction by Animals: Evolution and Sensory Perception*, *Bulletin of the Seismological Society of America*, 2000, pp. 312-323.

[132] M. Ikeya, *Earthquakes and Animals: from Folk Legends to Science*, World Scientific, London, 2004.

[133] S. Yokoi, et al., *Mouse circadian rhythm before the Kobe earthquake in 1995*, *Bioelectromagnetics*, 2003, pp. 289-291.

[134] A.P. Krueger, and E.J. Reed, *Biological impact of small air ions*, *Science*, 1976, pp. 1209-1213.

[135] A.P. Krueger, and S. Kotaka, *The effects of air ions on brain levels of serotonin in mice*, *Int. J. Biometeorol.*, 1969, pp. 25-38.

[136] M.J. Crockett, et al., *Serotonin Modulates Behavioral Reactions to Unfairness*, *Science*, 2008, pp. 1739.

[137] A.R. Hariri, Holmes, A., *Genetics of emotional regulation: the role of the serotonin transporter in neural function*, *Trends in Cognitive Sciences*, 2006, pp. 182-191.

[138] F.G. Sulman, et al., *Influence of artifical air ionization on human electroencephalograms*, *Int. J. Biometeorol.*, 1974, pp. 306-312.

[139] L.L. Morton, *Headaches prior to earthquakes*, *International J. Biometeorology*, 1988, pp. 147-148.

Journal of Atmospheric and Solar-Terrestrial Physics ▮ (▮▮▮▮) ▮▮▮–▮▮▮

Contents lists available at ScienceDirect

Journal of Atmospheric and Solar-Terrestrial Physics

journal homepage: www.elsevier.com/locate/jastp

Air ionization at rock surfaces and pre-earthquake signals

Friedemann T. Freund [a,b,e,*], Ipek G. Kulahci [b], Gary Cyr [c], Julia Ling [d,f], Matthew Winnick [e,g], Jeremy Tregloan-Reed [b,h], Minoru M. Freund [a]

[a] NASA Ames Research Center, Code SGE, Moffett Field, CA 94035-1000, USA
[b] Carl Sagan Center, SETI Institute, Mountain View, CA 94043, USA
[c] San Jose State University Foundation, San Jose, CA 95192-5569, USA
[d] NASA Academy 2007, NASA Ames Research Center, Moffett Field, CA 94025-1000, USA
[e] Department of Physics, REU Summer 2008, San Jose State University, San Jose, CA 95192-0106, USA
[f] Department of Physics, Princeton University, Princeton, NJ 08544, USA
[g] Department of Physics and Astronomy, Vassar College, Poughkeepsie, NY 12604-0745, USA
[h] Department of Physics, University of Lancaster, Lancaster LA1 4YQ, UK

ARTICLE INFO

Article history:
Received 4 January 2009
Received in revised form
10 June 2009
Accepted 10 July 2009

Keywords:
Pre-earthquake phenomena
Ionosphere
Air ionization
Corona discharges
Thermal infrared anomalies
Earthquake lights
Animal behavior

ABSTRACT

Pre-earthquake signals have been widely reported, including perturbations in the ionosphere. These precursory signals, though highly diverse, may be caused by just one underlying physical process: activation of highly mobile electronic charge carriers in rocks that are subjected to ever increasing levels of stress. The charge carriers are defect electrons associated with O^- in a matrix of O^{2-}. Known as positive holes or pholes $h^\bullet$, they flow out of the stressed rock into the unstressed rock volume, traveling meters in the laboratory, probably kilometers in the field. At the rock–air interface they cause: (i) positive surface potential, (ii) field-ionization of air molecules, (iii) corona discharges. The rate of formation of airborne ions can exceed $10^9\,cm^{-2}\,s^{-1}$. Massive air ionization prior to major earthquakes increases the electrical conductivity in the air column and may cause ionospheric perturbations, earthquake lights, and unusual animal behavior as well as infrared emission.

1. Introduction

Seismologists often state that earthquakes cannot not be predicted except within wide statistical margins, typically several years or decades (Geller, 1997; Kagan, 1997; Keilis-Borok, 2003). However, non-seismic signals that precede major earthquakes have been reported from essentially all tectonically active regions around the world. A partial list of these pre-earthquake signals includes: ionospheric perturbations: (Hayakawa and Sazhin, 1992; Liperovsky et al., 2000; Pulinets and Boyarchuk, 2004; Shalimov and Gokhberg, 1998); thermal infrared anomalies: (Saraf et al., 2008a, b; Tramutoli et al., 2005; Tronin, 2006); earthquake lights: (Derr, 1973; St-Laurent, 2000); fog, haze and cloud formation: (Aleksandrov et al., 2001; Guo and Wang, 2008); and unusual animal behavior: (Tributsch, 1984).

If these diverse and seemingly disjoint signals are truly precursory, the question arises how their generation may be linked to the earthquake preparation process.

In this report we present data from laboratory experiments that can help us gain insight into the generation of several of these pre-earthquake signals. Specifically we demonstrate that massive air ionization can take place at the surface of rocks, which are being stressed at one end. The build-up of stress within the Earth's crust prior to major earthquakes may likewise lead to processes at the Earth's surface, including massive air ionization, which can be expected to cause ionospheric perturbations and a host of other phenomena.

1.1. Stress-activated electronic charge carriers

Laboratory studies have shown that, when deviatoric stresses are applied to igneous or high-grade metamorphic rocks, electronic charge carriers are activated (Freund et al., 2006). These charge carriers are (i) electrons and (ii) defect electrons or holes, the latter also known as positive holes or pholes for short. Both electrons and pholes derive from pre-existing defects in the matrix of minerals in igneous and high-grade metamorphic rocks,

* Corresponding author at: San Jose State University, SETI Institute, Department of Physics, 515 N Whisman Road, CA 95192-0106, Mountain View, CA 94043, United States. Tel.: +1 650 604 5183; fax: +1 650 604 4680.
E-mail address: friedemann.t.freund@nasa.gov (F.T. Freund).

1364-6826/$ - see front matter © 2009 Elsevier Ltd. All rights reserved.
doi:10.1016/j.jastp.2009.07.013

specifically peroxy defects, O_3X–OO–YO_3, where X Y = Si^{4+}, Al^{3+} etc. The peroxy defects in turn derive from small amounts of O_3X–OH incorporated into nominally anhydrous minerals when they crystallize from H_2O–laden magmas or recrystallize in H_2O–laden high temperature metamorphic environments. The incorporation of "impurity" hydroxyl can be written as hydrolysis of an O_3X–O–YO_3 bond:

$$O_3X\text{–}O\text{–}YO_3 + H_2O \Leftrightarrow O_3X\text{–}OH\ HO\text{–}YO_3 \quad (1)$$

During cooling, at temperatures below about 500 °C, hydroxyl pairs rearrange electronically in such a way as to change the valence of their oxygens from O^{2-} to O^-, while reducing their protons from H^+ to H. The H combine to molecular H_2, while the O^- combine to form the peroxy bond. (Freund, 1985):

$$O_3X\text{–}OH\ HO\text{–}YO_3 \Rightarrow O_3X\text{–}OO\text{–}YO_3 + H_2 \quad (2)$$

During mechanical deformation, dislocations are mobilized and/or generated, sweeping through the mineral grains. When they intersect peroxy defects, the O^-–O^- bonds break (Freund, 2002). In the process an O^{2-} from outside the peroxy bond donates an electron e′, which is captured by the broken peroxy bond. The donor O^{2-} thereby turns into O^-, e.g. physically a defect electron in the O^{2-} matrix, h•, a mobile electronic charge carrier:

$$O_3X - OO - YO_3 + \underset{e' \text{ donor}}{[XO_4]^{4-}} \Leftrightarrow O_3X - O\bullet O - YO_3 + \underset{\text{captured } e'}{} \quad \underset{\text{phole h}^{\not\geq\geq\geq}}{[XO_4]^{3-}} \quad (3)$$

Here the donor O^{2-} is represented by a structural unit $[XO_4]^{4-}$ changing to $[XO_4]^{3-}$.

As an electronic state, the h• "live" at the upper edge of the valence band, which consists primarily of O 2sp-symmetry energy levels. The h• can propagate along the valence band, presumably by phonon-assisted electron hopping. Since the valence bands of all grains in a rock form an energetic continuum, the h• can cross grain boundaries and propagate through sand and soils. Theoretically the phase velocity of an h• wave is given by the phonon frequency $v \sim 10^{12}\,s^{-1}$, times the hopping distance l between oxygen sites, $\sim 2.8 \times 10^{-10}$ m. Hence the h• phase velocity should be $vl \approx 280\,m\,s^{-1}$, consistent with the measured speed of propagation of h• waves through different igneous rocks, $300 \pm 100\,m\,s^{-1}$ (Freund, 2002).

1.2. Rock battery

When stress is applied to a portion of a rock, the number density of electrons and pholes inside the stressed rock volume increases. The h• charge carriers can flow out of the stressed rock and into an adjacent unstressed rock, while the electrons, e′, stay behind. The reason for the electrons staying behind is that there are no energy levels in the unstressed rock, which they could access. Fig. 1 shows a block of rock that is stressed at one end. With the outflow of h• a potential difference develops between the stressed and unstressed rock, equivalent to a battery voltage. The h• outflow continues until an equilibrium is reached between the electric field and the h• concentration gradient.

The situation is analogous to an electrochemical battery, which delivers two types of charge carriers, electrons and cations. The electrolyte allows cations to flow out. Thus, the electrolyte turns positive. For electrons to also flow out, a metal contact must be attached somewhere to the electrolyte. In the set-up depicted in Fig. 1 the circuit is not closed.

1.3. Air ionization

An additional characteristic feature in Fig. 1 is the build-up of a surface charge. It forms because, as the h• ~~enters~~ the unstressed rock, they repel each other electrostatically. They build-up a surface potential, which is a function of (i) the number density of h•, and (ii) the dielectric constant (King and Freund, 1984).

The electric field reaches 400,000 V cm^{-1} on a flat surface of a dielectric with a dielectric constant $\varepsilon = 10$ containing 10^{18} cm^{-3} h• charge carriers, equivalent to 100 ppm. At edges and corners, where the radius of curvature is small, the electric field will be much higher, potentially exceeding the dielectric strength of air. This raises the question whether it might be possible to field-ionize air molecules at the rock surface.

2. Experimental

We used gabbro from Shanxi, China, a typical deep crustal, igneous rock, chemically identically to basalt, with ~40 modal% plagioclase, ~30% augitic clinopyroxene surrounded by alteration rims to amphibole and chlorite, plus ~25% opaques, a porosity of ~0.3%, and <1% total water, mostly due to hydroxyl-bearing minerals such as amphiboles.

The experiments were conducted with $30 \times 15 \times 10\,cm^3$ blocks with one polished surface and all other surfaces saw-cut. The blocks were placed inside an aluminum box ($50 \times 30 \times 30\,cm^3$) acting as a Faraday cage and fitted with a steel ~~below~~ to apply the load. The pistons were in electrical contact with the rock but insulated from the Faraday cage and the hydraulic press by polyethylene sheets with $>10^{14}\,\Omega$ resistance as depicted in Fig. 2a. Hardened stainless steel ball bearings, 6.3 mm diameter, were

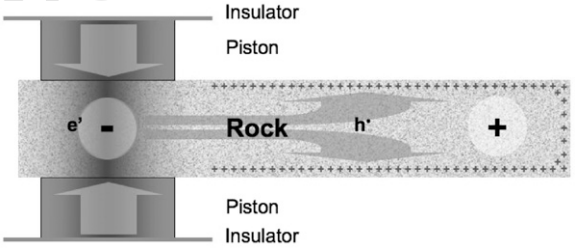

Fig. 1. Stress applied to one end of a rock activates electrons and hole, e′ and h•. The h• flow out of the stressed rock volume into the unstressed volume, creating a potential difference. The situation is similar to that of an open circuit electrochemical battery. The stressed volume is negative and the unstressed volume is positive. The h• charge carriers become trapped at the surface, leading to a positive surface charge.

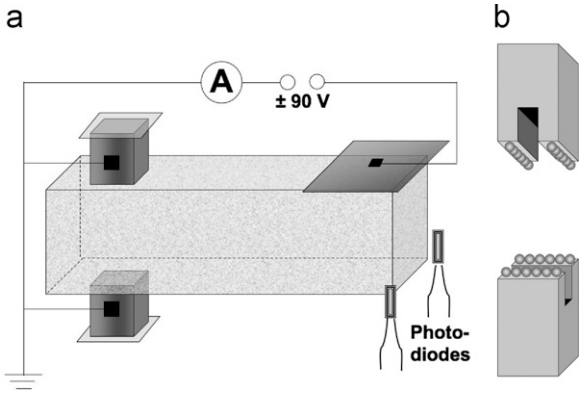

Fig. 2. (a) Configuration of the gabbro block inside the Faraday cage. (b) Detail view of the stainless steel pistons with rows of stainless steel ball bearings to act as stress concentrators.

Please cite this article as: Freund, F.T., et al., Air ionization at rock surfaces and pre-earthquake.... Journal of Atmospheric and Solar-Terrestrial Physics (2009), doi:10.1016/j.jastp.2009.07.013

glued onto the faces of the pistons as depicted in Fig. 2b. The ball bearings acted as stress concentrators causing the rocks to massively deform at the contact points. Because of the stress concentrators, we do not give the stresses in MPa but only report the load in pounds [lbs]. We loaded the rocks moderately fast, 200–300 lbs/s until failure, using a manually controlled hydraulic press.

During earlier impact experiments, we observed positive surface potentials accompanied by corona discharges along the rock edges (Freund, 2002). Similar positive surface potentials appeared in response to slow application of stress (Takeuchi et al., 2006). Values as high as +12 to +17 V were reported at high stress rates (Enomoto et al., 1993). In the present experiments, to detect surface potentials and measure airborne ions, we used an Al sheet ($10 \times 20\,cm^2$, 1 mm thick) as a capacitor plate or ion collector respectively. The Al sheet was placed above the rock on pieces of Styrofoam glued to the inside walls of the Faraday cage extending over the edges as depicted in Fig. 3. The air gap was ~5 mm. To collect positive and negative ions we biased the Al sheet at −90 and +90 V respectively, using ten 9 V batteries connected in series. Two photodiodes were aligned along one edge of the rock as depicted in Fig. 2a to capture flashes of light resulting from corona discharges.

Ion currents and surface potentials were recorded with a Keithley 487 picoammeter and a Keithley 617 electrometer respectively, using LabView 7.1. The photodiode output was recorded on a Tektronix TDS 224 oscilloscope at 100 MHz.

Fig. 3a shows the Faraday cage (with the front half of the cover removed) at the end of experiment #37 after the rock had slightly tilted. It shows the ion collector plate, which had initially been 5 mm above the rock and parallel to the rock surface. Fig. 3b shows details of the pistons with the ball bearings after a wedge-shaped section of the rock had cleaved off. Also seen are the polyethylene sheets used to electrically insulate the pistons from the press and one of the leads connecting the pistons to the picoammeter.

3. Results

3.1. Surface potentials

Fig. 4 shows an example of the surface potential using the Al plate as capacitor. The first sign of a positive potential appeared when the platen of the hydraulic press started to move upward

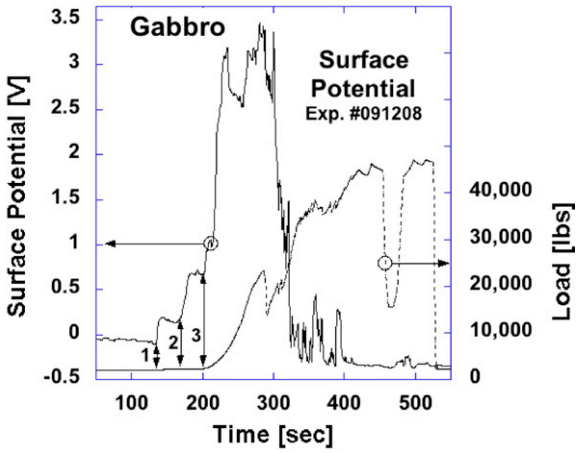

Fig. 4. Surface potential. Double arrow 1: the surface potential started to build-up as the platen of the press started to rise and caused enough acceleration to activate some charge carriers. Double arrow 2: first contact with piston of the press. Double arrow 3: start of loading. The rock did not break at the end of this run. The surface potential reached +3.4 V, and soon dropped to negative values (−0.3 V).

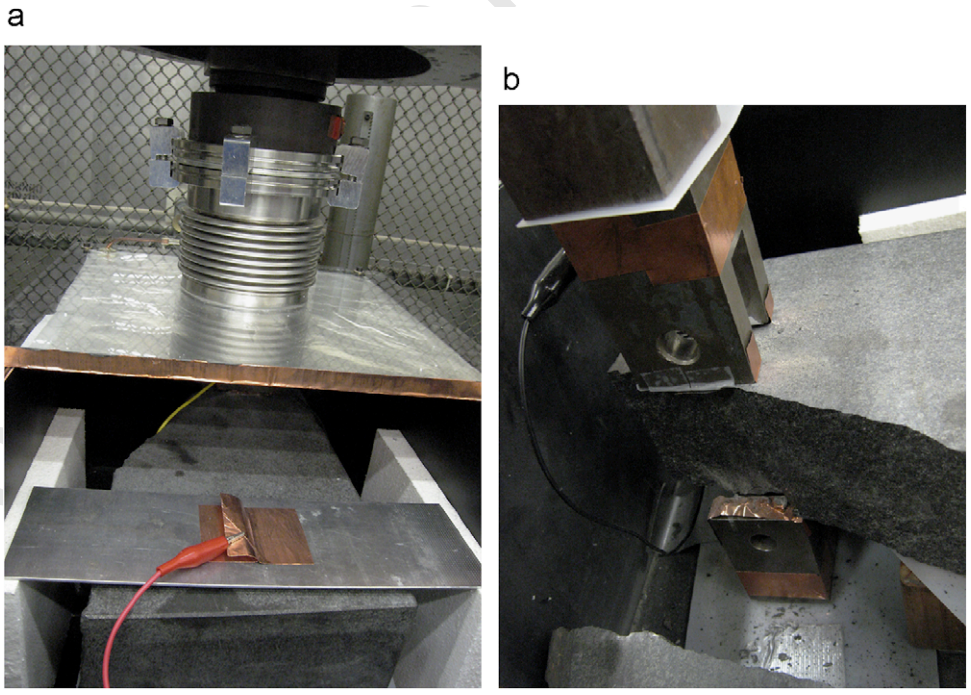

Fig. 3. (a/b): two inside views of the Faraday cage after completion of experiment #37, in which an approximately triangular portion the gabbro block split off laterally, causing the rock to only slightly tilt upon failure. (a) Position of the Al sheet used as ion collector or as capacitor place. (b) The pistons with stainless steel ball bearing stress concentrators and the polyethylene sheets.

(arrow 1). The stress caused by this modest acceleration was enough to activate some $h^{\bullet}$ charge carriers, which led to a positive surface potential of +300 mV. When the piston of the press made contact, the potential rose to +700 mV (arrow 2). When the press began loading the rock, about 200 s into the run (arrow 3), the surface potential rose rapidly reaching +3 V around 10,000 lbs. The surface potential remained high with further loading but fluctuated between +2.6 and +3.4 V. Discontinuities occurred in the loading curve, the first at about 280 s. They mark moments when the stainless steel ball bearings, e.g. the stress concentrators, are sinking into the rock, reducing temporarily the hydraulic pressure. Rock deformation episodes of this type were observed during all experiments described here.

Close to 300 s into the run, the surface potential around +3 V abruptly broke down as depicted in Fig. 4, turning negative to around −0.3 V with intermittent spikes. This general behavior, first a strong positive surface charge followed by abrupt transition to slightly negative values, was ~~repeatedly~~ observed during these experiments.

3.2. Positive air ions

To record positive ion currents across the air gap the Al plate was biased at −90 V. Fig. 5a/b ~~show~~ a typical run with the inset depicting the electric circuit. Before loading, the background ion current was in the low pA range. It remained low at low loads. However, when the load approached 10,000 lbs, after the ball bearings had already sunk into the rock as indicated by the discontinuities in the load vs. time curve, a positive ion current started to flow. Between 10,000 and 25,000 lbs several load vs. time discontinuities occurred. The positive ion current increased, fluctuating in the 10–25 nA range. The discontinuities in the load vs. time curve are not correlated to spikes in the ion current. The area of the collector plate was 200 cm^2. An ion current of 20 nA corresponds to an average ion production rate on the rock surface on the order of $10^9\ cm^{-2}\ s^{-1}$.

About 2 s before failure, at about 30,000 lbs, a 55 nA spike occurred, indicating a burst of positive ions from the rock surface. The rock failed at the 75.5 min time mark. The rock slightly tilted but did not touch the collector plate. The collector plate continued to measure an ion current, which increased sharply to 450 nA and then decreased exponentially over the next 30 s.

Fig. 6 shows another run under negative bias. In this case the positive ion current started soon after loading, but the overall level remained moderate at around 10 nA (left inset). In spite of several episodes with the ball bearings sinking into the rock, the positive ion current did not increase. It even dropped to near-background level between 785 and 800 s. At 815 s a sharp, prominent current spike occurred, reaching 185 nA. The rock failed at 830 s, splitting across its width, causing the rock to drop from underneath the ion collector plate without touching it. The ion current increased moderately after failure and then decreased exponentially over the next 30 s (right inset).

The recurring high levels of positive ions immediately after fracture and their decay with a characteristic decay time around 30 s suggest that, during fracture, bursts of ions are generated, filling the Faraday box. The ions slowly drifted to the walls to be neutralized.

The short current spikes during loading are distinctly different. Observed often but without clear correlation to the episodes of rapid rock deformation, these spikes typically last for only a few seconds as depicted in Fig. 6. Since corona discharges had been observed during earlier impact experiments (Freund, 2002), we changed the bias to +90 V to collect electrons and negative ions. In addition, light emission was monitored with the pair of photo-diodes situated as depicted in the inset in Fig. 2a.

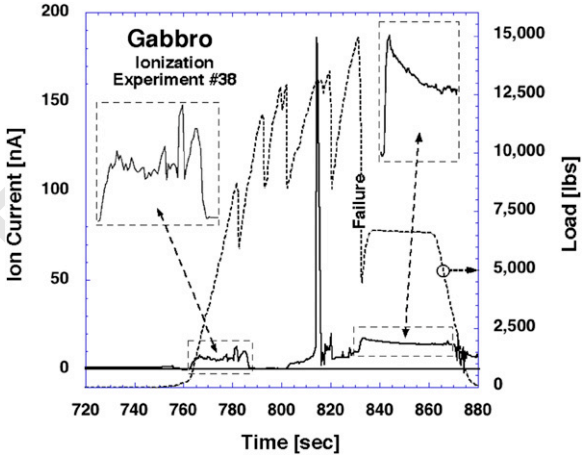

Fig. 6. Example of a run under −90 V bias marked by several massive deformation events but low levels of positive air ions. This run produced a particularly large narrow spike in the positive ion current at 815 s, indicative of a corona discharge.

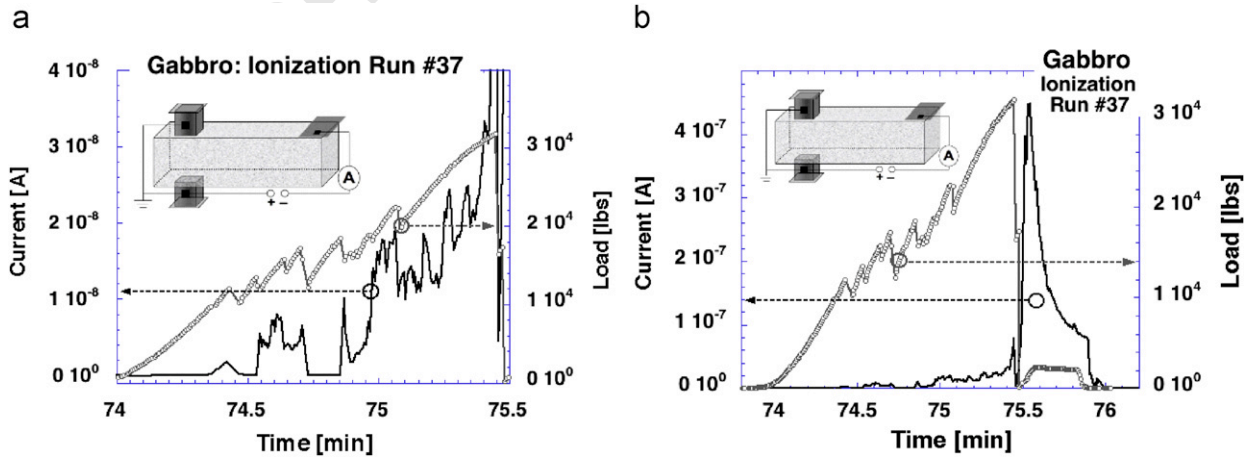

Fig. 5. (a/b): positive ion current during deformation of gabbro. The discontinuities in the load vs. time curves are caused by a drop in the oil pressure of the hydraulic press when the stainless steel balls are sinking into the rock. (a): Before failure; (b): whole run.

Please cite this article as: Freund, F.T., et al., Air ionization at rock surfaces and pre-earthquake.... Journal of Atmospheric and Solar-Terrestrial Physics (2009), doi:10.1016/j.jastp.2009.07.013

3.3. Corona discharges

The results obtained under +90 V bias were characteristically different from those under −90 V bias. Positive ions typically started to form at relatively low loads as demonstrated in Figs. 5 and 6. By contrast negative ions and/or electrons recorded under +90 V bias appeared only at higher loads, typically $\frac{1}{2}$ to 2/3 the load needed to cause failure.

Fig. 7 shows an example. Up to 20,000 lbs, the current remained at background levels, in the low pA range. Abruptly, at the 2434 s mark, the current rose to 100–115 nA, followed by a continuously high level around 65–70 nA, accentuated by multiple short spikes. The spikes are accompanied by light pulses, each about 1.5 ms long, one of which is shown in the inset. Light pulses indicate corona discharges.

4. Discussion

The presence of electrically inactive, dormant precursory peroxy defects in the structure of rock-forming minerals and of the electronic charge carriers, which they engender when the rocks are stressed, holds the key to many reported pre-earthquake signals. Their discovery may be as fundamental for geophysics as was the discovery of semiconducting properties in amorphous materials for solid state and applied physics (Ovshinsky and Adler, 1976).

4.1. Surface potential, positive airborne ions and corona discharges

Stressing one end of a block of igneous rock such as gabbro leads to a series of processes at the unstressed end. First, positive surface potentials uniformly across the rock surface, increasing rapidly with increasing stress and reaching about +3 V. Second, massive amounts of positive airborne ions are collected above the unstressed end of the rock. Third, massive amounts of electrons and/or negative airborne ions are collected.

The positive surface potentials confirm observations reported earlier (Freund, 2002) that, when an igneous rock is subjected to deviatoric stresses, electronic charge carriers are activated. These charge carriers are pholes $h^\bullet$ activated as described by Eq. (3) in Section 1.1. The activation is thought to involve dislocations that are mobilized in the stressed rock volume. The dislocations intersect pre-existing peroxy defects in the matrix of minerals and cause them to break. Electrons e' are activated alongside the pholes $h^\bullet$. However, while the pholes can flow out of the stressed rock volume, the electrons are unable to follow suit. Hence, as soon as $h^\bullet$ flow out, the stressed rock charges negatively relative to the unstressed rock. The unstressed rock becomes positively charged.

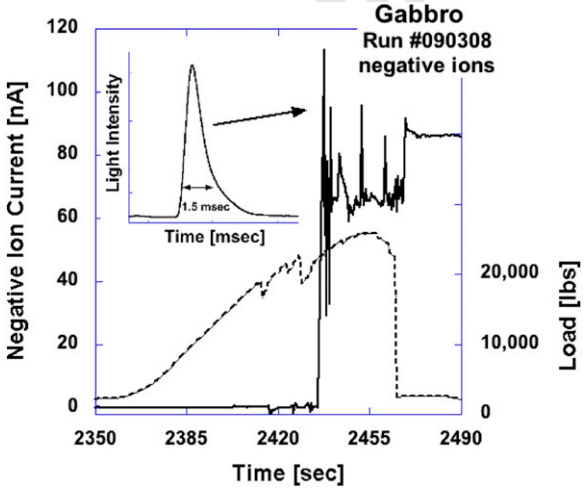

Fig. 7. Current recorded with +90 V bias on the ion collector plate, indicating free electrons and/or negative ions. Inset: light flash captured by the photodiode during the large ion current spike confirming a corona discharge.

The situation is analogous to that in an electrochemical battery where cations spread into the electrolyte leaving behind a negative charge. The electrons, unable to spread into the electrolyte, can flow out via a metal contact. It is important to note that, even without closing the circuit, a potential difference develops, the "battery voltage".

The difference between an electrochemical battery and the "rock battery" as presented here is that the positive charge carriers are not cations but positive holes, $h^\bullet$. Thus, when stressed, the rock turns into a type of semiconductor battery, which has not been previously described.

Positive charges on the surface of the rock appear even at low stress levels as demonstrated in Fig. 4. Under these conditions the number of $h^\bullet$ charge carriers available to flow out of the stressed rock volume may still be small but they suffice to build-up a surface potential (Freund et al., 2006). As the rock is loaded more, the surface potential increases, indicating a larger number of charge carriers activated in the stressed rock volume. At the moderately fast loading rates used here the surface potentials reach rapidly values around +3 V.

Fig. 8a/b shows the surface potential and associated electric fields calculated for a flat surface of a semi-infinite medium with the dielectric constant $\varepsilon = 10$ (King and Freund, 1984). Within the range of charge carrier concentration under consideration the surface potential is constant but the thickness (d) of the surface charge layer decreases with increasing $h^\bullet$ concentration. This means that the electric field, which builds up directly at the solid–air interface, increases as d decreases. At a relatively low charge carrier concentration of $10^{17}\,m^{-3}$ (~10 ppm), the calculated value for E is 120,000 V/cm. At a concentration of $10^{18}\,m^{-3}$, it increases to 400,000 V/cm. At still higher concentrations or at edges and corners, E is expected to soon exceed the dielectric break-down strength of air, $\sim 2\text{–}3 \times 10^6$ V/cm.

The electric fields due to the accumulation of charge carriers at and a few tens nanometer below the surface are not the same as the macroscopic vertical electric fields at the Earth surface that are normally given in units of V/m (Brown, 1985; Pulinets, 2009). The electric fields under consideration here are short-range and act only over short distances across the surface-to-air interface.

Fig. 8c shows a Monte Carlo simulation with 1000 mobile charges allowed to relax in a dielectric medium. The charge carrier concentration is very low inside, low on flat surfaces but high along edges and corners, predicting very high electric fields.

In a system as depicted in Fig. 1, where the battery circuit is not closed, the charge carriers flowing out of the stressed rock volume become stagnant in the unstressed rock. They should create a uniform and constant surface potential independent of the number of $h^\bullet$ charge carriers activated (King and Freund, 1984). However, as Fig. 4 shows, after the surface potential had increased to +3 V, it started to fluctuate between +2.6 and +3.4 V. Such fluctuations suggest a break-down of the open circuit approximation.

This suggests that, around +3 V, the electric field reaches high enough values to extract electrons from neutral gas molecules, e.g. to field-ionize them, in particular along edges and corners as depicted in Fig. 9. The most likely candidates for field-ionization are O_2 and H_2O, which have relatively low ionization potentials.

The measured ion current as shown in Fig. 5a is on the order of ~20 nA, equal to an ion generation rate $\sim 10^9\,cm^{-2}\,s^{-1}$. For each air molecule that is field-ionized at the rock surface, an electron is

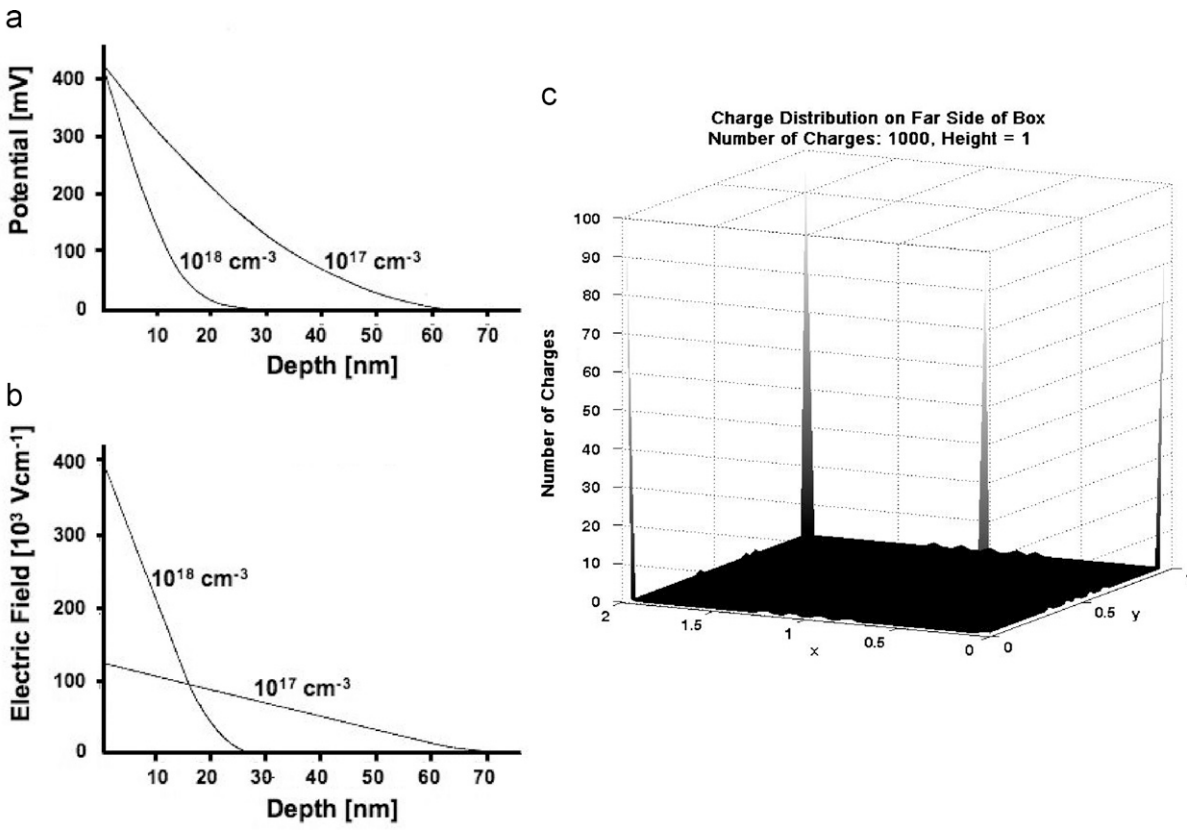

Fig. 8. Surface potential (a) and electric field (b) calculated for the surface of a semi-infinite insulator with a dielectric constant of 10 with charge carrier densities of 1 in 105 and 1 in 104 (King and Freund, 1984). (c): Simulation of 1000 charge carriers inside a dielectric medium, $\varepsilon = 10$, after reaching an equilibrium distribution due to their mutual repulsion in the bulk. The charge carrier concentration is projected onto the basal plane.

deposited into the rock surface. This must lower the positive surface potential.

The charge carrier density needed to produce a 1 V surface potential is on the order of $10^9\,cm^{-2}$ (Takeuchi and Nagahama, 2002). Therefore, if $10^9\,cm^{-2}\,s^{-1}$ air molecules become field-ionized, they deposit $10^9\,cm^{-2}\,s^{-1}$ electrons into the rock surface. This is obviously sufficient to cause a significant reduction of the positive surface potential. At the same time, more $h^\bullet$ charge carriers stream from the stressed portion of the rock to the unstressed portion and, hence, to the surface. These newly arriving $h^\bullet$ rebuild the positive charge of the surface almost as fast as it is reduced. This causes the positive surface potential to fluctuate wildly as shown in Fig. 4.

Fig. 4 also shows that, at still higher load, the positive surface potential drops abruptly and turns negative. The emission of light shown in the inset in Fig. 7 indicates corona discharges. This reversal of the sign, together with the light blips, suggest the production of electrons by the corona discharges. These electrons "rain down" onto the rock surface and annihilate the positive surface charge more effectively than the field-ionization of air molecules was able to do. In addition, through attachment to neutral gas molecules, the electrons form negative airborne ions.

Corona discharges are expected to manifest themselves in air ion current bursts, both under negative and positive bias. Concurrent electronic excitation and electron–ion recombination reactions will lead to the emission of visible light.

Ionization of air over the unstressed portion of the rock explains the break-down of the open circuit approximation of Fig. 1. As illustrated in Fig. 10, while electrons are delivered to the surface and recombine with $h^\bullet$ charge carriers, positive ions will

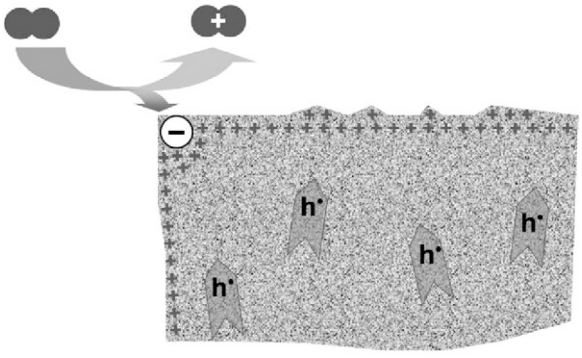

Fig. 9. Conceptual representation of field-ionization of air molecules at the rock surface, in particular at edges and corners, where the $h^\bullet$ densities are highest and where the electric field will be high enough to extract an electron from a gas molecule.

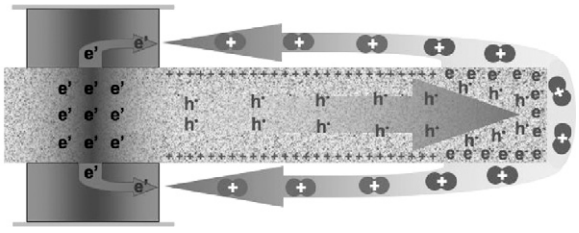

Fig. 10. Massive air ionization on the unstressed part of the rock will produce an electric current running through the air and closing the battery circuit.

Please cite this article as: Freund, F.T., et al., Air ionization at rock surfaces and pre-earthquake.... Journal of Atmospheric and Solar-Terrestrial Physics (2009), doi:10.1016/j.jastp.2009.07.013

drift toward the negatively charged pistons, which are in contact with the stressed rock. This closes the battery circuit.

In summary, the laboratory experiments, designed to measure surface potentials and airborne ion currents, have provided insight into processes at the rock surface when a portion of the rock is subjected to deviatoric stresses. With increasing stress the following processes occur sequentially at or above the rock surface:

(i) trapping of $h^\bullet$ charge carriers and appearance of positive surface charges;
(ii) field-ionization of air molecules and generation of positive air ions; and
(iii) corona discharges with bursts of ion current and flashes of light.

4.2. Air ionization and pre-earthquake phenomena

We can use these laboratory observations to address phenomena, which have been observed in the field and have been linked to impending seismic activity.

We start from the simple, but very basic premise that earthquakes represent the final stage of a long drawn-out process deep below, in the future hypocentral volume, marked by increasing levels of deviatoric stresses. How the stresses evolve, how they increase, decrease or change directions will vary enormously from case to case. However, close to a catastrophic rupture, the stresses in the hypocentral volume can be expected to locally concentrate and to increase fast. Another generally valid statement is that the hypocentral volume, where the stresses evolve toward catastrophic rupture, will always be surrounded by a larger volume of less stressed or unstressed rocks.

Therefore, the experimental set-up used in the experiments described here can be used to draw parallels to pre-earthquake situations in the Earth's crust. This is particularly true for the electric analog of an open battery circuit with the outflow of $h^\bullet$ charge carriers from the most stressed rock volume being the dominant process.

Under such conditions $h^\bullet$ charge carriers activated deep below are expected to spread out of the prospective hypocentral volume into the surrounding less stressed or unstressed rocks, while the electrons cannot flow out. Some $h^\bullet$ will travel upward and reach the Earth's surface. The higher the stresses in the hypocentral volume, the larger the number of $h^\bullet$ charge carriers flowing out and the larger the number of $h^\bullet$ charge carriers reaching the Earth's surface. With more $h^\bullet$ charge carriers arriving, the electric fields at the surface will increase. Eventually those fields can be expected to reach values high enough to initiate air ionization at the Earth's surface (leading to positive ions) and corona discharges (leading to free electrons and negative ions alongside positive ions).

The measured ion currents suggest rates on the order of 10^9–10^{10} ionization events per second and cm^2. Extrapolated to km^2, this is equivalent to an ion current on the order of 10–100 A rising off the Earth surface. Such currents, if they occur in nature, could constitute a significant part of the global electric circuit, which connects the solid Earth with the ionosphere (Roble and Tzur, 1986).

4.3. Perturbations in the ionosphere

Using a ground-based ionosonde to determine the total electron content (TEC) in the ionospheric foF2 layer, anomalies were recognized two to three days before most of the $M \geq 6.0$ earthquakes in the Taiwan area during 1994–1999 (Liu et al., 2000). Likewise, using GPS receivers, ionospheric anomalies were found to occur prior to 16 out of 20 $M \geq 6.0$ earthquakes in the Taiwan region between 1999 and 2002 (Liu et al., 2006). One day before the $M = 6.8$ Kythira earthquake in Greece on January 8, 2006, during a quiet period marked by the absence of magnetic storms, the TEC values above the epicentral region were found to have increased significantly, up to 50% relative to the surrounding region and the longtime average (Zakharenkova et al., 2007). In Japan statistically significant changes in the subionospheric propagation of low frequency radio waves prior to earthquakes have been recorded (Maekawa et al., 2006) as well as sporadic ionospheric E layer anomalies prior to the $M = 7.2$ Kobe earthquake of January 16, 1995 (Ondoh, 2003), and anomalies prior to the $M = 8.3$ Tokachi-oki of September 25, 2003 off the coast of Hokkaido (Hayakawa et al., 2005). Using satellite and ground-based GPS data anomalous fluctuations in the integrated TEC have also been described prior to the $M = 7.6$ Bhuj earthquake in Gujarat, India (Trigunait et al., 2004) and other events on the Indian subcontinent (Singh and Singh, 2007). Similar ionospheric variations were seen prior to the $M = 7.8$ Colima earthquake of January 21, 2003 in Mexico (Pulinets et al., 2005).

The ionospheric anomalies extend over several hundred to a few thousand kilometers. However, no consensus has been reached as to the cause or causes (Rishbeth, 2007). If a process exists that links the ground to the ionosphere, powerful enough to give rise to the reported perturbations, it must extend over large areas and it will most likely involve changes in thermospheric chemistry or in the electrodynamic drifts in the lower atmosphere.

Radon emission from the ground has been widely quoted as a possible cause for changes in the conductivity of the air linked to pre-earthquake ionospheric anomalies (Ondoh, 2003; Pulinets, 2007, 2009; Yasuoka et al., 2006). The basic concept is that, when stresses build-up across the "earthquake preparation zone", radioactive radon is released from the ground. The "earthquake preparation zone" is assumed to be centered around the future epicenter with a radius r given by the empirical relation $r = 10^{0.43\,M}$ km, where M is the magnitude of the earthquake (Dobrovolsky et al., 1979; Teisseyre, 1997). For magnitude 6, 7 and 8 events, the "earthquake preparation zones" would therefore cover areas as large as 500, 600 and 700 km across.

^{222}Rn with its half-life of 3.82 days is a progeny of radium, ^{226}Ra, which in turn derives from ^{238}U, an element enriched in granitic rocks. ^{222}Rn decays by emitting 5.49 MeV alpha particles to ^{218}Po with a half-life of 3.11 min, which decays by emitting 6.00 MeV alpha particles to short-lived ^{214}Pb and other progeny. In air, each alpha particle of the ^{222}Rn decay generates 150,000 to 200,000 electron–ion pairs. The entire ^{222}Rn decay chain in air therefore produces at most 10^6 ionization events.

While 10^6 ionization events look like a large number, the rate at which radon is released from the ground, even in areas dominated by granitic rocks, is very small. On the average, air ion concentrations due to radon and its progeny range from about 25 cm^{-3} to 250 cm^{-3}. Contributions from cosmic rays and secondary cosmic ray decay products at sea level are equally low, on the order of 2 ions cm^{-3} and 15 ions cm^{-3} respectively (Hoppel et al., 1986).

Measured over a 3-year period near Pune, India, the median radioactivity in air has reported to be 9.70 Bq m^{-3} due to radon itself and 2.84 Bq m^{-3} due to its progeny, producing a median air ion concentration of only 5.5 cm^{-3} s^{-1} (Nagarajaa et al., 2003). Using a network of 20 radon measuring stations along the western part of the North Anatolian Fault, placed into 0.5–1 m deep trenches or holes, the count rates due to radon decay over a period

Please cite this article as: Freund, F.T., et al., Air ionization at rock surfaces and pre-earthquake.... Journal of Atmospheric and Solar-Terrestrial Physics (2009), doi:10.1016/j.jastp.2009.07.013

of 1-year were found to vary from less than 0.3 to about 6 min^{-1} (İnan et al., 2008). At the same time, a total of 19 earthquakes of magnitudes 4–5 occurred in the region, some less than 20 km from a radon measuring station. At some stations $M>4$ earthquakes correlate with a small increase in radon release from the ground but, more generally, the radon release patterns are found to be broad and not directly correlated to any specific seismic event.

In California radon transects were taken across creeping, locked, and freshly ruptured sections of the San Andreas Fault (King et al., 1993). Along the actively creeping section the radon release increased 6–11 times over the typically low background values. Increased radon release was also found over the fault itself, only tens of meters wide, indicating a very localized effect.

It thus appears that, while radon is definitely coming out of the ground, its release rate increases only by a factor of about 10 in seismically active regions, mostly in the immediate neighborhood of active faults. Hence, the contribution of radon to the air conductivity is of minor importance, in particular when averaged over areas as large as those predicted by the "earthquake preparation zone" concept and necessary to cause the reported pre-earthquake ionospheric perturbations.

By contrast, much higher rates of air ionization can be expected to occur when a large number of $h^\bullet$ charge carriers, stress-activated at depth, arrive at the Earth surface. If our laboratory experiments are any indication of the potential magnitude of the effect, air ionization rates on the order of $10^9\,cm^{-2}\,s^{-1}$ and higher appears possible. Even if a large fraction of these ions are lost to recombination events, air ion concentrations orders of magnitudes higher than those achievable by radon decay are to be expected.

High concentrations of airborne ions have indeed been reported. Prior to the October 30, 2007 Alum Rock, California, M5.4 earthquake ultra low frequency (0.01–12 Hz) pulsations were detected with a three axis induction magnetometer located 2 km from the epicenter. The 1–12 s wide pulsations were 10–50 times more intense than 2-year background noise levels, and occurred 10–30 times more frequently in the 2 weeks prior to the event than during the previous 22 months. An air conductivity sensor at the same site saturated for over 16 h during the night and much of the day before the earthquake. Compared to the previous year's average, conductivity patterns at the site the conductivity was determined not to be caused by moisture contamination (Bleier et al., 2008, 2009). An increase in the air ionization was recorded at the same time at another station about 40 km from the epicenter, e.g. within the range of the "earthquake preparation zone".

An extended network of dedicated air conductivity sensors in Japan, the PISCO network, has also produced a large amount of data pointing at episodes of dramatically increased air ionization, tentatively associated with seismic activity within a radius given by the "earthquake preparation zone" (Hattori et al., 2008; Wasa and Wadatsumi, 2003). One such record obtained by a station at Kanagawa near Yokohama on the Tokyo Bay is given in Fig. 11. The 28 day long record shows a series of positive ion maxima, mostly by small ions, occasionally accompanied by negative ion maxima, mostly by large ions. Both positive and negative ions reach concentrations on the order of $>50{,}000\,cm^{-3}$. It is interesting to note that, while there are sometimes maxima of just positive ions, the negative ions seem to form only as a corollary to the positive ions. This is consistent with the sequence of first positive and then negative ion formation identified in our laboratory experiments.

If airborne ion concentrations at ground level increase significantly over such large areas, by many orders of magnitude over the normal background level, the ions can be expected to be transported upward, mostly due to thermal convection currents that will result from the release of the latent heat of condensation of water, when the ions act as condensation nuclei. Thus the electrical conductivity profile across the entire lower and middle atmosphere will be modified. This in turn will affect the electric field distribution between the lower edge of the ionosphere and the ground (Sorokin et al., 2006).

4.4. Thermal infrared anomalies

Night-time infrared (IR) satellite images have shown areas of enhanced IR emission from the epicentral regions prior to major earthquakes (Saraf et al., 2008a, b; Tramutoli et al., 2005; Tronin, 2000). Known as "thermal anomalies", they are also large areas, often 100–500 km across. They also reportedly appear a few days before major seismic events. They often fluctuate rapidly in areal extent and intensity. They reportedly disappear soon after the main shock and major aftershocks.

The rapidity with which the thermal anomalies appear and disappear rules out that they are caused by Joule heat rising from a source below and heating the rocks at the Earth's surface. Several alternative processes have been invoked to account for the apparent temperature increase: rising fluids, due to regional stresses, leading to the emanation of warm gases (Gornyi et al., 1988), diffuse CO_2 release from the ground, causing a local greenhouse effect (Quing et al., 1991; Tronin, 2000), and air ionization due to radon leading to the release of latent heat during condensation of water vapor (Pulinets et al., 2006). However, none of these explanations seem to adequately account for the characteristic features of the "thermal anomalies" as reported from satellite data.

A very different process has been proposed based on the activation of $h^\bullet$ charge carriers and their diffusion to the surface (Freund et al., 2007). As outlined above in Eqs. (2) and (3), the dormant precursor of the $h^\bullet$ charge carriers consists of peroxy links in which two O^- are tightly bonded together. Breaking the peroxy link costs energy, estimated to be on the order of 2.4 eV. This energy is supplied by the mechanical work done in the stressed rock volume and leads to the activation of $h^\bullet$. When the $h^\bullet$ arrives at the surface, they can recombine to restitute peroxy bonds. When this happens, energy on the order of 2.4 eV will be imparted to the two O^- participating in the recombination process. The two O^- will thus be "born" in a vibrationally highly excited state, equivalent to ~30,000 K. The best way for the two O^- to get rid of this large excess vibrational energy is to radiatively de-excite by emitting photons corresponding to the transitions between the quantum levels of the vibrational manifold of the peroxy bond.

The energy for the transition from the 1st excited level to the 0th ground level is known (Ricci et al., 2001). It is equivalent to a narrow emission band at 930 cm^{-1} or 10.7 μm. Accordingly, transitions between higher excited levels, $2\Rightarrow1$, $3\Rightarrow2$, $4\Rightarrow3$, etc., will lead to a series of narrow IR emissions on the long wavelength side of the 10.7 μm band as indeed observed. Because these narrow non-thermal IR bands occur within the spectral window of the broad thermal 300 K emission maximum and current satellite IR sensors cannot spectrally resolve them, they have been lumped together with the thermal emission. Hence the name "thermal anomalies".

Rapid fluctuations, both in areal extent and intensity, are a characteristic feature of pre-earthquake "thermal anomalies" recorded by IR satellites. Similar fluctuations in the IR emission have been noted during the laboratory study (Freund et al., 2007). In both situations the fluctuations may be due to waves of $h^\bullet$ charge carriers arriving at the surface, field-ionizing air molecules and thereby causing fluctuations of the positive surface potential

Please cite this article as: Freund, F.T., et al., Air ionization at rock surfaces and pre-earthquake.... Journal of Atmospheric and Solar-Terrestrial Physics (2009), doi:10.1016/j.jastp.2009.07.013

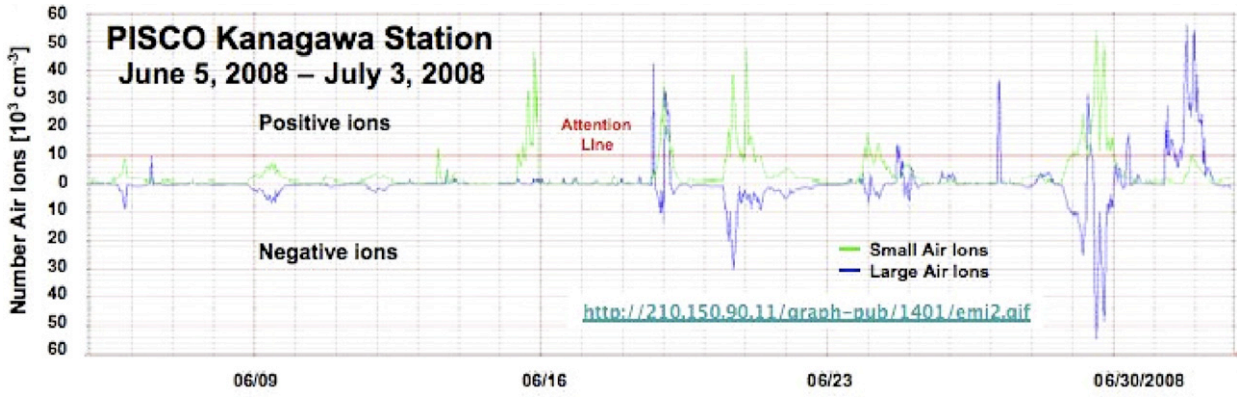

Fig. 11. Air ionization, broken down into positive and negative ions, small and large, as monitored by the PISCO network in Japan. Data from the Kanagawa Station for a 28 day period in June–July 2008.

as shown in Fig. 4. The surface potential fluctuations in turn lead to fluctuations in the number of $h^{\bullet}$ that might be available for recombination and, hence, IR emission.

4.5. Earthquake lights

Fleeting, short-lived luminous phenomena arising from the ground and apparently related to earthquake activity have been reported since ancient times (Derr, 1973; Tributsch, 1984). They are often referred to as earthquake lights, EQLs. Based on reports from several events in Japan (Musya, 1931) stated: "the observations were so abundant and so carefully made that we can no longer feel much doubt as to the reality of the phenomena". Nonetheless, doubts persisted in the scientific community at least until the late 1960s when EQLs were photographically documented during an earthquake swarm near Matsushiro, Japan (Yasui, 1973). EQLs have been reported from Mexico (Araiza-Quijano and Hernández-del-Valle, 1996), Canada (St-Laurent, 2000), and other seismically active regions of the world.

The most common explanations for EQLs invoke piezoelectricity as the physical process that can produce electric fields strong enough to cause a dielectric break-down of air and luminous discharges (Finkelstein et al., 1973; Johnston, 1991; Ouellet, 1990) or frictional heating of the fault during rupture (Lockner et al., 1983). However, on the basis of the experiments presented here a more likely explanation is that electric discharges at the Earth's surface are caused by $h^{\bullet}$ charge carriers arriving at the ground–air interface, building up sufficiently strong electric fields to cause field-ionization of air molecules and corona discharges. Such ionization events are expected to occur over areas as large as $h^{\bullet}$ charge carriers are able to spread after they have been stress-activated at depth. Pervasive corona discharges may cause luminous phenomena and may also be the cause for increased noise in the radiofrequency range that reportedly disrupted the telemetric data transfer from a seismometer network in India prior to an earthquake swarm at a distance of about 150 km (Kolvankar, 2001).

Local outbursts of light from the ground, often called EQLs, may be due to a condition in the Earth's crust that is theoretically predicted to occur when the number density of $h^{\bullet}$ in the rocks increases to a point where the electronic wavefunctions of the $h^{\bullet}$ charge carriers begin to overlap, creating a solid state plasma (St-Laurent et al., 2006). Such plasmas are expected to be inherently unstable, leading to a cloud of $h^{\bullet}$ charge carriers traveling outward at speeds around 200 m s^{-1} (Freund, 2002). When the wave front breaks through the Earth's surface, it will ionize the air and produce flashes of light. Depending on conditions yet to be fully understood, such process could also lead to "flames" coming out of the ground (Demetrescu and Petrescu, 1942; Galli, 1910; Mack, 1912) or to outbursts of light (St-Laurent, 2000).

4.6. Fog, haze and cloud formation

While there is a widespread tendency to associate fog, haze and cloud formations prior to earthquakes with air ionization due to radon emission (Araiza-Quijano and Hernández-del-Valle, 1996; Pulinets and Dunajeck, 2006; Pulinets et al., 2006), air ionization at the rock–air interface due to stress-activated $h^{\bullet}$ charge carriers appears to provide a more effective mechanism for the generation of large numbers of airborne ions.

Since most airborne ions will be positive, at least during the early phase of surface potential build-up, they will be repelled by the surface and rise into the air. Acting as nuclei for the condensation of water, they will cause the release of latent heat, which will lead to thermal updrafts. Ionized and convectionally unstable columns of air may thus form "streamers", which play a role in triggering cloud-to-ground lightning strikes (Aleksandrov et al., 2001).

4.7. Unusual animal behavior

High levels of positive air ions may also have biological consequences. Although effects of positive and negative airborne ions on humans and animals have been studied since the 1960s, the results have not been equivocal due to design faults (Krueger and Reed, 1976), or lack of proper controls (Hedge and Eleftherkis, 1982). However, a majority of these studies have found that high levels of positive ions, ranging from 2×10^3 to 1×10^6 ions cm^{-3}, have detrimental physiological and behavioral effects, including respiratory problems, possibly due to the swelling of the trachea, and increased levels of serotonin (5-hydroxytryptamine, 5-HT) levels in the blood (Krueger and Kotaka, 1969).

High serotonin levels can result in irritation, headaches, nervousness, and increased sensitivity to pain (Sulman et al., 1974). These effects are consistent with reported pre-earthquake changes in animal behavior. Laboratory data show changes in mouse circadian rhythms 24 h before earthquakes (Yokoi et al., 2003). Other causes quoted in literature for changes in animal behavior before earthquakes include low frequency vibrations, ground tilting, humidity changes, and magnetic field variations (Kirschvink, 2000).

Tributsch (Tributsch, 1982) suggested that changes in animal behavior before earthquakes may be caused by charged aerosol particles due to electrochemical glow. Hoenig (Hoenig, 1979) has shown that electrons and positive ions with current levels up to

Please cite this article as: Freund, F.T., et al., Air ionization at rock surfaces and pre-earthquake.... Journal of Atmospheric and Solar-Terrestrial Physics (2009), doi:10.1016/j.jastp.2009.07.013

10 pA are produced as rocks approach failure under laboratory settings. Although, in both cases the phenomena were attributed to piezoelectric effects, it is important to note that piezoelectricity always produces both positive and negative ions. The selective production of positive airborne ions as demonstrated in this paper may amplify the anomalous animal behavior before major earthquakes.

Acknowledgments

Supported by NASA grants "Earth Surface and Interior" #NNX08AG81G and "Exobiology" #NNX07AU04G, by the 2007 NASA Ames Academy, and a 2008 NSF–REU grant to the Department of Physics, SJSU. We thank the staff of the NASA Ames EEL (Engineering Evaluation Laboratory) Jerry Wang, Lynn Hofland, and Frank Pichay.

References

Aleksandrov, N.L., Bazelyan, E.M., Carpenter, R.B., Drabkin, M.M., Raizer, Yu P., 2001. The effect of coronae on leader initiation and development under thunderstorm conditions and in long air gaps. J. Phys. D: Appl. Phys. 34, 3256–3266.

Araiza-Quijano, M.R., Hernández-del-Valle, G., 1996. Some observations of atmospheric luminosity as a possible earthquake precursor. Geofis. Int. 35, 403–408.

Bleier, T., Dunson, C., Maniscalco, M., Bryant, N., Bambery, R., 2008. ULF Pulsations, Air Conductivity Changes, and Infrared (IR) Radiation Signatures Observed Prior to the 2008 Alum Rock (California) M5.4 Earthquake, AGU Fall Meeting. Abstract S53B-1826.

Bleier, T., Dunson, C., Maniscalco, M., Bryant, N., Bambery, R., Freund, F.T.. Investigation of ULF magnetic pulsations, air conductivity changes, and infrared signatures associated with the October 30, Alum Rock M5.4 earthquake. Nat. Hazards Earth Syst. Sci. in review.

Brown, L.W., 1985. Two experiments to measure the electric field at the Earth's surface and the variation of potential difference with height. Phys. Educ. 20, 287–291.

Demetrescu, G., Petrescu, G., 1942. Sur les phénomènes lumineux qui ont accompagné le tremblement de terre de Roumanie du 10 Novembre 1940. Bull. Sect. Sci. 23, 292–296.

Derr, J.S., 1973. Earthquake lights: a review of observations and present theories. Bull. Seismol. Soc. Am. 63, 2177–21287.

Dobrovolsky, I.P., Zubkov, S.I., Miachkin, V.I., 1979. Estimation of the size of earthquake preparation zones. Pure Appl. Geophys. 117, 1025–1044.

Enomoto, Y., Akai, M., Hashimoto, H., Mori, S., Asabe, Y., 1993. Exoelectron emission: possible relation to seismic geo-electromagnetic activities as a microscopic aspect in geotribology. Wear 168, 135–142.

Finkelstein, D., Hill, U.S., Powell, J.R., 1973. The piezoelectric theory of earthquake lightning. J. Geophys. Res. 78, 992–993.

Freund, F., 1985. Conversion of dissolved "water" into molecular hydrogen and peroxy linkages. J. Non-Cryst. Solids 71, 195–202.

Freund, F., 2002. Charge generation and propagation in rocks. J. Geodyn. 33 (4–5), 545–572.

Freund, F.T., Takeuchi, A., Lau, B.W., 2006. Electric currents streaming out of stressed igneous rocks—A step towards understanding pre-earthquake low frequency EM emissions. Phys. Chem. Earth 31 (4–9), 389–396.

Freund, F.T., Takeuchi, A., Lau, B.W.S., Al-Manaseer, A., Fu, C.C., Bryant, N.A., Ouzounov, D., 2007. Stimulated thermal IR emission from rocks: assessing a stress indicator. eEarth 2, 1–10.

Galli, I., 1910. Raccolta e classifzione di fenomeni luminosi osservati nei terremoti. Bolletino Soc. Sismol. Ital. 14, 221–448.

Geller, R.J., 1997. Earthquake prediction: a critical review. Geophys. J. Int. 131, 425–450.

Gornyi, V.I., Salman, A.G., Tronin, A.A., Shilin, B.B., 1988. The Earth's outgoing IR radiation as an indicator of seismic activity. Proc. Acad. Sci. USSR 301 (1), 67–69.

Guo, G., Wang, B., 2008. Cloud anomaly before Iran earthquake. Int. J. Remote Sensing 29 (7), 1921–1928.

Hattori, K., Wadatsumi, K., Furuya, R., Yada, N., Yamamoto, I., Ninagawa, K., Ideta, Y., Nishihashi, M., 2008. Variation of radioactive atmospheric ion concentration associated with large earthquakes, AGU Fall Meeting. Abstract S52A-03.

Hayakawa, M., Sazhin, S.S., 1992. Mid-latitude and plasmaspheric hiss: a review. Planet. Space Sci. 40, 1325–1338.

Hayakawa, M., Shvets, A.V., Maekawa, S., 2005. Subionospheric LF monitoring of ionospheric perturbations prior to the Tokachi-oki earthquake and a possible mechanism of lithosphere–ionosphere coupling. Adv. Polar Upper Atmos. Res. 18, 42–54.

Hedge, A., Eleftherkis, E., 1982. Air ionization: an evaluation of its physiological and psychological effects. Ann. Occup. Hyg. 25 (4), 409–419.

Hoenig, S.A., 1979. Aerosol anomalies preceding earthquakes. Nature 279 (5709), 169.

Hoppel, W.A., Anderson, R.V., Willet, J.C., 1986. Atmospheric Electricity in the Planetary Boundary Layer, The Earth's Electrical Environment. National Academic Press, p. 149–165.

İnan, S., Akgül, T., Seyis, C., Saatçılar, R., Baykut, S., Ergintav, S., Baş, M., 2008. Geochemical monitoring in the Marmara region (NW Turkey): a search for precursors of seismic activity. J. Geophys. Res. 113, B03401 03410.01029/02007JB005206.

Johnston, A.C., 1991. Light from seismic waves. Nature 354, 361.

Kagan, Y.Y., 1997. Are earthquakes predictable?. Geophys. J. Int. 131 (3), 505–525.

Keilis-Borok, V., 2003. Fundamentals of earthquake prediction: four paradigms. In: Keilis-Borok, V., Soloviev, A.A. (Eds.), Nonlinear Dynamics of the Lithosphere and Earthquake Prediction. Springer, pp. 1–36.

King, B.V., Freund, F., 1984. Surface charges and subsurface space charge distribution in magnesium oxide containing dissolved traces of water. Phys. Rev. B 29, 5814–5824.

King, C.-Y., Zhang, W., King, B.-S., 1993. Radon anomalies on three kinds of faults in California. Pure Appl. Geophys. 141, 111–124.

Kirschvink, J.L., 2000. Earthquake prediction by animals: evolution and sensory perception. Bull. Seismol. Soc. Am. 90 (2), 312–323.

Kolvankar, V.G., 2001. Report BARC-2001/E/006: Earthquake sequence of 1991 from Valsad region, Gujarat. Bhabha Atomic Research Centre, Seismology Div., Mumbai, India.

Krueger, A., Kotaka, S., 1969. The effects of air ions on brain levels of serotonin in mice. Int. J. Biometeorol. 13 (1), 25–38.

Krueger, A.P., Reed, E.J., 1976. Biological impact of small air ions. Science 193 (4259), 1209–1213.

Liperovsky, V.A., Pokhotelov, O.A., Liperovskaya, E.V., Parrot, M., Meister, C.-V., Alimov, O.A., 2000. Modification of sporadic E-layers caused by seismic activity. Surv. Geophys. 21 (5–6), 449–486.

Liu, J.Y., Chen, Y.I., Chuo, Y.J., Chen, C.S., 2006. A statistical investigation of preearthquake ionospheric anomaly. J. Geophys. Res. 111, A05304 05310.01029/02005ja011333.

Liu, J.Y., Chen, Y.I., Pulinets, S.A., Tsai, Y.B., Chuo, Y.J., 2000. Seismo-ionospheric signatures prior to $M \geq 6.0$ Taiwan earthquakes. Geophys. Res. Lett. 27 (19), 3113–3116.

Lockner, D.A., Johnston, M.J.S., Byerlee, J.D., 1983. A mechanism for the generation of earthquake lights. Nature 302, 28–33.

Mack, K., 1912. Das süddeutsche Erdbeben vom 16. November 1911, Abschnitt VII: Lichterscheinungen, Würtembergische Jahrbücher für Statistik and Landeskunde. p. 131.

Maekawa, S., Horie, T., Yamauchi, T., Sawaya, T., Ishikawa, M., Hayakawa, M., Sasaki, H., 2006. A statistical study on the effect of earthquakes on the ionosphere, based on the subionospheric LF propagation data in Japan. Ann. Geophys. 24, 2219–2225.

Musya, K., 1931. On the luminous phenomena that attended the Idu earthquake, November 6th, 1930. Bull. Earthquake Res. Inst. 9, 214–215.

Nagarajaa, K., Prasad, B.S.N., Madhavaa, M.S., Chandrashekaraa, M.S., Paramesha, L., Sannappaa, J., Pawarb, S.D., Murugavelb, P., Kamra, A.K., 2003. Radon and its short-lived progeny: variations near the ground. Radiat. Meas. 36 (1–6), 413–417.

Ondoh, T., 2003. Anomalous sporadic-E layers observed before M 7.2 Hyogo-ken Nanbu earthquake; Terrestrial gas emanation model. Adv. Polar Upper Atmos. Res. 17, 96–108.

Ouellet, M., 1990. Earthquake light and seismicity. Nature 348, 492.

Ovshinsky, S.R., Adler, D., 1976. Local structure, bonding, and electronic properties of covalent amorphous semiconductors. Contemp. Phys. 19 (2), 109–126.

Pulinets, S., 2007. Natural radioactivity, earthquakes, and the ionosphere. EOS 88 (20)10.1029/2007EO200001.

Pulinets, S.. Physical mechanism of the vertical electric field generation over active tectonic faults Adv. Space Res. in press.

Pulinets, S., Boyarchuk, K., 2004. Ionospheric Precursors of Earthquakes. Springer.

Pulinets, S.A., Dunajeck, M.A., 2006. Specific variations of air temperature and relative humidity around the time of Michoacan earthquake M8.1 September 19, 1985 as a possible indicator of interaction between tectonic plates. Tectonophysics 431 (1–4), 221–230.

Pulinets, S.A., Leyva Contreras, A., Bisiacchi-Giraldi, G., Ciraolo, L., 2005. Total electron content variations in the ionosphere before the Colima, Mexico, earthquake of 21 January 2003. Geofis. Int. 44 (4), 369–377.

Pulinets, S.A., Ouzounov, D., Karelin, A.V., Boyarchuk, K.A., Pokhmelnykh, L.A., 2006. The physical nature of thermal anomalies observed before strong earthquakes. Phys. Chem. Earth 31 (4–9), 143–153.

Quing, Z., Xiu-Deng, X., Chang-Gong, D., 1991. Thermal infrared anomaly—precursor of impending earthquakes. Chin. Sci. Bull. 36 (4), 319–323.

Ricci, D., Pacchioni, G., Szymanski, M.A., Shluger, A.L., Stoneham, A.M., 2001. Modeling disorder in amorphous silica with embedded clusters: the peroxy bridge defect center. Phys. Rev. B 64 (22) 224104-224101–224104-224108.

Rishbeth, H., 2007. Do earthquake precursors really exist?. EOS 88 (29)10.1029/2007EO290008.

Roble, R.G., Tzur, I., 1986. The Global Atmospheric–Electrical Circuit, The Earth's Electrical Environment. National Academic Press, p. 206–231.

Saraf, A.K., Rawa, V., Banerjee, P., Choudhury, S., Panda, S.K., Dasgupta, S., Das, J.D., 2008a. Satellite detection of earthquake thermal precursors in Iran. Natural Hazards, doi:10.1007/s11069-11007-19201-11067.

Saraf, A.K., Rawat, V., Banerjee, P., Choudhury, S., Panda, S.K., Dasgupta, S., Das, J.D., 2008b. Satellite detection of earthquake thermal infrared precursors in Iran. Nat. Hazards 47, 119–135.

Shalimov, S., Gokhberg, M., 1998. Lithosphere–ionosphere coupling mechanism and its application to the earthquake in Iran on June 20, 1990. A review of ionospheric measurements and basic assumptions. Phys. Earth Planet. Inter. 105 (3–4), 211–218.

Singh, C., Singh, O.P., 2007. Simultaneous ionospheric E- and F-layer perturbations caused by some major earthquakes in India. Ann. Geophys. 50 (1), 111–122.

Sorokin, V.M., Yaschenko, A.K., Hayakawa, M., 2006. Formation mechanism of the lower-ionospheric disturbances by the atmosphere electric current over a seismic region. J. Atmos. Solar Terr. Phys. 68 (11), 1260–1268.

St-Laurent, F., 2000. The Saguenay, Québec, earthquake lights of November 1988–January 1989. Seismol. Res. Lett. 71 (2), 160–174.

St-Laurent, F., Derr, J., Freund, F., 2006. Earthquake lights and the stress-activation of positive hole charge carriers in rocks. Phys. Chem. Earth 31 (4–9), 305–312.

Sulman, F.G., Levy, D., Levy, A., Pfeifer, Y., Superstine, E., Tal, E., 1974. Air-ionometry of hot, dry dessert winds(Sharav) and treatment with air ions of weather-sensitive subjects. Int. J. Biometeorol. 18 (4), 313–318.

Takeuchi, A., Lau, B.W., Freund, F.T., 2006. Current and surface potential induced by stress-activated positive holes in igneous rocks. Phys. Chem. Earth 31 (4–9), 240–247.

Takeuchi, A., Nagahama, H., 2002. Surface charging mechanism and scaling law related to earthquakes. J. Atmos. Electr. 22 (3), 183–190.

Teisseyre, R., 1997. Generation of electric field in an earthquake preparation zone. Ann. Geophys. 15, 297–304.

Tramutoli, V., Cuomob, V., Filizzolab, C., Pergolab, N., Pietrapertosa, C., 2005. Assessing the potential of thermal infrared satellite surveys for monitoring seismically active areas: the case of Kocaeli (Izmit) earthquake, August 17, 1999. Remote Sensing Environ. 96, 409–426.

Tributsch, H., 1982. When the Snakes Awake. The MIT Press.

Tributsch, H., 1984. When the Snakes Awake: Animals and Earthquake Prediction. MIT Press.

Trigunait, A., Parrot, M., Pulinets, S., Li, F., 2004. Variations of the ionospheric electron density during the Bhuj seismic event. Ann. Geophys. 22 (12), 4123–4131.

Tronin, A.A., 2000. Thermal IR satellite sensor data application for earthquake research in China. Int. J. Remote Sensing 21 (16), 3169–3177.

Tronin, A.A., 2006. Remote sensing and earthquakes: a review. Phys. Chem. Earth 31 (4–9), 138–142.

Wasa, Y., Wadatsumi, K., 2003. Functional strengthening and employment of macroscopic anomaly system by e-PISCO ASP. J. Jpn Soc. Inf. Knowl. 13 (2), 41–47.

Yasui, Y., 1973. A summary of studies on luminous phenomena accompanied with earthquakes. Mem. Kakioka Magn. Obs. 15 (2), 127–138.

Yasuoka, Y., Igarashi, G., Ishkawa, T., Tokonmai, S., Shinogi, M., 2006. Evidence of precursor phenomena in the Kobe earthquake obtained from atmospheric radon concentration. Appl. Geochem. 21, 61064–61072.

Yokoi, S., Ikeya, M., Yagi, T., Nagai, K., 2003. Mouse circadian rhythm before the Kobe earthquake in 1995. Bioelectromagnetics 24 (4), 289–291.

Zakharenkova, I.E., Shagimuratov, I.I., Krnakowski, A., 2007. Features of the ionosphere behavior before the Kythira 2006 earthquake. Acta Geophys. 55 (4), 524–534.

Please cite this article as: Freund, F.T., et al., Air ionization at rock surfaces and pre-earthquake.... Journal of Atmospheric and Solar-Terrestrial Physics (2009), doi:10.1016/j.jastp.2009.07.013

Earth and Planetary Science Letters 283 (2009) 87–92

Contents lists available at ScienceDirect

Earth and Planetary Science Letters

journal homepage: www.elsevier.com/locate/epsl

Oxidation of water to hydrogen peroxide at the rock–water interface due to stress-activated electric currents in rocks

Melike Balk [a,1], Milton Bose [b,2], Gözen Ertem [c,3], Dana A. Rogoff [d], Lynn J. Rothschild [a], Friedemann T. Freund [a,b,d,*]

[a] NASA Ames Research Center, Code SGE, Moffett Field, CA 94035, USA
[b] Department of Physics, San Jose State University, San Jose, CA 95192-0106, USA
[c] NASA Ames Research Center, Code SSX, Moffett Field, CA 94035, USA
[d] Carl Sagan Center, SETI Institute, 515 N Whisman Rd., Mountain View, CA 94043, USA

ARTICLE INFO

Article history:
Received 11 September 2008
Received in revised form 21 March 2009
Accepted 31 March 2009
Available online 6 May 2009

Editor: R.W. Carlson

Keywords:
hydrogen peroxide
rock–water interface
electric currents
rock battery
oxidation
early Earth
early life

ABSTRACT

Common igneous and high-grade metamorphic rocks contain dormant defects, which release electronic charge carriers when stressed. Rocks thereby behave like a battery. The charge carriers of interest are defect electrons $h^{\bullet}$, e.g. electronic states associated with O^- in a matrix of O^{2-}. Known as "positive holes" or pholes for short, the $h^{\bullet}$ travel along stress gradients over distances on the order of meters in the laboratory and kilometers in the field. At rock–water interfaces the $h^{\bullet}$ turn into •O radicals, e.g. highly reactive oxygen species, which oxidize H_2O to H_2O_2. For every two $h^{\bullet}$ charge carriers one H_2O_2 molecule is formed. In the laboratory the battery circuit is closed by running a Cu wire from the stressed to the unstressed rock. In the field closure of the circuit may be provided through the electrolytical conductivity of water. The discovery of $h^{\bullet}$ charge carriers, their stress-activation, and their effect on Earth's surface environment may help better understand the oxidation of the early Earth and the evolution of early life.

1. Introduction

Though most oxygen anions in oxide/silicate minerals occur in their common 2− valence state, some can exist in the more oxidized valence 1−, as O^-. In this paper we present evidence that oxygen anions in the valence state 1− in minerals, which make up the bulk of igneous and high-grade metamorphic rocks, give rise to some unexpected phenomena. The O^- are normally dormant, forming inconspicuous and electrically inactive point defects. However, they can be "awakened" when rocks are subjected to mechanical stress. Once activated, the electronic state associated with O^- can produce an electric current, which was previously unknown.

First we discuss how O^- are introduced into the mineral matrix, why they exist in a dormant form, and how they are become activated when mechanical stresses are applied. Second, we demonstrate that stress-activated electronic charge carriers can flow out of the stressed rock volume and propagate through unstressed rock. When they cross a rock–water interface, they oxidize H_2O to H_2O_2.

1.1. Dormant electronic charge carriers

It has been shown some time ago that hydroxyl pairs in MgO, introduced into the MgO matrix during crystallization from an H_2O-laden melt or recrystallization in an H_2O-laden environment, undergo a previously unknown redox reaction: they split off H_2 and form peroxy anions, O_2^{2-} (Martens et al., 1976; Freund and Wengeler, 1982):

$$OH^- \oplus^- HO \Leftrightarrow H_2 + \oplus O_2^{2-} \quad (1)$$

where ⊕ stands for an Mg^{2+} vacancy site. In the peroxy anion, O_2^{2-}, the two O^- are tightly bonded together, forming a self-trapped, localized, electrically inactive point defect.

Evidence suggests that the same type of redox reaction also occurs in fused silica, where O_3SiOH pairs are converted into H_2 plus peroxy links $O_3Si-OO-SiO_3$ (Freund and Masuda, 1991; Ricci et al., 2001).

* Corresponding author. Carl Sagan Center, SETI Institute, 515 N Whisman Rd., Mountain View, CA 94043, USA. Tel.: +1 650 810 0218; fax: +1 650 961 7099.
E-mail addresses: M.Balk@nioo.knaw.nl (M. Balk), milton.bose@gmail.com (M. Bose), gozen1ertem@gmail.com (G. Ertem), drogoff@mail.arc.nasa.gov (D.A. Rogoff), Lynn.J.Rothschild@nasa.gov (L.J. Rothschild), friedemann.T.freund@nasa.gov (F.T. Freund).
[1] Present address: NIOO-KNAW Centre for Limnology, Rijksstraatweg 6, 3631 AC Nieuwersluis, The Netherlands.
[2] Present address: Department of Physics and Astronomy, University of California, Riverside, CA 92521, USA.
[3] Present address: Karlsruhe Forschungszentrum, Weberstr. 5 D-76133 Karlsruhe, Germany.

0012-821X/$ – see front matter © 2009 Elsevier B.V. All rights reserved.
doi:10.1016/j.epsl.2009.03.044

Likewise nominally anhydrous silicate minerals (Freund, 1987, 2003) are known to always dissolve small amounts of H_2O when crystallizing in H_2O-laden magmas or H_2O-laden high temperature environments (Wilkins and Sabine, 1973; Rossman, 1996; Koga et al., 2003). The solute H_2O occurs in the form of $O_3(X,Y)OH$, where X, $Y = Si^{4+}$, Al^{3+} etc. Hydroxyl pairs are probably the most abundant, but they seem to undergo the same redox conversion, splitting off H_2 and forming peroxy links (Freund, 2003):

$$O_3X-OH\ HO-YO_3 \Leftrightarrow O_3X/^{OO}\backslash YO_3 + H_2 \quad (2)$$

Because crustal rocks consist mostly of nominally anhydrous minerals, which invariably contain small amounts of dissolved H_2O, peroxy links may be very ubiquitous.

From a semiconductor viewpoint, an O^- in a matrix of O^{2-} represents a defect electron or hole, also known as positive hole (Griscom, 1990) or phole for short, symbolized by $h^\bullet$. Accordingly, a peroxy link represents a positive hole pair, PHP (Freund et al., 2006), in which two O^- are self-trapped, immobilized and, hence, electrically inactive. PHPs break apart when rocks are subjected to deviatoric stresses, e.g. to stresses that exceed the elastic limit causing dislocations to be mobilized and new dislocations to be generated (Freund et al., 2006; Takeuchi et al., 2006). As dislocations move through the mineral grains, they intersect a PHP causing the peroxy bond to break:

$$\text{peroxy link} + O^{2-} \Leftrightarrow \text{loosely bound } e' + O^- = h^\bullet \quad (3)$$

$$O_3X/^{OO}\backslash YO_3 + [XO_4]^{n-} \Leftrightarrow O_3X/^{O}\bullet_O/YO_3 + [XO_4]^{(n-1)-}$$

Eq. (3) describes a process, by which an electron e' is transferred from a neighboring O^{2-} anion (here represented by $[XO_4]^{n-}$) onto the broken peroxy bond, which captures the electron e'. The donor O^{2-} turns into O^- (here $[XO_4]^{(n-1)-}$), e.g. a defect electron or phole $h^\bullet$. In other words, Eq. (3) describes the generation of an electron–hole pair.

In semiconductors like silicon electron–hole pairs recombine very rapidly, often within nanoseconds (Sze, 1981; Van Zeghbroeck, 1997). In the case of the e'–$h^\bullet$ pairs generated by the break-up of peroxy links in silicate matrices, the broken peroxy bond that has captured electron appears to relax in such a way as to delay recombination. Thus, e'–$h^\bullet$ pairs formed in silicates and, hence, in rocks are long-lived (Freund et al., 2006; Freund and Sornette, 2007).

1.2. Electric currents flowing through rocks

The $h^\bullet$ charge carriers in the silicates are associated with O 2sp energy levels at the upper edge of their valence bands (Canney et al., 1999). When mineral grains are in physical contact, the valence bands are electrically connected. Though their energies will shift from grain to grain, all valence bands form an energy continuum along which $h^\bullet$ charge carriers can propagate. The mode of propagation probably involves a phonon-assisted electron transfer, whereby $h^\bullet$ hop from O^{2-} to O^{2-}, maximally at the frequency of thermally activated lattice phonons, ~10^{12} Hz (Shluger et al., 1992). The O^- turn insulating silicate minerals into p-type semiconductors. From a chemistry perspective, an O^- is a highly oxidizing •O radical.

Hurovitz et al. described experiments, where freshly ground basaltic minerals immersed in aqueous solution produced detectable amounts of H_2O_2 (Hurowitz et al., 2007). The H_2O_2 production is thought to occur when water reacts with unspecified defects formed at the mineral surfaces during crushing. Possibly $h^\bullet$ charge carriers, activated by the high mechanical stresses levels during crushing, contribute to the oxidizing properties of freshly crushed rock surfaces.

In the experiments as described here, where only a subvolume of a large piece of rock is subjected to increased levels of mechanical stress, $h^\bullet$ charge carriers flow from the stressed into the unstressed rock volume. The stressed rock volume acts as the anode in a battery from where an electric current flows out (Freund et al., 2006). The unstressed rock acts as the electrolyte, through which the $h^\bullet$ flow to reach the Cu contact at the unstressed end of the rock as depicted in Fig. 1a. This Cu contact acts as the cathode.

The electrons e', co-activated according to Eq. (3), cannot spread from the stressed rock into the unstressed rock. However, they can pass from the stressed rock into a metal contact, in our case the steel pistons, and then proceed through a Cu wire to reach the same Cu contact attached to the far end of the unstressed rock. The Cu wire thereby closes the battery circuit. At the interface between the Cu contact and the unstressed rock the e' "shake hands" with $h^\bullet$ and recombine. Knowing that $h^\bullet = O^-$, we can write:

$$O^- + e^- \Longrightarrow O^{2-} \quad (4)$$

In the course of this study we addressed three questions:

(i) Can the $h^\bullet$ charge carriers flow not only through solid rock as depicted in Fig. 1a but also through water as depicted in Fig. 1b?
(ii) What happens at the rock–water interface?
(iii) How can the rock battery circuit be closed, if no wire is available to connect the stressed rock volume with the unstressed rock volume?

2. Experimental

We used a gabbro from Shanxi, China, ~40 modal% plagioclase, 30% augitic clinopyroxene with alteration rims to amphibole and chlorite, plus 25% opaques, a porosity of about 0.3%, and less than 1% total water mostly due to hydroxyl-bearing minerals such as amphiboles (Parkhomenko, 1967).

Fig. 2 depicts a block of this gabbro, $60 \times 7.5 \times 7.5$ cm^3, loaded at the center through two rectangular steel pistons with a contact area of 5×10 cm^2 covered by Cu tape with graphite-based conductive adhesive (3M). Two water pools 1 and 2 in Plexiglas frames, $5 \times 5 \times 0.6$ cm^3, symmetrically placed close to the unstressed ends of

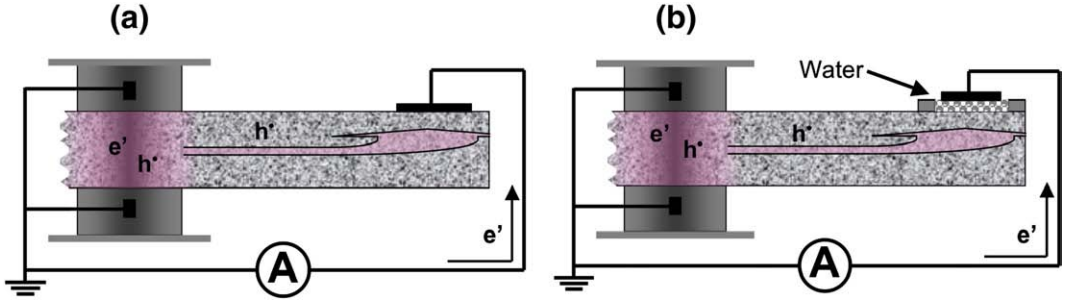

Fig. 1. a: Electric circuit to demonstrate the flow of stress-activated $h^\bullet$ charge carriers through a slab of rock, forming the "rock battery"; b: circuit to demonstrate that the electric current, transported through the rock by $h^\bullet$ charge carriers, also flows through water.

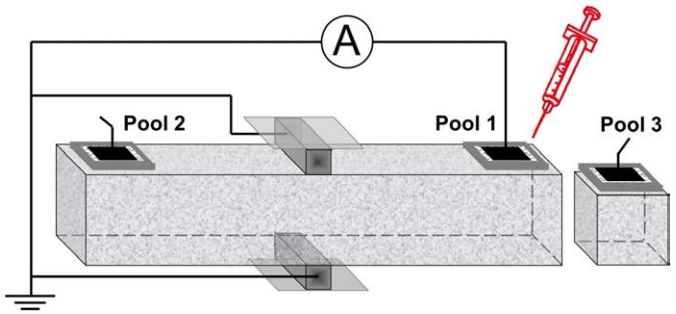

Fig. 2. Experimental set-up to test the flow of current carried by stress-activated h• through water. Gabbro slab, $7.5\times7.5\times60$ cm^3, loaded at the center by two steel pistons, electrically insulated from the press with sheets of polyethylene, resistance $>10^{14}$ Ω. Two water pools 5×5 cm^2, cut out of Plexiglas, each with a 4×4 cm^2 Cu electrode touching the water surface, Pool 1 and Pool 2, were set on the gabbro slab, ~20 cm on either side of the pistons. An identical control Pool 3, also with a 4×4 cm^2 Cu electrode, was set on a separate piece of the same gabbro not to be stressed. All water pools were filled 6 mm deep with distilled water. Pool 1 was connected to the battery circuit, while Cu electrodes in Pools 2 and 3 were left unconnected.

the rock, as well as an identical Pool 3 on a separate block of gabbro, were filled with distilled water to a depth of 6 mm. All pools had Cu electrodes, 4×4 cm^2, touching the water surface.

The rock was loaded using a manually operated hydraulic press. Immediately upon loading a battery current started to flow through the unstressed portion of the rock and through Pool 1. The current increased rapidly reaching a maximum of ~10 nA at less than 20 MPa, corresponding to <10% of the compressive strength of this rock. A current of ~10 nA flowing through our rock sample translates into a current density on the order of 5 μA m^2. The current passed through a maximum and then stabilized at a slightly lower level, around 7 nA, while the load was held constant at 30 ± 5 MPa. After 24 h the current had decayed to ~4.5 nA. The current flowing through the water of Pool 1 is of the same magnitude as currents flowing through Cu contacts of the same size attached directly to the dry rock surface (Freund et al., 2006). Pools 2 and 3 acted as references and were not connected to the battery circuit. None of the water pools were stirred.

H_2O_2 concentrations in Pools 1, 2 and 3 were measured in 50 μL aliquots, taken with a plastic syringe, using the Amplex Ultra Red Hydrogen Peroxide Assay Kit from Molecular Probes Inc. (Catalog # A22188 and A36006). In the presence of horseradish peroxidase, the Amplex Red reagent (N-acetyl-3,7-dihydroxyphenoxazine) reacts with H_2O_2 and probably other oxidizing species such as short-lived hydroxyl (•OH) and/or hydroperoxyl ($•HO_2$) radicals to produce a red-fluorescent oxidation product, resorufin. The intensity of the fluorescence was measured with a SpectraMax Gemini XS Scanning Fluorometer using the SoftMax Pro v. 5.0.1 program from Molecular Devices Corporation) and expressed at H_2O_2. To eliminate background H_2O_2 in the deionized water to be used in the fluorometric analysis we treated the water overnight at room temperature with 1 mg/L catalase (1000 U, Aldrich-Sigma Chemical Inc.), then autoclaved it at 121 °C to de-activate the enzyme. The catalase-treated water was used for H_2O_2 standards and all analyses. Each fluorometric analysis was repeated four times.

Using Pool 3, we separately determined the rate at which H_2O_2 decays as a function of time (t) in contact with the rock surface: we started with a 2 μmol H_2O_2 solution and measured the change in H_2O_2 concentration over 22 h. Each H_2O_2 analysis was repeated twice. We found the expected exponential H_2O_2 decay $F(t)$ with a time constant 0.179:

$$F(t) = 2.46e^{-0.179t}. \tag{5}$$

3. Results

Fig. 3 plots the battery current I flowing into and through Pool 1 integrated over time. After 24 h, the total charge C passing through the rock–water interface was 0.5 mC, $\approx2\times10^{15}$ h• charge carriers. C as a function of time (t) is given by:

$$C(t) = \int_{t=0}^{t} I(t)dt. \tag{6}$$

When the h• current flows into the water, interface reactions have to be considered. Being chemically equivalent to O^-, the h• charge carriers are expected to act as •O radicals at the rock–water interface. One possible reaction for the •O radicals in the rock surface is to subtract H from the H_2O in the pool and to form •OH radicals:

$$O^-_{surface} + H_2O \Longrightarrow OH^-_{surface} + •OH \tag{7}$$

By binding the OH^- into the surface, excess H_3O^+ will be left in the water to carry the current to the Cu electrode and discharge at the water–Cu interface:

$$H_3O^+ + e^- \Longrightarrow H_2O + 1/2\ H_2 \tag{8}$$

Two •OH radicals from Eq. (7) are expected to combine to hydrogen peroxide:

$$•OH + •OH \Longrightarrow H_2O_2 \tag{9}$$

Eqs. (7) and (9) predict that two h• charge carriers are needed to form one H_2O_2 molecule at the rock–water interface. The total number of H_2O_2 per mole, $G(t)$, is then given by:

$$G(t) = \frac{C(t)}{2eN_A} \tag{10}$$

where e is the electron charge and N_A Avogadro's number.

In the reference Pool 2 the H_2O_2 concentration became barely detectable shortly after loading the rock, then decreased below the detection limit within 1–2 h. In Pool 3 the H_2O_2 remained below the detection limit over the course of the 24 h long experiment.

The symbols in Fig. 4 give the H_2O_2 concentrations as measured in Pool 1. The solid curve represents the expected H_2O_2 concentrations obtained by using as input the H_2O_2 generation function $G(t)$ according to Eq. (10) and the empirical H_2O_2 decay function according to Eq. (5), shown in the insert in Fig. 4. The H_2O_2 decay gives an exponent of −0.179. The reported H_2O_2 concentrations are corrected for the removal of the 50 μL samples from the water pools.

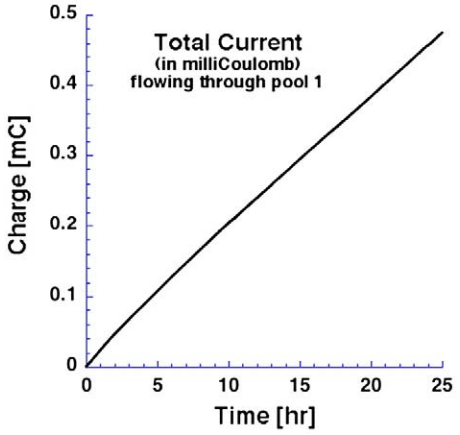

Fig. 3. Total charge flowing out of the stressed rock at constant stress level, 30 MPa, through the unstressed rock and 6 mm of water to a 4×4 cm^2 Cu electrode in Pool 1.

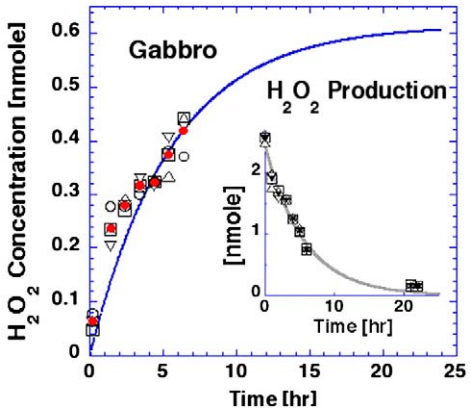

Fig. 4. H_2O_2 concentration in Pool 1 as a function of time. Bold curve: best fit to the experimental data assuming that two h• are needed to form one H_2O_2 molecule according to Eqs. (6) and (8). Solid dots: averaged of 4 measurements. Insert: H_2O_2 decay in contact with the rock surface in Pool 3.

The amount of H_2O_2, $M(t)$, present at any time in Pool 1 is given by the sum of the H_2O_2 generation according to Eq. (10) and the H_2O_2 decay according to Eq. (5):

$$M(t) = \alpha G(t) + F(t) \tag{11}$$

where α is an adjustable constant. Taking into account the 2:1 stoichiometry postulated in Eqs. (7) and (9) we find the numerical expression:

$$M(t) = 0.097te^{-0.177t} \tag{12}$$

which is plotted as the solid curve in Fig. 4.

The H_2O_2 decay exponent obtained through the curve fit, −0.177, agrees well with the exponent −0.179 obtained from the H_2O_2 decay measured separately (see insert in Fig. 4). The agreement between the experimental data and calculated H_2O_2 concentration is satisfactory, confirming the proposed stoichiometry for the formation of H_2O_2, one H_2O_2 molecule formed for every two h• charge carriers crossing the rock–water interface.

4. Discussion

Electric potentials and ground currents are common in nature. Self-potentials can be generated in conductive materials through transfer of charges. Known sources of self-potentials are streaming currents driven by the flow of water through porous rocks, thermo-electric currents associated with temperature gradients, and electro-chemical currents associated with a transfer of electrons during redox reactions or with the diffusion of ions (Cox and Singer, 1986; Bernabé, 1998; Revil and Linde, 2006; Revil, 2007; Crespy et al., 2008). Other mechanisms of generating self-potentials are provided by the piezo-electric effect (Tuck et al., 1977; Bishop, 1981; Lorne et al., 1999; Ogawa and Utada, 2000). In all these cases the currents are weak.

A fundamentally different process to generate electric currents in rocks has recently been described (Freund, 2002; Freund et al., 2006). It is based on the fact that pairs of oxygen anions, which changed their valence from 2− to 1−, ubiquitously occur in minerals that constitute the bulk of igneous and high-grade metamorphic silicate rocks. The O^- pairs, which are believed to form through a redox conversion as described by Eq. (2), represent point defects in the mineral structure, chemically equivalent to peroxy links $O_3Si-OO-SiO_3$ in silica and silicates.

As long as the peroxy links are intact, they are electrically inactive. When stresses are applied beyond the elastic limit and dislocations move through the mineral grains, the $O^- - O^-$ bonds break. In the process, two types of charge carriers are generated as indicated in Eq. (3), electrons e' and holes h•.

The electrons are trapped at the broken peroxy bond sites, while the h• are mobile. As outlined in the Introduction, the h• represent an electronic state associated with O^- in a matrix of O^{2-}. They are known as positive holes (Griscom, 1990) or pholes for short. Chemically they are highly oxidizing. Residing in O 2sp- symmetry energy levels at the upper edge of the valence band, the h• charge carriers can pass from O^{2-} to O^{2-}, presumably by a phonon-assisted electron hopping mechanism (Shluger et al., 1992). This is consistent with the speed with which a pulse carried by h• charge carriers can propagate through unstressed rock, on the order of 200 m/s (Freund, 2002).

While the electrons remain loosely attached to the broken peroxy links, the h• are highly mobile. They can cross grain boundaries using energy levels at the upper edge of the valence band and flow out of the stressed rock volume (Freund et al., 2006). Therefore, the stressed rock volume behaves as anode from where h• charge carriers flow out. In laboratory experiments the h• flow through meters of unstressed rock. In the field they can probably propagate over distances on the order of kilometers. The unstressed rock does not provide energy levels that the co-activated electrons could use to also flow out. They have to take a different path. In our laboratory experiment we provide a path for the electrons by running a Cu wire from the stressed rock to the unstressed rock.

The concentration of peroxy defects in typical rock-forming minerals and, hence, the number of h• charge carriers a given volume of rock, are still poorly known. If the average peroxy concentration in igneous and high-grade metamorphic rocks is 100 ppm (Batllo et al., 1990), every km^3 could produce about 10^{13} C km^{-3}, equivalent to a battery current of about 10^6 A flowing for 6 months.

However, any battery can deliver a current only when the electric circuit is closed. When the effect was first demonstrated (Freund et al., 2006), closure of the electric circuit was provided by the Cu wire as depicted in Fig. 1a.

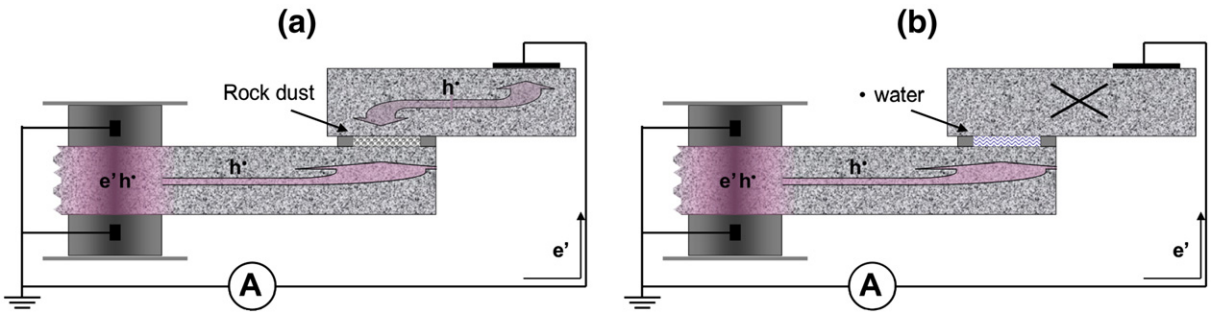

Fig. 5. a: Electric circuit to demonstrate that the "rock battery" works when a layer of rock dust is inserted into the current path between two blocks of rock, indicating that the h• charge carriers can flow through a layer of rock dust. b: When a layer of water is inserted into the current path, the flow of the current is interrupted, suggesting the water does not allow the h• charge carriers to pass through.

In nature the situation is different. Earth's crust is replete with tectonic stresses, which constantly deform rocks and cause dislocations to move (Reimold and Gibson, 2006). Hence, $h^\bullet$ charge carriers can be expected to be activated in many parts of the crust. They will be available to produce battery currents along stress gradients. However, closure of the battery circuit may not be readily achievable under conditions that prevail in the field. Obviously, there are no Cu wires to connect stressed and unstressed rock volumes.

Here we describe an experiment where we inserted a water path into the electric circuit. We find that the water does not stop the current as shown in Fig. 1b. There are two possibilities: either (i) the $h^\bullet$ charge carriers travel through the water without being altered or (ii) the $h^\bullet$ charge carriers convert at the rock–water interface into other forms of charge carriers, which can travel through the water.

To learn more about the two possibilities we conducted the following tests. As depicted in Fig. 5a, we filled the Plexiglas frame with fine gabbro dust and weighed it down with a second piece of gabbro to which we had attached a Cu electrode. As indicated by the arrows, the current continued to flow indicating that the $h^\bullet$ charge carriers are capable of crossing through the dust layer from the first rock into the second rock. This is consistent with the notion that, because every grain–grain contact provides a contact between the valence bands, the $h^\bullet$ charge carriers can pass through. Next, as depicted by Fig. 5b, we filled the Plexiglas frame with water and repeated the test with the same second piece of gabbro. Under these circumstances no battery current was recorded, indicating that the $h^\bullet$ charge carriers were unable to pass through the water, at least not unchanged, and thus unavailable to reenter the second rock.

As Eq. (7) states, when $h^\bullet$ charge carriers arrive at the rock–water interface, they "reveal" their chemical nature as O^-, e.g. as highly oxidizing •O radicals, capable of extracting an H from H_2O. The •O in the rock surface thereby convert into OH^-, while one H_2O is oxidized to •OH. Two •OH combine to H_2O_2 as indicated by Eq. (9) and confirmed by the data in Fig. 4. The current in the water continues to flow as an electrolytic current, carried by H_3O^+, and discharges at the Cu electrode immersed in the water as suggested by Eq. (8).

The result of this experiment is that water can close the battery circuit thanks to its own electrolytical conductivity. This allows us to design a "rock battery" without metal wires, where the outer circuit is provided by an electrolytically conductive water path. Such a situation would be able to close battery circuits in the field.

Fig. 6 shows the set-up. We used a slab of the same gabbro but attached two water reservoirs to its side, one to the portion to be stressed and one to the unstressed part. Both reservoirs were filled with distilled water and connected with a plastic capillary, 0.5 mm inner diameter, filled with dilute NaCl solution (simulated sea water). Instead of using an ammeter to measure the battery current we monitored the formation of H_2O_2 in the water pool attached to the unstressed end of the rock.

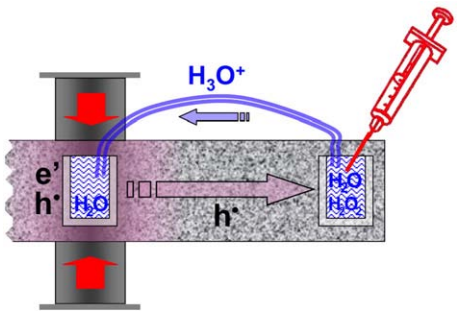

Fig. 6. Demonstration of a rock battery without use of any metal parts where closure of the battery circuit is achieved through the electrolytical conductivity of a capillary filled with NaCl solution.

Upon loading and keeping the load constant at the 30 MPa level, 50 μL aliquots for the H_2O_2 analysis were extracted in 15 min intervals from the water pool attached to the unstressed rock. After about 1 h the H_2O_2 concentration in this water pool began to rise, suggesting that the battery circuit had closed by drawing an electrolytical current through the capillary.

Battery currents flowing in the Earth's crust are probably linked to transient magnetic field changes that happen over time periods of hours, days, months or years. Such magnetic field variations have been reported in connection with the build-up of regional tectonic stresses prior to major earthquakes (Zeng et al., 2002). Battery currents may also be linked to transient changes in the electrical resistivity of the crust (Lu et al., 2004). Though changes in H_2O_2 concentrations in springs in the Yellowstone National Park and other geothermally active regions are thought to indicate UV-driven reactions (Wilson et al., 2000), an electrochemical reaction as described here may also play a role in forming H_2O_2 in natural environments where stresses would activate $h^\bullet$ charge carriers.

The H_2O_2 production observed during immersion of freshly crushed basaltic rock into water (Hurowitz et al., 2007) may also involve $h^\bullet$ charge carriers that were activated by the very high mechanical stresses exerted during crushing. When trapped at the rock surface, these $h^\bullet$ will cause the grain surfaces to become highly oxidizing.

As additional sources of H_2O_2 one has to also consider that, when H_2O_2 is produced according to Eq. (7), causing O^- at the rock surface to change into OH^-, cations can be expected to be released changing the spring water chemistry. If Fe^{2+} is released, it is to be noted that, under aerobic conditions, Fe^{2+} can react with dissolved O_2 to form superoxide radicals (Wilson et al., 2000):

$$Fe^{2+} + O_2 + H_2O \Rightarrow Fe^{3+} + {}^\bullet OOH + OH^- \quad (13)$$

Superoxide radicals in turn react with H_2O to H_2O_2 plus •OH (Espinosa-Garcia, 1993):

$${}^\bullet OOH + H_2O \Rightarrow H_2O_2 + {}^\bullet OH \quad (14)$$

Further work will be needed to determine whether or not the reactions described by Eqs. (13/14) take place to a significant extent when battery currents flow across rock–water interfaces.

Though it is still much too early to estimate the magnitudes of battery currents in the Earth's crust, some projection of the potential impact of oxidation processes at rock–water interfaces may be in order. Since Earth is tectonically active, rocks are constantly subjected to stresses and stress gradients (Reimold and Gibson, 2006). Such tectonic stresses surely acted on the crust throughout Earth's history (van Hunen and van den Berg, 2006). Therefore, it is to be expected that stress-activated phole currents have been part of Earth's history for a very long time. In the case described here we reach a current density on the order of only 5 μA per square meter cross section. In other experiments, with higher stresses, the current densities reach values on the order of 0.1–1 mA m^{-2} (Freund et al., 2006). Whenever and wherever such currents have been crossing rock–water interfaces, the positive hole charge carriers much have oxidized H_2O to H_2O_2. This continuous production of H_2O_2 on the tectonically active Earth may have contributed to the global oxidation. In particular, it may have played a significant, maybe dominant role, in the slow but seemingly unstoppable oxidation over the first 2–3 Gyrs of Earth's history (Goldblatt et al., 2006).

The production of H_2O_2 at the rock–water interface has also implications for early life and how life adapted to the presence of highly oxidizing "reactive oxygen species" (ROS). These ROS certainly became a major challenge to Life when free O_2 appeared in Earth's atmosphere 2.4 to 2.7 billion yrs ago. However, long before, O^- must have led to powerful ROS whenever stress-activated positive hole charge carriers passed through rock–water interfaces. Early microbial communities forming biofilms on rock–water interfaces were surely exposed to these

O^- in their microenvironments. Exposure to highly reactive and even potentially lethal ROS must have been a daily experience long before the rise of free O_2 in the atmosphere and long before the advent of oxygenic photosynthesis (Pierson, 1994; Towe and Des Marais, 2001; Dismukes et al., 2001; Eigenbrode and Freeman, 2006).

The consequences of exposure to strongly oxidizing conditions at rock–water interfaces early in Life's history may still be recognized today in the phylogeny of archaea, which are deeply rooted in the tree of life (Pace, 1997). A majority of archaea as well as a number of anaerobic bacteria contain distinct enzymatic systems, which evolved early to protect the cell from the detrimental effects of ROS. These enzymes include superoxide reductase to reduce superoxide to hydrogen peroxide and superoxide dismutases to disproportionate superoxide to H_2O_2 plus O_2 (Brines and Kovacs, 2007). Stress-activated positive hole charge carriers in crustal rocks, capable of oxidizing H_2O to H_2O_2 and producing ROS at rock–water interfaces, could have well provided the driving force for the development of such enzymes in the oldest life forms on Earth.

5. Conclusion

By studying the flow of stress-activated battery currents through a rock–water system we simulate oxidation processes that take place in the crust of a tectonically active body like Earth and that may have taken place throughout Earth's history. Electrochemical oxidation driven by stress-activated battery currents at rock–water interfaces may have played an important role in the evolution of the early Earth, specifically in the global oxidation, and in the evolution of early life.

Acknowledgments

This work was supported in part by a grant from the NASA Astrobiology Institute (NAI) Cooperative Agreement NNA04CC05A (to F.T.F and L.J.R.). M. Balk acknowledges a travel grant from the Netherlands Organization for Scientific Research (NWO). G.E. acknowledges a NASA Senior Fellowship through the National Research Council and the Oak Ridge Associated Universities (ORAU).

References

Batllo, F., LeRoy, R.C., Parvin, K., Freund, F., 1990. Dissociation of O_2^{2-} defects into paramagnetic O— in wide band gap insulators: a magnetic susceptibility study of magnesium oxide. J. Appl. Phys. 67, 588–596.
Bernabé, Y., 1998. Streaming potential in heterogenous networks. J. Geophys. Res. 103, 20,827–20,841.
Bishop, J.R., 1981. Piezoelectric effects in quartz-rich rocks. Tectonophys 77, 297–321.
Brines, L.M., Kovacs, J.A., 2007. Understanding the mechanism of superoxide reductase promoted reduction of superoxide. Europ. J. Inorg. Chem. 27–38.
Canney, S.A., Sashin, V.A., Ford, M.J., Kheifets, A.S., 1999. Electronic band structure of magnesium and magnesium oxide: experiment and theory. J. Phys. Condens. Matter 11, 7507–7522.
Cox, D.P., Singer, D.A., 1986. Mineral deposit models. US Geolog. Survey Bull. 1693, 379.
Crespy, A., Revil, A., Linde, N., Byrdina, S., Jardani, A., Bolève, A., Henry, P., 2008. Detection and localization of hydromechanical disturbances in a sandbox using the self-potential method. J. Geophys. Res. 113. doi:10.1029/2007JB005042.
Dismukes, G.C., Klimov, V.V., Baranov, S.V., Kozlov, Y.N., DasGupta, J., Tyryshkin, A., 2001. The origin of atmospheric oxygen on Earth: the innovation of oxygenic photosynthesis. Proc Natl. Acad. Sci. USA. 98, 2170–2175.
Eigenbrode, J.L., Freeman, K.H., 2006. Late Archaen rise of aerobic microbial ecosystems. Proc. Natl. Acad. Sci. USA 103, 15,759–15,764.
Espinosa-Garcia, J., 1993. New theoretical value of the enthalpy of formation of the OOH radical. Mol. Phys. 79, 445–447.
Freund, F., 1987. Hydrogen and carbon in solid solution in oxides and silicates. Phys. Chem. Miner. 15, 1–18.
Freund, F., 2002. Charge generation and propagation in rocks. J. Geodyn. 33, 545–572.
Freund, F.T., 2003. On the electrical conductivity structure of the stable continental crust. J. Geodyn. 35, 353–388.
Freund, F., Masuda, M.M., 1991. Highly mobile oxygen hole-type charge carriers in fused silica. J. Mater. Res. 8, 1619–1622.
Freund, F.T., Sornette, D., 2007. Electromagnetic earthquake bursts and critical rupture of peroxy bond networks in rocks. Tectonophys 431, 33–47.
Freund, F., Wengeler, H., 1982. The infrared spectrum of OH-compensated defect sites in C-doped MgO and CaO single crystals. J. Phys. Chem. Solids 43, 129–145.
Freund, F.T., Takeuchi, A., Lau, B.W., 2006. Electric currents streaming out of stressed igneous rocks — a step towards understanding pre-earthquake low frequency EM emissions. Phys. Chem. Earth 31, 389–396.
Goldblatt, C., Lenton, T.M., Watson, A.J., 2006. Bistability of atmospheric oxygen and the Great Oxidation. Nature 443, 683–686.
Griscom, D.L., 1990. Electron spin resonance. Glass Sci. Technol. 4B, 151–251.
Hurowitz, J.A., McLennan, S.M., Schoonen, M.A.A., Tosca, N.J., 2007. Production of hydrogen peroxide in martian and lunar soils. Earth Planet. Sci. Lett. 255, 41–52.
Koga, K., Hauri, E., Hirschmann, M., Bell, D., 2003. Hydrogen concentration analyses using SIMS and FTIR: comparison and calibration for nominally anhydrous minerals. Geochem., Geophys., Geosyst. 4, 1–20.
Lorne, B., Perrier, F., Avouac, J.-P., 1999. Streaming potential measurements 1. Properties of the electrical double layer from crushed rock samples. J. Geophys. Res. 104, 17,857–17,877.
Lu, J., Xue, S., Qian, F., Zhao, Y., Guan, H., Mao, X., Ruan, A., Yu, S., Xiao, W., 2004. Unexpected changes in resistivity monitoring for earthquakes of the Longmen Shan in Sichuan, China, with a fixed Schlumberger sounding array. Phys. Earth Planet Inter. 145, 87–97.
Martens, R., Gentsch, H., Freund, F., 1976. Hydrogen release during the thermal decomposition of magnesium hydroxide to magnesium oxide. J. Catalysis 44, 366–372.
Ogawa, T., Utada, H., 2000. Coseismic piezoelectric effects due to a dislocation 1. An analytical far and early-time solution in a homogeneous whole space. Phys. Earth Planet Inter. 121, 273–288.
Pace, N.R., 1997. A molecular view of microbial diversity and the biosphere. Science 276, 734–740.
Parkhomenko, E.I., 1967. Electrical Properties of Rocks. Plenum Press, New York, NY. 314 pp.
Pierson, B.K., 1994. The emergence, diversification, and role of photosynthetic eubacteria. In: Bengtson, S. (Ed.), Early Life on Earth. Columbia Univ. Press, New York, NY, pp. 161–180.
Reimold, W.U., Gibson, R.L. (Eds.), 2006. Processes on the Early Earth. Geol. Soc. America., p. 403.
Revil, A., 2007. Thermodynamics of transport of ions and water in charged and deformable porous media. J. Colloid Interface Sci. 307, 254–264.
Revil, A., Linde, N., 2006. Chemico–electromechanical coupling in microporous media. J. Colloid Interface Sci. 302, 482–694.
Ricci, D., Pacchion, G., Szymanski, M.A., Shluger, A.L., Stoneham, A.M., 2001. Modeling disorder in amorphous silica with embedded clusters: the peroxy bridge defect center. Phys. Rev. B 64 224104 224101–224108.
Rossman, G.R., 1996. Studies of OH in nominally anhydrous minerals. Phys. Chem. Miner. 23, 299–304.
Shluger, A.L., Heifets, E.N., Gale, J.D., Catlow, C.R.A., 1992. Theoretical simulation of localized holes in MgO. J. Phys.: Condens. Matter 4, 5711–5722.
Sze, S.M., 1981. Physics of semiconductor devices. Wiley, New York, NY.
Takeuchi, A., Lau, B.W., Freund, F.T., 2006. Current and surface potential induced by stress-activated positive holes in igneous rocks, Phys. Chem. Earth 31, 240–247.
Towe, K.M., Des Marais, D.J., 2001. On the origins of photosynthesis. Science 291, 436–437.
Tuck, B.T., Stacey, F.D., Starkey, J., 1977. A search for the piezoelectric effect in quartz-bearing rock. Tectonophys 39, 7–11.
van Hunen, J., van den Berg, A.P., 2006. Plate tectonics on the early Earth: limitations imposed by strength and buoyancy of subducted lithosphere. Lithos 103, 217–235.
Van Zeghbroeck, B., 1997. Photocurrents in a metal–semiconductor–metal photodetector. IEEE J. Quantum Electron. 22, 2188–2194.
Wilkins, R.W.T., Sabine, W., 1973. Water content of some nominally anhydrous silicates. Am. Mineral. 58, 508–516.
Wilson, C.L., Hinman, N.W., Sheridan, R.P., 2000. Hydrogen peroxide formation and decay in iron-rich geothermal waters: the relative roles of abiotic and biotic mechanisms. Photochem. Photobiol. 71, 691–699.
Zeng, X., Hayakawa, M., Lin, Y., Xu, C., 2002. Infrastructural analysis of geomagnetic field and earthquake prediction. In: Hayakawa, M., Molchanov, O.A. (Eds.), Seismo Electromagnetics: Lithosphere–Atmosphere–Ionosphere Coupling, pp. 463–468. Tokyo.

Nat. Hazards Earth Syst. Sci., 9, 585–603, 2009
www.nat-hazards-earth-syst-sci.net/9/585/2009/

Natural Hazards and Earth System Sciences

Investigation of ULF magnetic pulsations, air conductivity changes, and infra red signatures associated with the 30 October Alum Rock M5.4 earthquake

T. Bleier[1], **C. Dunson**[1], **M. Maniscalco**[1], **N. Bryant**[2], **R. Bambery**[2], **and F. Freund**[3]

[1]QuakeFinder Inc., Palo Alto, California 94306, USA
[2]NASA Jet Propulsion Laboratory (JPL), Pasadena, California 91109, USA
[3]NASA Ames Research Center, Moffett Field, California 94035, USA

Received: 11 September 2008 – Revised: 9 March 2009 – Accepted: 11 March 2009 – Published: 16 April 2009

Abstract. Several electromagnetic signal types were observed prior to and immediately after 30 October 2007 (Local Time) M5.4 earthquake at Alum Rock, Ca with an epicenter ∼15 km NE of San Jose Ca. The area where this event occurred had been monitored since November 2005 by a QuakeFinder magnetometer site, unit 609, 2 km from the epicenter. This instrument is one of 53 stations of the QuakeFinder (QF) California Magnetometer Network-CalMagNet. This station included an ultra low frequency (ULF) 3-axis induction magnetometer, a simple air conductivity sensor to measure relative airborne ion concentrations, and a geophone to identify the arrival of the P-wave from an earthquake. Similar in frequency content to the increased ULF activity reported two weeks prior to the Loma Prieta M7.0 quake in 1989 (Fraser-Smith, 1990, 1991), the QF station detected activity in the 0.01–12 Hz bands, but it consisted of an increasing number of short duration (1 to 30 s duration) pulsations. The pulsations peaked around 13 days prior to the event. The amplitudes of the pulses were strong, (3–20 nT), compared to the average ambient noise at the site, (10–250 pT), which included a component arising from the Bay Area Rapid Transit (BART) operations. The QF station also detected different pulse shapes, e.g. negative or positive only polarity, with some pulses including a combination of positive and negative. Typical pulse counts over the previous year ranged from 0–15 per day, while the count rose to 176 (east-west channel) on 17 October, 13 days prior to the quake. The air conductivity sensor saturated for over 14 h during the night and morning prior to the quake, which occurred at 20:29 LT. Anomalous IR signatures were also observed in the general area, within 50 km of the epicenter, during the 2 weeks prior to the quake. These three simultaneous EM phenomena were compared with data collected over a 1–2-year period at the site. The data was also compared against accounts of air ionization reported to be associated with radon emission from the ground (Ouzounov, 2007), and a series of laboratory rock stressing experiments (Freund, 2006, 2007a, b, c) to determine if field data was consistent either of these accounts. We could not find a data set with pre-earthquake radon measurements taken near the Alum Rock epicenter to compare against our field data. However, based on the Alum Rock data set example and another data set at Parkfield, the field tests are at least consistent with the lab experiments showing currents, magnetic field disturbances, air conductivity changes, and IR signatures. This is encouraging, but more instrumented earthquake examples are needed to prove a repeating pattern for these types of pre-earthquake EM signatures.

Correspondence to: T. Bleier
(tbleier@quakefinder.com)

1 Introduction

There have been many papers from the 1960's to present which reported electromagnetic signals prior to large earthquakes, These signals span the electromagnetic spectrum from slow moving DC magnetic field changes (Yen, 2004), ultra low frequency (ULF) magnetic field energy bursts (Fraser Smith, 2002; Molchanov, 2003, 2004), radio frequency signals from kHz to MHz (Fujinawa, 1990), infra red (IR) signatures (Ouzounov, 2007), visible earthquake lights (Derr, 1973), ionospheric disturbances (Pulinets, 2004; Molchanov, 2003, 2004; Liu, 2001, 2004), and others. Most of these phenomena are difficult to monitor in both space and

time due to the lack of sufficient instrumentation to cover large areas, and due to the large amounts of data required to be collected before infrequent earthquakes. Signatures collected using other parts of the EM spectrum (e.g. ULF, kHz, IR, etc.) are often contaminated with noise from cosmic, magnetospheric, anthropogenic or weather sources. Although these signals are interesting, the challenge is to determine if the signals correlate to specific earthquake preparation processes. This paper reports on a specific subset of the EM spectrum and the corresponding data sets collected for 30 October 2007 M5.4 Alum Rock earthquake. This paper looks for both temporal and spatial correlations between a medium strength earthquake, and ULF magnetic signals, IR signatures, and air conductivity changes. It further examines these signatures in the context of a recent theory of pre-earthquake processes. One theory (Freund, 2006, 2007a, b, c) involves the generation of p-hole charge carriers during asymmetric rock stress, and the resulting underground currents and ULF magnetic fields. The theory also addresses the migration of the charge carriers to the surface where they change the local surface air conductivity and may create apparent IR heating signatures as observed by satellite instruments during the earthquake preparation process. Another theory (Ouzounov, 2007) addresses the potential release of radon near epicenters, the subsequent ionization of local air molecules, and corresponding capture of water vapor and eventual release of latent heat (IR). This paper cannot conclusively prove that all these phenomena occur prior to all or even most large earthquakes (since the data is primarily from a single event), but simply strives to determine if the data collected is consistent with either of these theories. Also, since electromagnetic noise contamination is so prevalent in the field data, this paper also investigates potential noise sources in each data set to determine if the data collected can be legitimately attributed to geophysical sources (e.g. earthquake processes), or could they be contaminated by extraneous electromagnetic noise sources (e.g. man-made fields, lightning, solar storms, etc.).

2 Background

Fraser-Smith (1990, 1991) collected ULF data near Corralitos, Ca prior to the 1989 Loma Prieta earthquake, and detected a 20× increase of ULF energy in several bands, with the maximum signal contained in the 0.01–0.022 band, 14 days prior to the quake. The data were processed and saved to 30 min averages to record the average signal intensity for each of 18 filter bands. The raw data was not saved due to storage constraints, and as a result, it is impossible to determine the exact nature of the signal structure and dynamics.

Other ULF signatures have been recorded, but some like the Chi-Chi earthquake (Yen, 2004) in Taiwan, used DC magnetometers. These signatures were hampered by slow sampling, and therefore lost some of the higher frequency signal components. QuakeFinder started building and deploying ULF magnetometers in 2000, and now have 53 three axis instruments deployed throughout California in the CalMagNet (Cutler, 2008). Twenty-five of these instruments also include simple air conductivity sensors, and collect and store 32 SPS of raw data in each of 5 data channels (3 magnetometers, a geophone, and air conductivity) using GPS as a time reference. These multiple station locations and GPS-correlated time finally allow us to compare data in space and time, both near and far from significant California earthquakes.

3 Alum Rock quake

The Alum Rock M5.4 Alum Rock quake occurred at 03:04:54 UTC on 31 October 2007 (20:04:54, 30 October local) located near the Calaveras fault at 37.432° N, 121.776° W, and its depth was 9.2 km. QuakeFinder's QF-1005 magnetometer sensor (unit 609) was located 2 km SW of the epicenter, and that site's data had over two years of historical signal history. The raw data was collected with an instrument that used a 12 Hz low pass hardware filter in the instrument electronics, and the spectrogram was then generated using a Blackman window, 1024 FFT samples with a 16 factor overlap resulting in 513 frequency bins. Figure 1a is a sample of the daily data where pulsations (sharp vertical energy bands) were evident closer in time to the earthquake. This frequency spectrogram illustrated that the signals were observed in all three channels, and that the pulsations contained energy throughout the 5 Hz bandwidth. These pulsations were not part of the midnight and noon time calibrations signals (0.8 Hz for 5 min in duration) that are injected into the magnetometers each day.

Figure 1b illustrates a more detailed view of the DC to 0.16 Hz portion of the band, and particularly shows some energy in the 0.01 Hz band (orange horizontal energy band) where energy had been identified in the 1989 Loma Prieta earthquake (Fraser-Smith, 1990). Even more evident was the strong vertical pulsation signatures which had significant lower frequency energy content (vertical red bands).

One major question was whether these pulsations were observed at all sites (caused by global magnetospheric pulsations), or just detected at the site near the earthquake? Figure 1c shows a 2 h comparison of ULF time series data across the entire State of California. One can observe large pulses in the line labeled E. Milpitas which was 2 km from the epicenter. This early time period in the figure was also selected to show the BART train noise that typically starts around 3 a.m. each day. The BART noise can be clearly seen at the two sites (E. Milpitas and Portola Valley) which are in the Bay Area, at approximately 5–15 miles from the BART tracks respectively. The subject pulsations are much larger than these normal BART transients, and the pulsations appear to be unique

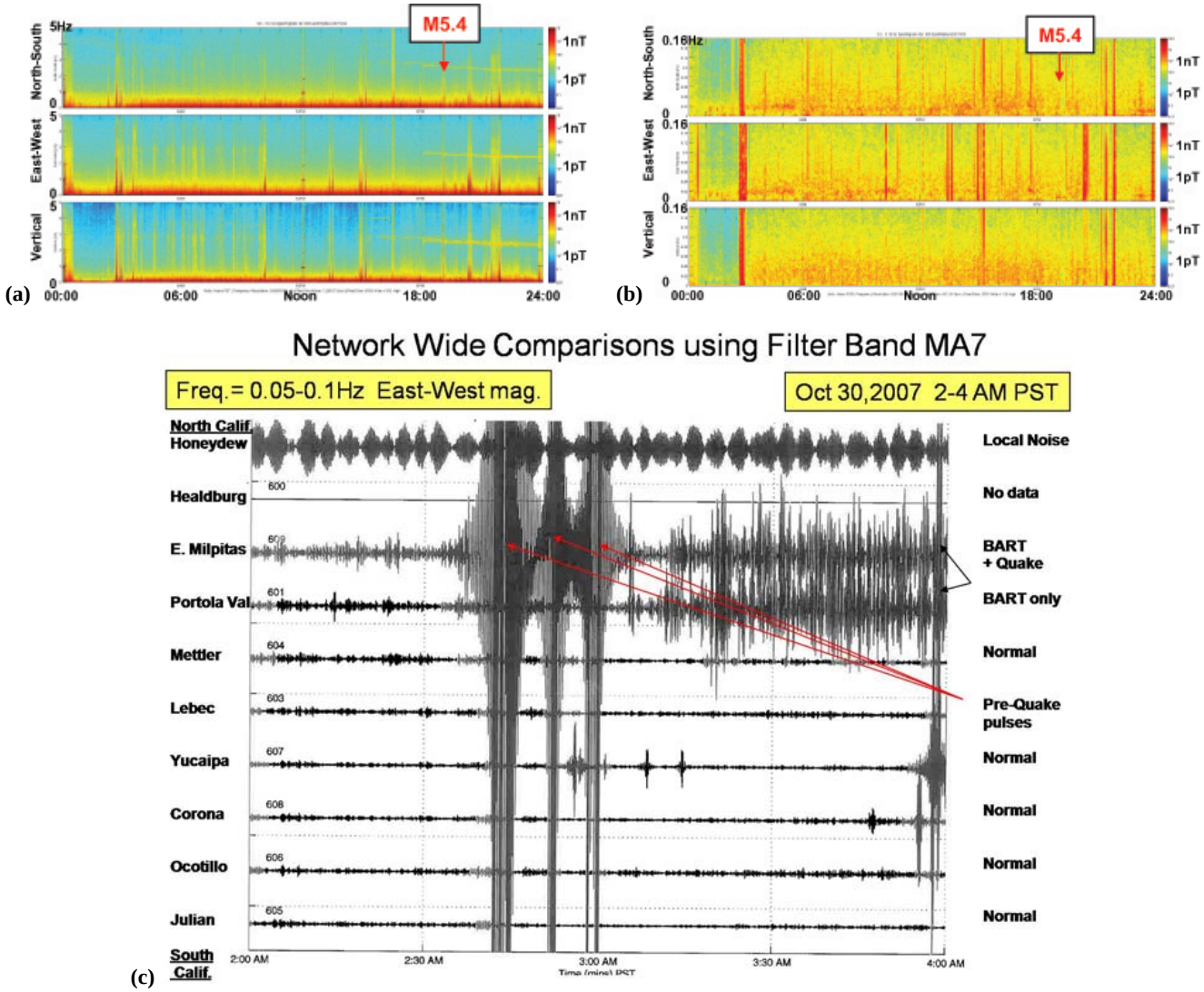

Fig. 1. **(a)** 24-h spectrogram display with north-south (top), east west (middle) and vertical magnetometer channel (bottom), frequency selected via software from 0.01 Hz to 5 Hz to display more low frequency detail. **(b)** 24-h spectrogram display with north-south (top), east west (middle) and vertical magnetometer channel (bottom), frequency selected via software from 0.01 Hz to 0.16 Hz to display more low frequency detail. **(c)** Two hour time slice of the 0.05–0.1 Hz Band time series plot comparison of all ten, high resolution, CalMagNet sites from Honeydew, Ca. (near Eureka, Ca), to Julian, Ca (east of San Diego, Ca).

to the East Milpitas, that is, they cannot be observed even at the closest site across the Bay, the Portola Valley site which is 30 km west of the epicenter. The noise on the top line (Healdsburg) is local machinery noise.

The specific site at E. Milpitas, near the epicenter, was analyzed, and a "normal" day (1 October 2007 in Fig. 2a) was compared to an "active day" (17 October 2007 in Fig. 2b) when there was considerable pulsation activity. Figure 2a illustrates the additional BART noise that can be seen all day, except between 1 a.m. and 3 a.m. when BART shuts down for maintenance. Figure 2b illustrates the same East West channel for 17 October 2007 when the pulsations increased in occurrence. Note the vertical scale has changed and the calibrations signal (0.8 Hz sine wave for 5 min) appears smaller, but are in fact, the same 8 nT peak-to-peak cal. signals. There were significant pulsations just after midnight, as well as throughout the day at approximately 04:00, 08:00, 14:00, 19:00, and 22–24:00. Figure 2c is a 24 h time series for the day of the earthquake (30 October 2007). There is a co-seismic signal evident when the coils shake during the P and S wave sequence at 20:04 local time (arrow), but the time series continued to show large impulses into the following night. The ellipse again highlights the area in the middle of the night where historically, the instrument site is usually very quiet, but this night, there were large pulsations. Figure 2d is that same night time data around 02:30, expanded to show the nature of the pulses including their unique polarity structures (positive only, negative only, and regular bi-polar

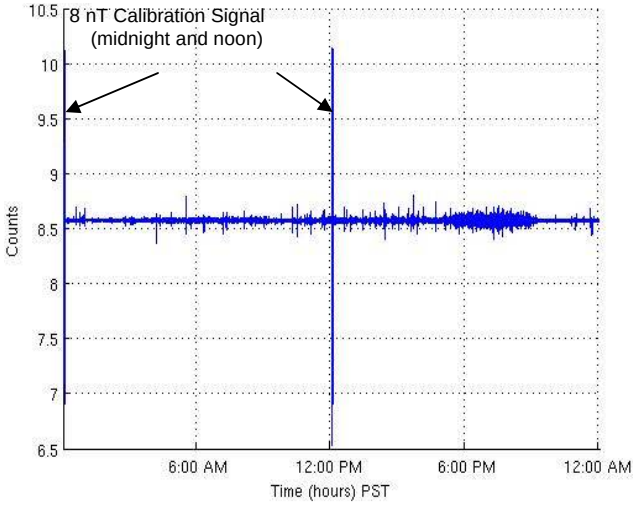

Fig. 2a. Time series E-W – quiet day (1 October).

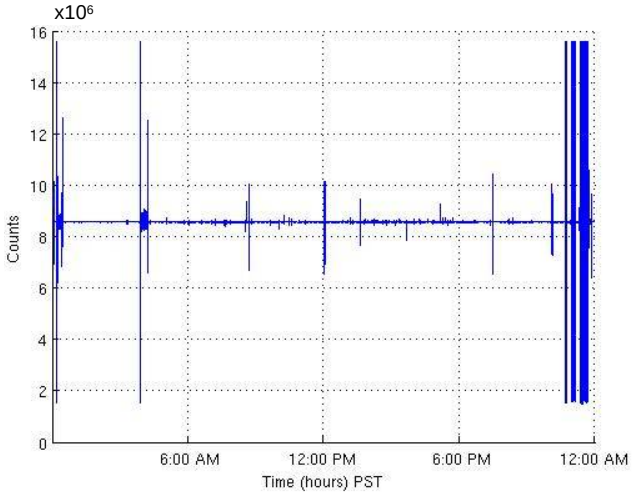

Fig. 2b. Time Series E-W – active day (17 October).

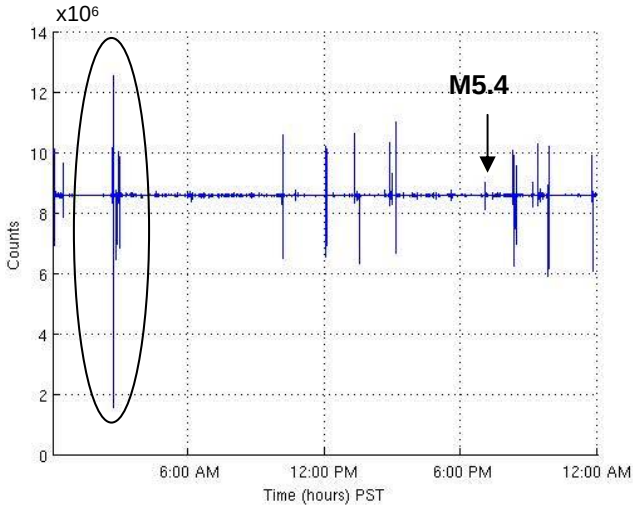

Fig. 2c. Time series E-W – day of quake (30 October).

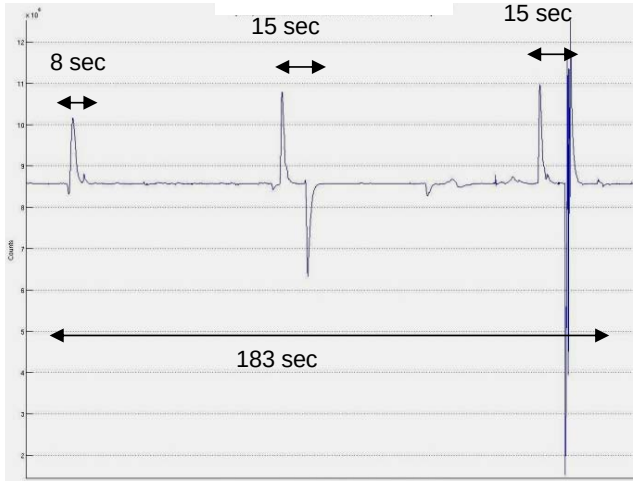

Fig. 2d. Area in ellipse (Fig. 2c) expanded.

pulses). This instrument is an induction (AC) magnetometer, and therefore only changes in the local magnetic field are detected. The magnetic pulsations were also observed to be rather long (8 s, 15 s, 15 s) within this 183 s segment of time. These longer pulsation times are quite different when compared to local lightning (0.1 to 0.5 s).

Every site has a characteristic local noise environment. As such, the site-specific area "background noise" was measured, and twice the largest noise signatures typically observed each day at each site was used as a "threshold level" to identify these unusual pulses. These pulse excursions were subsequently counted to quantify the rate of occurrence each day. Figure 3 illustrates a 24 h time series of one day, the day of earthquake at E. Milpitas, and the box in the lower left summarizes the pulses types and pulse counts for each type. Pulses above or below these threshold levels (8.9×10^6 counts for upper limit, and below 8.2×10^6 counts for the lower limit) were first identified, then classified by "type" (positive excursions, negative excursions, and bi-polar excursions), and then counted and incremented within the "type" bins. A pulse "type" is a predominantly "positive" excursion above the positive limit, a predominantly "negative" excursion below the lower limit, or a bipolar ($\pm$) pulsation which exceeds both limits.

In monitoring the noise environment, it should be noted that we typically never saw these long, single polarity pulsations associated with human noise at any sites. In the cases of man-made noise pulsations (e.g. a car passing), the waveform was always bipolar. The single polarity signatures suggested some type of electrical current or disturbance that started impulsively, and then relaxed slowly over several seconds without changing polarity. Lightning occasionally has this singular polarity "type", but the pulse durations are significantly shorter than 1 s.

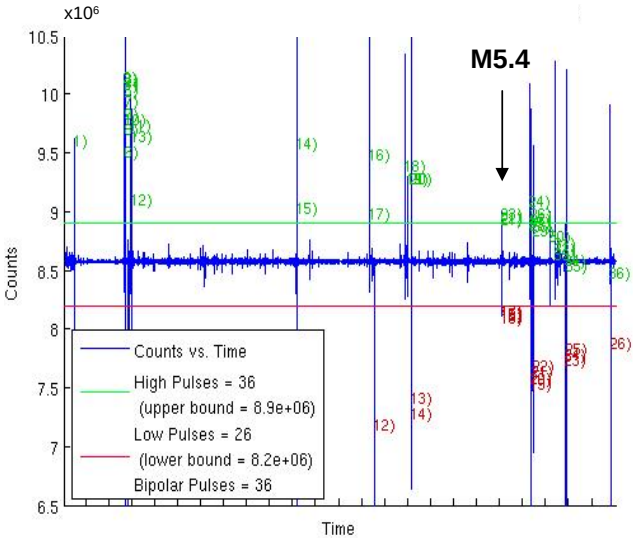

Fig. 3. Time Series E-W – Day of quake with high (green) and low (red) threshold limits (30 October). There are 36 pulses which exceeded the high threshold and 26 that exceeded the low threshold. In addition there were 36 pulses that exceeded both high and low thresholds.

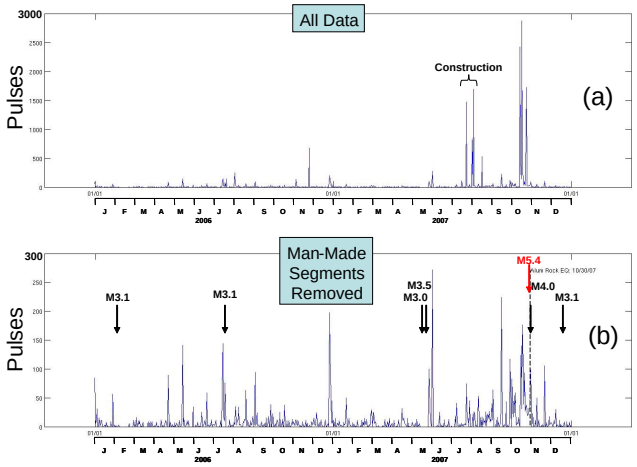

Fig. 4. Magnetic pulse count for E-W channel at E. Milpitas (2 km from epicenter), unedited plot with contamination **(a)**, and identified man-made contamination segments removed **(b)**.

Figure 4 is a plot of the number of pulses per day that exceed this 2× noise floor limit for the E. Milpitas site, and the plot was run over the entire 2 years of data in the site's history prior to the quake. After plotting all the data (a), it was apparent that there were data segments where man-made noise corrupted the data set, (e.g. tractor work near the magnetometers during July–August 2007, visits to the site by our maintenance staff (14 October 2007), and several other repeating man-made signals). We identified these contamination times, based on evidence in the area (one of our coils was actually damaged in July 2007) or interviews with the landowner noting the times of the local activities. These corrupted segments were subsequently removed from the second plot file (Fig. 4b). Both plots show elevated count totals during the summer, peaking near the end of October 2007. Note, the vertical scale has been compressed in Fig. 4b, but it continues to illustrate that there was a build up of pulses from the "normal" 0–10 pulse per day background levels. It was noted in Fig. 4b that there were 12–13 episodes of short periods of pulsations. Most of these periods were shorter than 2–3 days. These short periods of pulses would peak at 150–250 pulses per day during 2006–2007. Analysis of a typical sequence, e.g., from 26–30 December 2006 showed 2–3 short pulse sequences per day, and the sum of sequence durations equaled 1 h or less. Two of these short periods were followed within a week by a small earthquake (M3–4). This may or may not be significant. However, late in October 2007 prior to the Alum Rock earthquake, the pulse rate increased and sustained these higher levels for almost 2 weeks (similar to the Loma Prieta sequence), and then decreased back to background levels in a few days after the quake. This sustained sequence over 2 weeks we believe is significant in that the deformation process may be starting to avalanche.

The two M3+ quakes identified on Fig. 4b were the only quakes prior to the M5.4 that were identified within a 20 km radius of the epicenter (the expected range of the magnetometers).

4 Investigation of potential magnetic noise contamination sources

The pulsations in the data set at the E. Milpitas site could be "normal" noise from local and global geophysical sources (e.g. lightning, Pc 1, Pc 3, or Pc 4 magnetospheric pulsations), or contaminated by man-made activities, or, a combination of both. An investigation was started to identify and characterize specific signal sources at this site. Six potential sources (man-made noise and geophysical signals) were identified and investigated relative to these magnetic pulse signatures:

1. Man-made noise from electrical sources local within 100 m of the instrument (e.g. cars, trucks, power tools, water pumps). This also includes potential electrical impulses from nearby Lawrence Livermore Lab (National Ignition Facility-NIF testing) where large capacitor banks are discharged into one or more lasers.

2. Solar generated magnetospheric noise (e.g. Pc 1, Pc 3, Pc 4 micro-pulsations).

3. State-wide lightning.

4. Internal instrument noise (the QF-1005 instrument itself).

5. Power grid electrical currents due to electrical faults at customer locations.

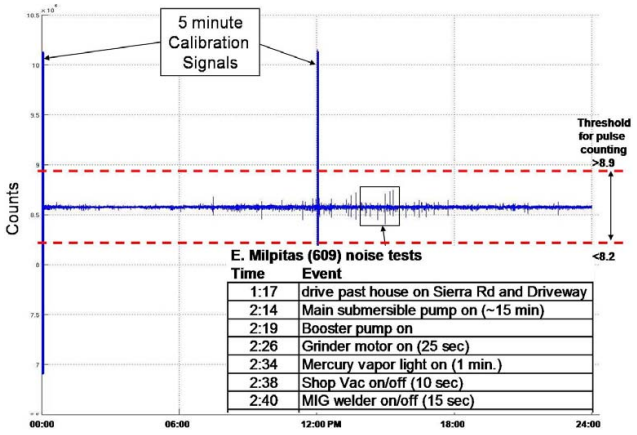

Fig. 5. Series of noise tests performed at E. Milpitas to develop a 2× noise threshold level.

4.1 Local man-made noise

The E. Milpitas (Site 609) is located approximately 100 m from two roads, and there are several equipment barns and 2 water pumping systems within 50 m. A special set of noise tests were performed on a Sunday afternoon when the local environment was relatively quiet and could be controlled. Each large current source in the local area was identified (e.g. a deep well pump, a booster pump, welder, shop vac., etc.) and cycled on/off in a controlled test sequence, each time observing the reaction of the magnetometer instrument. In addition, cars and trucks were driven along the nearby road, and times noted. Figure 5 shows a 24 h time series of magnetometer data in which these vehicles and equipment sets were turned on/off at various times and recorded. The box inset at the lower right of the figure lists the actual equipment start times, and durations. The worse case noise measured at the magnetometers was less than 0.85 nT peak to peak. That level was then doubled (1.7 nT) and subsequent upper and lower limits (8.9 and 8.2×10^6 counts) applied to future daily data plots as a limit threshold.

It may have been possible for large current users, other than BART trains, to generate pulse type noise. One example was identified at Lawrence Livermore National Labs, 30 km NE of the site. The Lab group was contacted to determine if their National Ignition Facility (NIF) laser system was firing during the time in question. They indicated that they had fired 1 laser bank (out of 192) occasionally that day, but the times did not correspond to any of the corresponding ULF pulse times. In addition the ULF pulses at E. Milpitas were too closely spaced in time to possibly be caused by the much slower NIF firing sequences.

4.2 Solar-generated ULF noise

The next test compared all ten 600 series sites, which include the highest resolution, 3-axis magnetometer systems in CalMagNet. These instruments have a frequency range from 0.01 to 12 Hz, with a noise floor of approximately 0.1 pT per root Hz at 1 Hz. These instruments were deployed along major faults from far Northern California to the Mexican border. A time period was selected when most sites were quiet (e.g. 2–4 a.m.) and the frequency band 0.01 to 0.022 Hz was selected which typically shows simultaneous Pc 3 and Pc 4 solar-generated micro-pulsations. Pc 3 and 4 signals are solar-generated magnetic disturbances that result in long period (e.g. 50–100 s) disturbances that can be detected world wide. Therefore, simultaneous Pc 3 and 4's can be seen across the network (See Fig. 6). However, the large pulsations detected at E. Milpitas (10–20× amplitude of Pc 3 and 4) had long durations (1–30 s) and did not resemble typical Pc 3 and 4's, and most importantly, they were only detected at E. Milpitas. Therefore, these large pulsations do not appear to be solar-generated signals.

4.3 Lightning

Since local lightning strikes could have caused similar pulses (at least those which were less than 1 s wide), a lightning survey was purchased from Vaisala, Inc which included the entire state of California, for the month of October 2007. The resulting data was scanned to see if any correlations existed between the pulses observed at E. Milpitas site and any lightning events in the greater California area. Much of the lightning activity was in the northern and eastern parts of the state, namely the Sierra Nevada mountains. 29 October was the one day with the most lightning activity in the state (4420 strikes reported), and the 20 closest strikes (within 30 km of E. Milpitas) were identified. Figure 7a is a time series of 29 October at E. Milpitas and the lightning activity that could be time correlated is highlighted in a narrow time period (e.g. the series of lightning strikes occur only between 15:50 to 17:00). The remaining lightning activity occurs more than 50 km from this site, and appears to fall below the threshold levels used is Sect. 4.1 (e.g. a typical distant strike is shown at 05:30), and therefore were not counted. In general for October, lightning was a very minor noise (pulse) source for the data set. We used a magnitude threshold in the pulse counting algorithm (Sec. 4.1), but in the future, one could create a pulse duration threshold to further eliminate lightning contamination, and this would eliminate the need to purchase lightning data bases from outside vendors. Figure 7b highlights the differences in the pulse shape and duration between lightning (bottom) and the subject pulsations (top).

Approaching the analysis from the opposite perspective, namely the pulsation activity, 17 and 24 October had the highest ULF pulse counts at E. Milpitas during October, however there were no lightning strikes on either of those days in all of California.

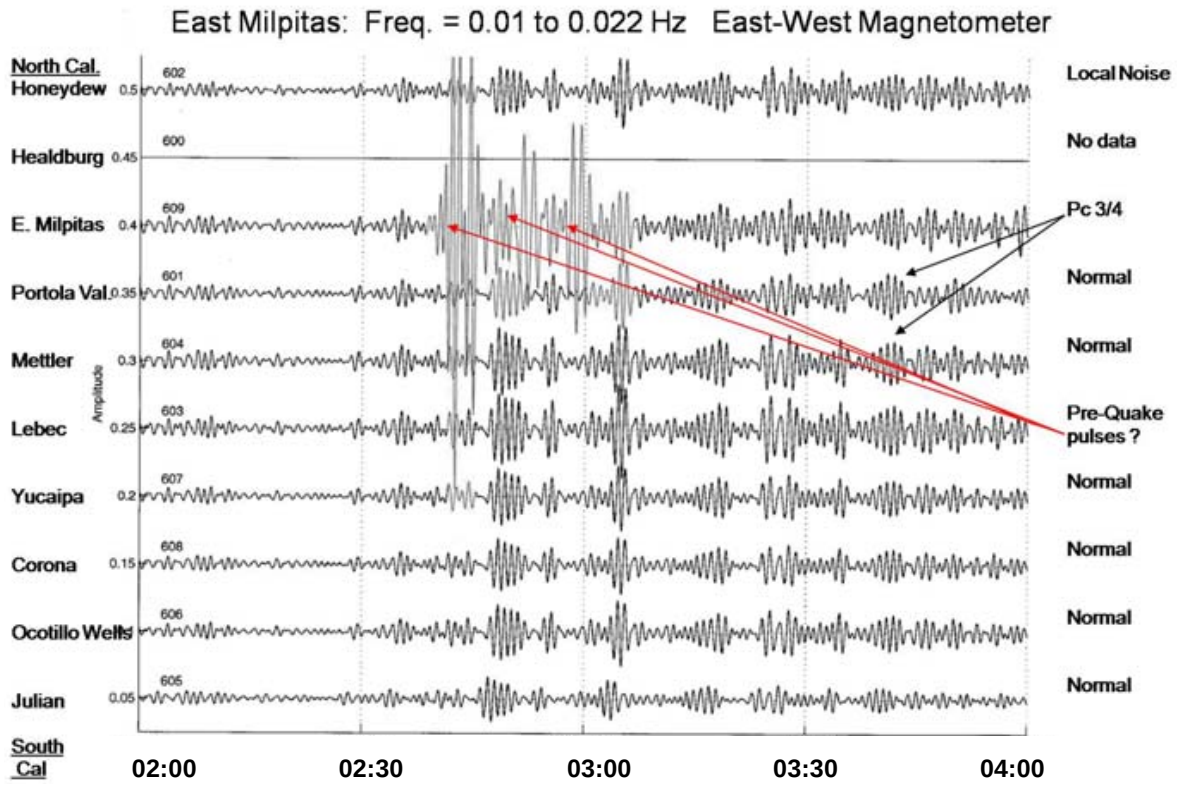

Fig. 6. Time-series comparison of Pc 3, 4 micro-pulsations from 10 California stations.

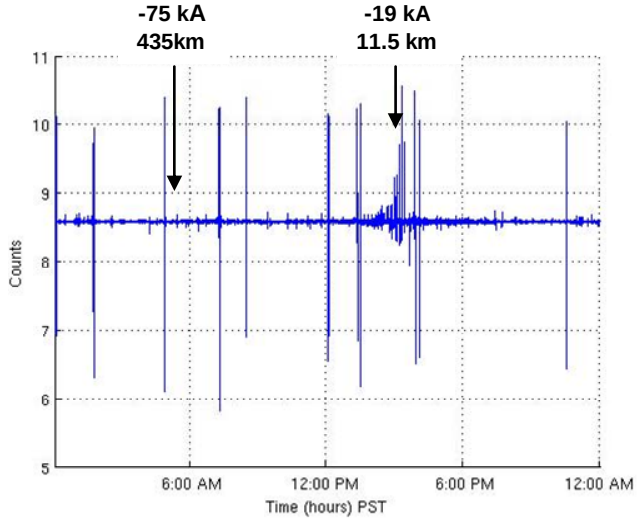

Fig. 7a. Examples of lightning detected at the E. Milpitas site on 29 October 2007. −75 kA refers to a cloud to ground lightning strike, 75 000 A, 435 km from the strike to the ULF magnetometer instrument at East Milpitas.

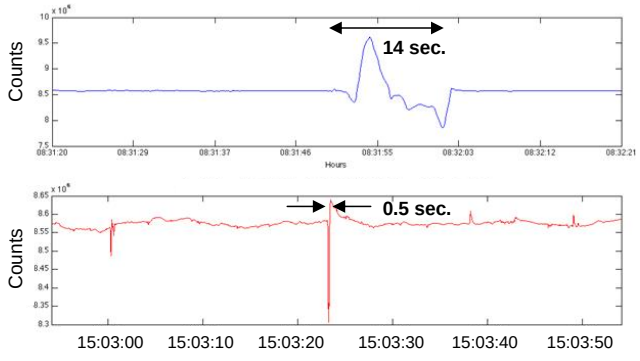

Fig. 7b. Comparison of ULF pulsation (top), possibly related to earthquakes, and lightning (bottom).

4.4 Internal instrument noise

Next, the instrument itself was tested to see if any internal electronics or software could cause the pulses. All three magnetometer channels saw the pulses at E. Milpitas, but the Air Conductivity sensor and Geophone, which share the same analog power supplies, never exhibited simultaneous pulses (hence the power supplies and analog-to-digital (A/D) converters appeared to function properly). The instrumentation power supply voltages were also recorded for a week, but no pulses were ever detected.

We looked for a case where two magnetometer instruments might have detected a local pulse to prove that a single instrument was not detecting an internally-generated noise

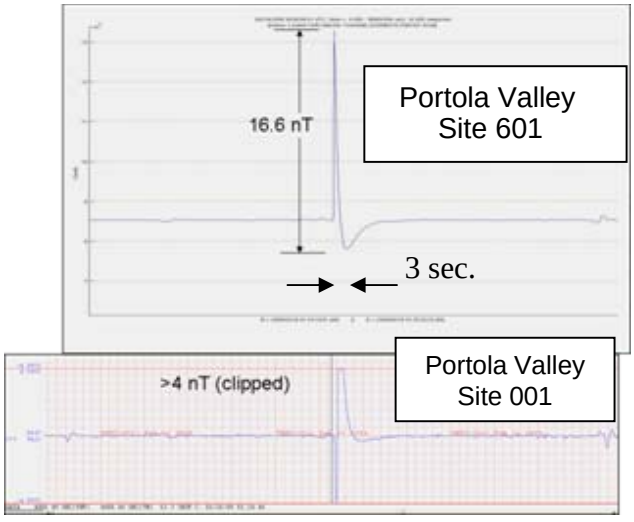

Fig. 8. The same ULF pulse, detected by 2 different magnetometer instruments, 100 m apart.

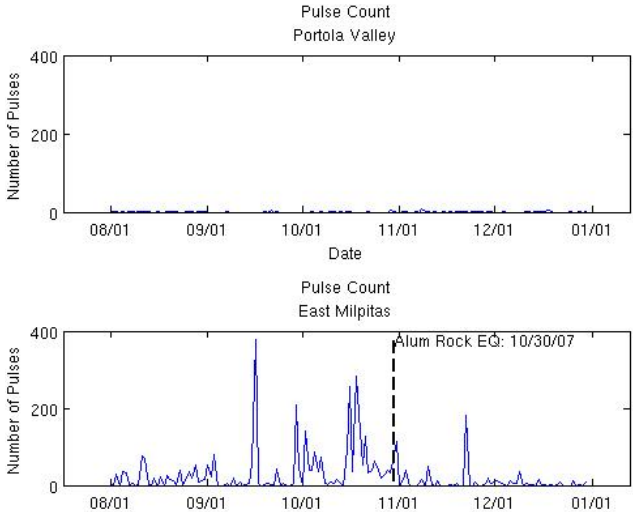

Fig. 9. Comparison of pulse counts at Portola Valley, 30 km west of Alum Rock (top), and East Milpitas, 2 km SW of Alum Rock (bottom).

pulse. We found an example of a pulse detected at the prime Portola Valley site (Site 601), and since it had a second magnetometer system (an original high school-built system, Site 001) 100 m west of the 601 site, we compared the two data sets. Figure 8 shows that the same pulse was detected on two different magnetometers, 100 m apart, and therefore could not be unique to noise in one instrument. The time is synchronized via GPS, and the time scales are identical in Fig. 8. The two magnetometers utilized different electronic amplifier designs, power supplies, and different A/D units. See the CalMagNet description (Cutler, 2008) for more site details.

4.5 Power grid fault current noise

The area around the magnetometer site was examined for power lines and potential paths between the local equipment loads and the source power transformer where short circuit faults and current return paths could contaminate the data. This Site 609 (E. Milpitas) was not in any such fault path, nor were any of the other CalMagNet instruments.

5 Alum Rock fault area signal characteristics

The E. Milpitas instrument detected a number of pulsations that appeared to increase within 2 weeks prior to the Alum Rock earthquake. In this section we investigate several parameters of these pulsations in order to understand their unique characteristics relative to the quake. These characteristics include the pulse counts observed over the 2 year period prior to the quake, the pulse durations, pulse polarities, and pulse signal propagation distances. When a large solar storm occurred, the magnetometers would detect continuous waveforms in the 0.01 to 5 Hz band. We monitor the worldwide average geomagnetic index, Kp, and know when these continuous sequences of Pc 1, Pc 3, and Pc 4 waveforms should arrive. These solar-generated waves would last for hours or days. The pulse types observed prior to the Alum Rock earthquake were unique in that they were individual pulsations that were longer than lightning, and had other unusual characteristics, namely that a significant number of them were “unipolar”, e.g. they had either a positive only or, a negative only component relative to the DC mean value of the time series data. After we looked for all discriminating features of the Alum Rock data set, we also looked for another example of a medium to large quake where there were in situ magnetometers (e.g. Parkfield M6.0 quake on 28 September 2004) to determine if similar pulsations existed in that earthquake sequence. See Sect. 6.

5.1 Pulse counts

We have seen the pattern of pulsation events in Fig. 4. Figure 9 here shows a comparison between the E. Milpitas site (609), 2 km from the epicenter on the Calaveras fault, and those observed over the same time period at the Portola Valley site (601), located approximately 300 m west of the San Andreas fault, and approximately 30 km to the west of E. Milpitas. Portola Valley has a typical background pulse rate of 0–4 pulses per day, and rarely contains over 10 pulses per day, did not demonstrate any elevated pulse counts prior to the Alum Rock earthquake. It can also be seen that there were some episodic pulse activities at E. Milpitas throughout the year in which pulse rates rose above 150 pulses per day, but these episodes usually lasted only 1–2 days. Some of these pulse sequences were very periodic, happened during

the workday, and through interviews with the landowner, could be attributed to local construction activities (e.g. tractors). These man-made sequences were removed from the data set. The majority of the pulse sequences were more random, and in the timeframe leading to the earthquake, the pulse rate appeared to increase above 50 to 176 per day, and remain active for more than a week, spread across both day and night. The pulse activity then returned to normal after several days post quake, and again looked normal.

5.2 Pulse durations

We investigated the duration of the pulsations by first identifying the pulsation above the thresholds described in Sect. 3. Once the pulsations' amplitude was detected to be greater than twice the site background noise, they were typed and counted. The duration of the pulsations were measured and binned from 1 to 30 s. Figure 10 shows the distribution of pulse durations over the 2 year period 2006 through 2007, and showed that there were many pulses in the range of 1–30 s. These durations were much longer than any human-generated noise source that we had observed during the noise characterization tests described in Sect. 4. Geophysical Pulsation-continuous activities such as Pc 3 and 4 signals did exist regularly in the data, but these signals were below the threshold used in Fig. 6, and were considerably smaller (0.1 to 3 nT) than the amplitude of the pre-earthquake pulsations in question (e.g. 3–20 nT).

5.3 Pulse polarities

Not only were the pulse durations unusual (1–30 s), but they also had unusual singular polarities (+ or − only) as well as bi-polar waveforms (±). The same data set for 2006 through 2007 was reviewed and a query was set to count the positive only, negative only, positive (starting) bi-polar, and negative (starting) bi-polar pulses. Table 1 below compares the 2 year totals of the polarity counts with the 2 week period just prior to the quake (15 to 31 October 2007). The percentages to the right of the table show that the 2 week pre-quake period is responsible for 36–45% of all the pulses (identified by polarity) over the 2 year period, even though this 2 week period only represents approximately 2% of the total time in the pre-quake 2 year data set. It is also interesting to note that the 2 week pre-quake period showed 7227 single polarity pulses (sum of the + and − pulses) as compared to 4396 total bi-polar pulses. All human-generated noise that was identified in the study was always bi-polar.

5.4 Propagation distance

Special field tests were performed using an identical portable magnetometer (unit 699) to the unit at E. Milpitas, and data was collected at 4 remote, temporary locations (labeled Temp1-Temp4) as shown on the map in Fig. 11. These data collections were performed on the day after the earthquake

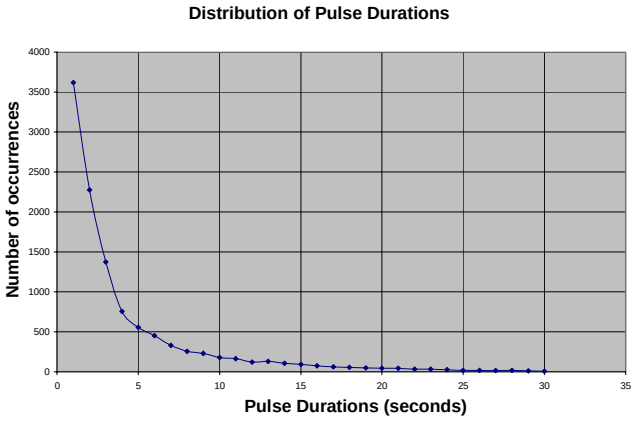

Fig. 10. Distribution of pulse durations that violated the 2× background noise threshold at E. Milpitas Site for all of 2006 and 2007.

Table 1. Counts of individual Pulse types at Alum Rock (E. Milpitas).

Pulses	2006–2007	5 to 31 Oct 2007	% of Total
UP	11 282	4108	36
DOWN	9176	3119	34
BIPOLAR_UP	5993	2689	45
BIPOLAR_DOWN	4757	1707	36

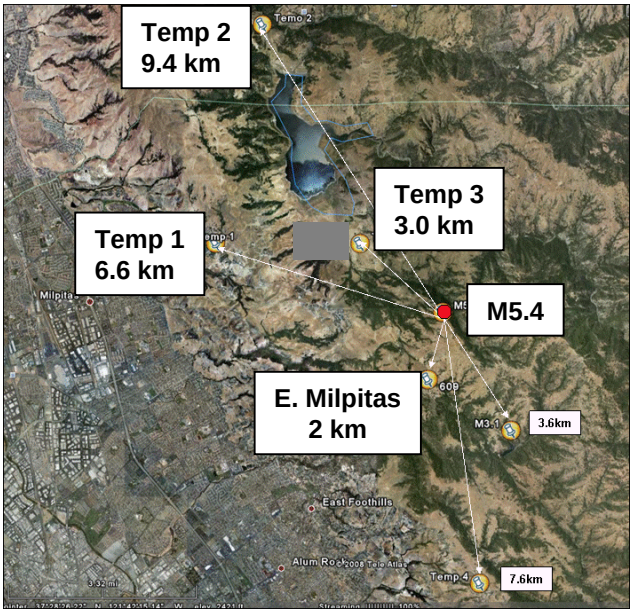

Fig. 11. Map showing relative locations of the M5.4 quake, Site 609 (E. Milpitas), and Temporary data collection sites: Temp 1–4.

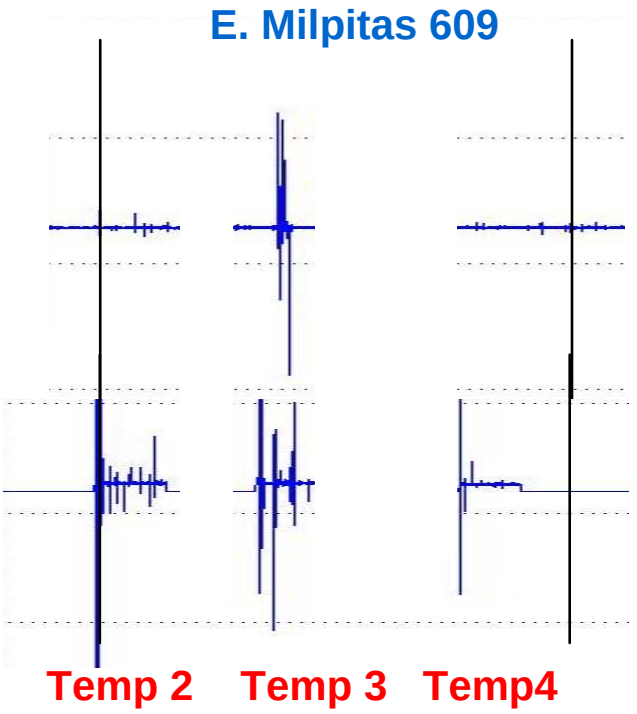

Fig. 12. Corresponding Time series data for fixed Site 609 (top) and Temporary Sites 2, 3, and 4 (bottom).

(31 October local) to determine how far the pulses could be detected from the epicenter. Figure 12 shows the overall signal comparison of TEMP sites 2, 3 and 4. Temp 1 was omitted from this figure, because it was 6.6 km away, located perpendicular to the fault trace, and did not show any correlation. Since we were only able to record for 30 min at each temporary site, many of the large pulses detected at the continuously recording Site 609 occurred when the portable unit (699) was being moved and was not recording. Figure 13 shows the signals from TEMP3 (699) and the fixed site (609), expanded to show more detail. Only three significant pulses were correlated at Temp 3 site, 4.3 km to the northwest of the fixed E. Milpitas site, 3.0 km from the epicenter, along the Calaveras fault trace. The amplitude and time scales are identical between Site 609 (E. Milpitas) and unit 699 (Temp site equipment). Both sites include identical instruments, both used GPS timing, and both sites showed strong correlation for small magnetospheric pulsations (Pc 1, 3, 4's). In Fig. 13, one can see a pattern of 3 spikes (but opposite in polarity) at the temporary site, and offset at the fixed site. Pulses A and B are similar to A' and B' (but opposite in polarity). The pattern continues with pulses C and C'. These Temp 3 pulse patterns are consistently offset by 8 s (earlier) from the fixed site. There is additional analysis of this offset in the Discussion Section.

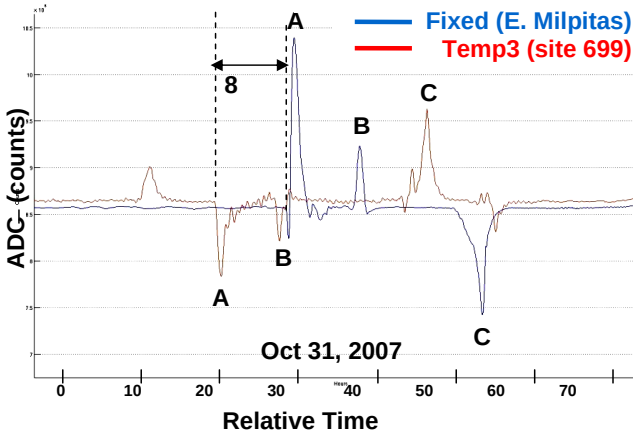

Fig. 13. Pulse comparison timeline showing 8-s offset between East Milpitas (Site 609) and Temp 3 (Site 699).

6 ULF comparison with another California Earthquake: Parkfield M6.0 28 September 2004

The only other significant earthquake example in which we had access to ULF data was Parkfield (M6.0 on 28 September 2004). We re-examined that event and discovered similar pulses in the raw data files. Figure 14a illustrates the pulse structure on 13 September, the start of the active pulsation period at Parkfield, 15 days prior to the M6 quake. Expansion of several pulse patterns identified by the ellipses in Fig. 14a show similar, large and elongated pulses over various time segments in Fig. 14b and c. The local area was quiet. Solar activity was nominal (Kp was 3, and Electron flux was 10^3) and there were no local quakes >M2.5 during this time period. The instrument is located on a farm, and since the activity continued for several days, and more importantly, at night, it did not seem likely that human activity was the cause for these pulsations. Figure 14d and e show the pulse activity for Parkfield over a one year period, 2004. The Vertical channel (PK3) was selected because it was relatively quiet. Figure 14e illustrates a relatively small pulse count increase prior to the quake at 14 days and 1 day prior to the earthquake. Analysis of the time series data for these smaller pulses in Fig. 14a showed occurrences of unipolar pulses, similar to those observed at Alum Rock. The post earthquake period also shows several periods of high pulse counts in Fig. 14e during which there were no aftershocks (similar to Alum Rock and Loma Prieta earthquakes). One might expect that the post quake period to include major stress redistributions, and perhaps, corresponding current generations. One major difference is that the pulses at PKD (Parkfield) were smaller than those seen near Alum Rock. This could be due to the quake epicenter being 19 km from the PKD magnetometer instrument (vice 2 km for Alum Rock). Although the Parkfield quake was larger (M6 vs. M5.4), the geology

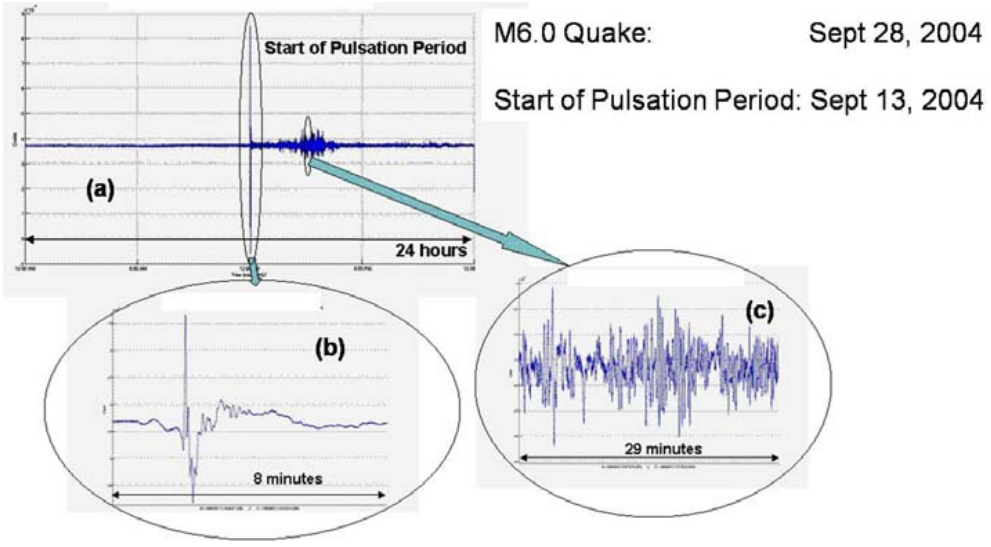

Fig. 14. (a) 24 h time series plot at Parkfield (PKD, and **(b)** and **(c)** time expansions showing pulsation activity at Parkfield station 15 days prior to the M6.0 earthquake.

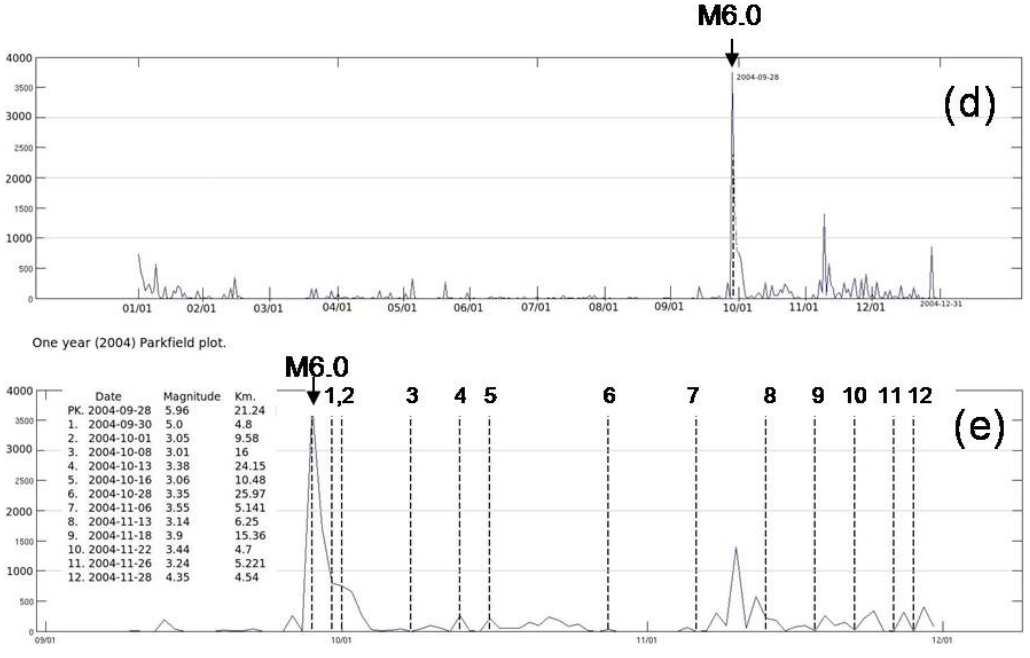

Fig. 14. (d) Pulse count for Parkfield (all 2004), and **(e)** expansion for September–December 2004 showing earthquakes (dotted lines) and table of corresponding magnitudes and distances from PKD site. Note: 13 more aftershocks occurred on 28 September 2004 with magnitudes from 3.06 to 4.71.

of the area northeast of the fault line has been determined to be highly conductive during an MT survey taken in the area (Unsworth, 2000), and this may have resulted in additional attenuation of the signal since the conductive layers exist between the epicenter and the PKD instrument.

The PKD site did not detect any significant 0.01 Hz signal similar to the Loma Prieta quake, but it did detect very large Pc 1 micropulsations (0.2 to 0.9 Hz energy band) from 2 a.m. until the quake at 9:15 a.m. local. These Pc 1 micropulsations were subsequently analyzed (Bortnik, 2007, 2008a, b), and even though they may not be generated by the quake itself, their propagation through the ionosphere to the ground appeared to be enhanced during quake episodes. Bortnik demonstrated that Pc 1 occurrences were statistically significant to earthquake occurrences near Parkfield, only when the Pc 1's appeared in the daytime within several days prior to

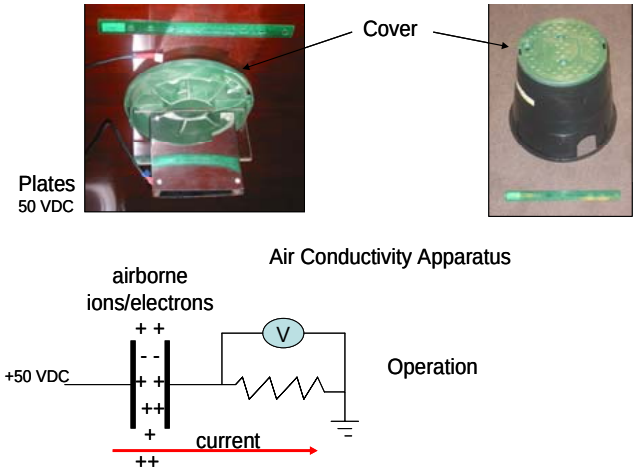

Fig. 15. Air Conductivity sensor description.

the quake. The alteration of the ionosphere above the epicenter region has been reported in a number of papers (Liu, 2001, 2004).

There were no air conductivity instruments near Parkfield prior to this earthquake.

7 Air conductivity observations at Alum Rock (Calaveras Fault)

An air conductivity (AC) sensor was placed at the East Milpitas site (609) for a year prior to the quake. The sensor (Fig. 15) consists of a simple pair of stainless plates, with one plate charged to 50 VDC, and the other plate connected through a resistor to ground. The systems were tested and shown to be responsive to both positive ions and negative (electrons) charge carriers. The air conductivity (AC) sensor at E. Milpitas was upgraded in May 2007 to cover the plates (using a closed-top fiberglass cylinder with an open bottom) so that rain would cause less contamination in the sensor.

Several days prior to the quake, there was no appreciable rain (a contamination source) and yet the sensor saturated for almost 13 h. Figure 16 illustrates the single day rise in conductivity levels (saturated for 13 h), while there was no rain that day and the relative humidity remained in the 70 percent range.

The primary difficulty with these units in the field is fog and rain which condenses moisture on the plastic plate separators and contaminates the data whenever the relative humidity (RH) exceeds 95%. Figure 17 illustrates the field verification of this effect.

Figure 18 is an expanded version of air conductivity data for the month of October 2007. It shows saturated periods due to rain (100% RH) on 9 and 12 October. However, the unit saturated prior to the quake for 13 h when RH was well below the saturation level (74%) as determined by checking 2 local weather stations in the hills near the site. Something else was causing the saturation.

The polarity of the signals from the AC instrument at E. Milpitas indicated that the ionization was predominantly positive ions, but further investigation showed that the sensor detected 4 periods of negative charge carriers (See negative areas identified in red within Fig. 18). This is significant because we had not detected negative signatures in the data prior to this time.

7.1 Other potential sources of air conductivity changes

The Air Conductivity instruments in the field are not mass spectrometers, and therefore they cannot discriminate between p-hole carriers (oxygen anions) and radon (or radon's secondary products). However, the data clearly showed that which ever mechanism causes this ionization phenomenon, it must be able to account for the high rates of ionization, as well as both the positive and negative charge products in the air above the quake area.

It has been reported that these ionizing particles also affect relative humidity, e.g. ions capture water molecules and reduce relative humidity. The present and future CalMagNet instruments are also being retrofitted now with relative humidity sensors mounted adjacent to the air conductivity assemblies to provide more accurate relative humidity information at each site.

8 IR data (GOES-West satellite)

The GOES satellite IR Imager data, specifically the long wave infra red-IR: (10.7–12 μm), was obtained to analyze the infra red environment around the greater San Jose (Alum Rock) area. This geosynchronous satellite instrument has a 4 km pixel dimension, and a specific pixel was identified just north of the epicenter, and subsequently analyzed for a night time cooling slope phenomenon. Every night after the sun sets on a portion of the earth, the corresponding area is expected to cool over 12 h, with a resulting negative slope in temperature profile for each pixel of the frame. The larger area image (hundreds of pixels) around the Bay Area was also analyzed to determine the overall trends for these temperature cooling curves. In recent research by NASA/JPL (N. Bryant, personal communication, 2007), areas surrounding an impending large earthquake suddenly manifest an "apparent heating" effect where the temperature appears to rise in the middle of the night. This rise in IR energy is not a function of black body radiation, but rather is a semiconductor effect whereby airborne ions are neutralized, and the energy given up is seen as an Infra Red (IR) energy burst. Figure 19 show a schematic of the concept of using the night time cooling curves to check for anomalous "apparent heating" during the night time. The 3 year history of the Alum Rock area data was reviewed and the night time cooling curve of the pixel, with a negative slope of -0.991 degrees per hour, was calculated and is shown with the (almost) horizontal red line as

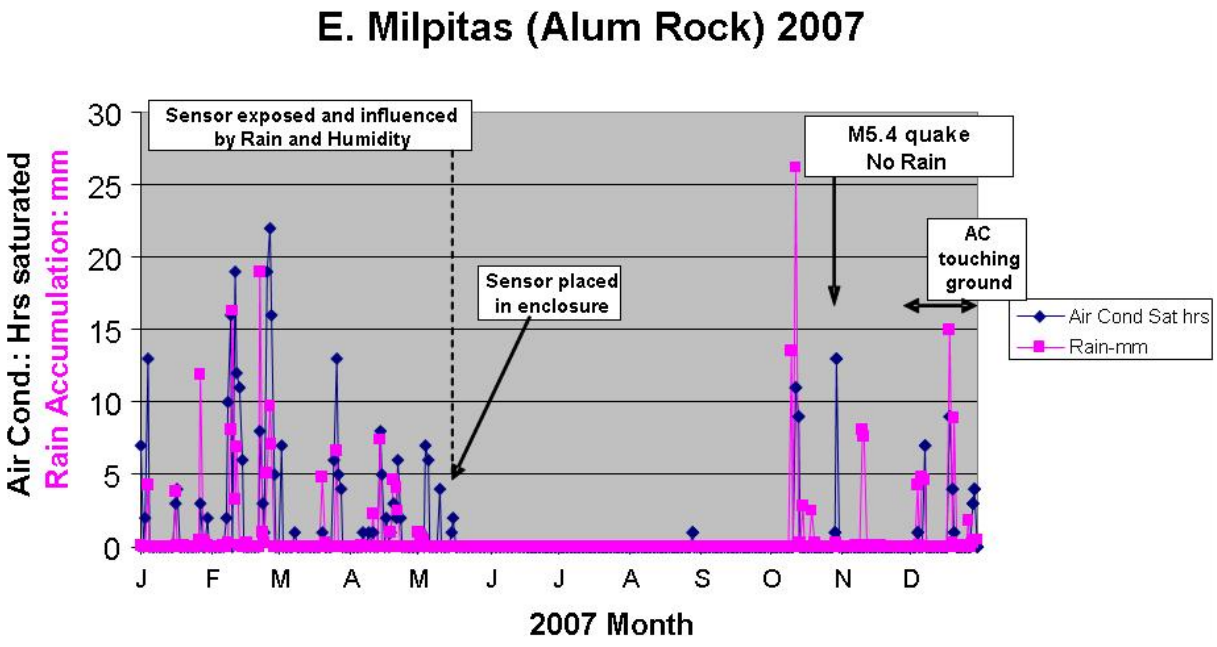

Fig. 16. Complete 2007 Air Conductivity and rain data for E. Milpitas (Site 609). Rainfall (red) contaminates the data (blue) and causes the sensor to saturate for hours at a time.

shown in graph in the right side of Fig. 19. The slope of the night time period for 17 October 2007 (13 days prior to the quake) however, is +0.3616 (blue line).

This "apparent heating" is not seen in the local ground temperature, but as an energy or "apparent heating" similar to the IR signal seen in lab experiments by Freund (2007a, b, c) using a Bomem IR spectrometer with the stressed granite sample. In this lab experiment, it was confirmed that the process of neutralizing the charge carriers (P holes) in the surrounding air resulted in an IR signature, with maximum energy in the 8 and 12 μm wavelength bands. See Sect. 8 of this paper.

The same slope study performed for all the pixels over the larger northern California scene, as illustrated in Fig. 20.

The white areas in the color enhanced images depict normal 3 year history of night time cooling (negative temperature slope), grey is cloud cover (too few points to calculate a slope), yellow and pink are increasingly positive slopes ($>$+0.2 and $>$+0.3, respectively), and red is more intense positive slope. Note: many of the "red" areas are suspect since they lie adjacent to grey (cloud) areas where there are too few data points to obtain accurate slopes. These red/grey transition areas were ignored. The Calaveras fault line is shown as a black line to the lower right of the San Francisco Bay in these images, and the quake event is shown as a red dot, only on the 30 October image. These images are for the evening and early morning of each day marked on the images (e.g. 10 p.m. of the prior day to 6 a.m. for the numbered day shown on the image).

It can be seen that the apparent heating (yellow and pink areas) were generated after comparison with slopes from the previous 3 year average, and these yellow areas are spread over a wider area than just the epicenter region. It is estimated that there is "noise" in these images which may be caused by compression heating of the westerly winds as they impact the coast, Easy Bay, and Sierra Nevada mountain ranges, before passing over the mountains. The yellow areas are very evident well away from the epicenter region, and since they are barely positive and so common, they were ignored. The stronger positive slope (pink area) near the area around the fault zone (e.g. 17 October) is consistent with other IR studies near larger earthquakes (Ouzounov, 2007), and may suggest that the increased stress pattern is spread over a significant area (tens of kilometers), well beyond just the local epicenter region. The signal-to-noise of this heating appears to be marginal, and this medium sized M5.4 quake may also be marginal for this heating effect. Larger earthquakes have shown higher signal-to-noise levels (Ouzounov, 2007).

9 Discussion

Having now looked at each EM data set, and the corresponding noise sources in each set, we compared the 3 sets together to see if there was a consistent pre-earthquake set of signals. Figure 21 shows each data set, normalized to their highest reading in October 2007, and plotted together to allow a comparison of the trends. It can be seen that there is a consistent increase in signal approximately 2 weeks prior to the quake

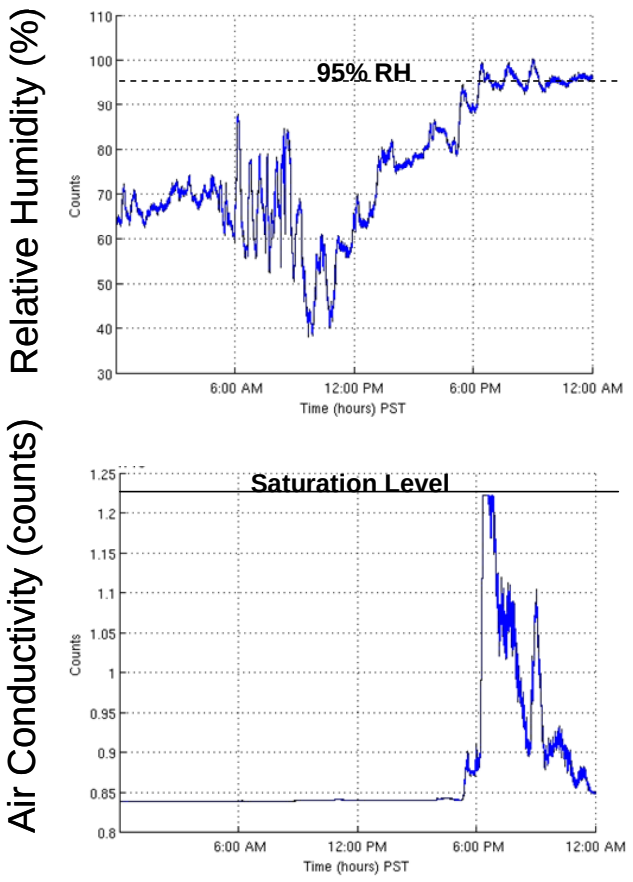

Fig. 17. Relative humidity (RH) contamination of the Air Conductivity sensor. When RH exceeds 95% (top panel), the plate separators become moist, start conducting, and the sensor output saturates (bottom panel).

when pulse counts reach a maximum, IR slope reaches its highest positive value for the pixel close to the epicenter, and air conductivity also starts a pattern of positive pulses before saturating during the evening prior to the quake.

Again, it should be noted that this quake is only a medium intensity quake, and the signal-to-noise ratio was not expected to be overwhelming. We plan to repeat this analysis for larger quakes, and determine if the signal-to-noise ratio (height of the signatures above background noise) is larger and more dramatic.

9.1 Lab data comparison

9.1.1 Magnetic fields

This field data can be compared, (at least qualitatively) with laboratory data collected during rock stressing experiments. Freund experiments with currents (Freund, 2006, 2007a, b, c) showed a strong correlation of currents passing through the rock samples when new stress was applied to the sample. These currents (pulses) would be expected to produce corresponding magnetic pulsations. When extrapolated from the small rock sample to the size of an earthquake rupture zone, these currents would be expected to grow accordingly. There is concern in the community whether the currents deep in the earth might be "neutralized" where there is ionic water which could "short circuit" the current paths. Subsequent lab tests have demonstrated that these currents can at least pass through ionic water boundaries and continue through adjacent rock layers. However, the lab tests are not necessarily representative of the conditions (pressure and temperature and rock interfaces) that exist deep in the hypocenter regions.

9.1.2 Pulse propagation

In order to understand this offset, we reviewed the lab experiments (Freund, 2006, 2007a, b, c) where the generated current impulse velocity was measured. That experiment showed that a rock sample being hit with a steel ball at supersonic speed will generate a current impulse that propagated along and through the rock sample. The current was first measured from the impact point at one end of the rock sample, and then detected at the other end of the sample. The propagation speed of this current pulse was measured at 200–250 m per s.

In the field test, the epicenter was 3.0 km from Temp3, and 2 km from the fixed Site 609 in Fig. 11. If the underground current source (similar to the p-hole carrier current demonstrated in the lab) had a propagation path component parallel to the E-W coils at the 2 observation points, and if this current burst originated between the two observing sites (near the epicenter area), then one would use the right hand rule (a current in a conductor induces a magnetic field around the conductor), and the polarity should be opposite at the two observing sites (up at one site and down at the other).

The 8 s offset between the arrival of the pulses at the fixed site (609) and the Temporary site (699) is also interesting. The distances to the epicenter from the fixed site and Temporary site in this field experiment (2 km and 3.0 km respectively) divided by 200 m/s propagation rate, results in propagation times of 10 s and 15 s respectively. If it took 10 s for the charge carriers to reach the vicinity of the TEMP3 observation point, and 15 s to reach the vicinity of the fixed site, the difference of the time of arrival (5 s calculated, versus 8 s observed) is certainly within a order of magnitude of what might be expected, based on what was observed in the lab. We also do not know that these pulses originated exactly at the epicenter, and they may have been farther from the epicenter, causing longer propagation times and increasing the 5 s delta. The difference in arrival time also seems to imply that the current/magnetic pulses are propagating at this slower rate to the magnetometer sites, where they are detected only when they are in the immediate vicinity. This could account for some of the larger amplitude signals when the $1/R^3$ signal attenuation is factored into the propagation equations. The large signals could be caused by either

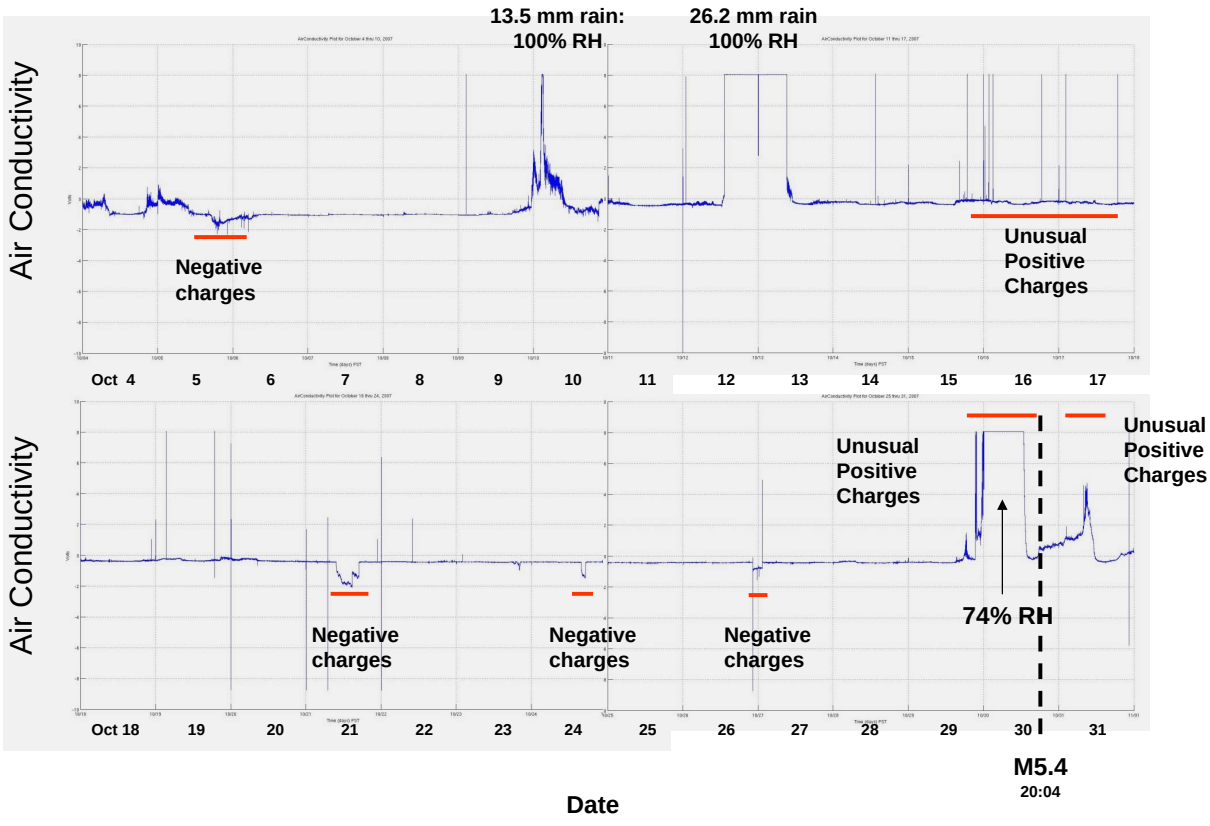

Fig. 18. Air Conductivity (expanded for October 2007) at E. Milpitas site. Unusual periods of positive and negative excursions are underlined in red (5, 15–17, 21, 24, 26, 30, and 31 October).

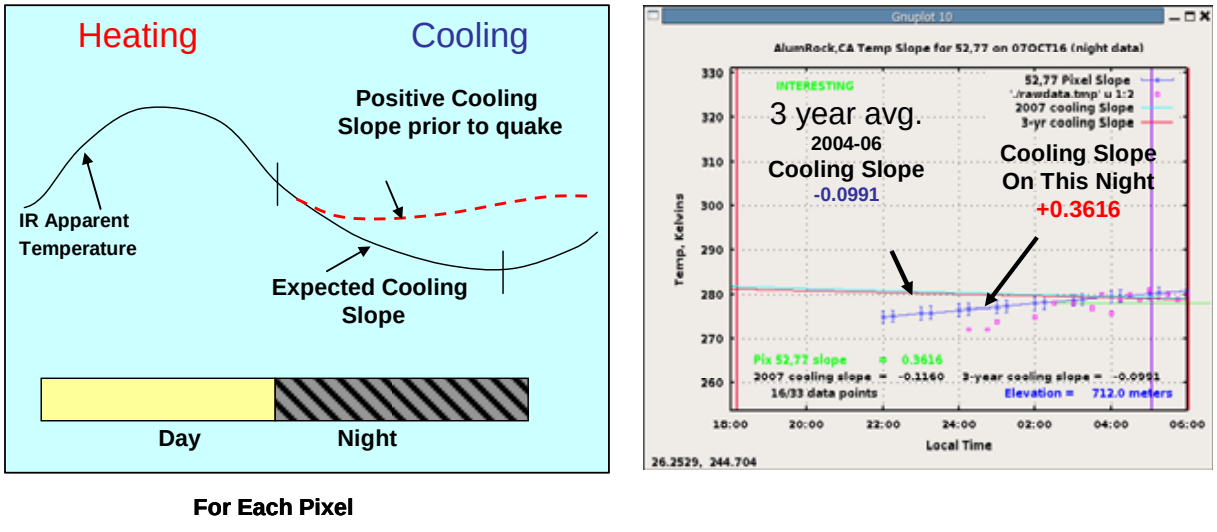

Fig. 19. Typical IR cooling at night time (left), with cooling slope at Alum Rock (right).

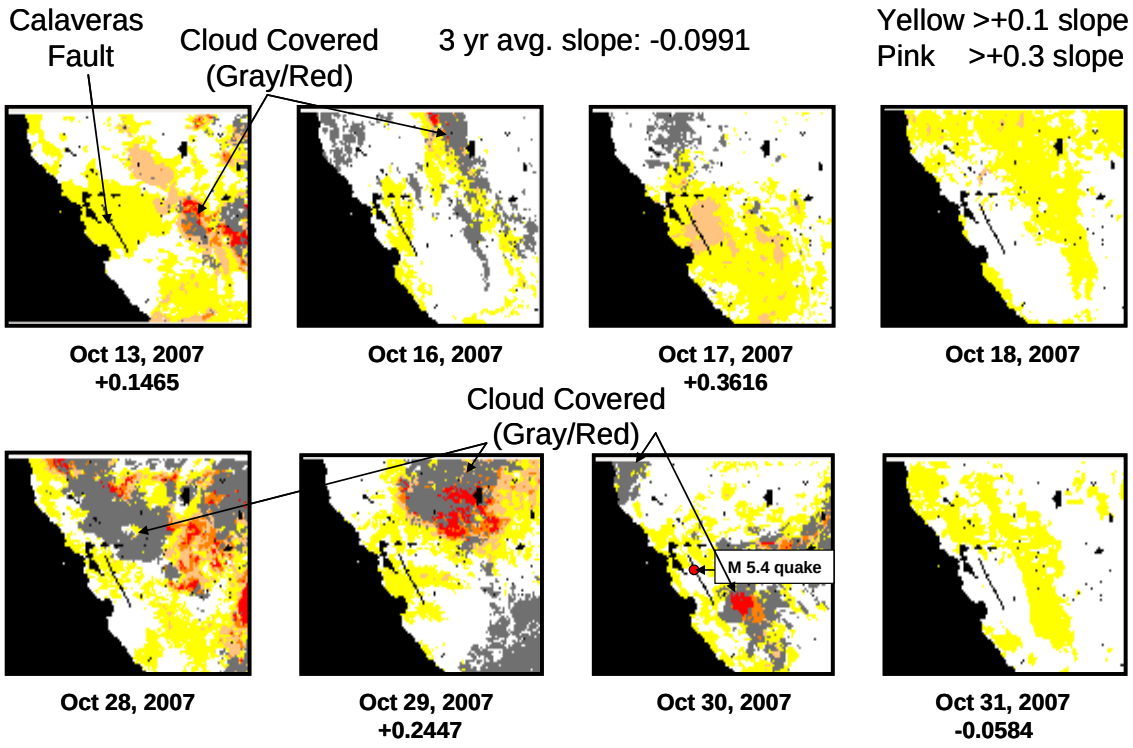

Fig. 20. IR night time temperature slopes, October 2007 Northern California. White=Negative, Yellow and Pink=more positive, Red is typically contaminated, Grey is cloud covered where no slope can be calculated.

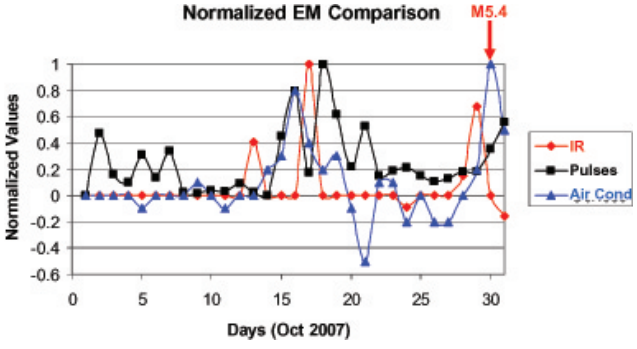

Fig. 21. Comparison of 3 electromagnetic (EM) signatures (IR slope, magnetic pulse count, changes in air conductivity) prior to the Alum Rock quake (M5.4 on 30 October 2007).

huge currents at the hypocenter (kilometers from the site), or smaller currents that have migrated to the surface, near (hundreds of meters) to the magnetometer site.

9.1.3 Air ionization

Figure 22 (Run #39) shows that current increases when stress is changed, and demonstrates positive ion currents migrate toward the negatively charged plates. The insets show the set up. The faces of the two pistons were modified by adding two rows of hardened steel bearings, 5 mm diameter, to act as stress concentrators. As the steel bearings sank into the rock with increasing load, the hydraulic responded, giving rise to the saw-tooth pattern.

Figure 23 (Run #42) shows negative currents flowing to a positively charged plate. Both figures show the current flowing up to the moment of failure from the rock surface to a 10×20 cm ion collector plate, biased +90 V or −90 V, through a 1 cm wide air gap.

What is noteworthy is the positive ion emission always begins after some load is applied to the rock. Before ion emission occurs, there is a build-up of positive surface charge due to the arrival of positive holes at the rock surface. The positive ion current is due to field-ionization of air molecules, probably O_2, at the rock surface. The negative ion plus electron emission always begins later, at higher loads. It is due to corona discharges that commences when the positive fields at the rock surface become so strong that the positive air ions are accelerated away from the rock surface to velocities sufficient to impact-ionize neutral gas molecules and thereby initiate a corona discharge. Each corona discharge is accompanied by a light blip (which have also been recorded) and by RF noise. On a larger scale in earthquake zones, these may be related to the "earthquake lights" (Derr, 1973) and strong RF (KHz to MHz) noise detected (Fujinawa, 1990) prior to large earthquakes.

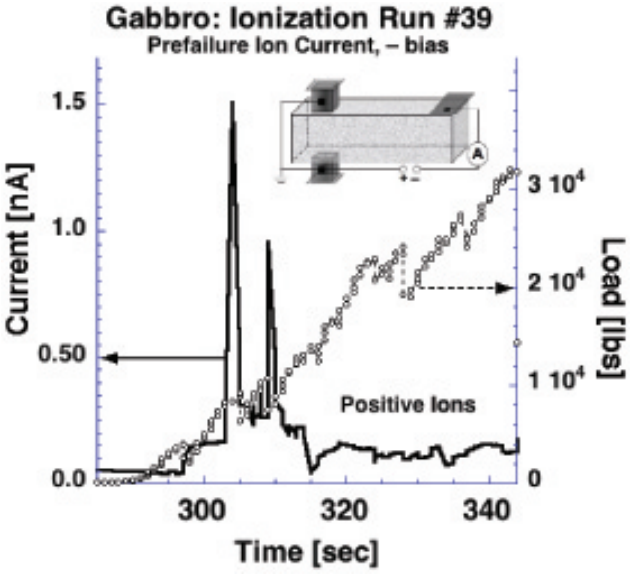

Fig. 22. Laboratory experiment (Freund, 2007a, b, c) showing positive currents after stress is applied.

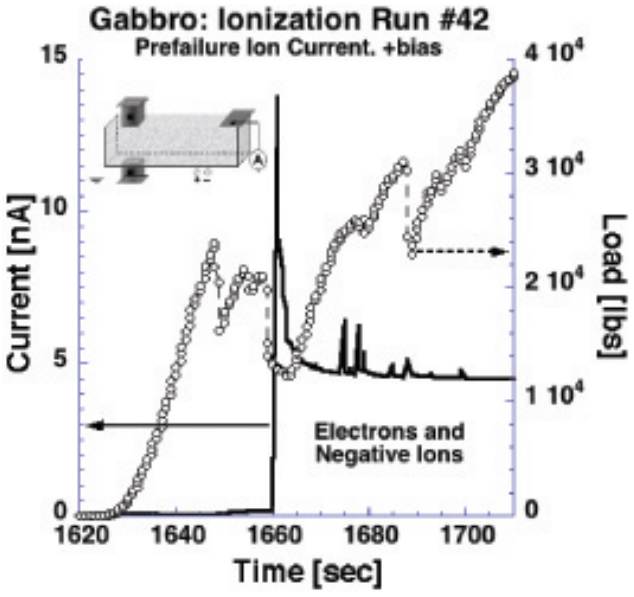

Fig. 23. Laboratory experiment (Freund, 2007a, b, c) showing negative currents after stress is applied.

9.1.4 Infrared emission

Additional experiments (Freund, 2007a, b, c) showed IR signatures (8–12.5 μm) detected using a Bomem IR spectrometer when this stress was applied. Figure 24 illustrates this effect, and as time progresses and more stress was applied (moving front to back, into the plot), one can see the increasing IR levels, especially in three narrow bands.

There is a natural question whether the laboratory data is indicative of what happens in the actual fault preparation process. Our field data is the first step in correlating these two data sets, and the field data appears to at least support the premise that stress concentration changes, occurring in the days to weeks prior to a medium-large earthquake, may produce underground currents, magnetic field disturbances, air conductivity changes near the epicenter area, and IR apparent heating as manifested in changes in the night time cooling slope near the epicenter region.

10 Conclusions and future plans

10.1 Conclusions

Each of the 3 EM signature types are summarized below.

10.1.1 ULF magnetic pulsations

Large magnetic pulsations were observed to increase in occurrence days prior to the Alum Rock earthquake (October 2007). Since the origin of the observed pulsations was unknown at the time (possibly from man-made noise sources or from the quake area itself), the area around the magnetometer instrument was surveyed and measured for any similar man-made noise contamination (pulsations from cars, trucks, local machinery, distant high current sources). The largest man-made noise measured was less than 1 nT in amplitude while the pulsations in question frequently exceeded 8–20 nT. The instrument itself at the site was also exonerated for possible instrument/power supply/data equipment noise. World wide solar magnetospheric noise e.g. Pc 1, Pc 3, and Pc 4 micro-pulsations were also examined and found to be minimal during the time of the local Alum Rock pulsations. Simultaneous comparisons of the ULF data from the nine other identical instruments, located over the entire State of California were examined, and no simultaneous pulses were found at the time of the strong ULF pulses observed at the quake site instrument, thus eliminating solar/magnetospheric activity as a potential cause. In reviewing all the CalMagNet sites in the network, it was observed that all sites have varying numbers of pulsations every day, depending on the site location. These pulsations may indicate that the fault segments close to these other sites also creep and redistribute stress on a regular basis, but very slowly. This creep and redistribution of stress is a generally accepted concept, especially in a lateral strike slip fault systems. However, when the pulse rate of these unusual unipolar signals increases significantly, AND the rate is sustained for longer than a week, some threshold is exceeded and the earthquake occurs. The 2004 Parkfield M6 quake data contained long time series records, and was also reviewed to see if it behaved in a similar manner. Parkfield, which used magnetometers and data acquisition equipment different from CalMagNet sites, also manifested a pulsation history. The induction magnetometers at Park-

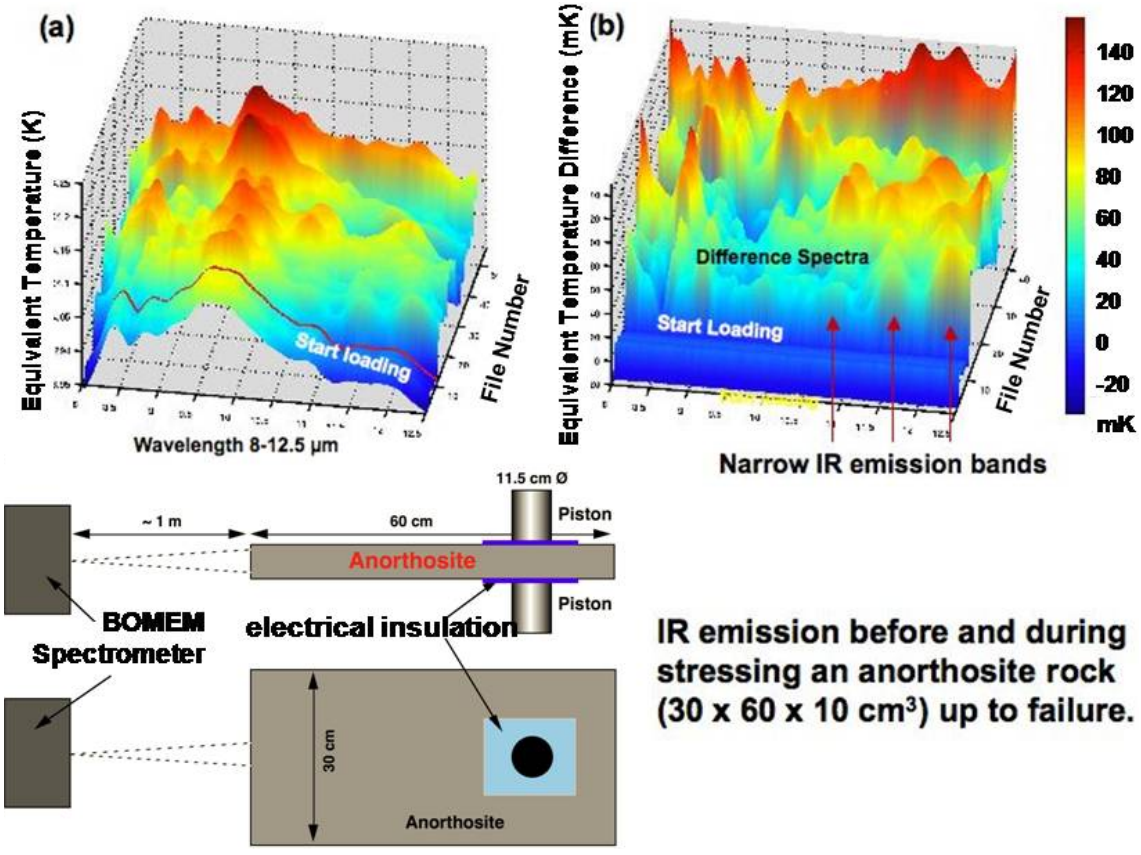

Fig. 24. Laboratory experiment (Freund, 2007a, b, c) showing increase in long wave IR after stress is applied.

field specifically exhibited a rise in daily pulse count on the 15th day prior to the quake. Although the magnitude of the pulsations collected at 19 km from the epicenter were much smaller than the Alum Rock (M5.4) pulses collected at 2 km from the epicenter, but this may have been caused by the greater distance between the epicenter and the instrument, and the high conductivity in the NE side of the fault between the epicenter and the instrument.

10.1.2 Air conductivity

The air conductivity instrument at the Alum Rock site was examined and showed a large increase in signal (number of ions per cm^3 per s). The instrument saturated from -20 to -7 h prior to the quake, and relative humidity (a contamination source) was relatively low (74%) during that time, and should not have caused contamination since it was below the instrument's saturation threshold (95% RH). Design changes in the sensor have been completed to help eliminate this humidity contamination in the future.

10.1.3 Infrared

Infrared signatures from the GOES-West geosynchronous satellite showed an unusual night time temperature slope "heating" effect compared with the 3 year average for the same area/pixels. These positive night time temperature slopes ($>+0.3$) appeared in an extended area around the quake zone compared with normal negative temperature slopes calculated from the previous 3 years of data. This technique is somewhat hampered by wind-driven, compression heating near mountains (areas where heating slope $>+0.2$) , but the area around the epicenter exceeded that noise level (slopes greater than +0.3) and were correlated with air conductivity and pulse data on the same days. There may need to be some positive threshold limit applied to this IR data to filter out this wind compression heating noise.

10.1.4 Combined EM comparisons with lab experiments

ULF pulsations, ion levels, and IR signatures are consistent with the currents, ionization, and IR signatures measured during dynamic stress measurements carried out by Freund in laboratory experiments with igneous rock samples. The primary question was whether the small signals observed in the lab would exist on a larger scale in the field, and would be detectable in the natural, noise-filled environment using a network of sensors that could be compared in space and time with the signals from the quake area. Based on field

data, it appears that there were some correlating EM signals collected at the Alum Rock and Parkfield areas, and this is a good start. While these two earthquakes do not validate the lab experiments, Alum Rock and Parkfield pulse history and IR data, and Alum Rock air conductivity data do provide some support for the rock stress-electromagnetic signal theory. However, as in any test of a theory, more statistical samples of significant earthquakes (>M5) are needed, and it is increasingly important that this data include calibrated local ULF, air conductivity, and IR measurements to help validate the connection between large earthquakes and these electromagnetic signatures.

10.2 Future plans

This team is now adding a pulse counting algorithm for many other CalMagNet instrument sites located throughout California to constantly monitor these signatures and compare them against the local averages to identify similar large pulsations that exceed a threshold level. A more sophisticated "pattern matching" algorithm may be developed in the future to account for the differences in pulse height at longer distances from the epicenter, and to eliminate shorter, lightning-generated pulses.

We are trying to collaborate with NASA Ames in routinely monitoring IR signatures over California using GOES-West IR data, and then comparing the daily IR results with our CalMagNet data. We hope to start this collaboration in 2009.

Other indicators such as ionospheric TEC changes over the earthquake area should also be added to the list of EM indicators for testing, but processing all this TEC satellite and ground-derived data, may be beyond the scope of funding for our team at this time.

Acknowledgements. The authors wish to acknowledge funding for this activity from C. Ford (Stellar Solutions), J. LaBrecque (NASA Hq Earth Surface and Interior Focus Area), and DHS/FEMA. We are also grateful for the supporting ULF data at PKD (Parkfield) from UC Berkeley, and GOES IR imager data from NASA and NOAA.

Edited by: M. Contadakis
Reviewed by: D. McPhee and D. Ouzounov

References

Bortnik, J., Cutler, J. W., Dunson, C., and Bleier, T.: An automatic wave detection algorithm applied to Pc1 pulsations, J. Geophys. Res., 112, A04204, doi:10.1029/2006JA011900, 2007.

Bortnik, J., Cutler, J. W., Dunson, C., and Bleier, T. E.: The possible statistical relation of Pc1 pulsations to Earthquake occurrence at low latitudes, Ann. Geophys., 26, 2825–2836, 2008a, http://www.ann-geophys.net/26/2825/2008/.

Bortnik, J., Cutler, J. W., Dunson, C., Bleier, T. E., and McPherron, R. L.: Characteristics of low latitude Pc1 pulsations during geomagnetic storms, J. Geophys. Res., 113, A04201, doi:10.1029/2007JA012867, 2008b.

Cutler, J., Bortnik, J., Dunson, C., Doering, J., and Bleier, T.: CalMagNet - an array of search coil magnetometers monitoring ultra low frequency activity in California, Nat. Hazards Earth Syst. Sci., 8, 359–368, 2008, http://www.nat-hazards-earth-syst-sci.net/8/359/2008/.

Derr, J. S.: Earthquake lights: a review of observations and present theories, B. Seismol. Soc. Am., 63, 2177–2187, 1973

Fraser-Smith, A. C., Bernardi, A., McGill, P. R., Ladd, M. E., Helliwell, R. A., and Villard Jr., O. G.: Low-Frequency Magnetic Field Measurements near the Epicenter of the Ms 7.1 Loma Prieta Earthquake, Geophys. Res. Lett., 17(9), 14651468, 1990.

Fraser-Smith, A. C., Bernadi, A., McGill, P. R., and Villard Jr., O. G.: ULF magnetic field measurements near the epicenter of the Ms 7.1 Loma Prieta Earthquake, Phys. Earth Planet. In., 68 45–63, 1991.

Freund, F. T.: Pre-earthquake signals - Part I: Deviatoric stresses turn rocks into a source of electric currents, Nat. Hazards Earth Syst. Sci., 7, 535–541, 2007a, http://www.nat-hazards-earth-syst-sci.net/7/535/2007/.

Freund, F. T.: Pre-earthquake signals - Part II: Flow of battery currents in the crust, Nat. Hazards Earth Syst. Sci., 7, 543–548, 2007b, http://www.nat-hazards-earth-syst-sci.net/7/543/2007/.

Freund, F. T.: Stimulated IR emission from rocks: Assessing a stress indicator, eEarth, 2, 1–10, 2007c.

Freund, F. T., Takeuchi, A., and Lau, B. W.: Electric currents streaming out of stressed igneous rocks – A step towards understanding pre-earthquake low frequency EM emissions, Phys. Chem. Earth, 31, 389–396, 2006.

Fujinawa, Y. and Takahashi, K.: Emission of electromagnetic radiation preceding the Ito seismic swarm of 1989, Nature, 347, 376–378, 1990.

Liu, J. Y., Chen, Y. I., Chuo, Y. J., and Tsai, H. F.: Variations of ionospheric total electron content during the Chi-Chi earthquake, Geophy. Res. Lett., 28, 1383–1386, 2001.

Molchanov, O., Schekotov, A., Fedorov, E., Belyaev, G., and Gordeev, E.: Preseismic ULF electromagnetic effect from observation at Kamchatka, Nat. Hazards Earth Syst. Sci., 3, 203–209, 2003, http://www.nat-hazards-earth-syst-sci.net/3/203/2003/.

Molchanov, O., Fedorov, E., Schekotov, A., Gordeev, E., Chebrov, V., Surkov, V., Rozhnoi, A., Andreevsky, S., Iudin, D., Yunga, S., Lutikov, A., Hayakawa, M., and Biagi, P. F.: Lithosphere-atmosphere-ionosphere coupling as governing mechanism for preseismic short-term events in atmosphere and ionosphere, Nat. Hazards Earth Syst. Sci., 4, 757–767, 2004, http://www.nat-hazards-earth-syst-sci.net/4/757/2004/.

Ouzounov, D., Liu, D., Kang, C., et al.: Outgoing long wave radiation variability from IR satellite data prior to major earthquakes, Tectonophysics, 431, 211–220, 2007.

Pulinets, S. and Boyarchuk, K.: Ionospheric Precursors of Earthquakes, Springer Verlag, 350 pp., 2004.

Unsworth, M., Bedrosian, P., Eisel, M., Egnert, G., and Siripunvaraporn, W.: Along strike variations in the electrical structure of the San Andreas Fault at Parkfield, California, Geophys. Res. Lett., 27, 3021–3024, 2000.

Yen, H. Y., Chen, C. H., and Liu, J. Y.: Geomagnetic fluctuations during the 1999 Chi-Chi earthquake in Taiwan, Earth Planets Space, 56, 39–45, 2004.

eEarth, 2, 1–10, 2007
www.electronic-earth.net/2/1/2007/

eEarth

Stimulated infrared emission from rocks: assessing a stress indicator

F. T. Freund[1,2], A. Takeuchi[2,3], B. W. S. Lau[2], A. Al-Manaseer[4], C. C. Fu[5], N. A. Bryant[6], and D. Ouzounov[7]

[1]Ecosystems Science and Technology Branch, Code SGE, NASA Ames Research Center, Moffett Field, CA 94035-1000, USA
[2]Department of Physics, San Jose State University, San Jose, CA 95192-0106, USA
[3]Department of Chemistry, Niigata University, Ikarashi-ninotyo, Niigata 950-2181, Japan
[4]Department of Civil Engineering, San Jose State University, San Jose, CA 95192-0083, USA
[5]Department of Civil Engineering, University of Maryland, College Park, MD 20742, USA
[6]Jet Propulsion Laboratory, Org. 3880, Pasadena, CA 91109-8099, USA
[7]CEORS, George Mason University, Fairfax, VA 22030-4444, USA

Received: 16 May 2006 – Published in eEarth Discuss.: 24 July 2006
Revised: 7 November 2006 – Accepted: 13 December 2006 – Published:

Abstract. To study the effect of stress-activated positive hole (p-hole) charge carriers on the infrared (IR) emission from rocks, we subjected a portion (∼10 vol.%) of a large ($30\times60\times7.5\,cm^3$) block of anorthosite, a nearly monomineralic (Ca-rich feldspar) igneous rock, to uniaxial deviatory stress up to failure. We measured the IR emission from a flat surface ≈40 cm from the stressed rock volume over the 800–1300 cm^{-1} (7.7–12.5 μm) range. Instantly, upon loading, the emission spectrum and intensity change. At first narrow bands appear at 930 cm^{-1} (10.75 μm), 880 cm^{-1} (11.36 μm), 820 cm^{-1} (12.4 μm) plus additional narrow bands in the 1000–1300 cm^{-1} (7.7–10.0 μm) range. The 10.75–12.4 μm bands are thought to arise from vibrationally excited O-O stretching modes, which form when p-hole charge carriers, which spread from the stressed rock volume into the unstressed rock, recombine at the surface. They radiatively decay, giving rise to "hot" bands due to transitions between excited states. Before failure the broad emission bands at 1170 cm^{-1} and 1030 cm^{-1} (8.7 and 9.7 μm) also increase slightly in intensity, suggesting a small increase in temperature due to thermalization of the energy deposited into the surface through p-hole recombination. Stimulated IR emission due to hole-hole recombination and its follow-on effects may help understand the enhanced IR emission seen in night-time satellite images of the land surface before major earthquakes known as "thermal anomalies".

Correspondence to: F. T. Freund
(ffreund@mail.arc.nasa.gov)

1 Introduction

In this paper we describe a laboratory experiment that may help understand the cause for the non-stationary, transient areas of enhanced IR emission from the land surface, which have been recognized since the late 1980s and early 1990s in night-time satellite images and linked to impending earthquake activity (Gornyi et al., 1988; Qiang et al., 1991, 1990; Srivastav et al., 1997). The reported increase in surface temperatures reach 2–4°C, occasionally higher. Such areas of enhanced IR emission are referred to as "thermal anomalies".

The phenomenon of thermal anomalies has remained enigmatic (Cui et al., 1999; Srivastav et al., 1997; Tronin, 2000, 2002; Tronin et al., 2004). In many cases the reported increase in temperature seems to correlate poorly with meteorological ground data. The rapidity with which the thermal anomalies appear and disappear rules out that they are caused by a flow of Joule heat from a source deep below that would heat the rocks. Several other processes have been invoked to account for the reported temperature increase: (i) rising fluids that could lead to the emanation of warm gases (Gorny et al., 1998); (ii) rising well water levels and changing moisture contents in the soil (Chadha et al., 2003); (iii) diffuse CO_2 emanation, causing a "local greenhouse" effect (Quing et al., 1991; Tronin, 1999, 2002); (iv) Near-ground air ionization due to enhanced radon emission leading to the condensation of water vapor from the atmosphere and, hence, to the release of latent heat (Pulinets et al., 2005). However, at closer inspection, none of these explanations seem to be able to adequately account for characteristic features of the "thermal anomalies".

Here we report on a laboratory experiment conducted to test a very different hypothesis: could it be that the enhanced

Published by Copernicus GmbH on behalf of the European Geosciences Union.

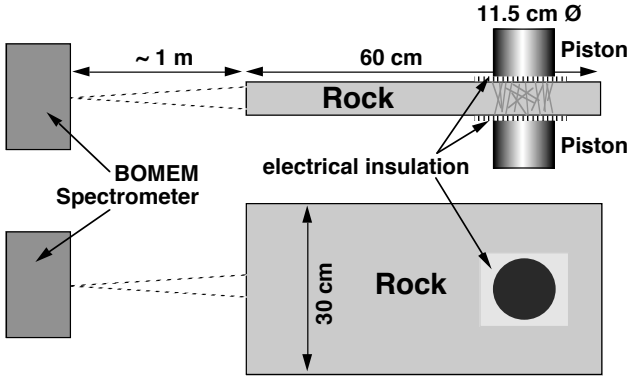

Fig. 1a. Schematic of the set-up used to measure the IR emission from the flat front face of a $60\times30\times7.5\,cm^3$ block of anorthosite, loaded over 40 cm away from the emitting rock surface.

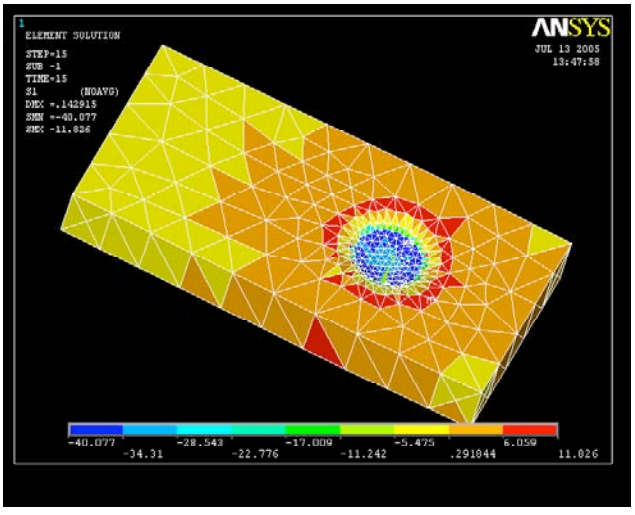

Fig. 1b. Finite analysis representation, using a variable grid size, of the stress distribution in the anorthosite block during asymmetric loading. Yellow to blue signify compressive stresses, yellow to red tensile stresses. The surface from where the IR emission is measured (circular, 5 cm diameter, $\sim$20 cm^2) is on the hidden surface on the upper left.

IR emission from the Earth's surface arises from electronic charge carriers from deep within the Earth's crust when rocks are subjected to increasing stresses prior to large earthquakes? We know that such electronic charge carriers are activated by stress and that they are highly mobile (Freund, 2002). We know that they diffuse rapidly to the surface where they become trapped (Freund et al., 2006; Takeuchi et al., 2006). The question that we seek to answer by our experiment is: do these electronic charge carriers recombine at the rock surface leading to a diagnostically distinct IR emission in the region of the thermal infrared?

2 Experimental part

Our sample was a block of anorthosite from Larvik, Norway, available under the trade name "Blue Pearl". Anorthosite is an igneous monomineralic feldspar rock composed mainly of Ca-rich plagioclase labradorite. The rock we used was coarse-grained with crystals up to 2–4 cm in size with a density of 2.7 g/cm^3 and an unconstrained compressive strength of 181–187 MPa.

We uniaxially stressed a relatively small subvolume, 10–12 vol.%, of an air-dry anorthosite slab, $60\times30\times7.5\,cm^3$, via a pair of pistons (11.25 cm diameter), electrically insulated from the rock through 0.8 mm thick sheets of high density polyethylene with a resistivity of $>10^{14}$ Ω cm. We applied the load off-center as sketched in Fig. 1a, about one piston diameter away from the edges and about four piston diameters (>40 cm) away from the surface, which emitted the IR radiation measured during our experiment. Figure 1b depicts the distribution of the principal stress as obtained by finite element analysis. The off-center loading concentrated the stresses in the back portion of the slab and kept the emitting front surface of the slab essentially stress-free, especially during the early phase of the loading run when the absolute stresses are still relatively small. We applied the load at a constant rate of 6.3 MPa/min up to failure, using a hydraulic SATEC press, model RD 2000 kN.

Emission spectra were recorded off a circular area, 5 cm diameter, from the flat front face of the rock, smooth "as received", i.e. as cut with a diamond saw. We used a Bomen MB-100 FT-IR spectroradiometer equipped with a Peltier-cooled HgCdTe detector and two integrated blackbody emitters for internal calibration, one at ambient temperature, the other at 60°C, collecting the IR radiation sequentially from the sample and the two blackbody emitters. This Bomen MB-100 has been used extensively for laboratory and field calibrations for NASA's MODIS spectrometers currently flying on the TERRA and AQUA satellites (Li et al., 1999; Wan et al., 1996).

During our experiment the laboratory was semi-darkened. The space between rock and spectroradiometer, about 1 m, was shielded from ambient light. The temperature in the laboratory was stable. As an additional precaution the movement of all personnel during the 36 min long run was restricted to avoid changes in the reflected IR radiation field.

The spectra were recorded over the wavenumber range 700–1400 cm^{-1} (7.14–14.25 μm) at 2 cm^{-1} resolution. Each FT-IR file consists of 25 scans off the rock surface plus 5 scans off the ambient temperature blackbody and 5 scans off the 60°C blackbody emitters for temperature calibration. It took 40 s to acquire and store each file. The radiometric noise at the single scan level was $\sim$100 mK, improving to $\sim$50 mK upon averaging 25 scans and to $\sim$10 mK upon averaging 250 scans. The run lasted a total 2200 s (36 min 40 s), during which 250 scans or 10 files were recorded during the first 400 s (6 min 40 s) without applying a load.

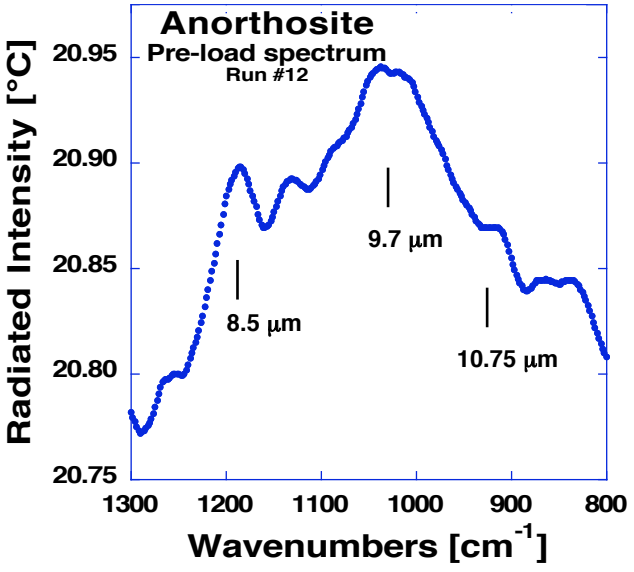

Fig. 2. IR emission spectrum at room temperature (average of 10 files of 25 scans each) from the flat front surface of the anorthosite block before loading.

The IR flux emitted from the rock surface was calculated in brightness temperature T_B with reference to the built-in calibration emitter surfaces, using the same algorithm as for MODIS calibration runs. T_B is an energy scale widely used in remote sensing, where the intensity at frequency ν is defined as $I_\nu = B_\nu$ (T_B) with B_ν in units of [Joule s^{-1} m^{-1} $ster^{-1}$ Hz^{-1}] given as $B_\nu \approx 2\nu^2\, kT_B/c^2$, with k the Boltzmann constant, T_B the absolute temperature, and c the speed of light. Expressing T_B in terms of wavelength λ, we obtain $T_B \approx [\lambda^4/2\,kc]\, I_\lambda$. This relation shows that, while T_B depends on the fourth power of the wavelength of the emitted light, changes in the actual (Joule) temperature will cause smooth intensity changes over the entire spectral range.

3 Results

Figure 2 shows the pre-loading room temperature (300 K) IR emission spectrum of the anorthosite from 800 to 1300 cm^{-1} (7.7–12.5 μm), averaged from the 250 pre-loading scans (10 files). The spectrum has two maxima, around 1030 and 1170 cm^{-1} (9.7 and 8.5 μm, respectively), plus a smaller emission peak around 1110 cm^{-1} (9.0 μm). These bands are characteristic of Si–O and Al–O stretching modes emitted from the first few μm of the rock surface (Johnson et al., 2002). This room temperature emission is caused by downward transitions of 3-dimensionally coupled Si–O and Al–O stretching modes, primarily from their populated first vibrationally excited states thermally at 300 K, e.g. from quantum number n=1, to the ground state n=0.

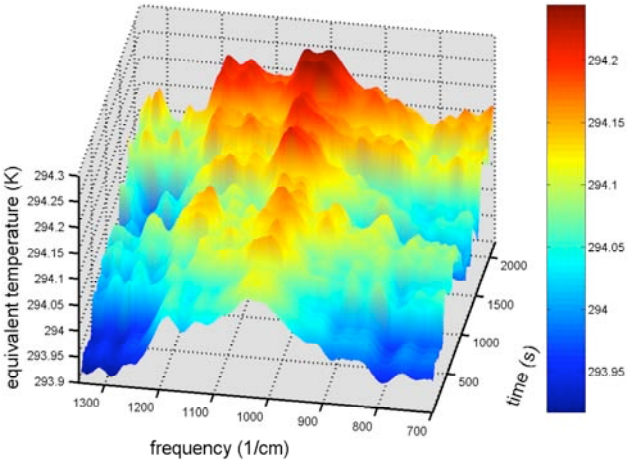

Fig. 3a. 3-D plot of the intensity evolution and spectral changes of the IR emission between 700–1350 cm^{-1} (7.37–14.3 μm) from the front face of the anorthosite block before and during loading up to failure, plotted as a function of time during loading (for details see text). The color scale is given in degrees K and is meant to emphasize the changing intensities.

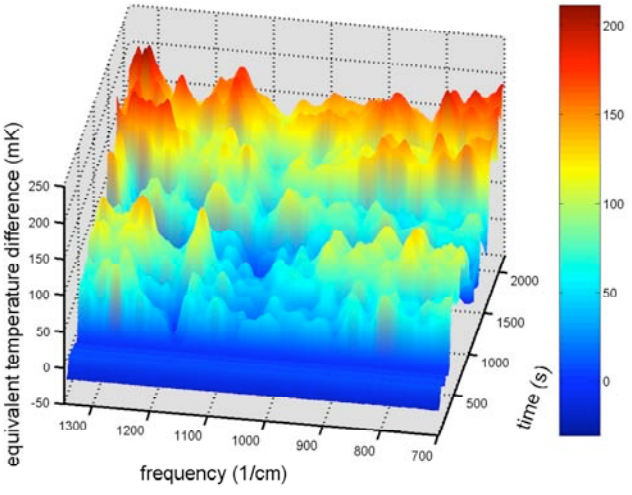

Fig. 3b. Difference plot of the intensity evolution and spectral changes of the IR emission from the front face of the anorthosite block obtained by subtracting each file recorded during loading from the average of the pre-load files. The color scale is given in degrees mK and is meant to emphasize the changing excess intensities.

Figure 3a shows a 3-D plot of the intensity variations over the 7.4–14.3 μm range (700 to 1350 cm^{-1}) as a function of time. The intensity axis is given in units of brightness temperature, T_B. The time axis is labeled in seconds. During the first 6 min 40 s, as we acquired 250 pre-load scans (10 files) with no stress applied, the emitted IR intensity is constant. This is consistent with a stable ambient temperature environment in the laboratory and the absence of any other

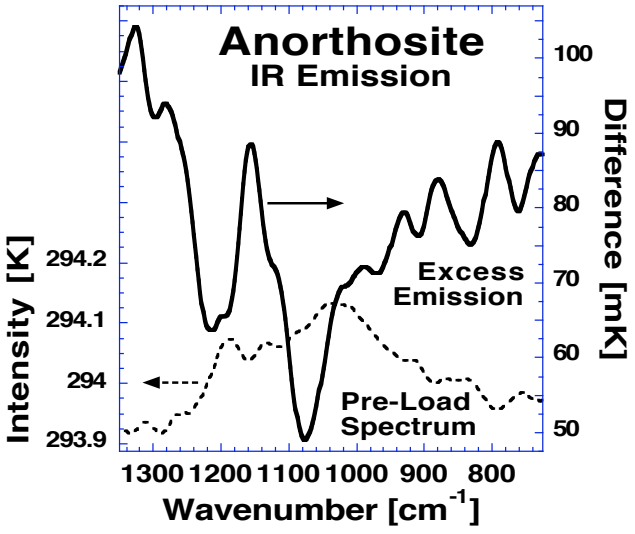

Fig. 4. Total excess intensity emitted over the 7.37–14.7 μm range from the front face of the anorthosite block during loading (solid line) compared to the pre-load spectrum (dotted line).

perturbations. After 6 min 40 s we began to apply the load and immediately saw a change in the spectral signature, in particular new narrow emission bands, plus an overall increase in IR intensity. Upon increasing the load, the intensities fluctuate. Such fluctuations had already been observed during earlier IR emission experiments with granite (Freund et al., 2002b, 2003). The IR intensity fluctuations resemble current fluctuations observed during measurements of "battery currents", which flow out of a stressed rock volume through the unstressed rock (Freund et al., 2004, 2006).

The difference spectra in Fig. 3b show the excess intensity emitted over the spectral range as a function of time. The difference spectra were obtained by subtracting the average of the first 250 pre-load scans (10 files) from each of the files acquired during loading up to failure. There are three outstanding features:

1. Narrow emission bands appear immediately upon loading, specifically three bands in the 800–950 cm^{-1} range (10.5–12.5 μm) plus narrow bands at higher wavenumbers (shorter wavelengths).

2. The intensity fluctuations as a function of time are synchronous across the entire spectral range, though the fluctuations of different bands are not evenly distributed.

3. The excess intensity emitted during loading is concentrated at wavelengths that are different from those of the two emission maxima in the pre-load emission spectrum.

This last point is highlighted in Fig. 4 where we superpose the pre-load 300 K spectrum and the excess IR intensity integrated over the entire run. The narrow emission bands are preserved even after integration, in particular the three diagnostically significant bands in the 800–950 cm^{-1} (10.5–12.5 μm) range, plus a prominent narrow band around 1150 cm^{-1} (8.7 μm). While the pre-load spectrum exhibits intensity maxima at 1030 cm^{-1} and 1170 cm^{-1} (9.7 and 8.5 μm), the excess emission has minima near these same wavenumber/wavelength values.

During two earlier measurement sessions with granite we already had the opportunity of record the IR emission from the surface of a large block of rock stressed a distance away from the emitting surface. We observed similar spectral features, in particular narrow emission bands at the start of loading (Freund et al., 2002a, 2003). Granite contains about 1/3 quartz, 1/3 plagioclase feldspar and 1/3 potassium feldspar. Similar to the observation reported here, excess IR was emitted in narrow bands in the 800–950 cm^{-1} (10.5–12.5 μm) range plus some bands in the 1150 cm^{-1} (8.7 μm) range. The present results confirm these earlier observations, though the narrow emission bands from granite occurred at slightly different wavenumbers, within $\sim$10 cm^{-1}, probably due to its more complex mineralogy.

4 Discussion

Rock fracture experiments as described in the literature are typically performed under conditions emulating ASTM C170-50 and DIN 52102 procedures, i.e. with cylindrical test samples loaded over their entire cross section (Brady and Rowell, 1986; Lockner, 1993; Rowell et al., 1981; Warwick et al., 1982; Yoshida and Ogawa, 2004).

Loading unconstrained cylindrical samples over their entire cross sections creates conditions that are very different from those described here and different from pre-earthquake conditions in the field. In the field, the rocks deep in the Earth's crust are subjected to increasing stress, while observations are made off the Earth's surface, far from the stressed rock volume. In the experiment described here we subject a relatively small subvolume of the large rock sample to deviatory stresses, thereby activating mobile electronic charge carriers. We thus create a gradient in the concentration of these charge carriers between the subvolume and the surrounding unstressed rock. No mechanical forces act on the surface from where the IR emission occurs. In the case of cylinders loaded over their entire cross section, the surface bulges outward, leading to tensile stresses in the surface, which in turn lead to microfracturing. Microfracturing is known to cause visible and IR emission over a broad spectral range (Brady and Rowell, 1986) due to a number of physical processes that take place in the opening cracks such as electric discharges, electron and atom or molecule emissions, ionization and electronic excitations, etc. (Dickinson, et al., 1986). Only the stressed rock volume emits light during these processes and the spectral composition of this light

is very different from the narrow band IR emission reported here.

The experiment presented here was designed from the beginning in such a way that the stresses generated during loading would be confined to the back portion of the slab and would not extend to the surface that emitted the IR emission radiation. Because of the large distance between the emitting surface and the stressed rock volume, >40 cm, we can rule out that frictional heat generated in the stressed rock could diffuse to the emitting surface within 40 s, the time needed to acquire 25 scans with the Bomen FT-IR spectroradiometer and to convert them into one file. Hence, under our conditions, the IR emission from the front surface of the block, cannot be due to Joule heat diffusing from the stressed subvolume to the emitting surface.

Another possibility is that, upon loading the subvolume, gases and possibly liquids contained in its pore space might be expelled and travel as a pressure wave through the pore space in the remainder of the rock, inducing rapid changes far from the stressed subvolume. However, we can discount this process on the basis of two arguments: (i) given the geometry of our rock sample and stress distribution illustrated by Fig. 1b, such a pressure wave, if it forms, would more likely discharge through the near-by surfaces under tensile stress rather than travel to the surface furthest from the stress subvolume; (ii) even if the pressure wave arrives at the emitting surface, it would more likely cool the surface through adiabatic decompression than cause the emission of excess IR intensity in the form of specific narrow bands.

Neither diffusion of frictional heat to the rock surface nor the arrival of a pore gas pressure wave can account for observed changes in the IR emission characteristics. Hence we conclude that there must be another process capable of transporting energy rapidly from the stressed rock subvolume to the rock surface, over a distance of >40 cm, and of causing the observed changes, both spectral and intensitywise, in the IR emission.

A candidate for such a process, for which we have strong supporting evidence, is the flow of electronic charge carriers from the stressed subvolume to the rock surface. Such charge carriers have been shown to exist in igneous rocks such as anorthosite, albeit in a dormant, electrically inactive form (Freund, 2002; Freund et al., 2006, 2004). In the following we briefly review what these charge carriers are and what is already known about them.

It is widely assumed in the geoscience community that oxygen anions in naturally occurring minerals are fixed in their 2-valence state. However, it has been shown some time ago that a reaction exists by which oxygen anions can change their valence from 2- to 1- (Freund and Wengeler, 1982; Martens et al., 1976). The reaction involves hydroxyl pairs, which are ubiquitous in all minerals that have crystallized in the presence of H_2O, even those that are nominally anhydrous. Hydroxyl pairs in the matrix of these nominally anhydrous minerals can split off H_2 while simultaneously converting their O^{2-} to the 1- (peroxy) state (Freund, 1985).

A single O^- in a matrix of O^{2-} represents a defect electron, resident in the valence band of otherwise insulating materials, also known as a positive hole or p-hole for short. Normally O^- form pairs, which we call positive hole pairs, PHP. In oxide materials the PHPs form peroxy anions, O_2^{2-} (Batllo et al., 1991; Freund et al., 1993). In silicate minerals they form peroxy links, $O_3X/^{OO}\backslash XO_3$ with X=Si^{4+}, Al^{3+} etc. Peroxy links in fused silica have attracted a large amount of attention because, when present in fused silica optical fibers exposed to high energy γ- or x-rays in space, they lead to color centers with an intense, broad absorption in the visible and near-IR regions (Edwards and Fowler, 1982; Ricci et al., 2001). The same peroxy links in fused silica generate mobile p-hole charge carriers when heated (Freund, 1985). Minerals that crystallize in the presence of H_2O invariably always incorporate some "water" in the form of hydroxyl (Ingrin and Skogby, 2000; Wilkins and Sabine, 1973). Hydroxyl pairs in the matrix of these minerals are thought to convert to peroxy links (Freund, 1985). This makes all igneous and high-grade metamorphic rocks candidates for containing PHPs (Freund, 2003).

As long as the O^- exist in the PHP or peroxy state, the p-holes are self-trapped and, hence, electrically inactive. When deviatory stresses are applied, the rocks begin to plastically deform through dislocations moving in large numbers through the mineral grains (Miguel et al., 2001; Moore and Lockner, 1995; Ohnaka, 1995). When moving dislocations intersect the PHPs, they instantly cause them to break apart and to release p-hole charge carriers (Freund et al., 2006).

As defect electrons in the valence band of the otherwise insulating silicate minerals the p-holes can move on the O 2sp-dominated levels close to the upper edge of the valence band by exchanging an electron with a neighboring O^{2-}. Theoretically the speed with which the p-holes could travel is on the order of 300 m/s, consistent with the group velocities in the range of 100–300 m/s measured experimentally (Freund, 2002). Because the valence band forms an energetic continuum the p-holes can jump grain boundaries. In experiments such as described here, where we stress a portion of a larger slab of rock, the p-holes can flow out of the stressed volume and into unstressed rock (Freund et al., 2006). When they reach the surface, they form a positive charge layer (Freund et al., 1993; King and Freund, 1984). Positive surface charges have also been observed during fracturing (Enomoto et al., 1993). Surface potentials measured under open circuit conditions can reach +1.5 V to +1.75 V. Charge densities on freshly fracture surfaces have been given as 10^{-5} Coulomb/m^2 or 10^{13}–10^{14} p-holes/m^2 (Takeuchi et al., 2006; Takeuchi and Nagahama, 2002b). The charge carrier densities at the rock surface achieved under conditions such as in our experiment may be lower, but the measured values give an estimate, by order of magnitude, of the number of p-hole charge carriers available at the rock surface.

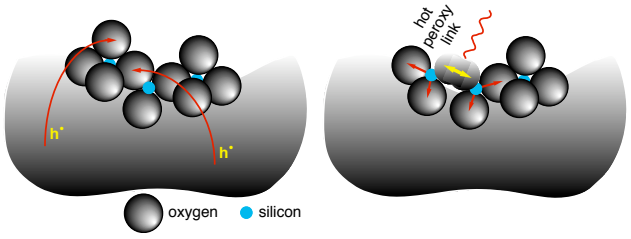

Fig. 5. Schematic representation of a mineral surface to illustrate the processes that may take place when p-holes (h) arrive at the surface (left). When the two p-holes recombine, recombination energy is released, leading to a vibrationally highly excited O-O bond, which can de-excite radiatively by emitting IR photons characteristic of transitions the energy levels of the O–O bond, and non-radiatively by channeling energy into neighboring bonds (right).

Of particular interest to the IR emission is the fact that it costs energy to break a peroxy bond. This energy is expended in the stressed rock volume in the form of mechanical work dispensed during plastic deformation. If the p-holes recombine at the surface to restitute peroxy bonds, some of this energy will be regained. However, this recombination energy will be deposited into the newly formed O^--O^- bonds, causing them to be "born" in a vibrationally highly excited state.

To estimate the energies involved we need to know at least approximately the O-O bond energy. The energy needed to photodissociate a peroxy link in fused silica is relatively high, 9.4 eV (Nishikawa et al., 1990). By contrast, the activation energy to thermally split a peroxy bond is much lower, on the order of 2.4 eV (Freund et al., 1993). The large difference is due to the fact that, during photodissociation, electrons must be excited across the large band gap at the same k-value in reciprocal space. By contrast, thermal bond break-up can be achieved through excitation of vibrational modes irrespective of the k-value in reciprocal space. When a bond breaks during the passage of a dislocation, i.e. during mechanical deformation, we expect the energy required to be similar to that of thermal break-up, i.e. around 2.4 eV. In addition we note that the energy of the peroxy bond as well as the O-O bond distance depend only weakly on the surrounding, i.e. they are closely the same for peroxy anions in the matrix of MgO and for peroxy links in matrix of fused silica. Without loss of generality we can extend this argument to silicate minerals and, by extension, to rocks (Freund, 2003). Hence, we adopt a value around 2.4 eV as the maximum energy that can become available when p-holes recombine at our rock surface to form PHPs.

In Fig. 5 we represent the rock surface by three corner-linked SiO_4 tetrahedra, two of which terminate with non-bonded oxygens. Typical distances between adjacent O^{2-} are on the order of 2.8 Å. On the left we show two p-holes arriving at the surface and settling on two adjacent oxygen anions changing them from O^{2-} to O^-. On the right we show these two O^- snapping together to form the very short, ∼1.5 Å, O^-–O^- bond characteristic of peroxy links (Ricci et al., 2001).

If an energy up to 2.4 eV is released during p-hole recombination, the new O^--O^- bond will be "born" in a vibrationally highly excited state. Due to its high frequency, such an excited state will be largely decoupled from the thermal vibrations of the surrounding matrix. To dissipate the excess energy two decay channels are available: (i) radiative decay by emitting photons at the characteristic energies of transitions within the O-O vibrational manifold or (ii) non-radiative decay by channeling energy onto neighboring Si-O and Al-O bonds. Those neighboring bonds in turn become excited and will emit at their characteristic vibrational frequencies.

As mentioned above the room temperature emission spectrum such as shown in Fig. 2 arises from downward transitions of vibrational modes from levels that are thermally excited at the temperature of 300 K. The probability to populate the levels E_n above the ground state E_o is given by a Boltzmann distribution, $\exp[-(E_n–E_0)/kT]$ where k is the Boltzmann constant and T the absolute temperature. We are interested in the IR emission around 1000 cm^{-1} or 10 μm. In this wavenumber or wavelength range the energy levels are separated by ≈100 meV. However, the mean thermal energy available at 300 K, kT_{300K}, is ≈25 meV. Hence, the probability to populate the first excited level n=1 in the 10–12 μm region, is $e^{-4} \approx 2 \times 10^{-2}$ or ≈2%. To populate the second excited level, n=2, ≈200 meV above E_0, the probability drops to $e^{-8} \approx 10^{-4}$ or ≈0.02% etc. Therefore, at thermal equilibrium at 300 K, vibrational levels n=2 and higher are sparsely populated. In other words, nearly all IR intensity emitted at 300 K is due to downward transitions from the n=1 level to the n=0 ground level. If higher vibrational levels can be excited by some other, non-thermal process, downward transitions will occur between the higher levels, for instance from n=2 to n=1 or n=3 to n=2, etc. Those emission bands are called "hot bands".

Remarkable about the difference spectra in Fig. 3b is that they clearly show narrow emission bands appearing already at the very beginning of loading. In particular we point to the three narrow bands toward the right. The band at 930 cm^{-1} (10.75 μm) is consistent with the fundamental stretching mode of the O^--O^- bond, arising from n=1 to n=0 transitions of peroxy links. The energy of this transition for $O_3Si/^{OO}\backslash SiO_3$ in amorphous SiO_2 has been determined by high level quantum-mechanical calculations to be 920–930 cm^{-1} (10.75–10.87 μm) (Ricci et al., 2001). The energies of "hot" transitions, from n=2 to n=1 and from n=3 to n=2, have not yet been calculated, However, they are expected to lie at slightly lower wavenumbers (longer wavelength) due to the asymmetry of the potential describing the O-O bond.

The energy V as a function of interatomic distance r of a diatomic oscillator such as O-O can be described by a Morse

potential, $V(r)=D_c\{1-\exp[-\alpha(r-r_0)/r_0]\}$, where D_c is the dissociation energy, r_0 the equilibrium distance, and α an adjustable constant. The Morse potential is a parabola that opens asymmetrically to one side. The eigenvalues, which can be obtained by solving the Schrödinger equation for the system, show a sequence of energy levels ever more narrowly spaced the higher the level n of vibrational excitation. If the narrow band at 930 cm^{-1} in Figs. 3a, b is the fundamental arising from n=1 to n=0 transitions, then the narrow bands at 870 cm^{-1} (11.5 μm), and 810 cm^{-1} (12.35 μm) are consistent with "hot" bands arising from n=2 to n=1 and n=3 to n=2 transitions respectively. In other words, these bands come from suprathermal transitions and suggest emissions that involve vibrationally excited states higher than n=2.

The intensity evolution of the three bands at 930 cm^{-1} (10.75 μm), 870 cm^{-1} (11.5 μm), and 810 cm^{-1} (12.35 μm) is plotted in Fig. 6 for the first three 2-min intervals after beginning of loading. The bands at 810 cm^{-1} (12.35 μm) and 870 cm^{-1} (11.5 μm), which we assign to hot transitions, exhibit high intensities in the beginning. Later the fundamental at 930 cm^{-1} (10.75 μm) gains intensity in relative and absolute terms, while the hot bands seem to merge.

The narrow bands in the 1000–1200 cm^{-1} (8.3–10 μm) range in Fig. 3b display a similar intensity evolution as a function of time and load. They are consistent with the concept shown in Fig. 5 depicting (on the right) that the vibrationally excited O^--O^- bond channels energy onto its Si-O neighbors, probably through combination with phonon modes. This causes those neighboring bonds to become excited and emit at their own characteristic frequencies.

In Fig. 4 we integrated the excess intensity emitted over the course of the experiment, from the beginning of loading to failure of the rock. The excess intensity curve exhibits narrow maxima around 1150 and 1300 cm^{-1} (7.7 and 8.7 μm, respectively) but minima close to where the 300 K spectrum has its broad emission maxima. This suggests that the energy gained by p-hole recombination at the surface is primarily used to excite local oscillators. While they give rise primarily to non-thermal emissions, they do not excite the pool of 3-dimensionally coupled lattice modes, i.e. they do not "heat" the surface. This is consistent with the statement made above that vibrationally highly excited levels are largely decoupled from the lattice modes that vibrate at their fundamental frequencies at 300 K. As a result the excess energy deposited during p-hole recombination into the newly born O^--O^- bonds is mainly radiated off as narrow-band IR photons at 930 cm^{-1} (10.75 μm), 870 cm^{-1} (11.5 μm), and 810 cm^{-1} (12.35 μm) and others at lower wavenumbers or longer wavelengths, which we did not measure in our experiment. A fraction of this energy is used to selectively excite next-nearest neighbor Si–O and Al–O bonds.

As this process continues, the next-nearest neighbor Si–O and Al–O bonds will in turn "kick" their neighbors and transfer energy to them so that they transition from their ground state n=0 to the first excited state n=1. In other words, the energy deposited into local O-O vibrations will eventually flow into the 3-dimensionally coupled lattice vibrations, i.e. thermalize and thereby cause the overall energy, kT, in a thin surface layer to increase. As Figs. 3a, b indicate, this thermalization and increase in kT are most pronounced shortly before failure of the rock.

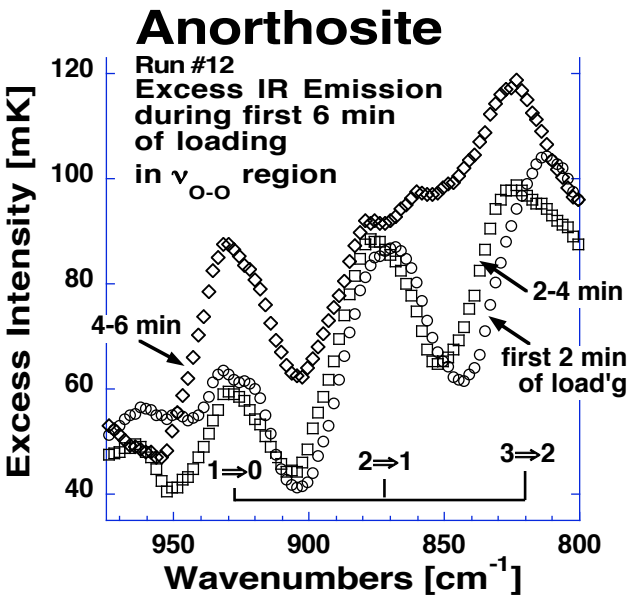

Fig. 6. Evolution of the IR emission bands in the spectral range expected to contain the O-O fundamental and "hot bands" during the first 6 min of loading, broken down in 2 min intervals.

Hence, the observations presented here support our proposition that the emission spectrum of the anorthosite rock during stressing is at first dominated by non-thermal processes, giving rise to the series of narrow emission bands that include "hot" bands. The "hot" bands can be described as "stimulated IR luminescence" due to exothermal p-hole recombination at the surface. Later, as more and more p-holes arrive at the rock surface and recombine, the energy deposited into the O-O bonds begins to spread out and thermalize. This causes an overall, albeit small, increase in kT, i.e. an increase in the actual temperature of a thin surface layer.

To estimate how much energy can be radiated during p-hole recombination we need to know (i) how many p-holes arrive at the surface and (ii) how much energy is released per p-hole recombination event.

(i) For a surface across a dielectric contrast from ε=10 to ε=1 theory predicts the build-up of a surface potential on the order of +0.4 V (King and Freund, 1984). Pulse-like values as high as +12 V to +17 V have been observed experimentally during crack formation (Enomoto et al., 1993; Freund et al., 2004). Steady state surface potentials reach values up to +0.1 V to +1.5 V depending on the geometry of the capacitive sensor, implying charge carrier densities of $\approx 10^{-5}$ Coulomb m^{-2},

equivalent to $\approx 10^{13}$ charges m^{-2} (Freund, 2002; Freund et al., 2006; Takeuchi et al., 2006; Takeuchi and Nagahama, 2002a, b).

(ii) We can estimate how many p-hole recombination events are needed to produce a 0.15 K increase of radiation temperature. The activation energy for breaking a peroxy bond is ≈2.4 eV (Freund, 2003). If this energy were to be fully regained during p-hole recombination, each recombination event would release 2.4 eV, equivalent in terms of thermal energy kT to ≈10 000 K. This means that $\approx 10^5$ recombination events spread over a surface area of 20 cm^2 (the size of our emitting surface) would suffice to increase the radiative temperature by 0.1 K.

Our emitting surface of 20 cm^2 contains $\approx 10^{16}$ O^{2-} anions. Accepting a charge carrier density of $\approx 10^{-5}$ Coulomb m^{-2} or $\approx 10^{13}$ charges m^{-2} (Takeuchi and Nagahama, 2002b), such a surface of 20 cm^2 will reach a surface potential of 1 V when $\approx 10^{10}$ p-holes have arrived. Since we estimated that as few as $\approx 10^5$ recombination events per unit time are needed to increase the radiative temperature of our emitting surface by 0.1 K, only a very small fraction of the p-holes, which reach the surface, $\approx 10^{-5}$, need to participate at any time in the IR emission process.

Such an order-of-magnitude estimate gives us confidence that the proposed mechanism for the observed increase in radiative temperature lies within the limit of our basic assumptions. We note that the rock surface, which emitted the IR radiation in our experiment, was smooth. If it had been rougher by a geometric factor of about 10, the radiative IR flux would probably have increased by approximately the same factor to an equivalent temperature around 2 K, closer to the 2–4°C temperature increases reported for the "thermal anomalies" before major earthquakes.

5 Conclusions

We have presented here just one experiment conducted under specific laboratory conditions with a block of monomineralic anorthosite. Our paper necessarily leaves many questions unaddressed. However, we have demonstrated that, by stressing a small subvolume of the rock far away from the emitting surface, the IR emission changes with respect to both, spectral composition and intensity. The changes are consistent with a fundamental process, never before described, that involves vibrationally highly excited states of O-O bonds at the rock surface. The most convincing indicator of such a process is the appearance of distinct narrow band emissions at the beginning of our experiment. Subsequently, as more and more energy is deposited into the surface layer through the recombination of more p-holes, an overall temperature increase occurs, presumably due to thermalization of the vibrationally excited O-O states.

It is reasonable to assume that this energy, which first causes localized vibrationally excited states and then heats up the surface through thermalization, can be transferred across the rock-air interface to the air. Such a secondary or tertiary process would be consistent with the suggestions made by a number of authors that the "thermal anomalies" as derived from satellite data arise in the near-ground air (Dey and Singh, 2003; Parnell, 2002; Tronin, 2002; Tronin et al., 2004).

When we apply stress over 40 cm away from the emitting rock surface and observe within 40 s or less changes in the IR emission, we can say with confidence that both, the IR intensity and IR spectrum, are consistent with (i) the flow of p-hole charge carriers from the stressed rock volume to the emitting surface and (ii) an exothermal recombination of p-holes to form positive hole pairs, PHP. It is consistent with a radiative decay of the vibrationally excited O-O bonds and with the channeling of some of their excess energy onto neighboring Si–O and Al–O bonds and eventual thermalization. The surface that emits the IR radiation is clearly too far from the stressed rock volume for frictional heat to reach the surface within such a short time.

Obviously, the areas of the Earth where "thermal anomalies" are observed are much more complex that the surface of the rock sample that we studied in the laboratory. Their surfaces are formed mainly of sedimentary deposits, soil and sand, rarely bare rocks. Preliminary laboratory studies (unpublished) have provided evidence that p-holes are capable of propagating through layers of soil and sand separating two blocks of rock and through layers of water.

The experiment described here and its interpretation suggest that p-holes provide a physically plausible mechanism to transport energy rapidly over macroscopic distances, from deep within the Earth's crust to the surface. At least a part of this energy is released at the surface following conversion into IR photons of specific wavelengths. Though further experiments are obviously needed to address these and many other questions raised by the study presented here, it appears probable that the recombination of p-hole charge carriers at the Earth's surface is the primary driver behind the pre-earthquake "thermal anomalies" identified in satellite images.

Acknowledgements. This work would not have been possible without support from Z. Wan and his coworkers Y. Zhang and Q. Zhang, ICESS, University of California at Santa Barbara, who brought their BOMEN radiospectrometer and other radiometric equipment three times to our laboratory. They helped us perform the experiments but do not necessarily subscribe to our interpretation of the results. We thank Y. Fei, Geophysical Laboratory, Carnegie Institution of Washington, and M. Jhabvala, NASA Goddard Space Flight Center, for help during the early phase of this project. We thank two anonymous reviewers for their thoughtful comments. We acknowledge financial support by a grant from the NASA Ames Research Center Director's Discretionary Fund. B. W. S. Lau was supported by a grant from the National Geospatial

Agency (NGA). A. Takeuchi acknowledges support from the Japan Society for the Promotion of Science (JSPS) for Young Scientists.

Edited by: J.-P. Valet

References

Batllo, F., LeRoy, R. C., Parvin, K., Freund, F., and Freund, M. M.: Positive hole centers in MgO – correlation between magnetic susceptibility, dielectric anomalies and electric conductivity, J. Appl. Phys., 69, 6031–6033, 1991.

Brady, B. T. and Rowell, G. A.: Laboratory investigation of the electrodynamics of rock fracture, Nature, 321, 488–492, 1986.

Chadha, R. K., Pandey, A. P., and Kuempel, H. J.: Search for earthquake precursors in well water levels in a localized seismically active area of Reservoir Triggered Earthquakes in India, Geophys. Res. Lett., 30, 69–71, 2003.

Cui, C., Zhang, J., Xiao, Q., Liu, Q., Luo, D. J., and Lu, Q.: Monitoring the thermal IR anomaly of Zhangbei earthquake precursor by satellite Remote sensing technique, paper presented at ACRS, 1999.

Dey, S. and Singh, R. P.: Surface latent heat flux as an earthquake precursor, Nat. Hazards Earth Syst. Sci., 3, 749–755, 2003.

Dickinson, J. T., Jensen, L. C., McKay, M. R., and Freund, F.: The emission of atoms and molecules accompanying fracture of single-crystal magnesium oxide, J. Vac. Sci. Technol., 4, 1648–1652, 1986.

Edwards, A. H. and Fowler, W. B.: Theory of the peroxy-radical defect in a-SiO2., Phys. Rev. B Solid State, 26, 6649–6660, 1982.

Enomoto, Y., Akai, M., Hashimoto, H., Mori, S., and Asabe, Y.: Exoelectron emission: Possible relation to seismic geoelectromagnetic activities as a microscopic aspect in geotribology, Wear, 168, 135–142, 1993.

Freund, F.: Conversion of dissolved "water" into molecular hydrogen and peroxy linkages, J. Non-Crystalline Solids, 71, 195–202, 1985.

Freund, F.: Charge generation and propagation in rocks, J. Geodynamics, 33, 545–572, 2002.

Freund, F., Freund, M. M., and Batllo, F.: Critical review of electrical conductivity measurements and charge distribution analysis of MgO, J. Geophys. Res., 98, 22 209–22 229, 1993.

Freund, F. T., Jhabvala, M., La, A., Shu, P., Tsay, S., Ouzounov, D., and Fei, Y.: Mid-infrared luminescence observed during rock deformation, paper presented at Spring Meeting, Amer. Geophys. Union, Washington, D.C., 2002a.

Freund, F. T., Ouzounov, D., Freund, M. M., Wan, Z., Zhang, Q., Zhang, Y., Jhabvala, M., La, A., McClare, M., Velle, A. M., Fei, Y., and Tsay, S.: Mid-Infrared radiation, electric charges and acoustic emission during rock deformation, paper presented at Fall Meeting, Amer. Geophys. Union, Washington, D.C., 2002b.

Freund, F. and Wengeler, H.: The infrared spectrum of OH–compensated defect sites in C-doped MgO and CaO single crystals, J. Phys. Chem. Solids, 43, 129–145, 1982.

Freund, F. T.: On the electrical conductivity structure of the stable continental crust, J. Geodynamics, 35, 353–388, 2003.

Freund, F. T., Ouzounov, D., Wan, Z., Zhang, Y., Zhang, Q., Post, R., Keefner, J., Mellon, J., and Al-Manaseer, A.: Stimulated IR emission from the surface of rocks during deformation, paper presented at American Geophysical Union, Fall Meeting 2003, AGU, San Francisco, CA, 2003.

Freund, F. T., Takeuchi, A., Lau, B. W. S., Post, R., Keefner, J., Mellon, J., and Al-Manaseer, A.: Stress-induced changes in the electrical conductivity of igneous rocks and the generation of ground currents, Terrestrial, Atmospheric and Oceanic Sciences (TAO), 15, 437–468, 2004.

Freund, F. T., Takeuchi, A., and Lau, B. W.: Electric currents streaming out of stressed igneous rocks – A step towards understanding pre-earthquake low frequency EM emissions, Phys. Chem. Earth, 31, 389–396, 2006.

Gornyi, V. I., Salman, A. G., Tronin, A. A., and Shilin, B. B.: The Earth's outgoing IR radiation as an indicator of seismic activity, Proc. Acad. Sci. USSR, 301, 67–69, 1988.

Ingrin, J. and Skogby, H.: Hydrogen in nominally anhydrous upper-mantle minerals: concentration levels and implications, European J. Mineralogy, 12, 543–570, 2000.

Johnson, J. R., Hörz, F., Lucey, P. G., and Christensen, P. R.: Thermal infrared spectroscopy of experimentally shocked anorthosite and pyroxenite: Implications for remote sensing of Mars, J. Geophys. Res., 107, 5073–5086, 2002.

King, B. V. and Freund, F.: Surface charges and subsurface space charge distribution in magnesium oxide containing dissolved traces of water., Phys. Rev., B29, 5814–5824, 1984.

Li, Z.-L., Becker, F., Stoll, M., Wan, Z., and Zhang, Y.: Channel selection for soil spectrum reconstruction in 8–13 μm region, J. Geophys. Res., 104, 22 271–22 286, 1999.

Lockner, D.: The role of acoustic emission in the study of rock fracture, Int. J. Rock Mechanics Mining Sci., 30, 883–899, 1993.

Martens, R., Gentsch, H., and Freund, F.: Hydrogen release during the thermal decomposition of magnesium hydroxide to magnesium oxide, J. Catalysis, 44, 366–372, 1976.

Miguel, M. C., Vespignani, A., Zapperi, S., Weiss, J., and Grass, J.-R.: Intermittent dislocation flow in viscoplastic deformation, Nature, 410, 667–671, 2001.

Moore, D. E. and Lockner, D. A.: The role of microcracking in shear-fracture propagation in granite, J. Struct. Geol., 17, 95–114, 1995.

Ohnaka, M.: A shear failure strength law of rock in the brittle-plastic transition regime, Geophys. Res. Lett., 22, 25–28, 1995.

Parnell, J.: Fluid Seeps at Continental Margins: towards an Integrated Plumbing System,Geofluids, 2, 57–65, 2002.

Pulinets, S. A, Ouzounov, D., Ciraolo, L., et al.: Thermal, atmospheric and ionospheric anomalies around the time of the Colima M7.8 earthquake of 21 January 2003, Ann. Geophys., 24, 835–849, 2006.

Qiang, Z.-J., Xu, X.-D., and Dian, C.-D.: Thermal infrared anomaly – precursor of impending earthquakes, Chinese Sci. Bull., 36, 319–323, 1991.

Qiang, Z. J., Xu, X. D., and Dian, C. G.: Abnormal infrared thermal satellite-forewarning of earthquakes, Chinese Sci. Bull., 35, 1324–1327, 1990.

Quing, Z., Xiu-Deng, X., and Chang-Gong, D.: Thermal infrared anomaly- precursor of impending earthquakes, Chinese Sci. Bull., 36, 319–323, 1991.

Ricci, D., Pacchioni, G., Szymanski, M. A., Shluger, A. L., and Stoneham, A. M.: Modeling disorder in amorphous silica with embedded clusters: The peroxy bridge defect center, Phys. Rev. B, 64, 224 104–224 108, 2001.

Rowell, G. A., Brady, B. T., Yoder, L. P., and Hanson, D. R.: Precursors of laboratory rock failure, in: Fracture Mechnanics for Ceramics, Rocks, and Concrete, edited by: Freiman, S. W. and Fuller, E. R., pp. 196–220, ASTM, Philadelphia, PA, 1981.

Srivastav, S. K., Dangwal, M., Bhattachary, A., and Reddy, P. R.: Satellite data reveals pre-earthquake thermal anomalies in Killari area, Maharashtra, Current Sci., 72, 880–884, 1997.

Takeuchi, A., Lau, B. W., and Freund, F. T.: Current and surface potential induced by stress-activated positive holes in igneous rocks, Phys. Chem. Earth, 31, 240–247, 2006.

Takeuchi, A. and Nagahama, H.: Interpretation of charging on fracture or frictional slip surface of rocks, Phys. Earth Planet. Inter., 130, 285–291, 2002a.

Takeuchi, A. and Nagahama, H.: Surface charging mechanism and scaling law related to earthquakes, J. Atmos. Electricity, 22, 183–190, 2002b.

Tronin, A. A. (Ed.): Satellite thermal survey application for earthquake prediction, 717–746 pp., Terra Sci. Publ., Tokyo, Japan, 1999.

Tronin, A. A.: Thermal satellite data for earthquake research, paper presented at IGARSS 2000, IEEE 2000 international geoscience and remote sensing symposium. Taking the pulse of the planet: the role of remote sensing in managing the environment, IEEE, Honolulu, HI, 2000.

Tronin, A. A.: Atmosphere-lithosphere coupling: Thermal anomalies on the Earth surface in seismic processes, in: Seismo-Electromagnetics: Lithosphere-Atmosphere-Ionosphere Coupling, edited by: Hayakawa, M. and Molchanov, O. A., 173–176, Terra Scientific Publ., Tokyo, 2002.

Tronin, A. A., Molchanov, O. A., and Biagi, P. F.: Thermal anomalies and well observations in Kamchatka, Int. J. Rem. Sens., 25, 2649–2655, 2004.

Wan, Z., Snyder, W., and Zhang, Y.: Validation of land-surface temperature retrieval from space, paper presented at IGARSS '96: Remote Sensing for a Sustainable Future, Geoscience and Remote Sensing Symposium, IGARSS, Lincoln, NE, 1996.

Warwick, J. W., Stoker, C., and Meyer, T. R.: Radio emission associated with rock fracture: Possible application to the great Chilean earthquake of May 22, 1960, J. Geophys. Res., 87, 2851–2859, 1982.

Wilkins, R. W. T. and Sabine, W.: Water contents of some nominally anhydrous silicates, Amer. Mineral., 58, 508–516, 1973.

Yoshida, S. and Ogawa, T.: Electromagnetic emissions from dry and wet granite associated with acoustic emissions, J. Geophys, Res., 109, B09204, doi:10.1029/2004JB003092, 2004.

MEETING: **American Geophysical Union Fall 2009 Meeting**

DATE: 14-18 December 2009

DEADLINE: 03 September 2009 for Abstract submission

VERSION: v5

Session: P22: Exploring Venus
Sponsor: Planetary Sciences

Convener: Jorn Helbert
DLR
DEU
Joern.Helbert@dlr.de

Nils Mueller
DLR
DEU
nils.mueller@dlr.de

Sue Smrekar
JPL
USA
suzanne.e.smrekar@jpl.nasa.gov

Index Terms: 0343 8149 6063 6295 .

Description: Venus exploration is experiencing a strong revival. The ESA mission Venus Express has been in orbit around Venus for more than 4 years, awaiting the arrival of JAXA's Venus Climate Orbiter at the end of 2010. The Russian space agency has confirmed the Venera-D mission and there are several Venus missions proposed in the US. Already our picture of Venus has changed significantly, opening up a number of new questions. Upcoming missions will most likely answer some of the questions and open new ones. It is therefore a good time to summarize what we know about Venus and which new questions we face, together with the old questions that are still open. This will allow us to define a framework for upcoming missions, giving guidance for the future exploration of Venus.

http://www.agu.org/meetings/fm09/program/abstract_submissions.php

Radar Reflectivity Changes of Rock Surfaces due to Thermally-Activated Charge Carriers: Contribution to the Understanding of the Magellan Venus Radar Reflectivity Data.

Colin Williams[1], George Tsoflias[2], Gary G. Cyr[3], Robert Dahlgren[4], John Keefner[5], and Friedemann Freund[4,6,7]

Radar observations of Venus collected by NASA's Magellan mission show unusually high radar reflectivity from the Maxwell Montes, a massif that reaches an elevation of about 11.4 km above the lowlands, and from other high mountain ranges. The high radar reflectivity suggests a surface layer with a high electric conductivity, but the nature of such a layer remains poorly understood.

In this work, the surface reflection coefficient of gabbro was measured in the laboratory with a ground-penetrating radar system operating at an RF frequency of 1.2 GHz. One end of a block of gabbro was placed into an electric furnace, and heated to 600°C. Positive electronic charge carriers in the oxygen anion sublattice, e.g. "positive holes" = O^- in a matrix of O^{2-}, become activated in two steps, at 300°C and more massively >430°C, while the negative charge carriers remain trapped. The positive holes flow out of the heated subvolume and diffuse into the colder portion of the rock. They accumulate at the cooler surface, giving rise to a surface/subsurface layer with enhanced electrical conductivity. The radar reflectivity from the cold end increased when the hot end reached 300°C and increased upon further heating, up to 5% above baseline at 25°C. These data suggest that the high radar reflectivity of high elevations on Venus may not by caused by a chemical surface deposit such as a sulfide layer. Rather, it appears to be due to the electrically conductive surface layer formed by positive holes, which are activated in the rocks of the hotter lowland regions and diffuse to cooler mountain tops. The temperature of the Venus lowlands is ~475°C, while that of the highlands is ~375°C. Further studies of heat-activated charge carriers in rocks and their drift in the presence of large-scale temperature gradients will deepen our understanding of physical and geological processes on Venus.

1 NSF-REU student 2009, Department of Physics, San José State University
2 Department of Geology, University of Kansas
3 San José State University Foundation
4 Department of Physics, San José State University
5 NASA Ames Research Center 2003 Academy
6 Carl Sagan Center, SETI Institute
7 Earth Science Division, NASA Ames Research Center